Imperial College London

Department of Materials

Phase Stability in Steels under Electropulsing

Wenjun Lu

A dissertation submitted in partial fulfilment of requirements for the degree of Doctor of Philosophy of Imperial College London September 2015

STATEMENT OF COPYRIGHT

The copyright of this thesis rests with the author and is made available under a Creative Commons Attribution Non-Commercial No Derivatives licence. Researchers are free to copy, distribute to transmit the thesis on the condition that they attribute it, that they do not use it for commercial purposes and that they do not alter, transform or build upon it. For any reuse or redistribution, researchers must make clear to others the licence terms of this work.

DECLARATION OF ORIGINALITY

Wenjun Lu, hereby declare that the contents of this thesis “Phase Stability in Steels by Electropulsing” belongs to my own. Neither this thesis nor the work contained within have been submitted elsewhere for any other qualification. The contents of this thesis are the results of my own research conducted under the supervision of Prof. Rongshan Qin. All work of others has been acknowledged and referenced in the form of a list of sources.

Abstract

There are increasing interests to alternate the microstructure and hence the properties of steels that are applied in various environment conditions using a work-efficient and energy-saving manner. The desirable microstructure evolution is often not achievable by means of conventional thermo-mechanical processing and solid-state phase transition. This thesis has considered four fundamental engineering problems, namely (i) the possibility of anti-aging processing for the aged steels in service at high temperature, (ii) the recovery of the lost strength for the steels at high temperature, (iii) the suspension of crack initiation and propagation during cold-working of steels with eutectoid microstructures and (iv) the regaining of strength during tempering of a steel containing martensite. Phase stability in the processing environment is the primary concern in each of the list problems because it presents, in thermodynamically, the possibility to achieve the goals using the designed processing. Electropulsing processing has been considered and integrated with the conventional thermomechanical processing in the development of this PhD thesis. The so-called electropulsing treatment utilises electric current pulses with high peak current density and short pulse duration. Due to the nature of the short duration pulse, the energy consumption is very low. The high current density enables a very strong impact of electropulsing on the microstructure evolution and hence is work efficient.

Following results have been obtained through the study：

- Using the appropriate electropulsing parameters, the formed secondary phase (e.g. χ-phase) by precipitation in 316L stainless steels at elevated temperature can be dissolved. Electropulsing processing can supress the precipitation and homogenize the alloying

elements in the stainless steel. The stability of the secondary phases in the stainless steel has been changed by the imposed electropulse.

- Electropulsing treatment is able to alternate the delta-ferrite phase transition. This has been proved in the treatment of 2205 duplex stainless steel. The new format of phase transition causes strengthening of the steel at high temperature. The stability of phases in the steel has been affected by the applied electropulsing treatment.

- For the light steels containing high aluminium composition, electropulsing is able to affect the thermodynamic stability and grain morphology of κ-carbide. This leads to significant improvement of steel formability.

- Application of electropulsing processing to dual-phase automotive steel changes the stability of martensite phase. The processing improve the mechanical properties and refined the microstructure of this steel.

The fundamental understanding of the experimental observations has been developed based on the thermodynamic and kinetic analysis.

Acknowledgements

The author is grateful to Prof Rongshan Qin for his encouragement and supervision throughout this project. He would like to thank Prof Kenneth C. Mills and Dr Xinfang Zhang for fruitful discussions, and also to all members of the Steel Processing Group for their advice and help.

The author is grateful to TATA Steel and Engineering and Physical Sciences Research Council (EPSRC) for financial support of this research.

The author would like to express his acknowledgement to his family members, friends and colleagues for their support and encouragement. The author would be harder without their help and support during the three years PhD study.

“Developing the ability of thinking and judging independently instead of obtaining professional knowledge should be put in the first place.”

Albert Einstein (Germany)

List of Figures

Figure 2.1: Schematic illustration of a linear relationship between flow stress and MFFP for a carbon steel.

Figure 2.2: The influence of secondary phases with different morphologies (spherical, pearlitic and elongated carbides) on the ductility of steel.

Figure 2.3: Schematic diagram of general corrosion process for steels under high-concentration chloride environments.

Figure 2.4: Schematic diagrams of molecular structure of (a) austenite (FCC) and (b) ferrite (BCC).

Figure 2.5: Schematic diagram of dislocation pile-up in (a) fine grain and (b) coarse grain.

Figure 2.6: The relationship between yield stress and grain size of mild steel at 18 ºC.

Figure 2.7: The relations between true strain and grain size for 1100-Al and interstitial free steel.

Figure 2.8: Schematic drawings of nano-scale twinning with twin layer thickness (λ) and twin boundary spacing (Δ), and a twin boundary structure.

Figure 2.9: Schematic showing of the dislocation motions in stage (1), stage (2) and stage (3).

Figure. 2.10: The effect of EPT on microstructure and properties of polycrystalline metals and alloys.

Figure 2.11: The grain refinement of materials under EPT: The fabrication of ultrafine grained microstructure via solidification (high temperature) and the formation of nano-scale grains via crystallization or solid state phase transformation (low temperature).

Figure 2.12: Schematic diagrams of inclusion movement in alloys under EPT.

Figure 2.13: Schematic diagram of dislocation movement under EPT. The motion of dislocation can be effectively accelerated by transferring energy from electrons via collision. The direction of electrons is opposite to the direction of electric filed between anode and cathode.

Figure 2.14: A process of crack healing in a medium carbon steel under EPT. Left: A precrack is manually created in steel sample; middle: EPT is applied across the steel sample between anode and cathode; and Right: The precrack is partially healed under EPT.

Figure 2.15: A schematic diagram to describe relationships between EPT and microstructure evolutions in literature.

Figure 2.16: A schematic diagram of EPT on phase stability via changing Gibbs free energy: $G_e < 0$ indicates the phase stability is favourable, whereas $G_e > 0$ shows the phase stability is disfavourable. $G_e = 0$ means no any influence on stability of phase in an electric-current free system.

Figure 2.17: A schematic description of effects of EPT on four specific steels especially the phase stabilities. This includes the precipitation in 316L austenitic stainless steel, phase transformation in 2205 duplex stainless steel, cracking in duplex lightweight steel and softening in dual-phase steel.

Figure 3.1: (a) a cold rolling machine and (b) a cutting machine.

Figure 3.2: Experimental set-up of EPT processing.

Figure 3.3: Photographs depicting sample preparation procedures: (a) a mounting machine with (b) Mounting power, (c) a grinding and polishing machine with (d) grinding and polishing lubricant, (e) chemical etching and (f) optical microscope.

Figure 3.4: Photographs showing (a) a SEM JEOL 6400 microscope with (b) WDS and (c) EBSD, and a SEM LEO microscope.

Figure 3.5: Photographs of (a) a sparking machine and (b) electro-jet polishing machine for TEM sample preparation, and (c) a TEM 2000FX microscope.

Figure 3.6: Photographs showing (a) a commercial 316L austenitic stainless steel plate, (b) a XRD spectra for as-received 316L stainless steel specimen, (c) an optical micrograph of hot-rolled steel specimen and (d) an optical micrograph of cold-rolled steel specimen.

Figure 3.7: An equilibrium phase diagram of 316L stainless steels calculated using a commercial software, Thermo_Calc 3.0 with TCFE7 database.

Figure 3.8: SEM micrographs of the cold rolled steel sample (83.3%) at 750 ^{o}C for (a), (c) and (e) 30 mins and for (b), (d) and (f) 60 mins.

Figure 3.9: (a) Typical SEM micrograph of steel sample at 750 ^{o}C for 60 mins, and EDS spectra for (b) white precipitates and (c) dark steel matrix.

Figure 3.10: TEM micrographs for the steel sample microstructure annealed at 750 ^{o}C for 60 mins.

Figure 3.11: (a) TEM image for bright field of steel microstructure, (b) and (d) are the SADP of austenite matrix and its corresponding schematic diagram, respectively, and (c) and (e) are the SADP of χ phase and its corresponding schematic diagram, respectively.

Figure 3.12: SEM images of (a), (c) and (e) the distribution of χ phase in the sample without EPT; (b), (d) and (f) the distribution of χ phase in steel sample with EPT. (g) and (h) the number distribution of χ phase in steel samples without and with EPT, respectively.

Figure 3.13: FIB-SIMS elementary mapping for Mo distribution in steel samples (a) without EPT and (b) with EPT.

Figure 3.14: EBSD mapping for grain size measurement: (a) and (c) steel sample without EPT at different magnifications; (b) and (d) steel sample with EPT at different magnifications.

Figure 3.15: EBSD mapping for grain boundary portion measurement: (a) and (c) steel sample without EPT at different magnifications; (b) and (d) steel sample with EPT at different magnifications.

Figure 3.16: Schematic diagrams of spherical precipitate in steel matrix under EPT. (a) represents the distribution of current across the microstructure consisting of a precipitate (B) and steel matrix (A): the electrical conductivity of precipitate is the same as steel matrix). The current lines directly pass the precipitate and matrix without any changing. (b) shows the distribution of current across the microstructure consisting of a precipitate (C) and steel matrix (A): the electrical conductivity of a precipitate is less than that of steel matrix. The current lines are altered due to the discrepancy of electrical conductivity between precipitate and matrix.

Figure 3.17: Gibbs free energy change as a function of temperature for χ-phase and austenite. The red line represent the phase transformation temperature (χ-phase ↔ austenite), whereas the green line correspond to the operation temperature of current experiment.

Figure 4.1: A schematic diagram illustrates the microstructure of 2205 duplex stainless steel consisting of austenite (blue) and delta-ferrite phases (orange).

Figure 4.2: A steel specimen (2×1.5×15 mm) and its microstructure on longitudinal plane (contains both delta-ferrite and austenite). Note: ED is electric current direction (marked by orange arrow), ND is normal direction, TD is transverse direction and RD is rolling direction.

Figure 4.3: Schematic diagram of the experimental set up for EPT.

Figure 4.4: Equilibrium phase diagram of a 2205 duplex stainless steel calculated by MTDATA with TCFE4 database. The blue, red and black lines represent the sigma, austenite and delta-ferrite phases, respectively.

Figure 4.5: SEM images for steel samples without EPT ((a) and (c)) and with EPT ((b) and (d)) in the longitudinal plane.

Figure 4.6: XRD spectra of steel samples without EPT and with EPT at 835°C.

Figure 4.7: EBSD map for phase fraction measurement: (a) steel sample without EPT and (b) steel sample with EPT. Red region represents austenite, green region corresponds to delta-ferrite and white region is sigma phase.

Figure 4.8: EBSD mapping for grain size measurement: (a) steel sample without EPT and (b) steel sample with EPT.

Figure 4.9: EBSD maps for Σ3 grain boundary distribution measurement: (a) steel sample without EPT and (b) steel sample with EPT.

Figure 4.10: EDS spectra for austenite, delta-ferrite and sigma phases in the duplex stainless steel treated at 835 ºC (a) without EPT and (b) with EPT. The positions 1, 2 and 3 correspond to the sigma, austenite and delta-ferrite phases, respectively.

Figure 4.11: Vickers hardness of the samples without and with EPT.

Figure 4.12: A schematic diagram showing the diffusion mechanisms of alloying elements between delta-ferrite and austenite at high temperature treatment. The sigma phase and secondary austenite precipitate along the phase boundary between austenite and delta-ferrite.

Figure 4.13: Electrical resistivity of iron as a function of temperature. Note: T_c is , $T_{\alpha \rightarrow \gamma}$ is transformation temperature from α-ferrite to γ-phase, $T_{\gamma \rightarrow \delta}$ is transformation temperature from γ-phase to δ-ferrite and T_m is melting point.

Figure 4.14: Schematic diagrams showing the effect of applying EPT on the phase transformation. (a) the original microstructure of alloy contains phase (B) and phase (A); (b) the phase transformation (i.e. the phase fraction change) is moved forward when the electrical conductivity of B is less than A; (c) the phase transformation is unaltered when the electrical conductivity of B is equal to A; (d) the phase transformation is retarded when the electrical conductivity of B is greater than A.

Figure 5.1: A schematic diagram showing the relationship between (D_α/D_γ) ratio and temperature.

Figure 5.2: SEM micrographs of steel specimens annealed at (a-b) 600 ^oC for 6h, (c-d) 700 ^oC for 6h and (e-f) 800 ^oC for 6h.

Figure 5.3: SEM micrographs of (a) the nano-ordered κ-carbide within austenite and (c) the rod-like κ-carbide within ferrite; TEM bright images of (b) the nano-ordered κ-carbide within austenite and (d) the rod-like κ-carbide within ferrite; (e) the SADP of the nano-ordered κ-carbide within austenite and their schematic diagram of SADP and (f) the SADP of rod-like κ-carbide within austenite and their schematic diagram of SADP.

Figure 5.4: (a) XRD spectra for steel specimens annealed at 600-800 ^{o}C for 6h, (b) the calculated volume fraction of phases (austenite, ferrite and κ-carbide) via XRD results and (c) the Vickers hardness value of steel specimens annealed at 600-800 ^{o}C for ferrite and austenite regions.

Figure 5.5: (a) SEM micrograph of the specific region contains three phases: austenite + ferrite, austenite + κ-carbide and carbide free austenite, (b) chemical compositions of alloying elements (Mn, Al and Fe) across the area marked by the red line, (c) a schematic diagram of lattice mismatch for 2 × 2 × 2 cells between κ-carbide and austenite, and (d) a schematic diagram of lattice mismatch for 2 × 2 × 2 cells between κ-carbide and ferrite.

Figure 5.6: Schematic diagram showing a standard κ-carbide crystal structure.

Figure 5.7: Photographs showing a process for steelmaking using induction furnace: (a) an induction furnace, (b) melting the steel and (c) waiting for the steel to cool.

Figure 5.8: Schematic diagram showing the preheat treatment, rolling and annealing parameters for Fe-26Mn-9Al-0.75C (wt.%) steel specimens.

Figure 5.9: (a) Optical, (b) SEM, (c) TEM pictures, (d)-(e) diffraction patterns analysis of austenite and (f)-(g) diffraction patterns analysis of ferrite in the cold rolled specimen. All yellow arrows represent the cold rolling directions.

Figure 5.10: Phase diagram of Fe-26Mn-9Al-0.75C (wt.%) steel.

Figure 5.11: X-ray diffraction spectra (Cu K_α incident radiation) of steel specimens annealed at 500-1000 ^oC.

Figure 5.12: The volume fraction of each phase and the Vickers hardness of sample as a function of temperature.

Figure 5.13: A schematic drawing of a stress-strain curve for the steel sample annealed at 600 ^oC for 6h.

Figure 5.14: SEM micrographs showing (a) the microstructure evolutions of A1 annealed at 500 ^oC for 6 h, (b) κ-carbides precipitated at the phase boundary between α and γ, (c) lamellar κ-carbides starting to form at the grain boundary of γ and (d) particulate κ-carbides precipitated within α. Note: the position 1, 2 and 3 represent the austenite, phase boundary and ferrite, respectively.

Figure 5.15: SEM micrographs showing (a) the microstructure evolutions of A2 annealed at 600 ^oC for 6 h ,(b) κ-carbides coarsen at the phase boundary between α and γ, (c) lamellar κ-carbides fully precipitated by eutectiod decomposition within and γ and (d) particular κ-carbides coarsen within α.

Figure 5.16: SEM micrographs illustrating (a) the microstructure evolution of sample A5 annealed at 700 ^oC for 6 h, (b) κ-carbides continually coarsen at the phase boundary between α and γ, (c) lamellar κ-carbides starting to spherodize and (d) particulate κ-carbides continually coarsening at grain boundary of α as band shape and in the grain interior as needle shape.

Figure 5.17: SEM micrographs illustrating (a) the microstructure evolutions of A8 annealed at 800 ^oC for 6 h, (b) κ-carbides dissolving completely at the phase boundary between α and γ, (c) spherical κ-carbides partially dissolving within the austenite matrix and (d) all κ-carbides dissolving within the ferrite matrix.

Figure 5.18: SEM micrographs illustrating (a) the microstructure evolution of sample A11, annealed at 900 ^{o}C for 6 h and (b) the microstructure evolution of sample A12 annealed at 1000 ^{o}C for 6 h. All κ-carbides in either position 1, 2 or 3 are dissolved completely.

Figure 5.19: A schematic graph showing the 5 stages of microstructure evolution of steel specimens as a function of temperature.

Figure 5.20: (a) TEM bright field image of A2 steel specimen, (b) SADP and (c) its corresponding schematic diagram of the N-W orientation relationship between κ-carbide and ferrite.

Figure 5.21: TEM micrographs in A11 steel show (a) bright field image of austenite and (b) its associated SADP; (c) bright field image of ferrite and (d) its corresponding SADP.

Figure 5.22: SEM micrographs of the (a-b) A2 with different magnifications, (c-d) A3 with different magnifications and (e-f) A4 with different magnifications, and they show that lamellar κ-carbides are continually coarsening in the steel matrix at 600 ^{o}C for 6 to 100h.

Figure 5.23: SEM micrographs of the (a-b) A5 with different magnifications, (c-d) A6 with different magnifications and (e-f) A7 with different magnifications, and they show that lamellar κ-carbides are transformed into spherical particles within austenite region and some boundary κ-carbide and needle -shaped κ-carbide start to precipitate in ferrite region at 700 ^{o}C for 6 to 100h.

Figure 5.24: SEM micrographs of the (a-b) A8 with different magnification, (c-d) A9 with different magnification, (e-f) A10 with different magnification. They show that the spherical κ-carbide within the austenite region is growing continually and all κ-carbide in the ferrite region dissolves at 800 ^{o}C for 6 to 100h.

Figure 5.25: Vickers hardness of κ-carbide with (a) lamellar- shaped carbide in austenite at 600 ^{o}C for 6-100 h, (b) spherical- shaped carbide in austenite at 700 ^{o}C for 6-100 h and (c) spherical- shaped carbide in austenite at 800 ^{o}C for 6-100 h.

Figure 5.26: Diagrams showing (a) the growth rate of κ-carbide and (b) the increase in hardness rate as functions of temperature.

Figure 5.27: Diagrams showing calculated equilibrium concentration of (a) C, (b) Al and (c) Mn in ferrite and austenite using Thermo-Calc software.

Figure 5.28: Diagram showing the relationship between the phase ratio, γ/α and temperature for C, Al and Mn in Fe-26Mn-9Al-0.75C steel.

Figure 5.29: A schematic graph of diffusion coefficient as a function of temperature for C, Al and Mn in steels.

Figure 5.30: (a) XRD spectra of $(111)_{\gamma}$ peaks and (b) the *d*-spacing of $(111)_{\gamma}$ peaks as a function of temperature; (c) XRD spectra of $(110)_{\alpha}$ peaks and the *d*-spacing of $(110)_{\alpha}$ peaks as a function of temperature. The red lines indicate the dissolution temperature of κ-carbides.

Figure 5.31: Schematic diagrams showing the EPT experiment.

Figure 5.32: Optical micrographs of steel specimens (a) with 26Mn (b) with 34Mn, and their corresponding SEM images for microstructure (c) with 26Mn (d) with 34Mn. The TEM micrographs of (e) lamellar κ-carbide and (f) nano-ordered κ-carbide and their corresponding (g) SADP between lamellar κ-carbide and ferrite matrix, and (h) SADP between nano-ordered κ-carbide and austenite matrix.

Figure 5.33: SEM micrographs of steel specimens (a) without and (b) with EPT. Most of lamellar κ-carbides are fragmented into nano-sized spherical κ-carbide particles. The EBSD

maps of steel specimen with EPT (c-d) at different magnifications. The average grain size of steel specimen after EPT is appromately 1.46 μm.

Figure 5.34: TEM bright images of steel samples (a and c) without EPT and (b and d) with EPT. Selected area diffraction patterns of (e) κ-carbide, (f) ferrite and (g and h) the N-W orientation relationship between κ-carbide and ferrite and its corresponding schematic diagram, respectively.

Figure 6.1: Four stages in the softening process for the tempering of martenite in dual-phase steels.

Figure 6.2: Schematic diagrams showing (a) experimental set-up of EPT; (b) a dog-bone shape sample (length: 24 mm; width: 5 mm and thickness: 0.5 mm); (c) an optical microstructure of dual-phase steel consisting of ferrite and martensite and (d) a XRD spectrum showing only body centred cubic phases (ferrite or martensite) exist in the steel sample. Note: F is ferrite and M is martensite.

Figure 6.3: SEM images of steel samples (a and c) without EPT at different magnifications, (b and d) with EPT at different magnifications; TEM bright images of steel samples (e) without EPT and (f) with EPT; selected area diffraction pattern (SADP) for (g) martensite laths and (h) ferrite grains with cementite particle. Note: α' is martensite, $T\alpha'(\alpha+\theta)$ is tempering martensite and α is ferrite.

Figure 6.4: Diagram showing typical tensile engineering stress-strain curves of dual-phase steel samples (with and without EPT).

Figure 6.5: Diagrams showing a typical softening process contains four stages for the hardness of Fe-C martensitic steel tempered 1h at 100-700 ^{o}C and (b) the hardness of dual-

phase steels tempered at about 700 ^{o}C for 110 μs (EPT), 0.1s<t<1 s (non-isothermal tempering), 300s (isothermal tempering) and 5400s (isothermal tempering), respectively.

Figure 6.6: Diagrams showing (a) the microstructural evolution of dislocations in cold-formed steel sample, (b) the effect of EPT on intersection and annihilation of two partial dislocations and (c) the formation of ultrafine-grained ferrite with nano-cementite particles after EPT.

Tables

Table 2.1: Applications of electric-current treatments on precipitations in alloys.

Table 2.2: Applications of EPT on phase transformations in alloys.

Table 2.3: Applications of EPT on grain refinement for alloys.

Table 2.4: Applications of EPT on grain rotation and texture for alloys.

Table 2.5: Applications of EPT on motion of electrically non-metallic particles in alloys.

Table 2.6: Applications of EPT on dislocation movement in alloys.

Table 2.7: Applications of EPT on crack healing for alloys.

Table 4.1: The volume fraction of all phases (delta-ferrite, austenite and sigma phases) in steels without and with EPT.

Table 4.2: Chemical compositions of austenite, delta-ferrite and sigma phases measured by EDS for the steel samples without and with EPT.

Table 5.1: Thermomechanical processing parameters for Fe-26Mn-9Al-0.75C steel.

Table 5.2: 5 phase transformation stages in Fe-26Mn-9Al-0.75C steel.

Table 5.3: Factors related to diffusion coefficient of C, Mn and Al in steels.

Table 5.4: Chemical compositions of two steels used in current experiment.

Table 5.5: The thermomechanical processing parameters for two steels.

Table 6.1: Mechanical properties (e.g. yield stress, UTS and elongation) of steel samples without and with EPT.

Table 7.1: Thesis review consists of four main sections.

Table 8.1: Tasks achieved by EPT in thesis and future applications.

Symbols

EPT - electropulsing treatment

τ_s - yield strength

τ_0 or σ_y - yield stress

H_v - Vickers hardness

T - dislocation's line tension

b - burger vector

Λ - interparticle spacing

ϕ - the constant

G - shear modulus

r - radius

MFFP - mean uninterrupted free ferrite path

d - grain size

σ_0 - friction stress constants

K_y - unpinning parameters (breaking away of dislocation from interstitial sites)

λ - twin layer thickness

Δ - twin boundary spacing

DPD – dynamic plastic deformation

SPD – severe plastic deformation

d.c. – direct current

a.c. alternative current

m - mass

C_p - specific heat

ρ_d - density

ρ_e - electrical resistivity

V - volume

ΔT - temperature increment

j - current density

t - time interval

$\sigma_{(t)}$ - maximum compressive force

E - Young's modulus of material

T_{max} - maximum temperature increment

α - thermal expansion of material

$\theta_{(t)}$ - dimensionless temperature increment

$l_{(t)}$ - dimensionless thermal expansion

$\Delta T_{(t)}$ - instant temperature change

$\Delta l_{(t)}$ - instant thermal expansion

Δl_{max} - maximum thermal expansion

n - density of conduction electron

n_d - density of defects

ρ_d - defect resistivity

ρ - resistivity

m_o - free-electron mass

m^* - effective electron mass

e - elementary charge

E - macroscopic electric field

Z_{wind}^* - effective valence

J_t - atomic flux induced by temperature

J_a - atomic flux produced by electric current

D - lattice diffusion coefficient

N - density of atom species

D_a - atomic diffusion coefficient

f - pulsed current frequency

τ_p - duration of each pulse

k - gas constant

T - absolute temperature

I_r^{EPT} - nucleation rate with EPT

I_r^o - constant related to recrystallization

I_r - nucleation rate without EPT

λ - jump distance

n_o - total number of atoms

n - number of nuclei under electric-current treatments

ΔV - volume of material

$g = \mu\left[\frac{3}{2}\ln\left(\frac{R}{a}\right) - \frac{65}{48} - \frac{5}{48}\frac{\sigma_2 - \sigma_1}{\sigma_1 + 2\sigma_2}\right]R^2\Delta V$ - geometric factor

$\xi(\sigma_1, \sigma_2)$ - a factor

σ_1 - electrical conductivity of phase 1

σ_2 - electrical conductivity of phase 2

ΔG_o - Gibbs free energy without electric current

ΔG_e - Gibbs free energy with electric current

ΔG_c - chemical free energy

ΔG_i - interfacial energy

ΔG_s - strain-stress energy

δV - infinitesimal volume

$\delta \vec{S}$ - infinitesimal displacement

$\vec{F}_e$ - local electrophoresis force

ρ_c - density of conductive electron

$\vec{v}_d$ - electron movement velocity

δt - time for electrons movement

$\vec{H}$ - magnetic field strength

$\vec{D}$ - electric displacement

$\vec{B}$ - magnetic field

$\vec{A}$ - vector potential

r - random position of material

μ - magnetic permeability

M_a - pre-exponential factor dependent on the frequency of atom hipping and lattice distance

M - mobility

ΔE_k - kinetic barrier

K - Boltzmann constant

M – mobility

σ_A - electrical conductivity of steel matrix A

σ_B - electrical conductivity of precipitate B

σ_C - electrical conductivity of precipitate B

$\Delta G_{total}^{\gamma \to \chi}$ - total system free energy of 316L stainless steel without EPT

ΔG_{chem} - chemical free energy of the bulk phases

ΔG_{surf} - surface energy

$\vec{j}_b(r)$ - current density distribution before EPT

$\vec{j}_a(r)$ - current density distributions after EPT

R - electrical resistance

X_i - concentration of the ith solute

i^{th} - atom species

N_i - density of the i^{th} atom species

Ω - atom volume

$-\frac{\partial \sigma}{\partial X}$ - stress gradient

g - positive geometric factor for coarse grained materials

$\Delta \upsilon$ - volume of a nucleus

A - frequency

Q - activation energy

γ - the surface energy

L - the spacing between pinning points

FCC – face centred cubic

BCC - body centred cubic

$T_{\alpha \to \gamma}$ - transformation temperature from α-ferrite to γ-phase

$T_{\gamma \to \delta}$ - transformation temperature from γ-phase to δ-ferrite

T_m - melting point

δ - delta-ferrite

σ - sigma-phase

γ' - secondary austenite phase

γ - austenite phase

α - ferrite

α' - martensite

θ - cementite

Tα'(α+θ) - tempering martensite

κ - kappa carbide

χ – Chi phase

d.c. - direct current

a.c. - alternative current

σ_γ - electrical conductivity of austenite

σ_α - electrical conductivity of ferrite

σ_θ - electrical conductivity of cementite

σ_δ - electrical conductivity of delta-ferrite

σ_χ - electrical conductivity of chi-phase

σ_σ - electrical conductivity of sigma-phase

σ_κ - electrical conductivity of κ-carbide

TEM - Transmission Electron Microscopy

SEM - Scanning Electron Microscopy

XRD - X-rays Diffraction

SADP – Selected Area Diffraction Pattern

Content

Chapter 1 Introduction.....35

1.1. Background 35

1.2. Aims of the research.....36

1.3. Outline of the thesis.....37

Chapter 2 Assessment of the literature.....40

2.1 Microstructure and properties of steels 40

2.1.1 Precipitation.....40

2.1.2 Solid-state phase transformation 46

2.1.3 Grain size effect.....48

2.2 Effects of electropulsing on microstructure evolutions and properties.....54

2.2.1 Precipitation.....56

2.2.2 Phase transformation 60

2.2.3 Grain size.....63

2.2.4 Grain orientation and texture.....67

2.2.5 Control electrically non-metallic particles motion 71

2.2.6 Dislocation.....73

2.2.7 Crack healing.....76

2.2.8 Theoretical analysis of EPT.....78

Chapter 3 Stability of chi-phase in austenitic stainless steel during pulsed electric current treatment.....91

3.1 Introduction 91

3.2 Materials and methods 93

3.3 Experimental results 99

3.3.1 Effects of annealing on 316L stainless steel 99

3.3.2 Effects of EPT on 316L stainless steel 107

3.4 Discussion 113

3.4.1 Thermal effects of EPT on 316L stainless steels 113

3.4.2 Electric effects of EPT on 316L stainless steels 114

3.5 Conclusion 118

Chapter 4 Stability of delta-ferrite in 2205 duplex stainless steel with electropulsing 119

4.1 Introduction 119

4.2 Materials and methods 122

4.2.1 Materials selection and prior treatments 122

4.2.2 Experimental set-up of EPT 123

4.2.3 Metallographic observations and properties test 124

4.3 Experimental results 125

4.3.1 Thermodynamic calculation of equilibrium phase diagram 125

4.3.2 Microstructure observations 126

4.3.3 Property measurements 133

4.4 Discussion 134

4.4.1 Thermal effect of EPT 134

4.4.2 Electric effect of EPT 135

4.5 Conclusions 142

Chapter 5 Stability of κ-carbide in duplex lightweight steels under electropulsing 144

5.1 Structure and properties of κ-carbides in duplex lightweight steels 144

5.1.1 Introduction 144

5.1.2 Materials and methods 145

5.1.3 Experimental results and discussion 146

5.1.4 Conclusion 155

5.2 κ-carbide hardening in a low-density high-Al high-Mn multiphase steel 156

5.2.1 Introduction 156

5.2.2 Materials and methods 160

5.2.3 Experimental results 164

5.2.4 Discussion 183

5.2.5 Conclusion 194

5.3 Electropulse-induced nanocrystallization of κ-carbide in duplex lightweight steels 195

5.3.1 Introduction 195

5.3.2 Materials and methods 197

5.3.3 Experimental results 200

5.3.4 Discussion 205

5.3.5 Conclusion 209

Chapter 6 Stability of martensite with pulsed electric current in dual-phase steels 210

6.1 Introduction 210

6.2 Materials and methods 213

6.2.1 Material selections 213

6.2.2 Experimental setting 214

6.2.3 Microstructure observation 215

6.2.4 Property measurement 216

6.3 Results 216

6.3.1 Effects of EPT on microstructure evolutions 216

6.3.2 Effects of EPT on mechanical properties 218

6.4 Discussion 220

6.4.1 Thermal effect of EPT 220

6.4.2 Electric effect of EPT 222

6.5 Conclusions 226

Chapter 7 Conclusion 227

Chapter 8 Suggestions of future work 230

Reference 233

Chapter 9 Appendix 253

Publication list 253

Chapter 1 Introduction

1.1. Background

Steels play an important role in improving the quality of life and servicing the manufacturing industry. This is achieved through its endless variety of microstructures and properties which can be produced by a series of complex routes such as, solid-state transformation (e.g. eutectoid transformation and spinodal decomposition) and thermo-mechanical processing (e.g. severe plastic deformation and dynamic plastic deformation) [1]. In comparison with other emerging, structural materials (e.g. Ti alloys, Ni alloys, Al alloys, Mg alloys and etc.), steels are high performance materials which have extraordinary properties. These properties include high strength, high ductility and good corrosion and oxidization resistance. In addition, steels have other attractive features, such as, low cost, high abundance of source materials (Fe and C) and good recyclability. These help steels to maintain its prime position in modern industry and society. The standard definition of steel is "*Any iron based alloy, in which no other single element is present in excess of 30 % weight, and for which the iron content amounts to, at least, 55 % weight present and carbon is limited to a maximum of 2 % weight presenting*" [2]. There are over 25000 different steels being developed by manipulating the microstructure evolution, phase transformations and alloying elements of the Fe-alloys in the world. Although steel is not a novel alloy (which frequently leads to a common misunderstanding that "*everything in steel is established*") for those outside the field, the investigation of steel is probably the most challenging area in materials sciences, due to the many unknowns in steel design and processing.

Over the last decades, steels have been classified into various groups based on their microstructures and corresponding properties. A microstructure of steel matrix, with a wide

range of size and morphology of secondary phases and intermetallic compounds, frequently result in changes of the physical and chemical performance of steels at high temperatures. For instance, the segregation of alloying elements (e.g. Cr, Ni and Mo) around grain boundaries in stainless steel at high temperatures can introduce negative effects, such as pitting corrosion, thermal crack development and brittle transition of structure [1, 3]. Meanwhile, the phase transformation, initiated by various heat treatments, fundamentally changes the lattice structure and properties of steels [1]. Furthermore, on the basis of the Hall-Petch relationship [1], a microstructure with a smaller grain size induces higher strength in most polycrystalline steels. In addition, a promotion of dislocation mobility and reduction of residual stress within microstructures effectively enhance the formability of steels (especially, the ductility and superplasticity behaviour) during deformation. Therefore, microstructure evolution plays a dominant role in steel design and processing in order to achieve desired properties.

1.2. Aims of the research

The aim of this research was to develop a novel approach to achieve precise control of microstructure evolution in order to generate the desirable properties. The new approach changes the phase stability of the steels in the processing. Four fundamental problems are considered to seek the engineering implementation of the new processing, namely:

- *Ageing treatment*: The segregation of alloying elements during the precipitation of chi-phase in 316L stainless steels.
- *Annealing treatment*: The softening effect during delta-ferrite phase transformations in 2205 duplex stainless steels at high temperature.
- *Cold rolling*: Crack initiation and propagation within eutectoid lamellar carbides in duplex lightweight steels (Fe-26Mn-9Al-0.75C).

- *Tempering treatment*: The loss of strength during the tempering of martensite in dual-phase steels (DP600).

In order to minimize the detrimental effects of the above engineering problems in steel processing, the newly developed processing method is expected to be capable of (i) suppressing precipitation and thereby homogenising the alloying elements, (ii) introducing the strengthening effect during high temperature phase transformation, (iii) prohibiting crack-formation during cold deformation and (iv) delaying the loss of strength in tempering of martensite. In addition to this, the kinetics and thermodynamics involved in the processing are investigated. ***Electropusling treatment*** (EPT) has been implemented for purposes. EPT is unlike conventional methods but involves several modifiable parameters such as voltage (v), current density (A/m^2), pulse duration (μs), pulse frequency (Hz) etc. It is capable of providing accurate control of microstructure evolution and properties whilst maintaining high work-efficiency and low energy-consumption. EPT has been very successful in modifying microstructures for most of polycrystalline metals and alloys, and has been selected in this thesis to address the earlier list four problems for 316L stainless steels, 2205 duplex stainless steels, duplex lightweight steels (Fe-26Mn-9Al-0.75C) and dual-phase steels (DP600) respectively. There are no alternative solutions to address these problems to be found in the literature.

1.3. Outline of the thesis

The thesis is organised to demonstrate the investigation of the phase stability under EPT in four steels containing different phases and in service in different environments, which cover: (i) the suppression of precipitation by homogenizing alloying elements in 316L stainless steels, (ii) the promotion of high temperature phase transformation to strengthen 2205 duplex

stainless steel matrix, (iii) the enhancement of formability by refining carbides in duplex lightweight steels and (iv) the recovery of the loss of strength within tempering martensite in dual-phase steels. Following are brief descriptions for each investigation.

- 316L stainless steels

  A treatment to suppress and dissolve the precipitates in 316L stainless steel in a temperature range between 650 ^{o}C and 850 ^{o}C has been investigated. There is no published report on the effect of electric current on precipitates in austenitic stainless steels in the temperature range before this work. The effect of electric current on segregation of alloying elements has not been studied to date. There are no published data on the suppression and dissolution of precipitates using low power EPT (low current density $\sim 6.3 \times 10^{7}$ A/m^{2}) in such alloys.

- 2205 duplex stainless steels

  The 2205 duplex stainless steel containing high Cr and high Ni contents undergoes a eutectoid decomposition from delta-ferrite to austenite and sigma phases below 840 ^{o}C. However, the steel loses its strength when the temperature attains 840 ^{o}C. Conventionally, changing the alloying additions has proved to be an effective way of altering delta-ferrite phase transformation behaviour (such as extending the temperature range for phase transformation). In the present work**,** low power EPT (using an electric current density around 5.0×10^{7} A/m^{2}) has been utilized to stabilize the austenite and sigma phases and hence to strengthen the steels at high temperature.

- Fe-26Mn-9Al-0.75C duplex lightweight steels

  Fe-Mn-Al-C quaternary steel is a typical type of lightweight steel with low density (e.g. 6.47 g/m^{3}, which gives 17.10 % density reduction in comparison with pure iron). It has

been extensively investigated in automotive and aerospace fields due to its excellent combination of strength and ductility, good corrosion and oxidization resistance in comparison with TWIP or TRIP steels. However, the formation of lamellar κ-carbide ($(Fe,Mn)_3AlC$) in these lightweight steels causes catastrophic cracking during cold forming. High power EPT (electric current density is around 1.92×10^9 A/m^2) has been used here to (i) transform the lamellar κ-carbide to nano-sized spherical particles (about 110 μs) and (ii) refine the microstructure of ferrite matrix. This inhibits cracking during cold forming.

- Dual-phase steels (DP600)

  The dual-phase steel becomes soft during isothermal tempering of martensite. Recently, non-isothermal tempering has been implemented to decrease the softening process in dual-phase steels. The use of a high power EPT has been found to be able to enhance the strengthening effects via the formation of ultrafine-grained ferrite with nano-cementite particles in tempered martensitic-ferritic steels. To the best of my knowledge, EPT is the first candidate to provide a better solution for the softening problems encountered in the tempering of martensite than that achieved with isothermal and non-isothermal tempering.

In summary, EPT has been designed to control precipitation behaviour, phase transformation, formability and strengthening of steels. The fundamental understanding of the effect of EPT on the phase stability has been studied from kinetic and thermodynamic grounds. The application of EPT to the control of steel microstructure and properties has been outlined and discussed in this thesis.

Chapter 2 Assessment of the literature

The microstructure evolutions in precipitation and phase transformation, their effects on the steels properties, and the various approaches used in modifying the steels microstructures and the associated properties are introduced in Section 2.1. Section 2.2 introduces the backgrounds and applications of EPT on polycrystalline metals and alloys.

2.1 Microstructure and properties of steels

2.1.1 Precipitation

The generic precipitation behaviour in steels has been described well in textbooks [1]. This section focuses on the review of the microstructure evolutions during precipitation that affect the properties of steels.

Most of the bulk polycrystalline steels possess precipitates in their matrix after heat treatments. The precipitation temperature and the size, morphologies and crystallographic structure of precipitates are dependent on the composition of alloying elements [1]. The alloying elements such as C, Cr, Ni, Mo, V, W and Ti are frequently added into the steels to form various precipitates in order to modify the physical, chemical and mechanical properties of the steels [1]. In metallurgical fields, precipitates are generally referred as secondary phases or intermetallic compounds which have relative high thermal stability at high temperatures. For steels consist of different compositions of alloying elements, the precipitation mechanisms are described roughly as three routes with continuous increase of temperature and time [1]:

(1) The *in-situ* nucleation of precipitates [1]:

In the first route, the precipitates instantaneously nucleate on the interfaces between the cementite and ferrite phases. With continuous coarsening of the precipitates, the adjacent cementite provides more carbon to diffuse into these precipitates.

(2) The separation of nucleation of precipitates [1]:

With further increasing temperature and time, a huge amount of fine precipitates starts to nucleate at pre-existing, high density, dislocation regions in the steel matrix.

(3) The nucleation of precipitates at different types of grain boundaries [1]:

Precipitates eventually nucleate and coarsen at various types of specific areas such as the prior austenite grain boundaries, former martensitic lath boundaries and the new ferrite boundaries.

In addition, adding various types of alloying elements can effectively change the precipitation process. For example, adding Cr leads to a Cr carbides precipitation process to take place in the steel matrix under heat treatment. This is because Cr is a strong carbide former, which reacts with carbon to generate Cr carbides (e.g. $Cr_{23}C_6$). A typical precipitation sequence of Cr carbides is as following [1]:

$$Matrix \rightarrow (FeCr)_3C \rightarrow Cr_{17}C_3 \rightarrow Cr_{23}C_6 \tag{2.1}$$

When 4-6 wt.% Mo is added to the steel, the carbides precipitation sequence is expressed in Equation 2.2 [1].

$$Fe_3C \rightarrow M_2C \rightarrow M_6C \tag{2.2}$$

2.1.1.1 Precipitation and mechanical properties

Steels strengthening can be achieved by a number of mechanisms. Precipitation is one of them. In comparison with other strengthening methods such as solid-state phase transformation and microstructure refinement, the formation of precipitation can be controlled by adding various types of metallic alloying elements. Cementite (Fe_3C) as one typical example of precipitates is found frequently in steel matrix containing relatively high carbon concentration [1]. The morphologies of these precipitates are varied from lamellar structure to spherical particles depending on the heat treatments. Using an alternative heat treatments, the dispersion strengthening of precipitates can be optimized by a relation between the size of precipitates and mechanical properties (i.e. yield stress) [1]:

$$\tau_0 = \tau_s + \frac{T}{b\Lambda/2} \tag{2.3}$$

where τ_s is the yield strength, τ_0 the yield stress, T a dislocation's line tension, b the burger vector and Λ the interparticle spacing. The presence of a directional relationship between spacing of precipitate and yield stress of steel apparently indicates the strengthening effect can be maximized by a significant reduction of precipitate spacing. In order to further accurately model the strengthening effect of precipitates (taking into account the size of precipitate), an empirical equation is expressed in Equation 2.4 [1]:

$$\tau_0 = \tau_s + \frac{G}{4r}\phi \ln\left(\frac{\Lambda - 2r}{2b}\right)\left(\frac{1}{(\Lambda - 2r)/2}\right) \tag{2.4}$$

where ϕ is the constant, G a shear modulus and r the size of precipitate. A remarkable example of strengthening effect generated by the precipitation of lamellar cementite within ferrite matrix mathematically depicts a relationship between flow stress and mean uninterrupted free ferrite path (MFFP) in a carbon steel, as schematically illustrated in Figure 2.1 [4].

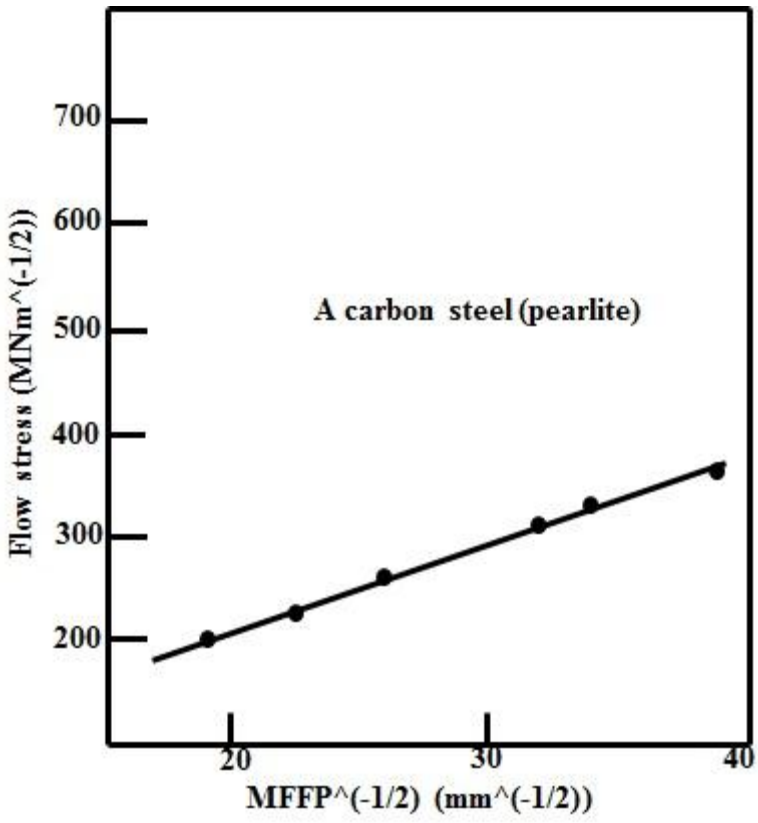


Figure 2.1: Schematic illustration of a linear relationship between flow stress and MFFP for a carbon steel [4].

In addition, the occurrence of various volume fraction and morphology of precipitates in steel matrix can, by increasing ductility, benefit carbon steels which have high formability during

manufacturing process. For example, a low volume fraction of spherical cementite particle with high strength in carbon steel possesses relatively low potential to initiate crack forming and decohesion even at small strain in comparison with that of lamellar cementite [5]. This indicates that steels with a small amount of precipitates can sustain significant deformation before initiation and propagation of voids. Simultaneously, spherical precipitates have higher capability to withdraw substantial deformation reduction than that lamellar precipitates. Figure 2.2 depicts a standard true strain to fracture and volume of precipitates curve for a carbon steel [5].

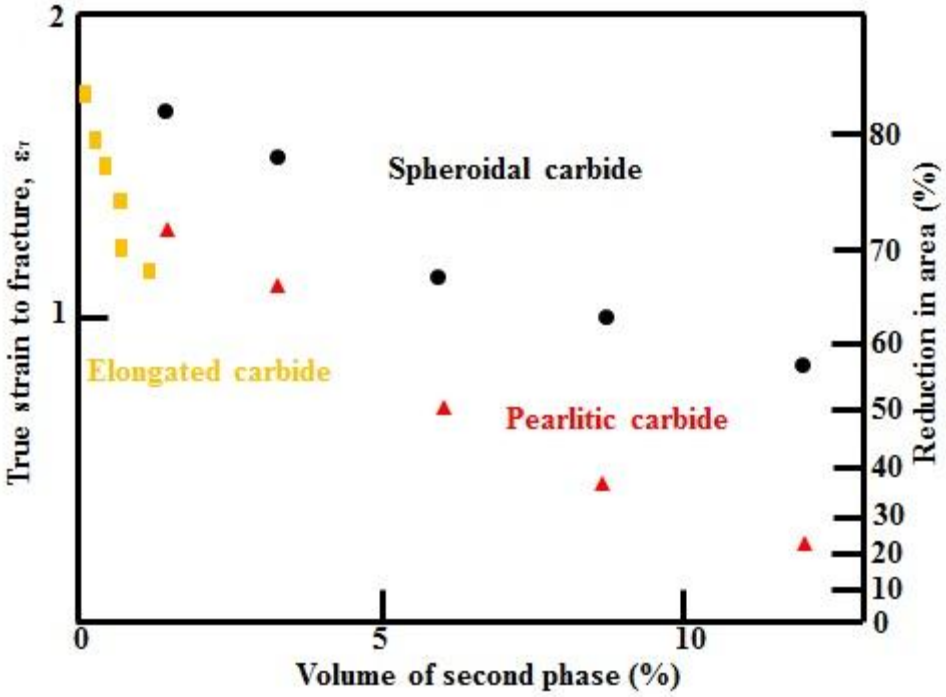


Figure 2.2: The influence of secondary phases with different morphologies (spherical, pearlitic and elongated carbides) on the ductility of steel [5].

From Figure 2.2, it is obviously seen that the required strain to fracture is inversely proportional to the volume fraction of spheroidal carbides. This hints that the formability of steels can be maximized by keeping the volume fraction of precipitates at a relatively low level and controlling the morphology of precipitates as spherical particle.

2.1.1.2 Precipitation and chemical properties

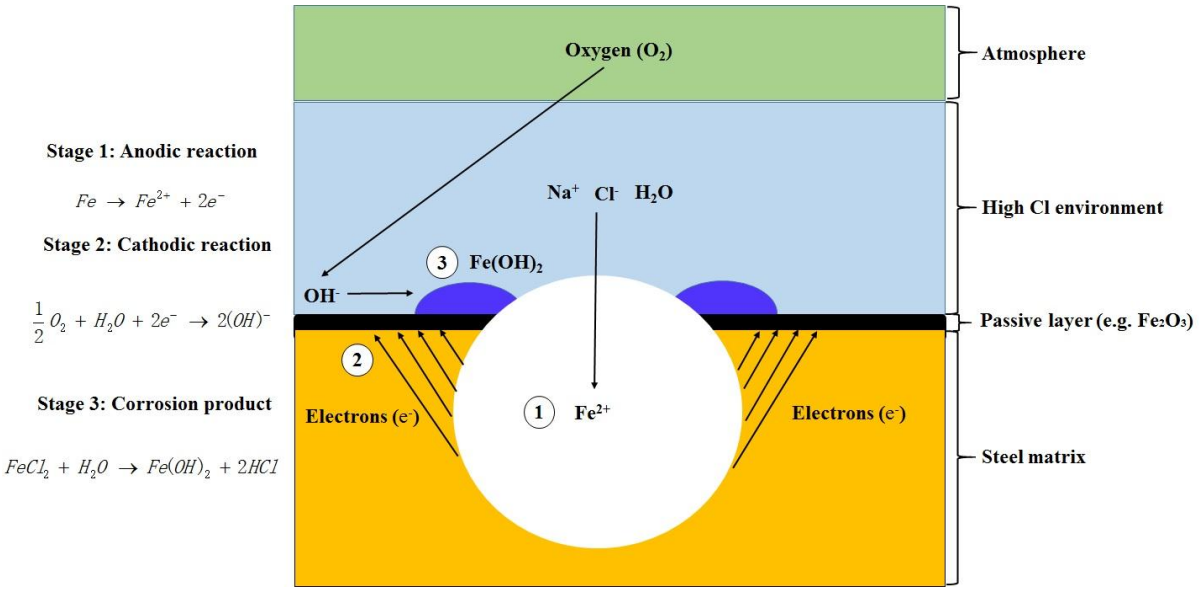


Figure 2.3: Schematic diagram of general corrosion process for steels under high-concentration chloride environments.

Although the dispersion of precipitates in steel matrix benefits the mechanical properties such as strength and ductility, it still causes other detrimental effects in steel applications. For instance, a typical stainless steel with high concentration of alloying elements (e.g. Cr, Ni and Mo) is widely applied in many fields of automotive, subsea pipeline, medicine, food industry and nuclear power plants due to its extraordinary corrosion and oxidization resistance [1, 6-

17]. This is mainly attributed to the high concentration of alloying elements such as Cr. The addition of Cr in stainless steels can generate a passive layer (Cr oxides, Cr_2O_3) that efficiently covers the whole surface area of stainless steel to avoid corrosion attacking. However, this passive layer used to protect corrosion attacking can become invalid due to the segregation of alloying elements to form precipitates at some specific positions (e.g. grain boundary) under heat treatments. A standard process of corrosion initiation is vividly described in Figure 2.3.

2.1.2 Solid-state phase transformation

Phase transformation is one of the major means of the optimizing the steel properties. Steel, as one of the oldest multiphase alloys contains hundreds of various types of phases depending on the various alloying element additions and heat treatments. Two of the most common phase transformations include reconstructive phase transformation and displace phase transformation, exist in solid steels.

For a reconstructive phase transformation, the lattice structure is completely rearranged by breaking most of the atomic bonds to form a new lattice structure. This rearrangement of atoms is mainly controlled by the diffusion of atoms within lattice structure. Normally, the atom diffusion rate is higher at high temperature than that at low temperature. For iron, the phase transformation from delta-ferrite, with a body-centred-cubic (BCC) structure, to austenite with a face-centred-cubic (FCC) structure, occurs at a temperature about 1394 °C [1]. The lattice structure of delta-ferrite is completely changed via atomic rearrangement. Followed by the further reduction in temperature to about 912 °C, the austenite starts losing its stability and the phase transformation from austenite (FCC) to alpha-ferrite (BCC) is activated. During this phase transformation, the volume is increased by 0.21 cm^3/mol because

the FCC structure is more compacted than the BCC structure [1]. Figure 2.4a and b present the crystallographic structures of FCC and BCC, respectively.

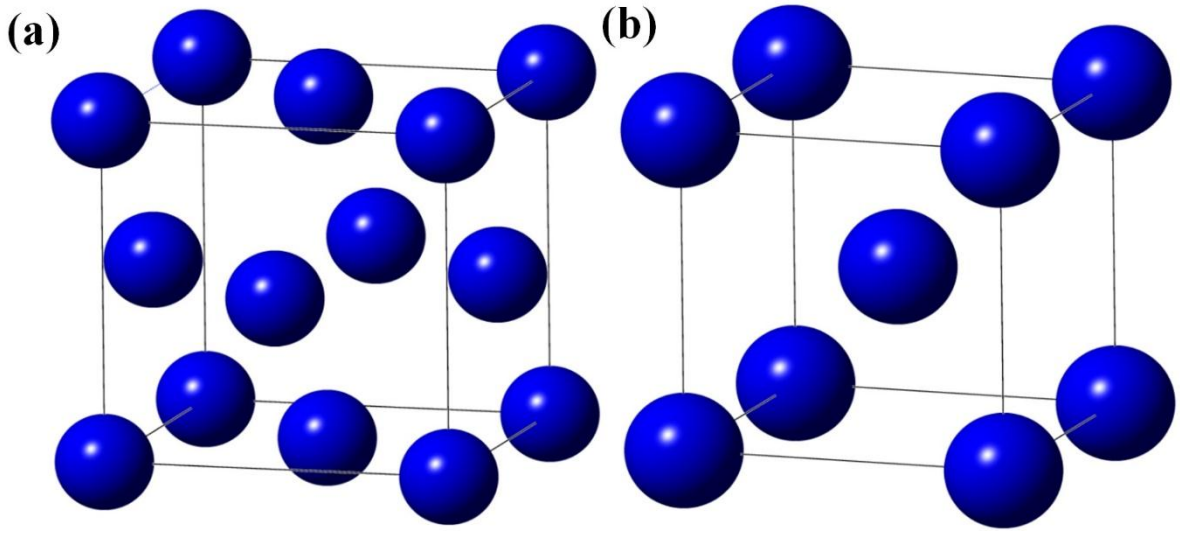


Figure 2.4: Schematic diagrams of molecular structure of (a) austenite (FCC) and (b) ferrite (BCC) [18].

Besides heat treatments, control of alloying elements such as carbon in steels can effectively control the phase transformation (e.g. an appropriate carbon composition in steel can have eutectoid phase transformation to generate a mixture of ferrite and cementite phases, called pearlite, from original austenite phase). The formation of pearlite structure can significantly enhance the mechanical properties such as yield stress, tensile strength and wear ability of the steels [1, 19].

At low temperature, the atom mobility is retarded. This retardation of atom diffusion makes the reconstructive phase transformation impossible. The displacive transformation takes place

in this occasion [1]. Instead of atom diffusion, a plastic transformation is involved to generate the new structure from the original structure.

Martensitic transformation as a typical displacive transformation has been investigated in steels [1]. The volume of a crystal is expanded by a transformation from FCC to BCC structures due to the density change. This causes the generation of internal stress inside the crystal [20]. The internal stress in the crystal is unable to be released at the low temperature. Instead of volume expansion, the shearing of crystal in a specific direction can effectively release internal stress during displacive transformation. As a result, a martensite phase is produced without changing solute composition from the original austenite. Martensite phase is one of common phases which significantly enhance the strength property of steels [21-23].

2.1.3 Grain size effect

The modification of the average grain size is one of the effective methods to alter the mechanical properties of steels. For example, a grain refinement of polycrystalline ferrite phase can enhance the strength of ferritic steels. [1]. The Hall-Petch relationship is an empirical relation between grain size and yield stress, which was proposed by Hall and Petch for a pure iron and is expressed as following [24-25]

$$\sigma_y = \sigma_0 + K_y d^{-\frac{1}{2}} \tag{2.5}$$

where σ_y is yield stress, d is the grain size, σ_0 are friction stress constants for yield and hardness measurements, K_y is a coefficient. The grain size effect on strength can be roughly referred to as dislocation movements and accumulations around grain boundaries in the materials. A fine grain size will result in an improvement of strength in comparison with a

coarse grain size. A schematic diagram of movements and accumulations of dislocations within fine and coarse grains are plotted in Figure 2.5a and b, respectively [1].

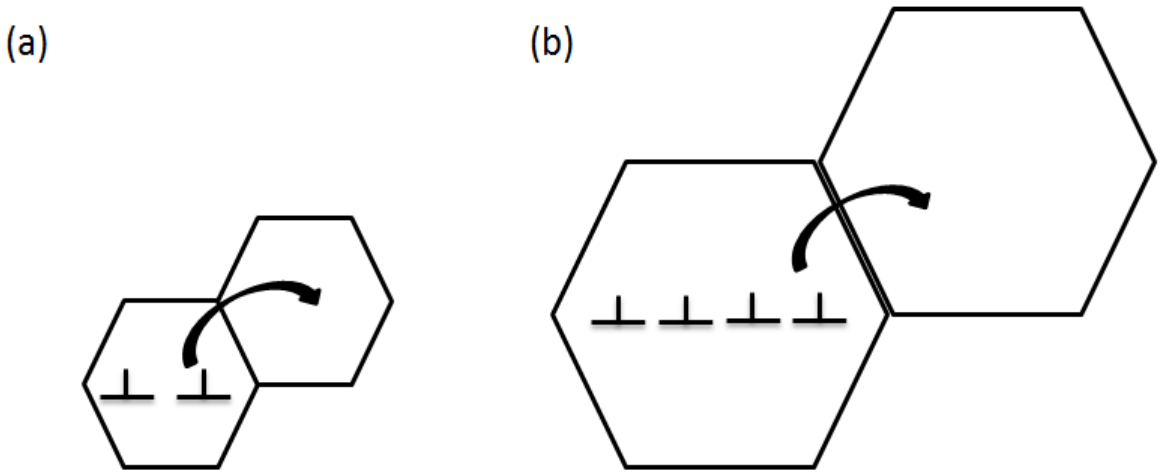


Figure 2.5: Schematic diagram of dislocation pile-up in (a) fine grain and (b) coarse grain.

The Hall-Petch relationship has been applied in many polycrystalline metals and alloys. Mild steel, for example, has shown the applicability of the relationship. A diagram describing the relation between yield stress and grain size for a mild steel is plotted in Figure 2.6 [26].

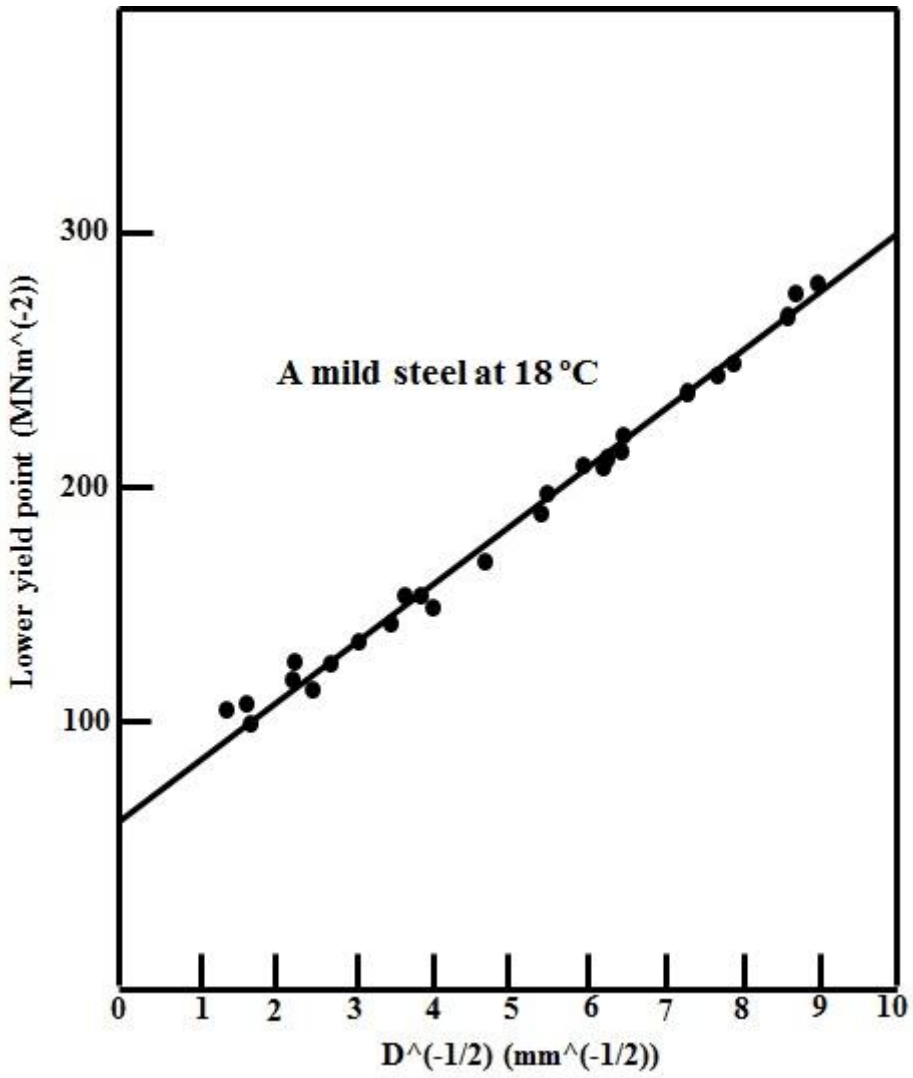


Figure 2.6: The relationship between yield stress and grain size of mild steel at 18 ºC [26].

Besides the strengthening effect, the grain size can also influence the ductility of materials. A significant reduction in ductility appears as the grain size is continuously decreased. There are two typical examples (1100-Al and interstitial free steel) depicting the relations between ductility (true strain) and grain size, as shown in Figure 2.7 [27].

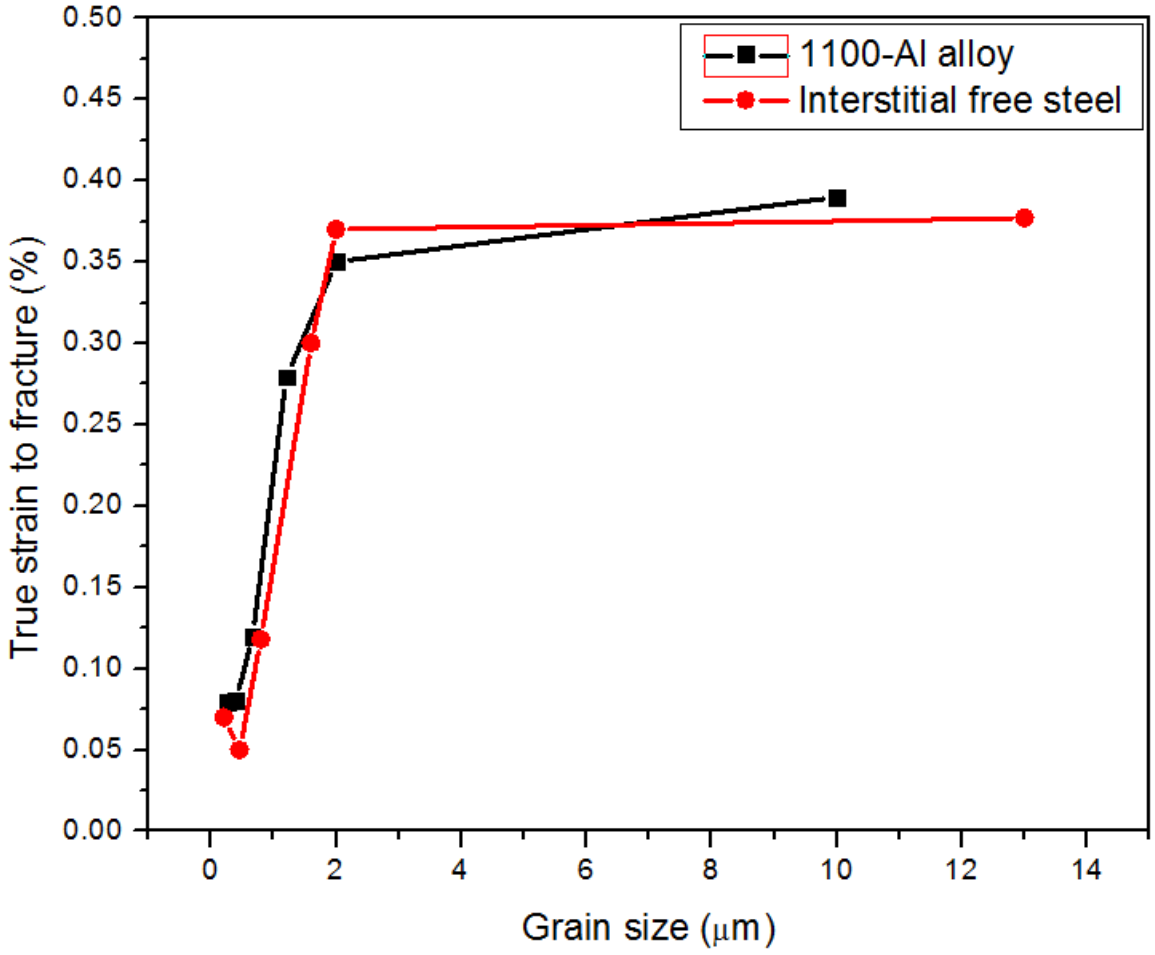


Figure 2.7: The relations between true strain to fracture and grain size for 1100-Al and interstitial free steel [27].

Steels with nanoscale grain size have attracted significant attention. Nano-crystals have large interface areas to act as an effective barrier, to block the dislocation motion, and hence to increase the yield stress. However, the nanoscale grain refinement can also cause a completely opposite phenomenon on strengthening when the grain size is less than about 20 nm [1]. This opposite phenomenon leads to the failure of Hall-Petch relationship due to grain boundary sliding. This is because the grain boundary sliding will make it impossible accumulate of dislocations during deformation [1]. In order to overcome these barriers

induced by nano-crystallization (e.g. failure of Hall-Petch relationship), a suitable strategy to improve the strength and ductility of materials simultaneously is urgently required. The fabrication of nano-twinning may be one of potential methods which can reach the requirement. Nano-twinning (smallest feature size is less than 100 nm) as a coherent grain boundary with a high degree of symmetry, one side of which contains arrangement of atoms that are mirror reflections of those on the other side, separated by the twin composition plane (shown in Figure 2.8) have ultrahigh coherency with surrounding matrix [28]. Thus, the nano-twinning has good thermal, electrical and mechanical stabilities [28].

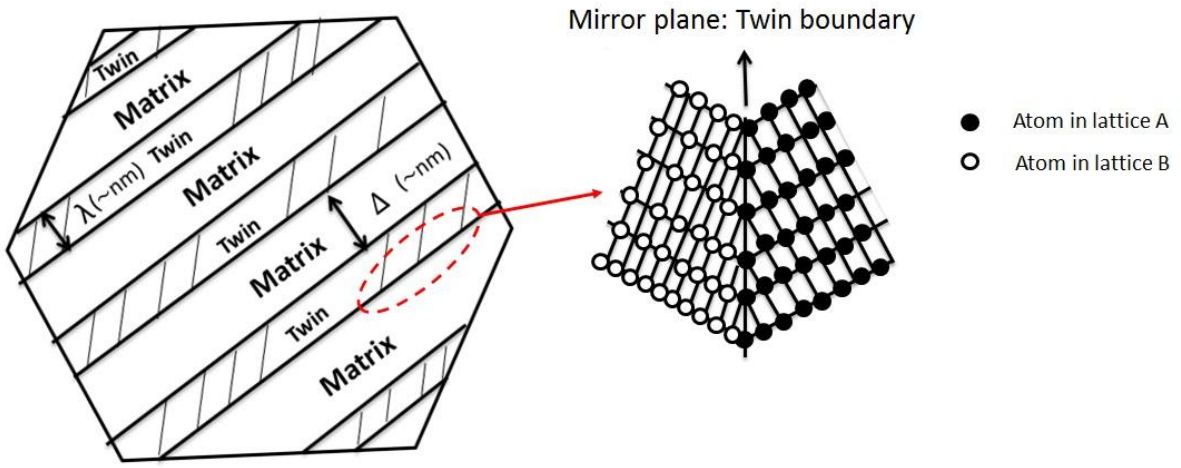


Figure 2.8: Schematic drawings of nano-scale twinning with twin layer thickness (λ) and twin boundary spacing (Δ), and a twin boundary structure [28].

A higher percentage of nano-twinning fabricated in materials leads to a better balance of mechanical properties [29–32]. This is mainly attributed to the specific properties of twinning grain boundary. In comparison with normal grain boundary within nanoscale grains, a nano-twinning boundary not only has greater strengthening effect as blocking the motion of sessile

dislocations, but also enhances significantly the ductility as promoting extra slip system for climbing and sliding of glissile dislocations. The effects of nano-twinning on dislocation motion are described in Figure 2.9 comprehensively [28, 31].

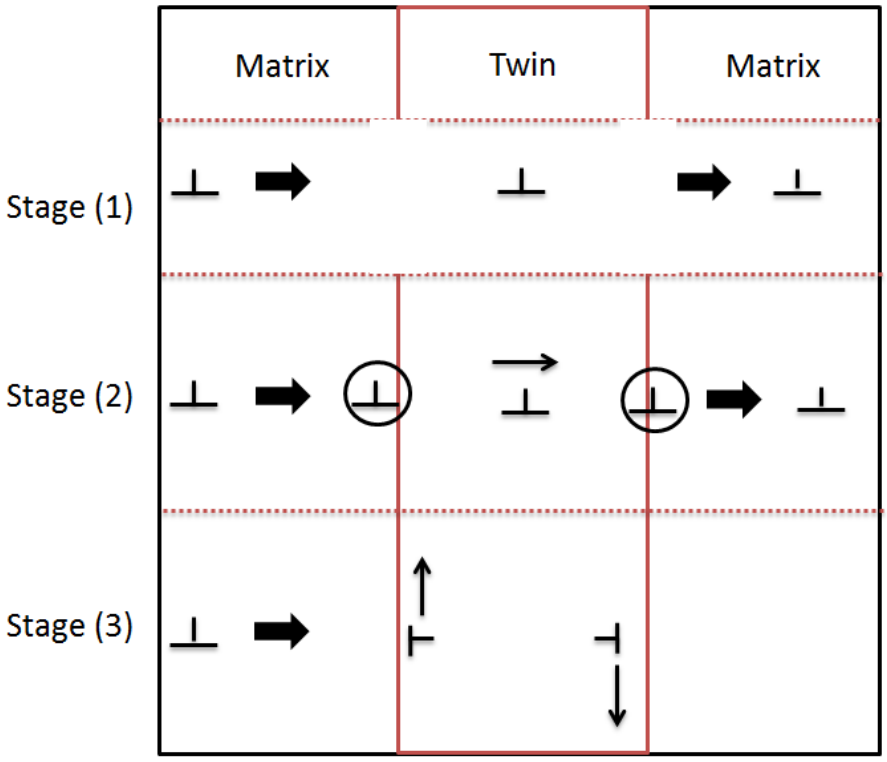


Figure 2.9: Schematic showing of the dislocation motions in stage (1), stage (2) and stage (3) [28, 31].

In stage 1, if no twin boundary exists in the microstructure, the dislocation can move directly from left matrix to right matrix without changing of its direction. In stage 2, the strengthening effect can be initiated by the dissociation of Shockley partials when the dislocation slips across the twin boundary. This is because the Shockley partials can transmit though the twin

boundary into adjoining twins accompanied by the emission of a stacking fault ribbon or sessile locks at the twin boundary. Oppositely, softening effect can be generated by the emission of additional Shockley partials slip along twin boundary in the stage 3.

Fabrication of large amount of nanoscale twins during manufacturing of materials has attracted significant interests in recent years. Three methods, i.e. pulsed electrodeposition, sputter deposition and dynamic plastic deformation (DPD), have been utilized to achieve the goal for polycrystalline metals and alloys [28]. For example, the pulsed electrodeposition is used to generate nanoscale twinning in thin foil, where the twin layer thickness (about 100 nm) can be efficiently controlled by alternating the current density, deposition temperature and the ratio of on time/off time. Similarly, appropriate use of sputter deposition can also fabricate nanoscale twinning in thin foil. In comparison with the former two methods, DPD as one of thermo-mechanical processes reliably manufactures bulk materials with high density of nanoscale twinning. This is predominantly attributed to the competing mechanism (dislocation slip and deformation twinning) during plastic deformation. For a polycrystalline materials treated at cryogenic temperature and high strain rate, the twinning process will be dominant rather than dislocation slip. As a consequence, a high density nanoscale twinning is formed in bulk materials under DPD.

2.2 Effects of electropulsing on microstructure evolutions and properties

In this section, the background of EPT and its applications to optimize the microstructures and properties of polycrystalline metals and alloys are introduced. Figure 2.10 demonstrates the effect. It illustrates seven fundamental microstructure evolutions, precipitation [33–48], phase transformation [49–67], grain size [68–133], grain orientation [72, 79, 101, 102, 112, 134–148], motion of electrically non-metallic particles [72, 142, 144, 145, 149, 150],

dislocation [38, 45–47, 52–56, 61, 63–67, 73, 79–81, 86–88, 92, 93, 95, 98, 102, 105, 113, 116–125, 128, 129, 151–156] and cracking healing [151–161] are affected significantly by the application of EPT to materials for various conditions. Due to the specific properties of EPT (e.g. instantaneous method, high energy input and no production of pollutants), it has been widely used in many types of alloys such as steels, Ti alloys, Al alloys, Mg alloys, Ni alloys, Cu alloys, amorphous alloys, tungsten alloys, Zn-Al alloys, Ni-Ti alloys, metallic glass and thin films. EPT can effectively change their microstructures and corresponding properties with high work efficiency, low energy consumption and less impact on environments in comparison with other conventional methods [33–162]. The experimental observations, kinetic and thermodynamic understanding of EPT on the optimization of microstructures and properties for polycrystalline metals and alloys are summarized in this section.

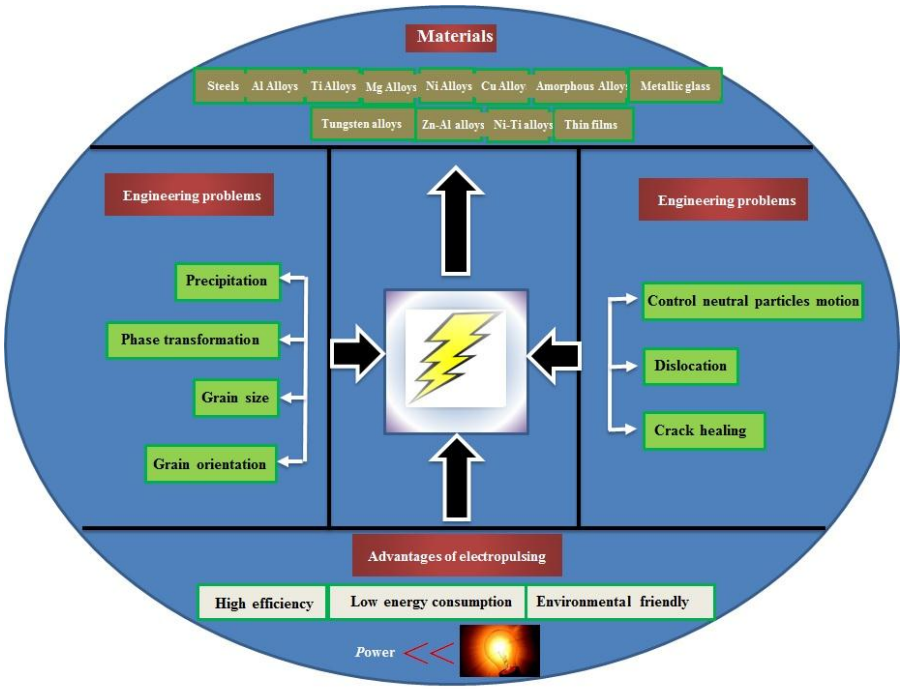


Figure. 2.10: The effect of EPT on microstructure and properties of polycrystalline metals and alloys.

2.2.1 Precipitation

As previously mentioned in Section 2.1, precipitation can take place in polycrystalline metals and alloys during various heat treatments. Once precipitates nucleate within a materials matrix, the alloying elements will start to segregate. The segregation of alloying elements can significantly influence the properties of polycrystalline metals and alloys. Precipitates in metals and alloys are known for their beneficial or/detrimental roles during processing depending on their types, morphologies, size and density. In order to attain a good understanding about how the properties can be optimized by effective controlling of precipitates parameters, several metals and alloys including Al alloys, Mg alloys and steels are selected as model materials, which are treated by EPT at different process conditions. The change of microstructure evolutions and properties induced by precipitation via EPT are presented. Thereby the relationship between precipitation behaviours and EPT can be outlined and analysed definitely and thoughtfully, which may provide a promising direction for optimizing properties using precipitation under EPT and improving the reliability of materials.

In this section, a systemic introduction of the applications of EPT on precipitates in various metals and alloys is presented. This is to provide insight and understanding to the effects of electric current on precipitation behaviour.

2.2.1.1 EPT on precipitation behaviour

Since the first observation of abnormal precipitation under electric-current treatment in Al-3.98 wt% Cu alloy [37], many researchers have studied the phenomenon in Al alloys (2024 Al alloy [45], Al-3.3 wt% Mg alloy [44], Al-4 wt% Cu alloy [43], Al-5.6 wt% Zn alloy [42]), Mg alloys (Mg-3Al-1Zn alloy [38], Mg-6Al-1Zn alloy [33], Mg-9Al-1Zn alloy [34–36, 46, 47]) and steels (Low carbon steel and Fe-Mn-Si-Ni-Nb-C alloy [39–41, 48]). Once the electric-current treatments are applied to those alloys, the precipitation behaviour are significantly altered and the properties of the alloys are changed. Table 2.1 summarized the results reported in literature.

Table 2.1: Applications of electric-current treatments on precipitations in alloys.

Materials	**Treatments**	**Precipitations**	**Observations**
Al-3.98 wt% Cu alloy	d.c. current	GP zones	Promoted [37]
2024 Al alloy	EPT	T-phase	Promoted [45]
Low carbon Nb steel	EPT	NbCN	Promoted [48]
Fe-Mn-Si-Ni-Nb-C alloy	EPT	NbC	Promoted [39–41]
Al-3.3 wt% Mg alloy	d.c. current	GP zones	Retarded [44]
Al-4 wt% Cu alloy	d.c. current	GP zones	Retarded [43]
Al-5.6 wt% Zn alloy	a.c. current	GP zones	Retarded [42]
Mg-3Al-1Zn alloy	EPT	β-$Mg_{17}Al_{12}$	Retarded [38]
Mg-6Al-1Zn alloy	EPT	β-$Mg_{17}Al_{12}$	Retarded [33]
Mg-9Al-1Zn alloy	EPT	β-$Mg_{17}Al_{12}$	Retarded [34–36, 46, 47]

Note: d.c. is direct current; a.c. is alternative current; EPT is electropulsing.

Table 2.1 shows that the effects of electric current on precipitation can be classified into two types, one is to promote the precipitation (forward effect) and another is to retard (reverse effect) the precipitations.

2.2.1.2 Enhancement of precipitation by electric current

For the forward effect of electric current on precipitation, the precipitation of GP zones within Al-3.98 wt% Cu alloy are accelerated by direct current [37]. The higher direct current leads to higher atom diffusivity hence to promote the precipitation reaction. This is mainly attributed to the thermal effect of electric current. Electric-current-promoted precipitation has been implemented widely in other types of alloy to optimize their mechanical properties in recent years.

For instance, the precipitation of T-phase ($Al_{20}Cu_2Mn_3$) in a typical 2024 Al alloys retards the grain growth during recrystallization and hence effectively refines the grain size. A uniform and dispersed T-phase precipitates is an essential requirement for optimizing mechanical properties of 2024 Al alloys by changing its grain size. Therefore, the forward effect of electric current (EPT) have been used to accelerate T-phase precipitation in 2024 Al alloys and subsequently improve their strength [45]. This promoted precipitation of T-phase is due to the acceleration of atom diffusion by thermal effect of electric current.

Beside Al alloys, the acceleration of precipitation induced by the thermal effect of electric current (EPT) is also utilized to affect the precipitation behaviours of NbCN particles in low carbon Nb steel [48]. The nucleation and precipitation rate of NbCN particles are

significantly enhanced by electric-current treatments to accelerate atom diffusion and thereafter, to provide extra nucleation sites for austenite to ferrite phase transformation.

Furthermore, the forward effect of electric current on precipitation has been implemented to modify the shape memory effect for Fe-Mn-Si-Ni-Nb-C alloys. Fe-Mn-Si alloys with excellent shape memory effect benefits its workability, machinability and weldability. In order to enhance the shape memory effect, the ultrafine precipitates such as NbC carbides are necessary in Fe-Mn-Si-Ni-Nb-C alloys. This strengthening effect of NbC carbides to the austenitic matrix can suppress the permanent deformation. Electric-current treatments such as EPT can promote the precipitation of NbC carbides and refine their size due to the thermal effect [39–41]. As a result, the finer NbC carbides formed by EPT have better shape memory effect in comparison to coarsen carbides after the normal ageing treatment.

2.2.1.3 Retardation of precipitation by electric current

Interestingly, a completely opposite effect of electric-current treatment on precipitation behaviour has been noticed in Al based alloys (Al-3.3 wt% Mg alloy, Al-4 wt% Cu alloy and Al-5.6 wt% Zn alloy). In comparison with the promoted precipitation in Al-3.98 wt% Cu alloy under d.c. current, electric current (d.c. or a.c.) can generate stress to effectively retard the precipitation process due to the electric effect [42–44].

By using the concept of the electric effect on retardation of precipitation, the precipitation of β-$Mg_{17}Al_{12}$ phase in Mg alloys (Mg-3Al-1Zn alloy, Mg-6Al-1Zn alloy and Mg-9Al-1Zn alloy) has been successfully retarded. During the application of electric-current, the electric effect becomes a dominant factor to retard the precipitation of β-$Mg_{17}Al_{12}$ by changing the total Gibbs free energy due to the discrepancy of electrical properties in Mg alloys [33–36, 38,

46, 47]. This is mainly attributed to the electric effect of EPT on reduction of the thermodynamic barrier for β-$Mg_{17}Al_{12}$ to alpha phase transformation. As a consequence, a remarkable elongation improvement of Mg alloys can be reached by reduction in β-$Mg_{17}Al_{12}$ via EPT.

To sum up, the forward effect of electric current on precipitation can be generally considered as the thermal effect of electric current, which can accelerate the atom diffusion and then promote the rate of nucleation for precipitation. Oppositely, a reverse effect of electric current on precipitation has been outlined, which efficiently affects the Gibbs free energy variation and subsequently retards the dissolution of the precipitates. On the basis of the above literature, an appropriate experimental design of electric-current treatment is required to optimize properties of materials to control precipitation through the thermal or electric effects. But, which effects of electric-current treatment becomes a dominant factor to contrast precipitation and how does it affect the properties of materials? The answers are very important for manufacturing and optimization of materials for our experiments.

2.2.2 Phase transformation

The phase transformation in materials is generally categorized into two types, one is reconstructive phase transformation and another is displacive phase transformation. Among them, the reconstructive phase transformation uses atom diffusional control. Once this phase transformation is activated, the overall lattice structure of materials will be changed. These changes of structure induce a variation of properties and subsequently influence the reliability of materials. Due to the specific properties of reconstructive phase transformation, the direction of phase transformation (forward or reverse) are of particular interest. Thus, the methods on how to effectively control phase transformation direction in materials is of

particular concern in order to optimize properties in recent years. In comparison with traditional thermo-mechanical processing, electric-current treatments not only provide advantages such as ultrafast duration, high energy input and environmental friendly route, but also can efficiently control the direction of phase transformation. From literature, there are six typical types of materials including Mg alloys (Mg-6Al-1Zn alloy [33] and Mg-9Al-1Zn alloy [34–36, 46, 47]), Fe-based alloys [58], Cu-Zn alloys [61, 62], Ti alloys [51, 56, 57, 60], metallic glass [49] and Zn-Al alloys (ZA22 and ZA27) [52–55, 63–67] as model materials to verify the reliability of electric-current treatments for alternating phase transformation. The general information about the effects of electric current on direction of phase transformation are summarized in Table 2.2.

Table 2.2: Applications of EPT on phase transformations in alloys.

Materials	**Effects of EPT**	**Phase transformation**
Cu-Zn alloy	Forward	$\alpha + \beta' \rightarrow \beta$ [61, 62]
Fe-Cr-Ni alloy	Forward	Austenite $\rightarrow$ ferrite [58]
Mg alloys (Mg-6Al-1Zn alloy and Mg-9Al-1Zn alloy)	Forward	β-$Mg_{17}Al_{12}$ $\rightarrow$ α [33–36, 46, 47]
Ti-6Al-4V alloy	Forward	$\beta \rightarrow \alpha$ [56, 57]
Metallic glass ($Zr_{50}Cu_{50}$)	Reverse	Crystallite to amorphous phase [49]
Zn-Al alloys (ZA22 and ZA27)	Reverse	$T' + \eta \rightarrow \alpha + \varepsilon$ [52–55, 63–67]

2.2.2.1 EPT on forward phase transformation

As long as the atom diffusion mechanisms can be controlled, the phase transformation can be affected. For example, the $\alpha + \beta' \rightarrow \beta$ reaction occurs in Cu-Zn alloys is predominantly determined by the long range diffusion of atoms at high temperature. In comparison with conventional rapid heating method (e.g. laser heating), electric-current treatment significantly accelerates the diffusion of atoms by reducing the activation energy of motion and hence by promotes the forward phase transformation [61, 62]. In addition, another strong evidence for supporting forward phase transformation, induced by electric-current treatments, has been observed in Fe-Cr-Ni alloy [58]. This observation shows that the phase transformation from austenite to ferrite is promoted by electric current during the solidification process. Although the authors have not provided a reasonable explanation for this, it is believed that electric current plays a dominant role in influencing the direction of phase transformation by changing the stability of phases in Fe-Cr-Ni alloy.

Recently, the concepts of electric current on forward phase transformation have been widely used in engineering alloys such as Mg alloys (Mg-6Al-1Zn alloy and Mg-9Al-1Zn alloy) [33–36, 46-47] and Ti alloys (Ti-6Al-4V alloy) [56-57]. The occurrence of phase transformations in Mg alloys and Ti alloys are $\beta\text{-}Mg_{17}Al_{12} \rightarrow \alpha$ and $\beta \rightarrow \alpha$, respectively. Both reactions can be dramatically accelerated by applying electric current.

2.2.2.2 EPT on reverse phase transformation

The reverse phase transformation in materials can also be promoted by applying electric current. This was first observed in metallic glass (Zr50Cu50) [49]. In Zr50Cu50, a reverse phase transformation from crystalline to amorphous state appears with electric-current

treatments. Recently, people also reported that electric current plays an important role in altering phase transformation direction in Zn-Al alloys [52–55, 63–67]. Normally, a forward phase transformation $\alpha+\varepsilon \rightarrow T'+\eta$ occurs in Zn-Al alloys at a temperature about 268 ^{o}C. Application of electric current at the same temperature, a reverse phase transformation $T'+\eta \rightarrow \alpha+\varepsilon$ is activated. This abnormal phenomenon is related to the discrepancy of electrical conductivity in the phases. In Zn-Al alloys, it is predicted that the total electrical conductivity of $T'+\eta \rightarrow \alpha+\varepsilon$ is greater than that of $\alpha+\varepsilon \rightarrow T'+\eta$. The higher electrical conductivity of $T'+\eta \rightarrow \alpha+\varepsilon$ becomes more stable, compared with the lower electrical conductivity of $\alpha+\varepsilon \rightarrow T'+\eta$ under electric current during phase transformation.

2.2.3 Grain size

According to the Hall-Petch relationship, a material with smaller grain size is stronger. There are various of means to refine the grain size of materials. EPT is one of them. This section reviews the applications of EPT on grain refinement for pure metals (pure Al, Cu and W) [85, 90, 113, 114, 120, 133, 123] and alloys (Al-Cu alloys [91], Al-Si alloys [100, 126], Al alloys [118, 128], Mg alloys [79–81, 92, 115–117, 119], Ni superalloys [93], Pb-Sn alloys [68], Ti alloys [104, 105, 121, 122], Ti-Al-Nb alloys [106], Sn-Bi alloys [110, 111], Ti-Ni alloys [98], Zn-Al alloys [75], graphite iron [86–88], Al-Mg-Cu-Zn alloys [130], Fe-B-Si alloys [71, 83, 108, 109], Nb-Fe-Co-B alloys [89], Ti-C/Ni-Cr cermet [125], Fe-Co alloys [84], steels [77, 78, 94–96, 99, 101–103, 127, 130, 132] and Cu-Zn alloys [72–74, 112, 124, 129, 131]). It is listed in Table 2.3.

Table 2.3: Applications of EPT on grain refinement for alloys.

Materials	**Processing**	**Microstructure observations**
Pure Al	Solidification with EPT	Refined solidified grains [85, 90]
Al-Si alloys	Solidification with EPT	Refined solidified grains [100, 126]
Al-Cu alloys	Solidification with EPT	Reducing cellular spacing [91]
Pure Cu	Solid state with EPT	Refined grains [113-114, 120, 133]
Pure W	Solid state with EPT	Refined recrystallized grains [123]
Al alloys (2024 and 6061)	Solid state with EPT	Refined recrystallized grains [118, 128]
Mg alloys (Mg-3Al-1Zn, Mg-6Al-1Zn and Mg-9Al-1Zn)	Solid state with EPT	Refined recrystallized grains [79–81, 92, 115–117, 119]
Ni superalloys	Solid state with EPT	Refined recrystallized grains [93]
Ti -6Al-4V alloys	Solid state with EPT	Refined recrystallized grains [104, 105, 121-122]
Ti-Al-Nb alloys	Solid state with EPT	Refined recrystallized grains [106]
Pb-Sn alloys	Solid state with EPT	Refined recrystallized grains [68]
Sn-Bi alloys	Solid state with EPT	Refined recrystallized grains [110, 111]
Ti-Ni alloys	Solid state with EPT	Refined recrystallized grains [98]
Zn-Al alloys	Solid state with EPT	Refined recrystallized grains [75]
Spherical graphite iron	Solid state with EPT	Refined graphite particles [86–88]

Al-Mg-Cu-Zn alloys	Solid state with EPT	Nano-crystallization [130]
Fe-B-Si alloys	Solid state with EPT	Nano-crystallization [71, 83, 108, 109]
Nd-Fe-Co-B alloys	Solid state with EPT	Nano-crystallization [89]
Ti-C/Ni-Cr cermet	Solid state with EPT	Nano-crystallization [125]
Fe-Co alloys	Solid state with EPT	Nano-crystallization [84]
Steels	Solid state with EPT	1. Refined recrystallized grains [77-78, 94, 96, 101-102, 130, 132] 2. Nano-crystallization [95, 99, 103, 127]
Cu-Zn alloys	Solid state with EPT	1. Refined inclusions [72] 2. Nano-crystallization [74, 124, 129, 131] 3. Nano-twins [73, 112]

In general, the extent of grain refinement of materials under EPT can be divided into two types, which are strongly dependent on the processing conditions (e.g. solidification or solid state), as shown in Figure 2.11.

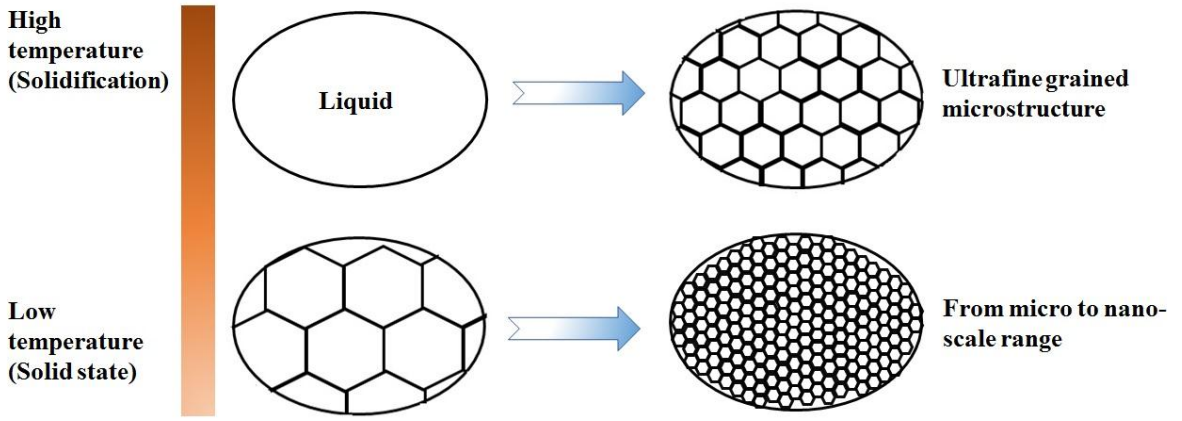


Figure 2.11: The grain refinement of materials under EPT: The fabrication of ultrafine grained microstructure via solidification (high temperature) and the formation of nano-scale grains via crystallization or solid state phase transformation (low temperature).

2.2.3.1 EPT on solidification

In solidification process, EPT increases nucleation rate and causes the formation of ultrafine grained microstructure [85, 90-91, 100, 126]. Both the thermal and electric effect of EPT contributes to the promotion of nucleation rate. EPT provides extra free energy to reduce the activation barrier for nucleation.

2.2.3.2 EPT on solid state materials

Application of EPT on solid state materials (e.g. pure Cu, pure W, Mg alloys, Al alloys, Ni superalloys, Pb-Sn alloys, Ti alloys, Ti-Al-Nb alloys, Sn-Bi alloys, Ti-Ni alloys, spherical graphite iron and Zn-Al alloys) can also refine their grain size. This fabrication of ultrafine grained microstructure is mainly attributed to the accelerated recrystallization and subsequently retarded grain growth process by EPT [113, 114, 120, 133]. Due to the specific properties of EPT (fast and high energy input), the thermal effect of EPT can cause

temperature increment to initiate the recrystallization and the electric effects of EPT reduces the activation energy of recrystallization [79–81, 92, 115–117, 119]. In addition, the short duration of EPT limits the recrystallization time, which prevents the grains from growing. The small size of grains are obtained finally [72–74, 112, 124, 129, 131]. With further strengthen the effects of EPT on solid state materials (e.g. Al-Mg-Cu-Zn alloys, Fe-B-Si alloys, Nd-Fe-Co-B alloys, Ti-C/Ni-Cr cermet, Fe-Co alloys, steels and Cu-Zn alloys), the grain refinement can be achieved even into nano-scale range, which is called nano-crystallization. Nano-crystallization fabricated by EPT, can significantly optimize the mechanical properties of materials and EPT has a much higher work efficiency and lower energy consumption in comparison with that conventional methods (SPD or DPD). Recently, researchers observed that the nanotwins can be produced by EPT in solid state Cu-Zn alloys [73, 112], which improves the strength and ductility of materials simultaneously [28, 32, 163].

2.2.4 Grain orientation and texture

Grain orientation affects the anisotropic property of materials. For magnetic materials, the magnetic properties are required to be maximized in a particular direction [137, 139]. The strength of materials are sometimes also required to be maximised in some directions [79, 134, 135, 138, 143, 146]. Electric-current treatment has been used to adjust the grain orientation and texture formation in various metals and alloys such as Zn-Al alloys (ZA22 and ZA27) [148], ferritic-pearlitic steels [101, 102], Cu-Zn alloys [72, 112, 142], thin films [147], Cu-Sn alloys [141], carbon steels [144, 145], Si steels [137, 139], Ti-6Al-4V alloys [143], Mg alloys [79, 134–136, 138] and pure Cu metals [146] and hence to optimize their properties. The details of effects of electric-current treatments on grain orientation and texture adjustment are depicted in Table 2.4.

Table 2.4: The effect of EPT on crystal rotation and textures

Materials	**Processing**	**Effects of EPT**
Zn-Al alloys (ZA22 and ZA27)	Solid state with EPT	Acceleration of the preferred crystal orientation of nanophase η'_n formation from (0002) to (10-11) [148]
Ferritic-pearlitic steels	Solid state with EPT	Alignment of the formation of cementite with current direction [101, 102]
Cu-Zn alloys	Solid state with EPT	A promotion of oriented nanotwins [112]
Thin films	Solid state with EPT	Change the crystal orientation [147]
Cu-Sn alloys	Solid state with d.c. current	1. Cu_3Sn grew in the <020> and <400> directions [141] 2. Cu_6Sn_5 grew in the <204> and <62-3> directions [141]
Carbon steels	Liquid state with EPT	Alignment of MnS with current direction [145]
Fe- 3wt% Si steel	Solid state with EPT	Promotion of G-texture [139]

Ti-6Al-4V alloys	Solid state with EPT	Weakening basal texture [143]
Mg-9Al-1Zn alloys	Solid state with EPT	Weakening basal texture [79, 140]
Pure Cu metals	Solid state with EPT	1. Strengthening P (011)<12-2> texture [146] 2. Weakening S (123)<63-4> and Bs (110)<1-12> texture [146]

Note: d.c. is direct current and EPT is electropulsing treatment

2.2.4.1 Electric-current treatments on grain orientation

EPT was found to be more powerful than the conventional methods (e.g. thermal treatments) in altering nanophase η'_n orientation in solid state Zn-Al alloys [148]. Although experimental results confirmed that the preferred crystal orientation of nanophase η'_n was changed from (0002) to (10-11) under EPT, the authors haven't presented a clear explanation for the effects of electric current on orientation adjustment. To further investigate the effects of electric current on grain orientation, more experiments need to be performed. Recently, it was observed that the newly formed phases (e.g. the cementite plates in ferritic-pearlitic steels [101, 102], the MnS inclusions in carbon steels [144, 145], the (111) oriented nanotwins in Cu-Zn alloys [72, 112, 142] and the (0,1,11) oriented precipitation of $Sb_{2.9}Te_{7.1}$ in thin films of $(Bi_{0.25}Sb_{0.75})Te_3$) [147] are aligned with the electric current direction. All alignments are associated to the reduction of system free energy (i.e. electric effects of electric current).

More interestingly, applying d.c. current to Cu-Sn alloys can also promote the formation of Cu_3Sn in the <020> and <400> directions and Cu_6Sn_5 in the <204> and <62-3> directions [141]. These newly nucleated phases in Cu-Sn alloys are strongly related to direction of electric current in order to increase the electrical conductivity.

2.2.4.2 Electric-current treatments on texture

Macroscopically, the texture of polycrystalline materials can be effectively modified by electric-current treatments. For example, a formation of Goss texture (G-texture) (011)<001> in Si steels can efficiently increase the magnetic properties by reducing the magnetic loss under a magnetic field collinear with rolling direction. The formation of G-texture in Si steels strongly relates to stored energy of grains, reduction of rolling and annealing parameters during recrystallization. EPT, as a high energy input method which can instantaneously promote the formation of G-texture in Si steels during recrystallization [137, 139]. This G-texture promotion under EPT is mainly attributed to the electric effects of EPT in reducing Gibbs free energy and increasing the electrical conductivity. Oppositely, a weakening effect for basal texture formation induced by EPT has been found in Ti-6Al-4V and Mg-9Al-1Zn alloys [79, 140, 143]. In this case, the electric effects of EPT mainly contribute to the weakening effect and hence to increase the formability of Ti-6Al-4V and Mg-9Al-1Zn alloys. According to the electric effects of EPT on the promotion of texture with higher electrical conductivity, a successful development of EPT had been recently utilized to strengthen P (011)<12-2> texture and weaken S (123)<63-4> and Bs (110)<1-12> textures simultaneously in pure Cu metals [146].

2.2.5 Control electrically non-metallic particles motion

Generally, non-metallic oxides inclusions have relatively lower electrical conductivity in comparison with the liquid metals [149]. Inclusions have a detrimental effect on the performance of engineering alloys (e.g. formality) by increasing the risk for mechanical and corrosive failure. For example, inclusions cause failure of steels depending on their morphologies, sizes and positions [144, 145]. Thus how to effectively remove those inclusions is important in fabrication of steels. The steel industry uses several methods including filtration, bubbling and electromagnetic stirring to eliminate those inclusions from steels. But those methods are not effective in removal of the inclusions whose sizes are smaller than 50 μm [144]. EPT can remove small inclusions with little energy consumption. Two typical engineering alloys have been used to verify the reliability of EPT on removal of the electrically non-metallic particles: first is the Cu-Zn alloys [72, 142] and the second is carbon steels [144, 145, 149]. The details of motion of electrically non-metallic particles under EPT in those two alloys are reviewed in Table 2.5.

Table 2.5: Applications of EPT on motion of electrically non-metallic particles in alloys.

Materials	**Processing**	**Effects of EPT**
Cu-Zn alloys	Solid state with EPT	Move inclusions (Pb) to grain boundaries [72, 142]
Carbon steels	Liquid state with EPT	Move inclusions (MnS and Al_2O_3) from middle regions to surroundings [144, 145, 149]

In Cu-Zn alloys, lead (Pb) inclusions can be efficiently moved from random distributed regions to grain boundaries or defects by EPT. This movement of Pb inclusions induced by EPT is mainly attributed to the electric effects of EPT, which strongly depends on the discrepancy of electrical conductivity of phases. MnS and Al_2O_3 are also removed from middle regions to surroundings in molten carbon steel at high temperature and hence to produce clean steel. The mechanisms for inclusion removal are schematically illustrated in Figure 2.12.

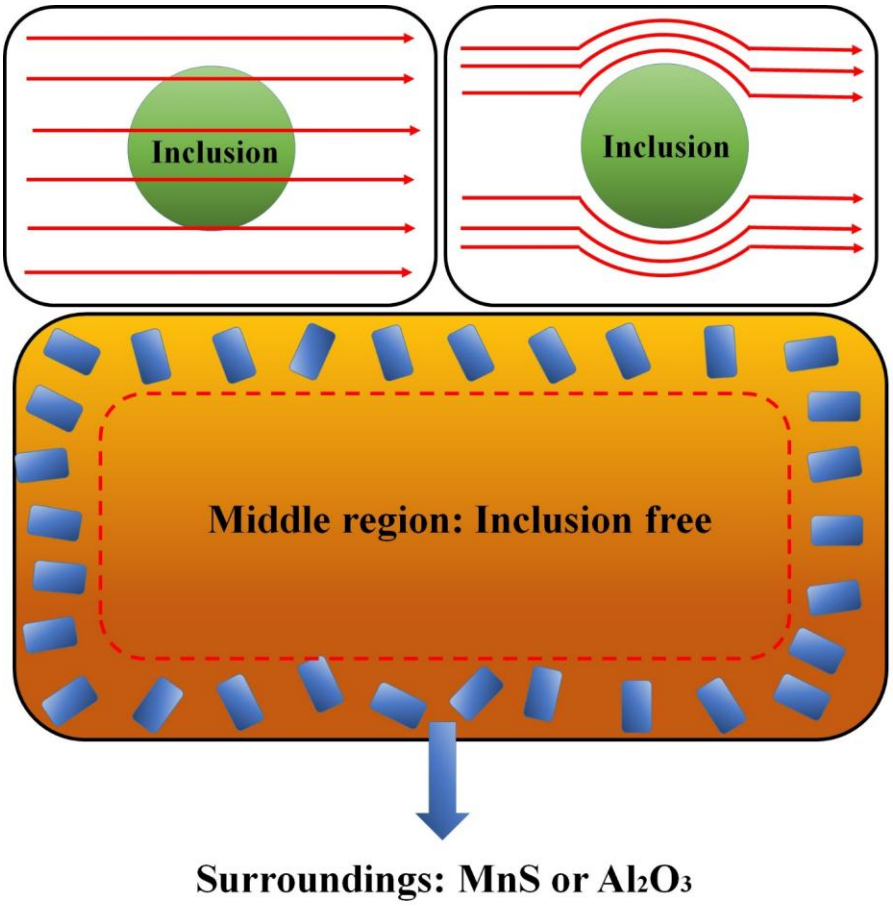


Figure 2.12: Schematic diagrams of inclusion movement in alloys under EPT.

The upper left picture represents the distribution of current across the microstructure consisting of an inclusion and matrix (the electrical conductivity of inclusion is the same as that of the matrix). The current lines directly pass the inclusion and matrix without any change. The upper right picture shows the distribution of current across the microstructure consisting of an inclusion and matrix where the electrical conductivity of inclusion is less than that of the matrix. The current lines are altered due to the discrepancy of electrical conductivity between inclusion and matrix. Bottom picture depicts the microstructure consisting of a number of inclusions (MnS and Al_2O_3) and matrix after EPT. EPT move inclusions from the middle region to the surroundings [72, 142, 144, 145, 149].

2.2.6 Dislocation

Dislocation is one of crystallographic defects that can significantly affect many properties of polycrystalline metals and alloys. For example, the movement and annihilation (two opposite orientation of dislocation can bring together and cancel each other) of dislocations play an important role in influencing the plasticity of materials during the deformation process [18]. Traditionally, thermal and themo-mechanical processing can be used to modify the dislocation behaviour but they are too expensive and have low efficiency [1, 18]. Recently, it is proposed that EPT (electric effect) can be an alternative method to effectively control the dislocation behaviour and hence to improve the plasticity of materials with high work efficiency and low energy consumption [164, 165]. Under EPT, electron wind force generated by the knock-on collision of ultrasonic speed electrons with atomic nuclei, was greatly beneficial to the mobility of dislocations. This is because the process of transference energy from electrons to dislocations induced by electron wind force is much higher than that by traditional thermal and themo-mechanical processing. This transference energy can

effectively accelerate the motion of dislocations by reducing the energy barrier. A schematic drawing of effect of EPT on dislocation movement is illustrated in Figure 2.13.

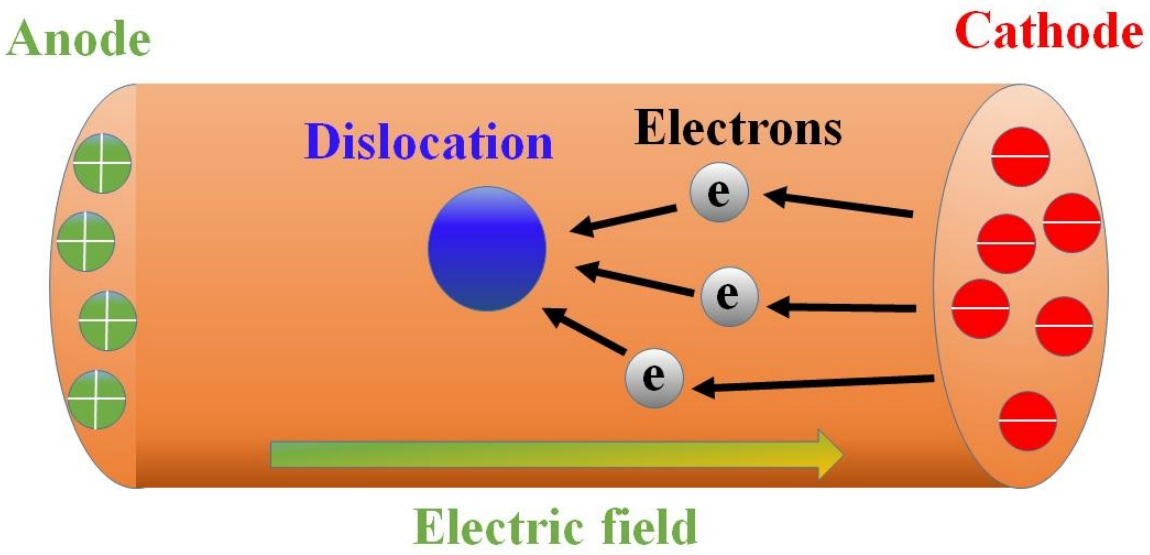


Figure 2.13: Schematic diagram of dislocation movement under EPT. The motion of dislocation can be effectively accelerated by transfer of energy from electrons via collision. The direction of electrons is opposite to the direction of the electric field between anode and cathode.

EPT have been utilized to change their dislocation behaviour and corresponding plasticity for a wide range of materials such as pure metals (Ti, Cu and W metals) [105, 113, 120, 123], alloys, (Mg alloys, Al alloys, Ti alloys, Ni alloys, Cu-Zn alloys, Zn-Al alloys and Fe-based alloys) [38, 45–47, 52–56, 61, 63–67, 73, 79–81, 86–88, 92, 93, 95, 98, 102, 116–119, 121, 122, 124, 125, 128, 129, 151–156]. This is called eletroplasticity. The literature is summarized in Table 2.6.

Table 2.6: Applications of EPT on dislocation movement in alloys.

Materials	Effects of EPT
Pure Ti sheet	Decrease dislocation tangles and enhance dislocation mobility [105]
Pure Cu metal	Increasing the mobility of dislocation and accelerate dislocation annihilation [113, 120]
Pure W metal	Acceleration of rearrangement of dislocation [123]
Mg alloys (Mg-3Al-1Zn alloy, Mg-6Al-1Zn alloy and Mg-9Al-1Zn alloy)	Increase the movement of dislocation and hence to promote the annihilation process [38, 46, 47, 79–81, 92, 116, 117, 119]
2024 Al alloys	Accelerating dislocation motion and opening tangle of dislocation, thus to promote dislocation annihilation [45, 118]
6061 Al alloys	Accelerate the movement of dislocation and hence to increase the recrystallization process [128]
Ti-6Al-4V alloys	Weakening dislocation entangling and piling up to speed up the dislocation migration and interaction [56, 121, 122, 156]
TC4 Ti alloys	Reducing dislocation density and enhancing the mobility of dislocation [155]
GH4169 Superalloys	Promoting dislocation motion to reduce deformation resistance [93]
Cu-Zn alloys	Change in dislocation arrays and nodes [61, 73, 124, 129]
Zn-Al alloys	Acceleration of the movement of both dislocation and vacancies to promote annihilation [52–55, 63–67]
Graphite iron	Acceleration of dislocation accumulation around the grain boundary to promote nucleation of graphite [86–88]
Hot working die steel	Enhancement of dislocation motion [153, 154]

2.2.7 Crack healing

The formability indicates the capability of engineering alloys to undergo plastic deformation without fracture. Cracks may initiate and propagate in the alloys during the mechanical forming process. This section reviews the influence of a pulsed electric current on cracking behaviour in materials including steels (medium carbon steels [159], 1045 steels [158, 161], hand-worked saw blade [160], cast hot working die steels [154] and 316 austenitic steels [151]), Ti alloys (TC4 Ti alloys [155] and Ti-6Al-4V alloys [156]) and NiTi alloys [157]. The effects of both temperature and Gibbs free energy increment induced by electric current are considered. From the literature, it is shown that a pulsed electric current has a positive effect on cracking healing depending on prior treatment of the materials, processing conditions and types of cracks. This can improve the formability of engineering alloys. The details of effects of EPT on cracking of engineering alloys are listed in Table 2.7.

Table 2.7: Applications of EPT on crack healing for alloys.

Materials	**Effects of EPT**
Medium carbon steels	Partly heal precracks [159]
1405 steels	Heal quenched cracks [158, 161]
Handworked saw blade	Heal microcracks resulted from quenching martensite [160]
TC4 Ti alloys	Heal microcracks resulted from plastic deformation [155]
Hot worked die steels	Delayed the propagation of thermal fatigue cracks [153, 154]
Ti-6Al-4V alloys	Heal fatigue cracks [156]
316 austenitic steels	Heal fatigue cracks [151]
Porous NiTi alloys	Reduce the pores' dimensions and volume [157]

In order to investigate the effects of EPT on cracking of engineering alloys, researchers created a crack within a medium carbon steel sample and subsequently treated the sample using EPT, as shown in Figure 2.14.

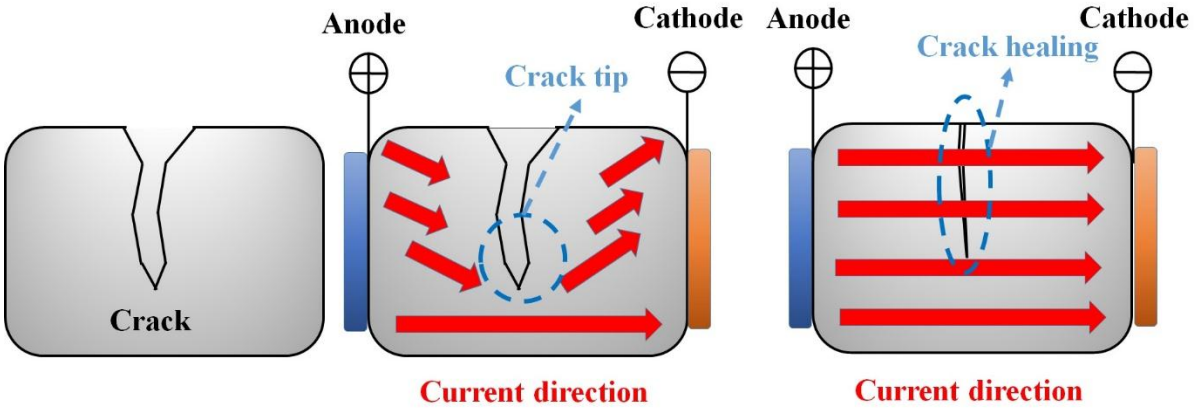


Figure 2.14: A process of crack healing in a medium carbon steel under EPT. Left: A precrack is manually created in steel sample; middle: EPT is applied across the steel sample between anode and cathode; and Right: The precrack is partially healed under EPT.

The crack was partially healed by EPT. This is mainly attributed to the thermal effect and EPT-promotion of atom diffusion. Due to the partial healing effect induced by EPT, more researchers started to investigate the effect of EPT on cracking behaviour and they found that the quenched cracks can be completely healed in several engineering alloys by high current density EPT [161]. Besides the quenched cracking healing, the cracks created by fatigue can also be healed under EPT in steels and Ti alloys [151–155]. The joule heating and thermal compressive stress due to the temperature increment and thermal expansion, all contributed to the crack healing. The mathematical analysis of crack healing induced by EPT has been systemically demonstrated, which revealed that the healing driving force depends on the current density, crack geometry, Young's modulus and sample size [158]. More interestingly, recent works show that not only the size of pore, but also the volume of pores can be

significantly reduced by applying EPT in NiTi alloys [157]. As a result, the reasonably use of thermal effects of EPT make it a promising method to heal cracks in engineering alloys and hence to improve their formability.

2.2.8 Theoretical analysis of EPT

Based on experimental observations of the EPT on microstructure evolution (precipitation, phase transformation, grain size, grain orientation, motion of electrically non-metallic particles, dislocation and crack healing) and properties (optimizing mechanical properties) for polycrystalline metals and alloys, the effects of EPT can be roughly divided into two types, one is thermal effect and another is electric effect. Both effects play important roles in influencing the microstructure and properties of materials. The relationships are schematically illustrated in Figure 2.15.

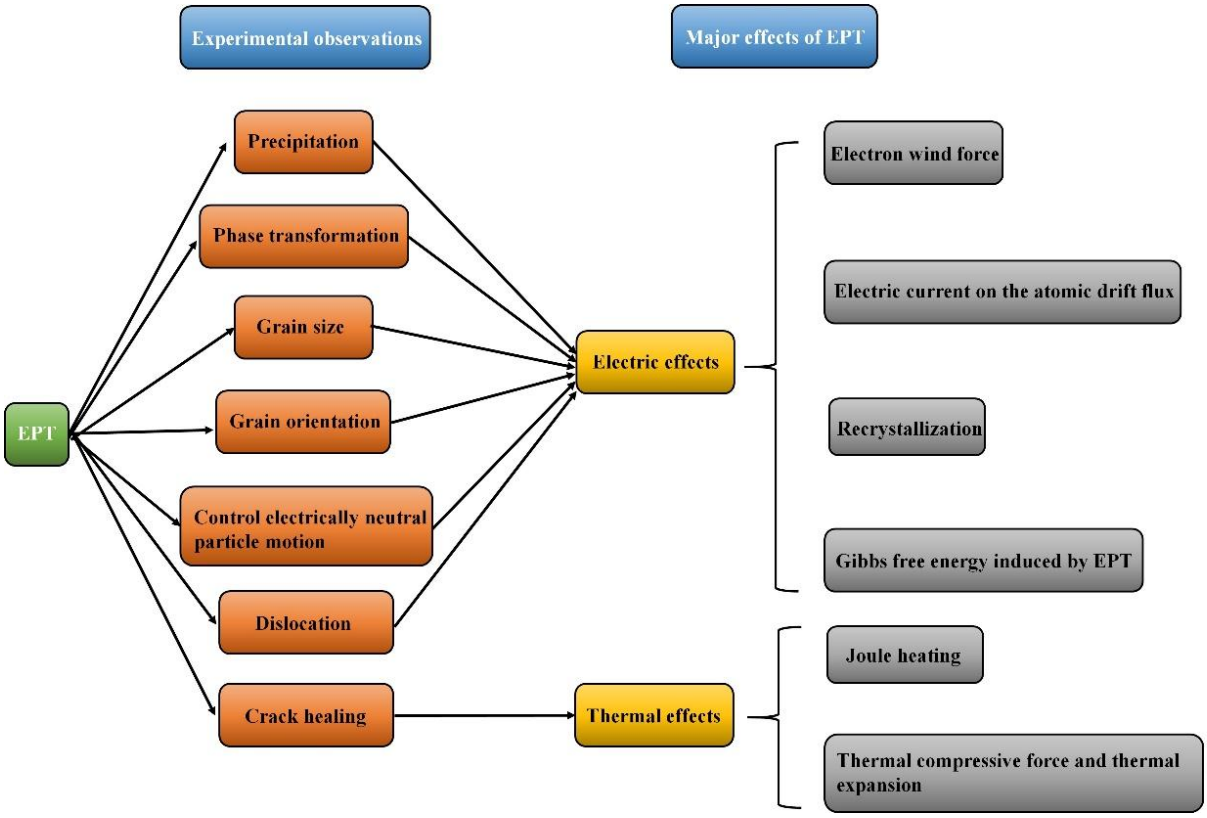


Figure 2.15: A schematic diagram to describe relationships between EPT and microstructure evolutions in literature [33–162].

2.2.8.1 Thermal effects of EPT

2.2.8.1.1 Temperature increment due to electric current

For the thermal effects, passing electric current generates temperature increment inside materials, which can be expressed as

$$\Delta T = (C_p \rho_d)^{-1} \rho_e \int j^2(t) dt \tag{2.6}$$

where C_p is specific heat of material, ρ_d is the density of material, ρ_e is the electrical resistivity, j is the current density, t is the time interval and ΔT is temperature increment.

This is a standard equation for calculation of temperature increment ΔT induced by Joule heating of electric current. Once the current density at a sample is known, the average temperature increment at this sample can be calculated.

2.2.8.1.2 Thermal compressive force generated by electric current

Thermal compressive force due to EPT is utilized to alter microstructure evolutions such as crack healing. The standard calculation of the thermal compressive force induced by EPT is expressed as

$$\sigma_{(t)} = E\alpha\Delta T_{\max}[\theta_{(t)} - l_{(t)}] \tag{2.7}$$

where $\sigma_{(t)}$ is the maximum compressive force, E is Young's modulus of material, ΔT_{max} is the temperature increment, α is thermal expansion of material, $\theta_{(t)}$ is the dimensionless temperature increment and $l_{(t)}$ is the dimensionless thermal expansion. $\theta_{(t)}$ can be expressed as

$$\theta_{(t)} = \frac{\Delta T_{(t)}}{\Delta T_{(max)}} \tag{2.8}$$

where $\Delta T_{(t)}$ is instant temperature change and $\Delta T_{(max)}$ is maximum temperature change. $l_{(t)}$ can be expressed as

$$l_{(t)} = \frac{\Delta l_{(t)}}{\Delta l_{(max)}} \tag{2.9}$$

where $\Delta l_{(t)}$ is instant thermal expansion and $\Delta l_{(max)}$ is maximum thermal expansion. Differentiating both sides of Equation 2.7 gives

$$\frac{d\sigma_{(t)}}{dt} = E\alpha\Delta T \frac{d[\theta_{(t)} - l_{(t)}]}{dt} \tag{2.10}$$

The thermal compressive force can be maximized when $\frac{d\sigma_{(t)}}{dt} = E\alpha\Delta T \frac{d[\theta_{(t)} - l_{(t)}]}{dt} = 0$, $\frac{d^2[\theta_{(t)}]}{dt^2} \le 0; \frac{d^2[l_{(t)}]}{dt^2} \le 0$ and $\frac{d^2[\theta_{(t)}]}{dt^2} - \frac{d^2[l_{(t)}]}{dt^2} \le 0$.

One has $\theta_{(t)} = 1_{(t)}$. The maximum thermal compressive force induced by EPT can be obtained

$$\sigma_{\max} = E\alpha\Delta T_{\max} \tag{2.11}$$

2.2.8.2 Electric effects of EPT

For the polycrystalline metals and alloys under electric-current treatments, their microstructure evolutions are affected by the electric effects. These electric effects contain kinetics (e.g. electric wind force) and thermodynamics (electric current induced free energy change).

2.2.8.2.1 Kinetics of electric current

Under electric-current treatments, the drift electrons generated by the electric current can exert a pushing force on the mobile defects, such as dislocations, along the direction of electron flow. This pushing force, namely, electron wind force, arises from applying a local electric potential and electrons in conductive materials. Due to the interaction of electron wind force between electrons and dislocations, the momentum transfer from electrons to dislocations provides favourable conditions for dislocation accumulation and annihilation and hence to rearrangement of dislocation structures (e.g. reduction of dislocation density, dislocation de-pining, breaking entangle and etc.).

According to the classical scattering model, the electron wind force can be expressed as

$$F_{\max} = -\frac{n\rho_d m_o}{n_d \rho m^*} eE \tag{2.12}$$

where n is the density of conduction electrons, n_d is the density of defects, ρ_d is the defect resistivity, ρ is the metal resistivity, m^o is the free-electron mass, m^* is the effective electron mass, e is the elementary charge and E is the macroscopic electric field.

The total driving force can be simplified to

$$F_{\max} = F_{wind} = Z_{wind}^{*} eE \tag{2.13}$$

where Z_{wind}^{*} is effective valence.

Using the Nernst-Einstein relation, the drift velocity V_d of dislocation can be empirically expressed as

$$V_d = \frac{D_a}{kT} Z_{wind}^{*} eE \tag{2.14}$$

where D_a is a constant.

From Equation 2.14, it is obviously that a higher electron wind force leads to a higher drift velocity of dislocation. The high drift velocity of dislocation accelerates the rearrangement of dislocation structures.

Besides the dislocations, electric wind force can also affect the atomic drift flux. The atomic flux due to electric current is

$$J_i = \frac{N_i D_i}{kT}\left(kT\frac{\partial \ln x_i}{\partial x} - \Omega\frac{\partial \sigma}{\partial x} + Z^* e\rho j\right) \tag{2.15}$$

Equation 2.15 can be simplified as

$$J_i = J_t + J_a \tag{2.16}$$

Where J_t is the atomic flux is induced by temperature and J_a is the atomic flux produced by electric current. Because the thermal effect of electric current on atomic flux is extremely small: $J_t \approx 0$, the electric effects play an important role in influencing the overall atomic flux. The total atomic flux can be simplified as

$$J_i = J_a = \frac{2NDZ_{wind}^{*}\rho_d efj\tau_p}{\pi kT} \tag{2.17}$$

where D is lattice diffusion coefficient, N is the density of atom species, j is the current density, f is the pulsed current frequency, τ_p is the duration of each pulse, k is the gas constant and T is the absolute temperature.

Equation 2.17 can be transferred to Equation 2.18

$$J_i = J_a = 2NDZ^{*}\rho efj\tau_p \tag{2.18}$$

From Equation 2.18, it is observed that the electropulsing parameters (e.g. frequency, duration and current density) are proportional to the total atomic flux.

2.2.8.2.2 Thermodynamics of electric current

According to the nucleation theory, the nucleation rate without electric current is expressed as

$$I_r = I_r^{o}(\frac{D}{\lambda^2})\exp(\frac{-\Delta G_o}{RT}) \tag{2.19}$$

where I_r is the nucleation rate without EPT, I_r^o is constant, λ is jump distance, D is diffusivity, k is gas constant and T is absolute temperature. If an electric current is applied to the system, Equation 2.19 is changed into

$$I_r^{EPT} = I_r^o(\frac{D}{\lambda^2})\exp(-\frac{\Delta G_o + \Delta G_e}{RT}) \tag{2.20}$$

where I_r^{EPT} is the nucleation rate with EPT and ΔG_e is the Gibbs free energy induced by EPT. Equation 2.20 can be transformed to

$$I_r^{EPT} = I_r \exp(\frac{-\Delta G_e}{RT}) \tag{2.21}$$

The value of ΔG_e strongly depends on the discrepancy of electrical conductivity of phases as

$$\Delta G_e = \mu g \xi(\sigma_1, \sigma_2) j^2 \Delta v \tag{2.22}$$

where μ is magnetic permeability, j is current density, ΔV is volume of material, $g = \mu\left[\frac{3}{2}\ln\left(\frac{R}{a}\right) - \frac{65}{48} - \frac{5}{48}\frac{\sigma_2 - \sigma_1}{\sigma_1 + 2\sigma_2}\right]R^2\Delta V$ is geometric factor and $\xi(\sigma_1, \sigma_2)$ is a factor. The factor ξ can be expressed as

$$\xi(\sigma_1, \sigma_2) = \frac{\sigma_2 - \sigma_1}{\sigma_1 + \sigma_2} \tag{2.23}$$

When $\sigma_1 > \sigma_2$, $\Delta G_e < 0$. This gives $I_r^{EPT} > I_r$ which means that electric current can increase nucleation rate by decreasing the thermodynamic barrier in comparison with other conventional methods.

The extra free energy induced by electrical current influences the number of nuclei. Based on the classical nucleation theory, the number of nuclei under electric-current treatments can be expressed as

$$n = n_0 \exp(-\frac{\Delta G_o + \Delta G_e}{kT}) \tag{2.24}$$

where n_o is the total number of atoms, ΔG_0 is the Gibb free energy without electric current and ΔG_e is the Gibbs free energy with electric current. Substituting Equation 2.22 into Equation 2.24:

$$n = n_0 \exp(-\frac{\Delta G_r^{\ o} + \mu g \frac{\sigma_2 - \sigma_1}{\sigma_1 + 2\sigma_2} j^2 \Delta v}{kT}) \tag{2.25}$$

From Equation 2.25, it is easily found that the number of nuclei is strongly related to the discrepancies of electrical conductivity of phases.

In order to more accurately describe the relationship between electrical properties and extra free energy induced by electric current, a derivation has been performed. The total free energy of system is

$$\Delta G_0 = \Delta G_c + \Delta G_i + \Delta G_s + \Delta G_e \tag{2.26}$$

where ΔG_c is chemical free energy, ΔG_i is interfacial energy, ΔG_s is strain-stress energy and ΔG_e is electric current free energy. Consider conductive electrons are forced to move toward the direction of an applied electric field $\vec{E}$ within an infinitesimal volume δV of

material. The total work required to drift electrons with an infinitesimal displacement $\delta\vec{S}$ under the local electrophoresis force $\vec{F}_e$ can be expressed as

$$\delta W = \vec{F}_e \cdot \delta\vec{S} \tag{2.27}$$

where $\vec{F}_e = \vec{E}\rho_c$ and $\delta\vec{S} = \vec{v}_d\,\delta t$. So Equation 2.27 can be transferred to

$$\delta w = (\vec{E}\rho_c)\cdot(\vec{v}_d\,\delta t) = \vec{E}\cdot(\rho_c\,\vec{v}_d)\delta t = \vec{E}\cdot\vec{j}\,\delta t \tag{2.28}$$

where ρ_c is the density of conductive electrons, $\vec{v}_d$ is the electron movement velocity, δt is the time for electrons movement and $\vec{j}$ is the current density.

Since $\nabla\times\vec{H} = \vec{j} + \frac{\partial\vec{D}}{\partial t}$ and $\frac{\partial\vec{D}}{\partial t} = 0$ based on the Ampere's law,

$$\delta w = \vec{E}\cdot\vec{j}\,\delta t = \vec{E}\cdot(\nabla\times\vec{H})\delta t = \nabla\cdot(\vec{E}\times\vec{H})\delta t - \vec{H}\cdot(\nabla\times\vec{E})\delta t \tag{2.29}$$

where $\vec{H}$ is the magnetic field strength and $\vec{D}$ is the electric displacement.

Integrating Equation 2.29 throughout the total volume δV can obtain the total work for moving electrons in a time duration δt

$$\delta W = \iiint \delta w dV = \iiint [\nabla\cdot(\vec{E}\times\vec{H})\delta t - \vec{H}\cdot(\nabla\times\vec{E})\delta t]dV \tag{2.30}$$

Since $\iiint \nabla\cdot(\vec{E}\times\vec{H})dV = \oint(\vec{E}\times\vec{H})\cdot d\vec{S} = 0$

So

$$\delta W = \iiint -\left[\vec{H}\cdot(\nabla\times\vec{E})\delta t\right]dV \tag{2.31}$$

According to the Faraday's law

$$\nabla \times \vec{E} = -\frac{\delta \vec{B}}{\delta t} \tag{2.32}$$

Substituting Equation 2.32 into Equation 2.31:

$$\delta W = \iiint (\vec{H} \cdot \delta \vec{B}) dV \tag{2.33}$$

where $\vec{B} = \nabla \times \vec{A}$ is the magnetic field and $\vec{A}$ is the vector potential. The Equation 2.33 can be converted to

$$\delta W = \iiint (\vec{H} \cdot \delta \vec{B}) dV = \iiint \left[\vec{H} \cdot \delta (\nabla \times \vec{A}) \right] dV \tag{2.34}$$

Since $\vec{H} \cdot (\nabla \times \vec{A}) = \vec{A} \cdot (\nabla \times \vec{H}) - \nabla \cdot (\vec{H} \times \vec{A})$ and $\iiint \left[\nabla \cdot (\vec{H} \times \vec{A}) \right] dV = 0$. The Equation 2.34 can be

$$\delta W = \iiint \left[\vec{A} \cdot (\nabla \times \vec{H}) \right] dV \tag{2.35}$$

From Equations 2.33 and 2.35, the Gibbs free energy changed under magnetic field can be expressed as

$$G_e = -\frac{1}{2} \iiint (\vec{H} \cdot \vec{B}) dV = -\frac{1}{2} \iiint [\vec{A} \cdot (\nabla \times \vec{H})] dV = -\frac{1}{2} \iiint (\vec{A} \cdot \vec{j}) dV \tag{2.36}$$

Within the material, the Gibbs energy change is

$$G_e = -\frac{1}{2} \int_V \vec{A}(r) \cdot \vec{j}(r) dr \tag{2.37}$$

where r is the random position in the materials. We know $\vec{B} = \nabla \times \vec{A}$ and differentiating $\vec{B}$ can obtain

$$\nabla \times \vec{B} = \nabla \times (\nabla \times \vec{A}) = \nabla(\nabla \cdot \vec{A}) - \nabla^2 \vec{A} = -\nabla^2 \vec{A} \tag{2.38}$$

According to the electromagnetism, the magnetic field $\vec{B}$ is a function of auxiliary magnetic field $\vec{H}$, which can be used to describe the dipole migration and magnetic dipole. The magnetic field can be expressed as

$$\vec{B} = \mu \vec{H} \tag{2.39}$$

where μ is the magnetic permeability.

So $$\nabla \times \vec{B} = \mu \nabla \times \vec{H} \tag{2.40}$$

Since $\vec{j} = \nabla \times \vec{H}$

$$\nabla \times \vec{B} = \mu \vec{j} \tag{2.41}$$

Substituting Equation 2.38 into Equation 2.41:

$$\nabla^2 \vec{A} = -\mu \vec{j} \tag{2.42}$$

Based on the general solution of Poisson equation, the potential vector $\vec{A}(r)$ can be expressed as

$$\vec{A}(r) = \frac{1}{4\pi} \int_V \frac{\mu(r') \vec{j}(r')}{|r - r'|} dr' \tag{2.43}$$

where r' is another position of material. Substituting Equation 2.43 into Equation 2.37, the total Gibbs free energy changed under electric-current treatments can be expressed as

$$G_e = -\frac{1}{8\pi}\int_V \int_V \frac{\mu(r')\vec{j}(r')\cdot\vec{j}(r)}{|r-r'|}drdr' \tag{2.44}$$

According to the Equation 2.44, the phase stability can be affected by electropulse-induced free energy, as shown in Figure 2.16.

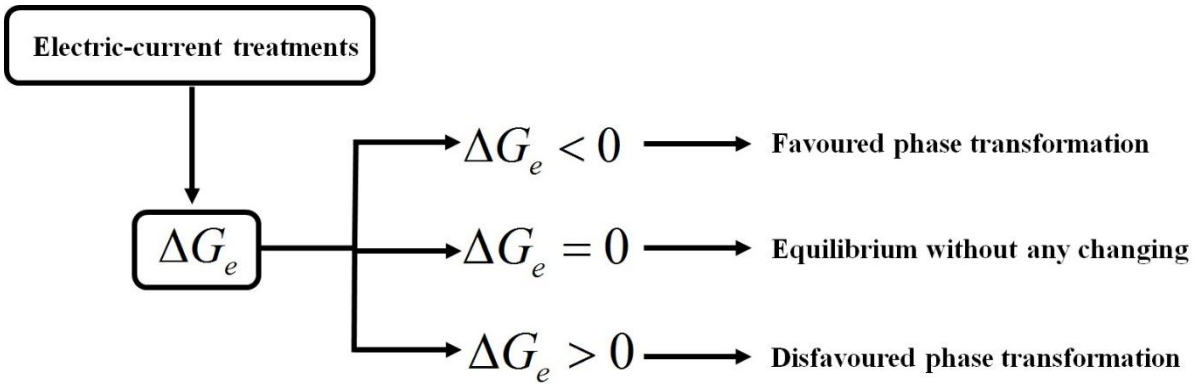


Figure 2.16: A schematic diagram of the effect of EPT on phase stability via changing Gibbs free energy: $G_e < 0$ indicates the phase stability is favourable, whereas $G_e > 0$ shows the phase stability is unfavourable. $G_e = 0$ means no influence on the stability of the phase in an electric-current-free system.

From Figure 2.16, it was found that the phase stability (phase transformation) is favoured when $G_e < 0$ by reducing the total free energy of the system, whereas the phase stability is not favoured when $G_e > 0$ by increasing the total free energy of the system. For $G_e = 0$, the phase stability is non-affected in an electric-current-free system.

In addition to the general description of the applications of EPT on polycrystalline metals and alloys; their corresponding properties and theoretical analysis from literature, the following sections introduce the applications of EPT on four kinds of steels: 316L stainless steel, 2205 duplex stainless steel, duplex lightweight steel and dual-phase steel, as illustrated in Figure 2.17.

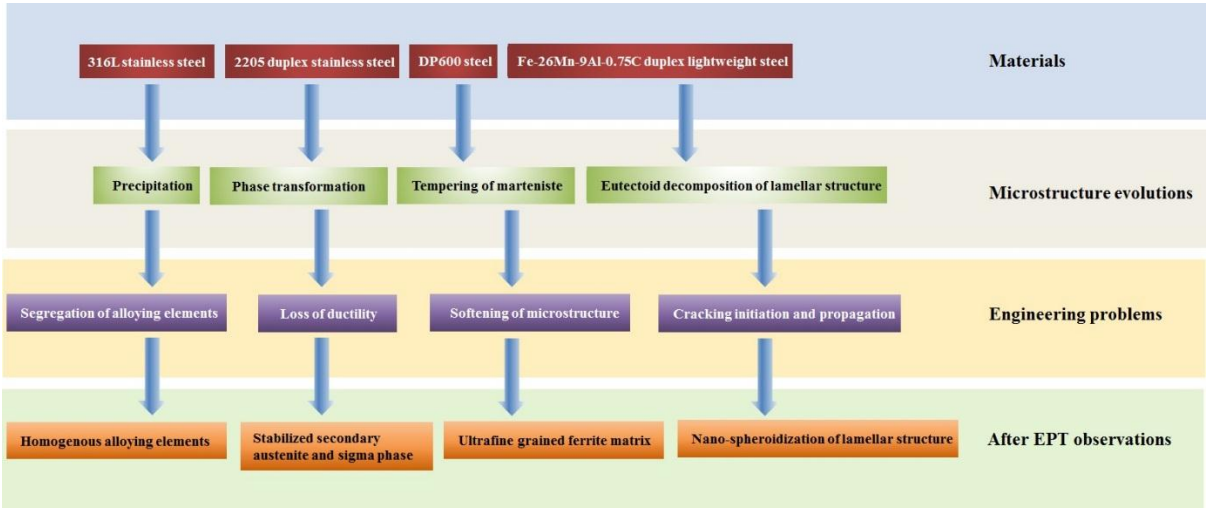


Figure 2.17: A schematic description of the effects of EPT on four specific steels on the phase stabilities. This includes the precipitation in 316L austenitic stainless steel, phase transformation in 2205 duplex stainless steel, cracking in duplex lightweight steel and softening in dual-phase steel.

Chapter 3 Stability of chi-phase in austenitic stainless steel during pulsed electric current treatment

3.1 Introduction

Stainless steels with suitable mechanical properties are implemented in biomedical industry and in nuclear reactors [6, 7, 9, 10, 13–15, 17, 166, 167]. Pitting, intergranular corrosion and stress cracking affect the performance of the stainless steels [10, 14, 15, 167]. Those detrimental effects are frequently induced by the nucleation of precipitates (with high concentrations of alloying elements around grain boundaries). Precipitates cause dramatic drop of corrosion resistance and mechanical properties in highly concentrated chloride environments and at high operation temperatures [7, 9, 14, 166].

Austenitic stainless steel is a single phase alloy. 316L stainless steel contains high concentrations molybdenum (Mo), chromium (Cr) and nickel (Ni) [12]. Segregation of these elements causes Mo-depleted or Cr-depleted areas which are less resistant to the general corrosion and oxidization. Precipitates are tiny particles formed in supersaturated alloys [166]. Coarsening of those precipitates frequently results in reduction of strength, localization of stress, crack initiation, creeping etc. [7, 9]. This can take place at elevated temperatures (above 300 ^{o}C) over long periods of time [13]. Such typical environments include the reactor vessels, boilers and piping systems in nuclear engineering [14] and turbine blades in nuclear power plant [9, 13].

In practice, stainless steel undergoes hot work at a temperature above 1000 ^{o}C and then is quenched to ambient temperature to avoid the formation of precipitates. The possible precipitates are secondary austenite phase, sigma phase, delta phase, $M_{23}C_6$ carbides, Chi-

phase (χ phase), etc. [6–8, 10, 11, 13, 15, 99]. All of those precipitates contain higher Mo, and Cr and lower Ni contents. The areas around the precipitates have lower-than average Mo and Cr contents and higher-than average Ni contents [168].

Fully austenitic 316L stainless steel containing 2-3 wt.% Mo, 16-18.5 wt.% Cr and 10-14 wt.% Ni implemented in the nuclear power plant has χ phase formed at the service temperature (>300 ^{o}C) [8, 11, 168]. χ phase is an intermetallic compound, has a chemical composition of $Fe_{36}Cr_{12}Mo_{10}$ and has a body centred cubic (BCC) structure (lattice parameter = 8.920Å). The formation of χ phase particles causes Cr- and Mo- depletion in the matrix adjacent to the precipitates. This destroys the oxide layer and leads to drops in corrosion resistance [8, 11].

Grain boundary engineering (GBE) has proved to be an effective method in suppressing the precipitation. GBE increases the corrosion resistance by introducing twin boundaries (i.e. Σ3 grain boundaries based on coincidence site lattice mode). Scientific evidence indicates that Σ3 grain boundaries have a remarkable resistance to the precipitation. Furthermore, they have an extremely good softening effect due to their highly regular and coherent structure, when compared with normal grain boundaries (i.e. high angle grain boundaries) [169–171]. Thermomechanical processing is frequently used to increase the formation of Σ3 grain boundaries [171]. However, GBE requires complex pre-treatments which is high-cost and low-efficiency.

Normally, the precipitates and Σ3 grain boundaries have different electrical conductivities to those of the steel matrix and normal grain boundaries, respectively [28]. These differences in electrical conductivity affect the electrical current distribution in the whole system because of the different configurations of the precipitates and Σ3 grain boundaries in the steel. The different current distributions correspond to different system free energies [99, 168, 172]. It has been suggested that the electric current promotes the formation of objects with a higher

electrical conductivity. This suggests that electric current can be used to affect both the formation of precipitates (such as χ phase) and the frequency of Σ3 grain boundaries in 316L stainless steels.

Conrad reported that a direct current (d.c.) accelerated the aging rate of Al-4 wt.% Cu alloy but retarded the aging rate of Al–12.5 wt.% Zn alloys. The effect becoming stronger as the current density increased [37, 43]. In order to avoid the considerable Joule heating generated by high-density electric currents, d.c. has been replaced by a short- duration pulse. Jiang et al. found that the EPT enhanced the dissolution rate of β-$Mg_{17}Al_{12}$ phase in aged Mg-9Al-1Zn alloy [36]. Wang et al noticed that the segregation of Pb in Cu-Zn alloy was promoted by the EPT which drove Pb to the grain boundaries [142].

In this chapter, using electric current to change microstructure evolutions has been proposed. It is aimed to use electric current to retard the nucleation and growth of precipitates particles and to enhance the formation of Σ3 grain boundaries. The phenomenon would be of great interest and is of industrial importance if the resulting microstructure evolution follows the plan. An understanding of how EPT affects both the precipitation and Σ3 grain boundaries is developed on the grounds of the kinetics and thermodynamics.

3.2 Materials and methods

A commercial 316L stainless steel with chemical composition (wt. %) 2-3 Mo, 16-18.5 Cr and 10-14 Ni was received. It was hot- rolled to 3 mm thickness plates and annealed at high temperature to obtain the fully austenitic microstructure, equiaxed grains and homogeneous solute distribution. The plates were further cold-rolled to 83.3% reduction from 3.00 mm to 0.5 mm thickness by a cold rolling machine (Figure 3.1a) and subsequently, cut into square

shaped specimens (via a cutting machine) with the longest edge perpendicular to the rolling direction (Figure 3.1b).

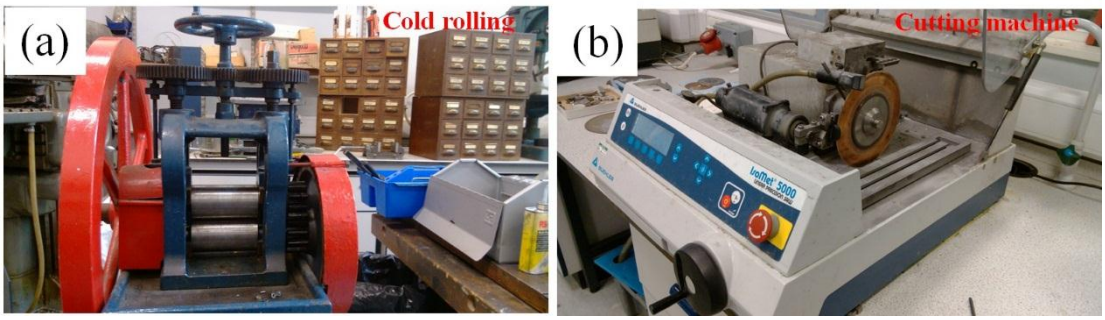


Figure 3.1: (a) a cold rolling machine and (b) a cutting machine.

EPT process was performed for 60 min by applying an electric current with 6.3×10^7 A/m^2, 1 Hz, 60 μs and 24 V at a temperature of 750 ^{o}C in a furnace. The pulsed current was provided by an electropulse-generator linked to a direct current power. Copper wires were used to connect the sample to the electropulse-generator. The direction of the electric current was perpendicular to the rolling direction. An oscilloscope was used to monitor the electropulse. The temperature was measured by a thermocouple. The embedded electrical feed-back system in the pulse generator enables one to maintian a constant current. The setting of the experimental facilities is schematically demonstrated in Figure 3.2.

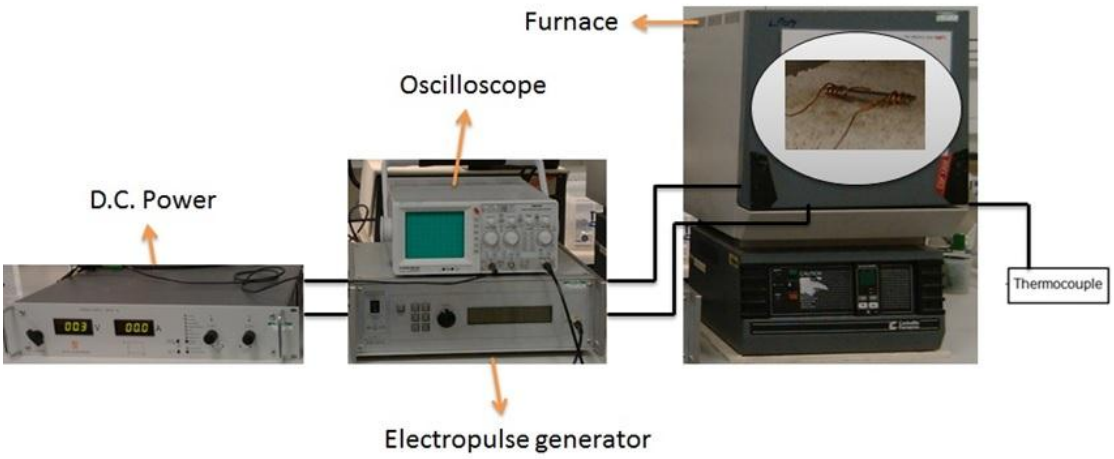


Figure 3.2: Experimental set-up of EPT processing.

During EPT, another identical specimen was placed next to the sample but no EPT was applied to this specimen. This ensures that both the actual and blank samples have been exposed to the exactly same annealing conditions and the only difference between them is that one underwent EPT and the other did not. After EPT, both samples were quenched into water to ambient temperature. The consumed electric power in the electric current pulse processing was 0.0028 Watts.

The specimens were mounted (Figure 3.3a and b) then mechanically- ground and polished (Figure 3.3c and d) and, finally, chemically etched with a solution made up of 20 ml hydrochloric acid, 10 ml nitric acid and 20 ml glycerine (Figure 3.3e).

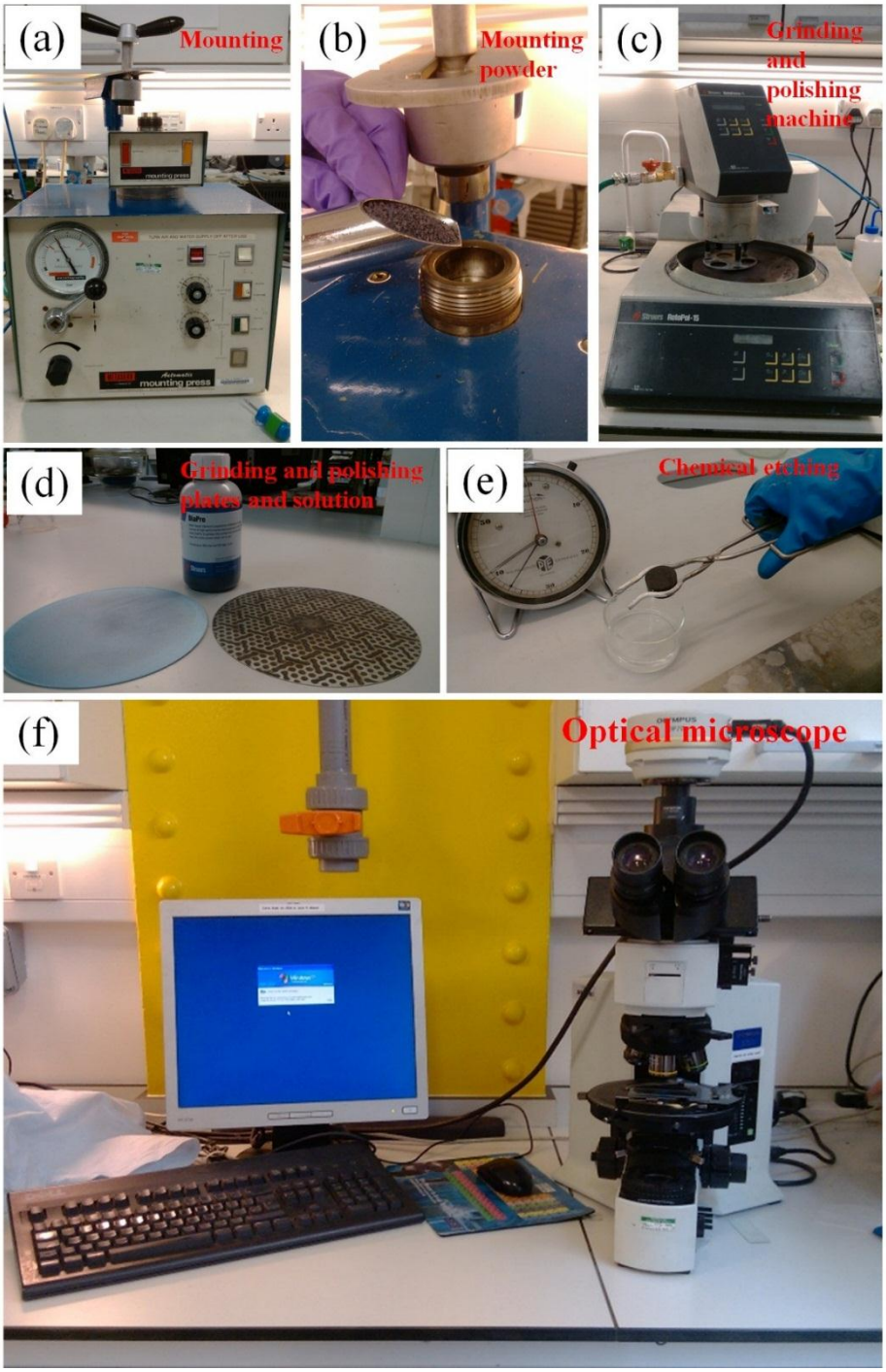


Figure 3.3: Photographs depicting sample preparation procedures: (a) a mounting machine with (b) Mounting power, (c) a grinding and polishing machine with (d) grinding and polishing lubricant, (e) chemical etching and (f) optical microscope.

The microstructure characterizations were carried out using an optical microscope (Figure 3.3f) and a Scanning Electron Microscopes (SEM LEO) (Figure 3.4d). The chemical compositions of the phases within the steel sample were determined by the energy dispersive X-ray spectroscopy (EDS) from the SEM JEOL 6400 (Figure 3.4a and b). The average grain size and the percentage of Σ3 grain boundary were measured by Electron Backscattered Diffraction (EBSD) derived with the SEM JEOL 6400 (Figure 3.4a and c).

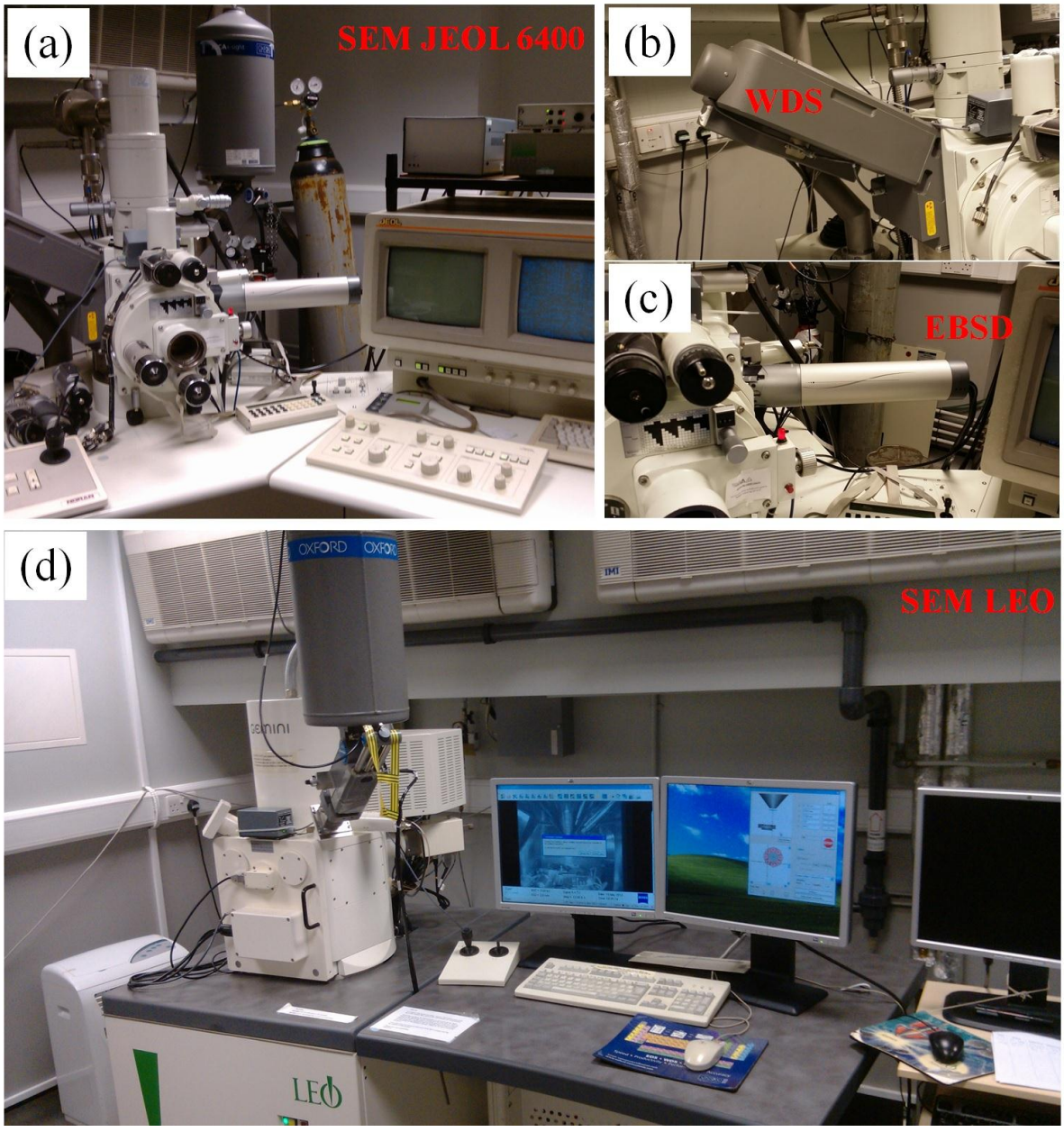


Figure 3.4: Photographs showing (a) a SEM JEOL 6400 microscope with (b) WDS and (c) EBSD, and a SEM LEO microscope.

The phases present in the steels were identified by Transmission Electron Microscopy (TEM 2000FX) (Figure 3.5c). For the TEM observation, specimens were mechanically polished to a thickness of 30μm, punched to disc specimens (3 mm in diameter) by a brass cutter in a sparking machine (Figure 3.5a and b).

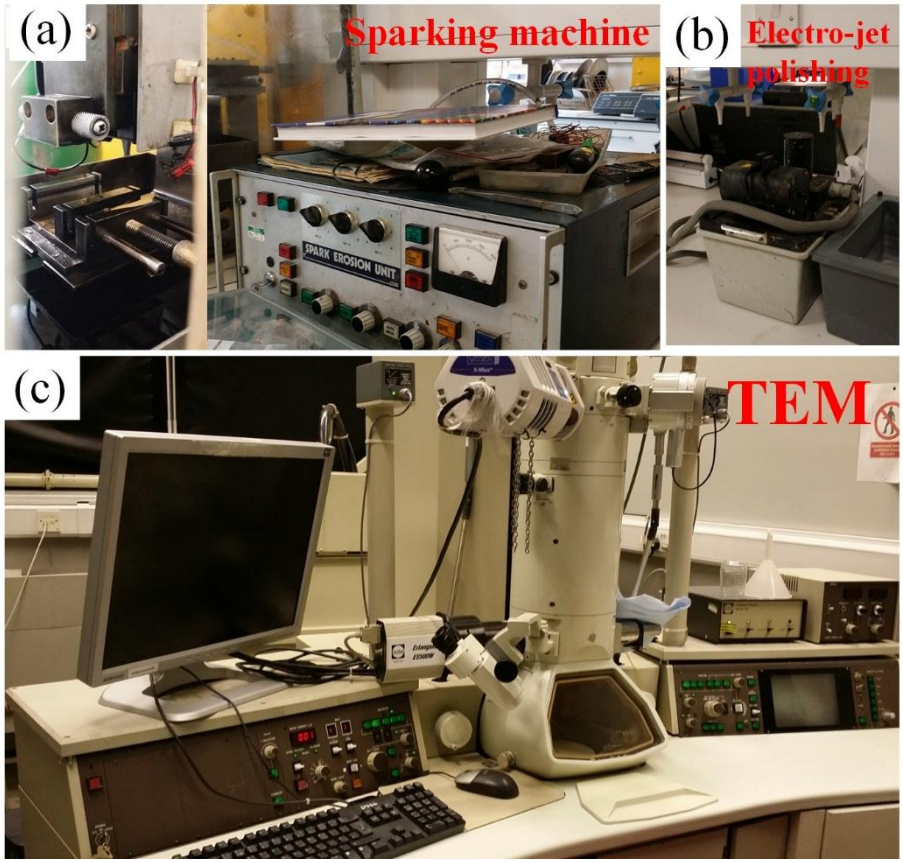


Figure 3.5: Photographs of (a) a sparking machine and (b) electro-jet polishing machine for TEM sample preparation, and (c) a TEM 2000FX microscope.

The thin film specimens were electrically- polished using a solution (30 ml perchloric acid and 270 ml acetic acid) at around 288K (15 ^{o}C) (Figure 3.5b) and were observed by TEM operated with an acceleration voltage of 200 kV (Figure 3.5c). The electrical resistance of actual and blank specimens (ie. subjected and not-subjected to EPT, respectively) were measured by Microhmmeter (DO5000). Vickers hardness was measured using a Zwick Digital 3103 IRHD Micro Compact Hardness Tester with 2 kg load for all specimens.

3.3 Experimental results

3.3.1 Effects of annealing on 316L stainless steel

The as received 316L stainless steel was investigated, as shown in Figure 3.6. Figure 3.6b shows a XRD spectrum. It reveals a fully austenitic structure for the as-received sample. Figure 3.6c presents a microstructure of hot- rolled 316L stainless steel sample consisting of equiaxed austenite grains and annealing twins only. After cold rolling to about 83.3% reduction, those equiaxed austenite grains were elongated along the rolling direction and a large amount of deformation twins and slip bands were formed within the steel matrix, as shown in Figure 3.6d.

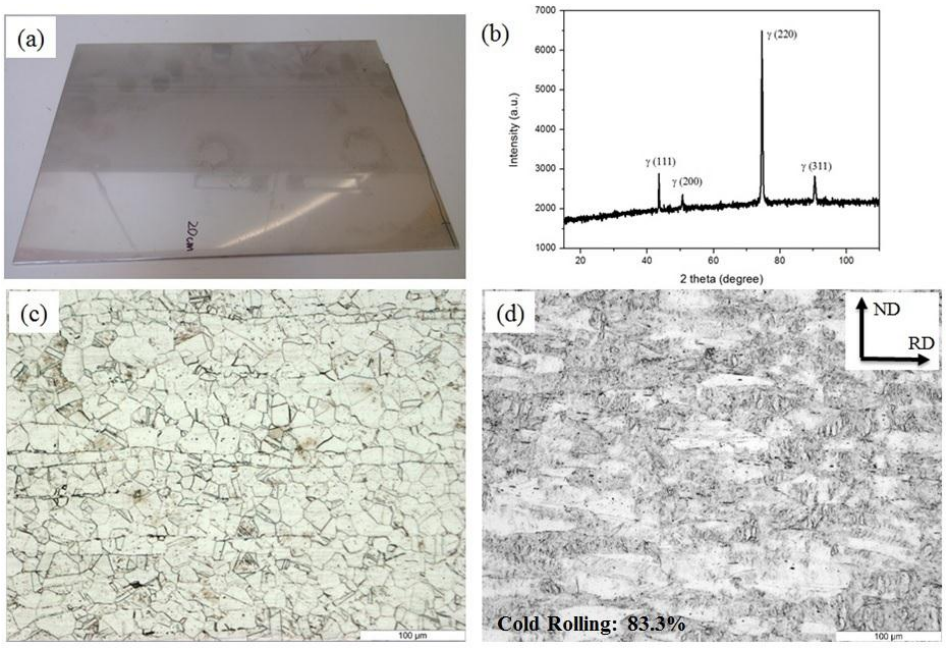


Figure 3.6: Photographs showing (a) a commercial 316L austenitic stainless steel plate, (b) a XRD spectra for as-received 316L stainless steel specimen, (c) an optical micrograph of hot-rolled steel specimen and (d) an optical micrograph of cold-rolled steel specimen.

The equilibrium phase diagram of 316L stainless steels has be calculated by using Thermo_Calc 3.1 software with the TCFE7 commercial database, as shown in Figure 3.7.

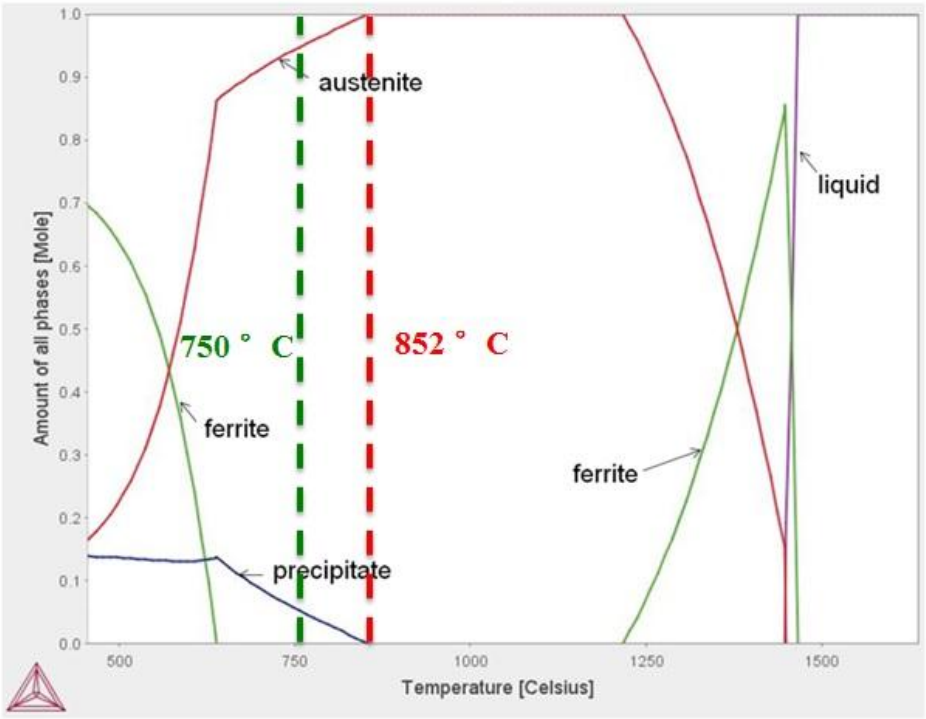


Figure 3.7: An equilibrium phase diagram of 316L stainless steels calculated using a commercial software, Thermo_Calc 3.0 with the TCFE7 database.

Figure 3.7 shows that a fully austenite microstructure exists for temperatures greater than 852 ^{o}C. Below 852 ^{o}C, various kinds of precipitates (e.g. χ phase) start to form. During the manufacturing process, the stainless steels are quenched from about 1000 ^{o}C to avoid the formation of precipitates. The low mobility of alloying elements (e.g. Cr or Mo) at ambient temperatures prevents the formation of precipitates. However, precipitates start to form when the steel is subjected to an elevated temperature (e.g. 300 ^{o}C) for long time. The principal purpose of this experiment is to verify whether the precipitates in 316L stainless steels can be retarded or dissolved by electropulsing. In the first stage, a heating temperature of about 750 ^{o}C was used.

Figure 3.8 shows the SEM images taken by SEM LEO equipment for the steel annealed at 750 ^{o}C for 30 mins and 60 mins, respectively. Considerable amounts of white particles were

formed in the dark background. These particles are the precipitates and the background is the steel austenite matrix. Figures 3.8a, c and e are for a steel sample (30 mins) at different resolutions and Figures 3.8b, d and f are for a steel sample (60 mins) at different resolutions. It proves that the segregation occurs at this annealing temperature. Figure 3.8a contains some areas with much lower concentrations of white particles than in other areas. This indicates that segregation has not been fully developed. In Figure 3.8b, the white particles are distributed more homogeneously than in Figure 3.8a. The white particles are coarsening with increasing annealing time (from 30 to 60 mins). A close examination of the white particles, as that illustrated in Figure 3.8e and f, reveals that the precipitates are mainly located at the grain boundary, whereas few precipitates are nucleated inside the matrix grains. This is due to the fact that the solute diffusivity along the grain boundary is much larger than that in the bulk grains. The greater diffusivity results in quicker growth of both the precipitates and the segregation. Precipitate nucleation is more likely to occur at the grain boundary due to the higher free energy at interface than that inside the grains. The chemical compositions of the matrix and the precipitates shown in Figure 3.9a were examined by the EDS analysis, as shown in Figure 3.9b and c. This gives the composition in the matrix (position 2) as 2.02 wt.% Mo, 16.68 wt.% Cr, 10.45 wt.% Ni and 68.37 wt.% Fe, and a composition in the precipitates (position 1) as 6.57 wt.% Mo, 24.13 wt.% Cr, 7.78 wt.% Ni and 63.68 wt.% Fe. The x-ray spectrum does not show any peak other than that for austenite phase. This implies that the precipitates are either the face-centred-cubic crystal or cannot be identified because of its low fraction and small size.

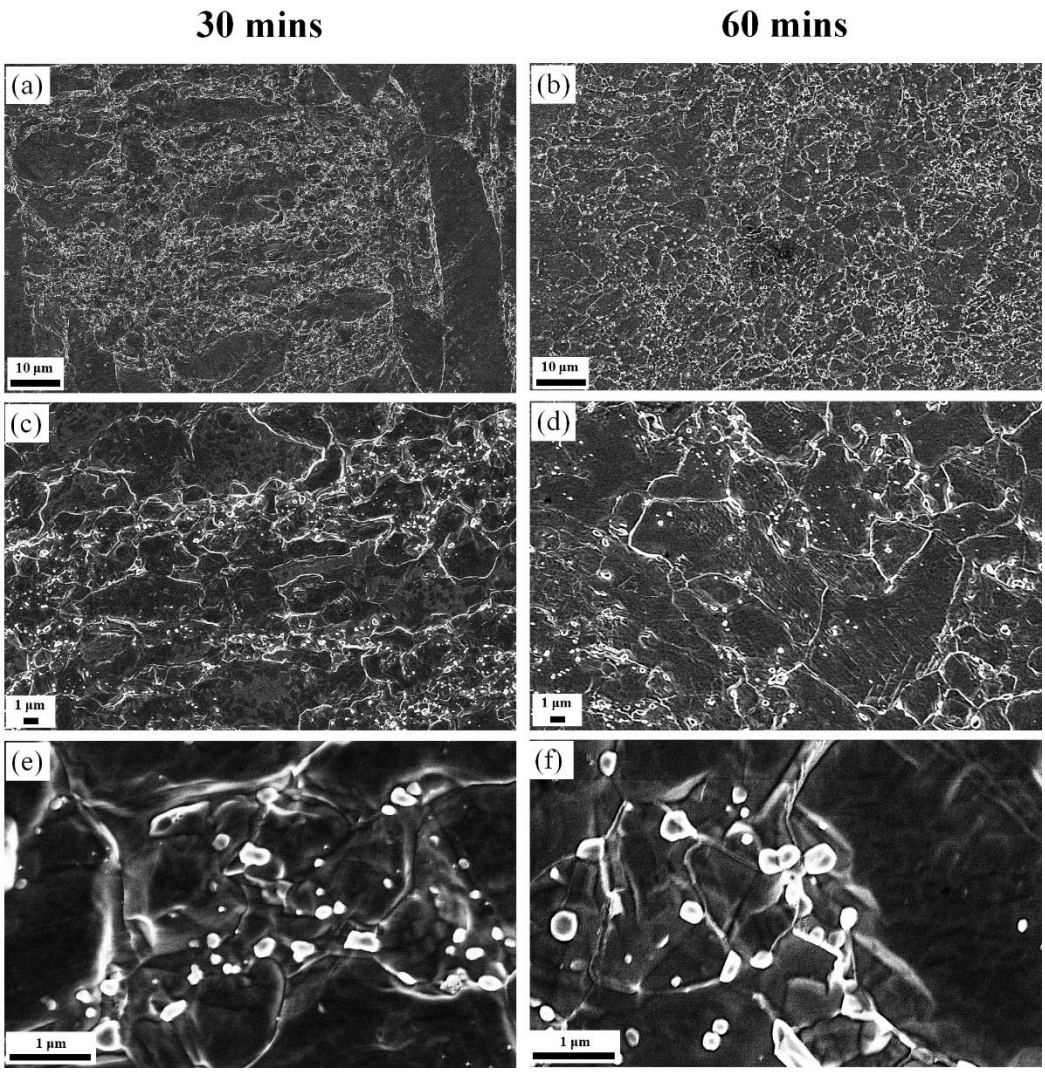


Figure 3.8: SEM micrographs of the cold rolled steel sample (83.3%) at 750 ^{o}C for (a), (c) and (e) 30 mins and for (b), (d) and (f) 60 mins.

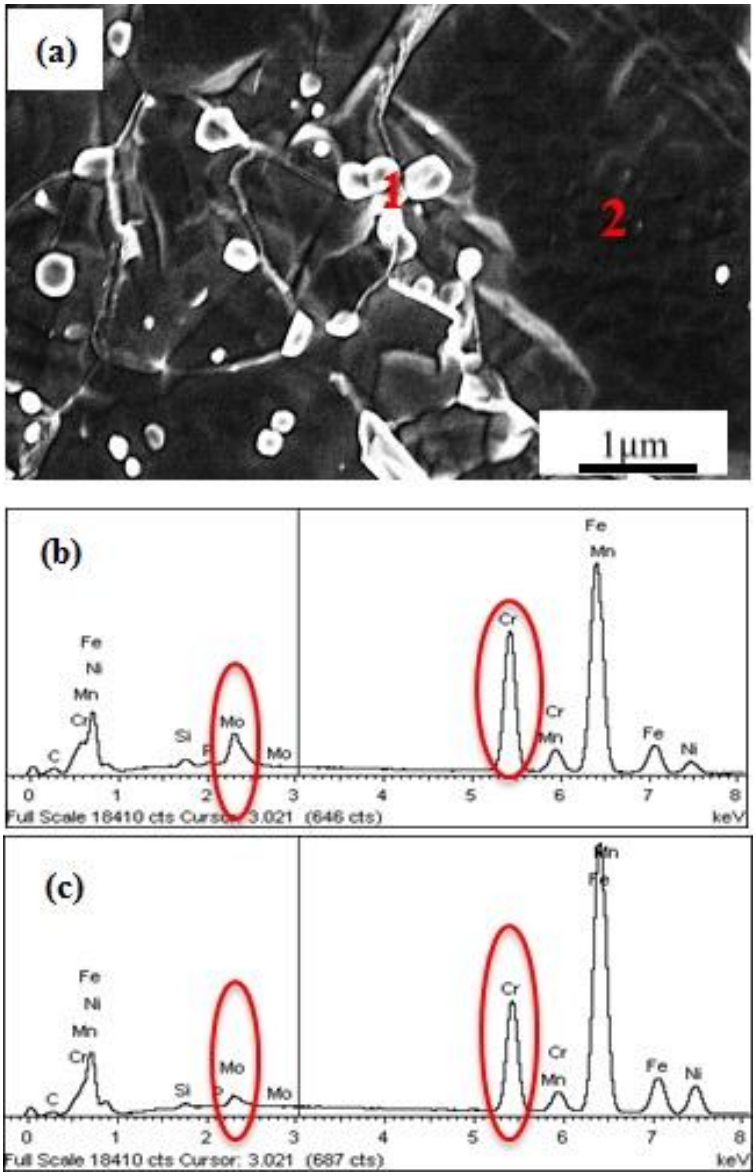


Figure 3.9: (a) Typical SEM micrograph of steel sample at 750 ^{o}C for 60 mins, and EDS spectra for (b) white precipitates and (c) dark steel matrix.

The microstructure evolution of 316L stainless steel after annealing treatments at 750 ^{o}C for 60 min was observed using TEM. Figure 3.10a-d shows the TEM bright-filled image. A large number of dark particles can be observed. The particles are located not only along the grain boundaries, but also within the grain.

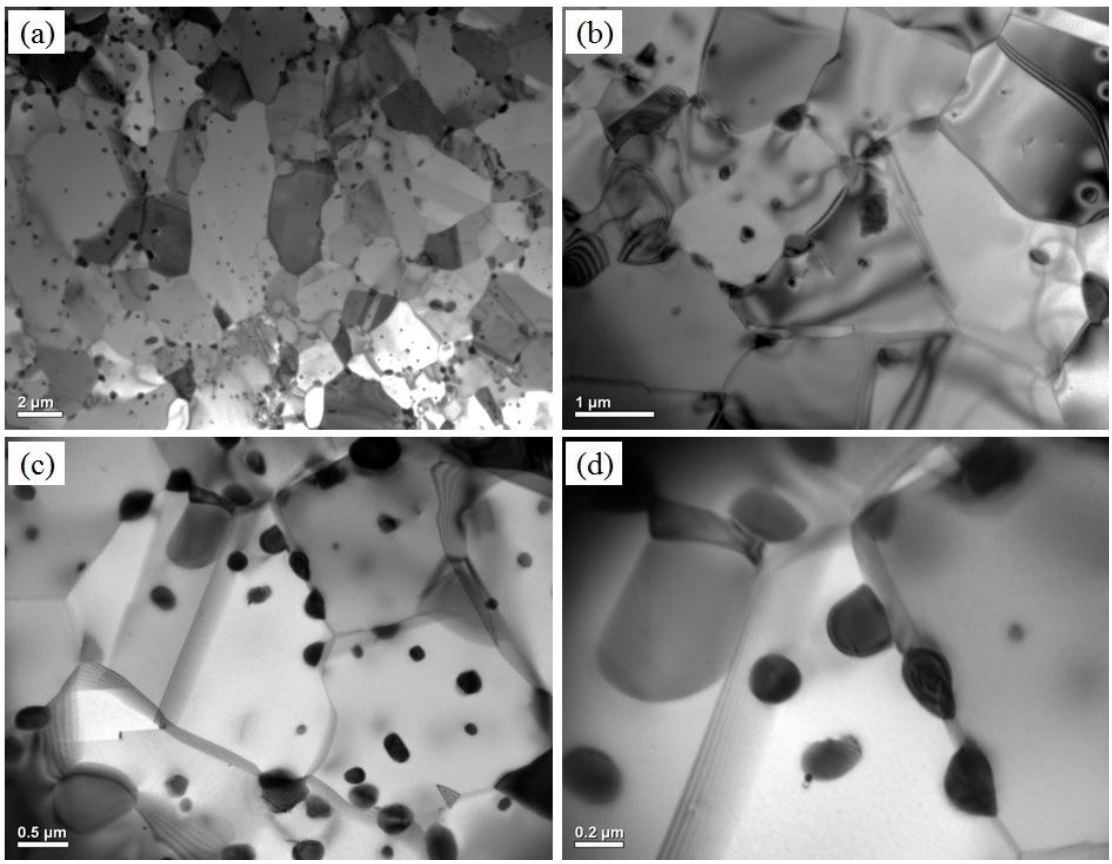


Figure 3.10: TEM micrographs for the steel sample microstructure annealed at 750 ^{o}C for 60 mins.

The particles shown in Figure 3.8 (white particles in SEM pictures) and Figure 3.10 (dark particles in TEM pictures) are the same precipitate. To identify the crystal structure of precipitates, a bright field image was utilized and then the selected area diffraction pattern was obtained for specific regions, as shown in Figure 3.11.

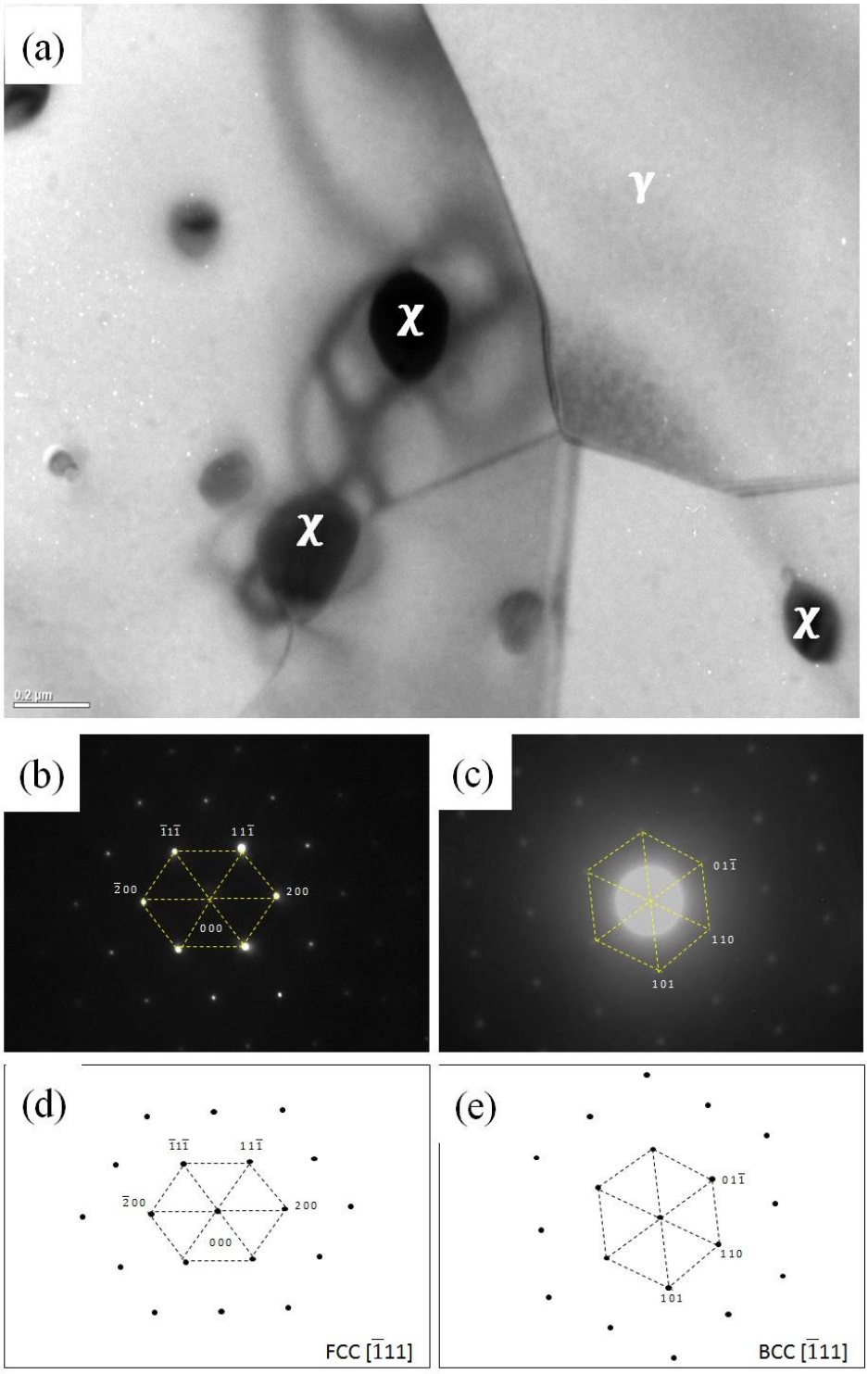


Figure 3.11: (a) TEM image for bright field of steel microstructure, (b) and (d) are the SADP of austenite matrix and its corresponding schematic diagram, respectively, and (c) and (e) are the SADP of χ phase and its corresponding schematic diagram, respectively.

According to the calculation for lattice parameters and crystal structure, Figure 3.11b and d show the diffraction patterns of steel matrix, whereas Figure 3.11c and e show the diffraction patterns of precipitates which were identified as the austenitic phase (FCC) and χ phase (BCC with lattice parameters of 8.98 Å), respectively. These experimental results indicated that χ phase has formed in 316L stainless steel at a temperature around 750 ^{o}C.

3.3.2 Effects of EPT on 316L stainless steel

Figure 3.12a shows the distribution of χ-phase in the austenitic matrix for the untreated steel. The particles are distributed randomly in the matrix (indicated by the arrows). However, they have partially- disappeared in the pulse-treated steel and have a much smaller size (Figure 3.12b). The number and size of the particles were determined and sorted into groups and then histograms were derived for the distribution. Peak-fitting was carried out using a Lorentzian distribution (Figure 3.12c and d). Each χ-phase particle with equivalent circular diameter were measured (shown in Figure 3.12c and d). The particles in the untreated (blank) steel had a wide variation in size (43 nm<particle<330 nm), with the size distribution mainly concentrated around 143 nm (according to Lorentzian fitting, Figure 3.12g). The particles for the pulse-treated steel were dispersed and varied in size between 25 and 105 nm, with the distribution mainly concentrated around 25 nm (Figure 3.12h). Furthermore, the number of particles (～1.51×10^{6} per unit area) in the pulse-treated steel were fewer (3.7 times smaller) than the blank steel (ie. without pulse with～5.63×10^{6} per unit area). Therefore, both the size and the number of particles were dramatically reduced by the application of an electric current. This indicates that the nucleation of the particles is indeed greatly retarded by an electric current. χ-particle is a hard and brittle intermetallic phase causing embrittlement [12]. Therefore, the reduced size and number of χ-particle after applying an electric current will

improve the mechanical properties. This electric-current-assisted treatment is far superior to the conventional methods reported in literature [171].

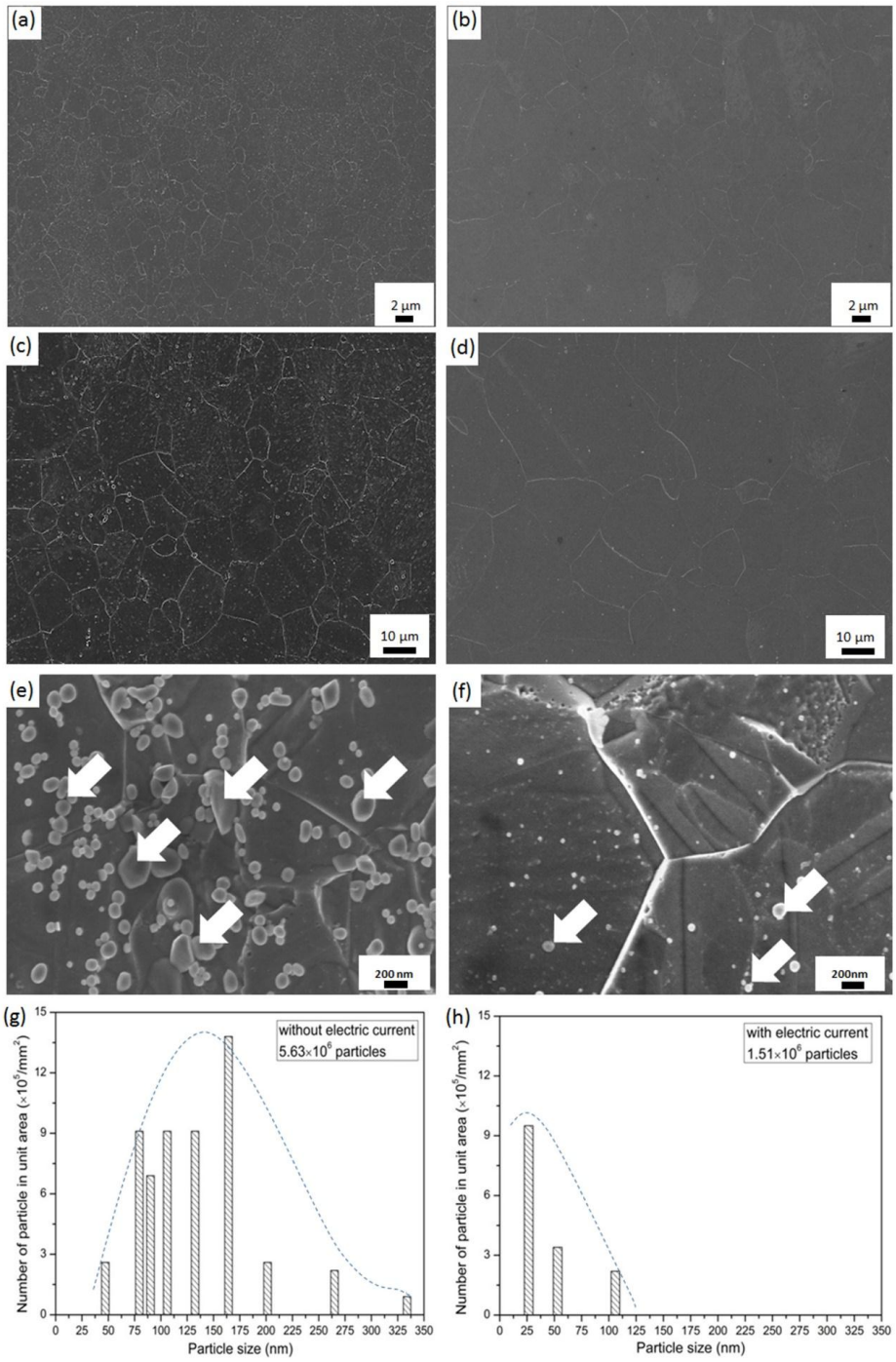


Figure 3.12: SEM images of (a), (c) and (e) the distribution of χ phase in the sample without EPT; (b), (d) and (f) the distribution of χ phase in steel sample with EPT. (g) and (h) the number distribution of χ phase in steel samples without and with EPT, respectively.

FIB-SIMS is a sensitive analytical technique that can provide parts per million (ppm) to parts per billion (ppb) sensitivity for most elements when relatively large areas of analysis are available. It has the great advantages for analysing molybdenum in χ phase. Figure 3.13 shows the micrograph and chemical mapping of molybdenum in the untreated and pulse-treated steels, respectively. For the untreated steel, χ-phases were randomly dispersed in the matrix and molybdenum was mainly concentrated on these particles (indicated by arrows in Figure 3.13a). After applying an electric current, most of the χ phases disappeared and molybdenum was almost homogenously distributed in the matrix (Figure 3.13b). The mapping analysis, provided by SIMS, suggests that electric current inhibits the precipitates and promotes homogenization of elemental distribution.

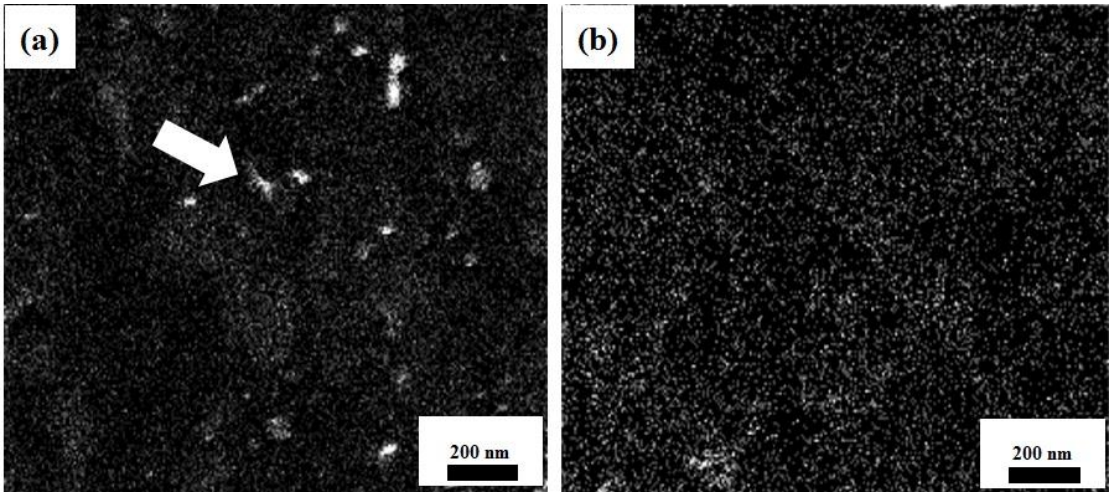


Figure 3.13: FIB-SIMS elementary mapping for Mo distribution in steel samples (a) without EPT and (b) with EPT.

The grain size and Σ3 grain boundary in steel samples with and without EPT are measured by EBSD, as shown in Figure 3.14 and Figure 3.15, respectively. From Figure 3.14, it can be seen that the austenite grain size (～15.7 μm) in the untreated steel is 1.6 times smaller than that of the pulse-treated steel (～24.5 μm). The electric current affects the grain size during recrystallization [62, 99, 114]. This is probably due to a reduction in the pinning effect of precipitates in 316L stainless steels under EPT.

Furthermore, the frequency of Σ3 grain boundaries increased from 14.5% to 41.0% when the EPT was applied. This had been indicated in the grain boundary distribution maps for the untreated (Figure 3.15a and c) and pulse-treated steels (Figure 3.15b and d), respectively. As mentioned above; according to the grain boundary engineering, higher frequency of Σ3 grain boundaries leads to strong corrosion resistance [169–171]. Increases in the Σ3 grain boundaries also increase the ductility of the metal; this is due to its highly regular and coherent structure with lower energy state than that of other high angle grain boundaries [28].

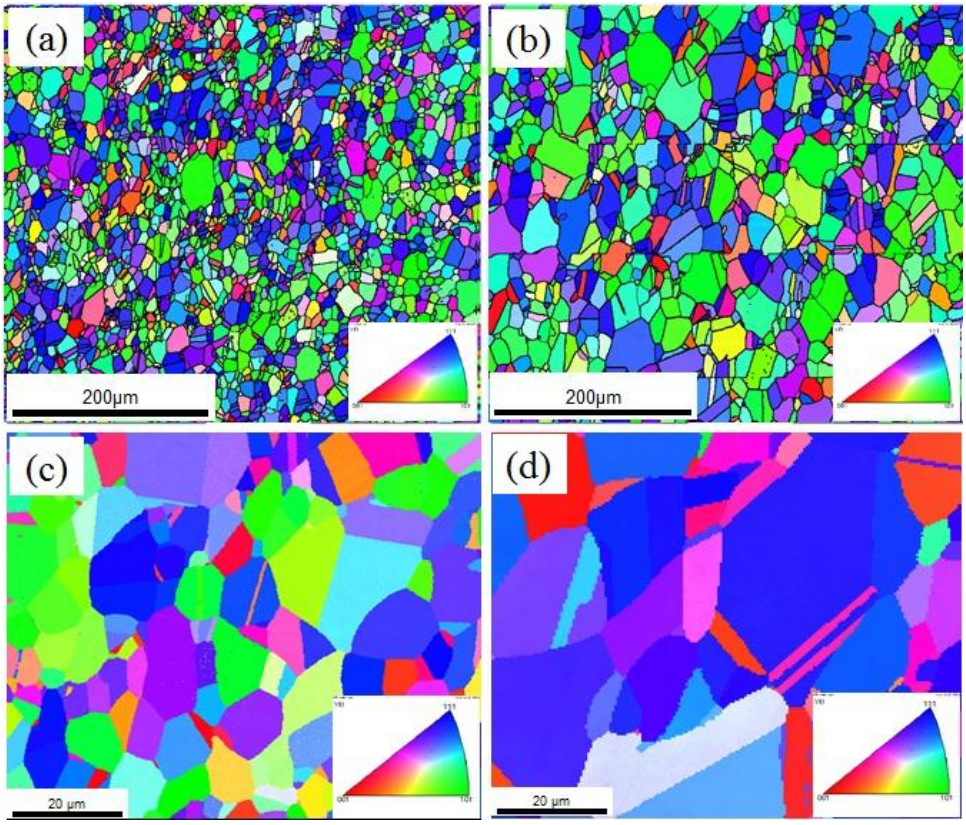


Figure 3.14: EBSD mapping for grain size measurement: (a) and (c) steel sample without EPT at different magnifications; (b) and (d) steel sample with EPT at different magnifications.

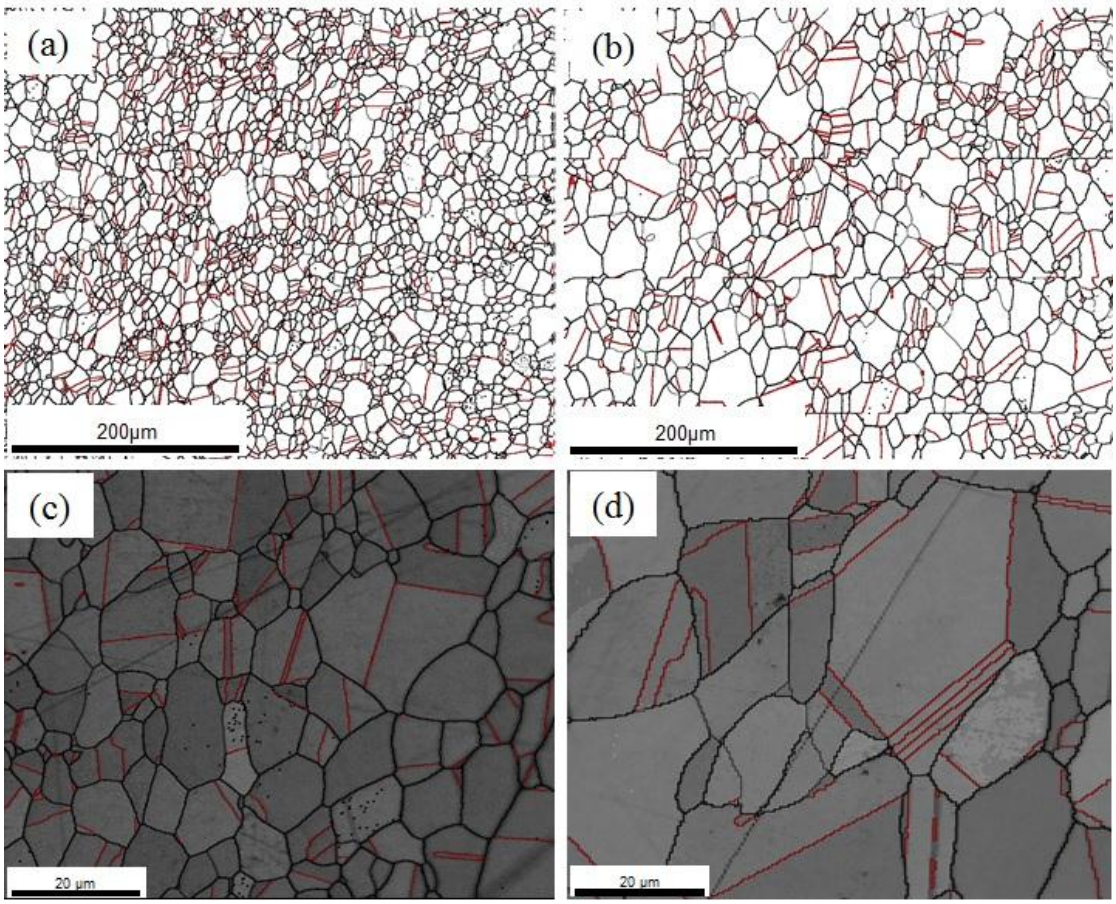


Figure 3.15: EBSD mapping for grain boundary portion measurement: (a) and (c) steel sample without EPT at different magnifications; (b) and (d) steel sample with EPT at different magnifications.

The Vickers's hardness of the specimens without EPT is 267 HV_2, while the value for the sample with EPT is 185 HV_2. The reduction of hardness reflects the effects of both grain coarsening and the higher frequency of Σ3 grain boundary in the specimen and is in agreement with microstructural observations [169–171]. It is worth pointing out that for cold-worked alloys the application of EPT frequently leads to a decrease of hardness due to an acceleration of movement of dislocations (accumulation and annihilation) and which improves the ductility.

3.4 Discussion

3.4.1 Thermal effects of EPT on 316L stainless steels

Passing an electric current through a steel sample causes temperature elevation. In the present work, the facility provides a constant electric current (I). The total energy for each electropulse (J) is $Q_e = I^2 R\Delta t$, where R is the electrical resistance (Ω) of the sample and Δt is the pulse duration. When Q_e is fully consumed to heat up the sample, it has $Q_e = mc\Delta T$, where m and c are the mass and specific heat of the steel sample, respectively. ΔT is the temperature increase resulting from the electrical energy. This gives $\Delta T = I^2 R\Delta t/(mc)$. It is known that $R = \rho_e L/S$ and $m = \rho_d LS$, where ρ_e, L, S and ρ_d are the electrical resistivity, length, cross-section area and density of the sample. Substituting R and m into the equation, one gets [33–48].

$$\Delta T = \frac{I^2 \rho_e \Delta t}{S^2 c\rho_d} = \frac{j^2 \rho_e \Delta t}{c\rho_d} \tag{3.1}$$

where j is the average electric current density (A/m^2) and Δt is the pulse duration (μs). Values for the stainless steel specimen are: c = 450 J/(kg·K), ρ_d = 7.8×10^3 kg/m^3 and ρ_e= 9.58×10^{-8} Ω.m. The largest current density used in the present work, j= 6.3×10^7 A/m^2, would give rise to a temperature increase of 6.5×10^{-3} K for an electropulse of 60 μs duration. The electric current was applied at 1 Hz frequency. This means that the maximum rate of temperature rise by applying an electric current is 6.5×10^{-3} K/s. The Joule heating is hence negligible in the present work. The observed effect of electric current on stainless steel must be due to the electric effect and not Joule heating.

3.4.2 Electric effects of EPT on 316L stainless steels

It is well-known that the EPT accelerates the solute diffusion, dislocation migration and interface kinetics [99, 168, 173, 174]. This is mainly attributed to the drift electrons driven by the applied electrical potential being scattered unevenly around defects. This uneven distribution of electrons around the defects causes an anisotropic shielding effect to the electromagnetic forces between two atoms and hence reduces the kinetic barrier [175]. As a result, the mobilities of substitutional atoms, dislocations and interfaces can be significantly enhanced, as shown below

$$M = M_a \exp\left(-\frac{\Delta E_k}{KT}\right), \tag{3.2}$$

where M_a is the pre-exponential factor dependent on the frequency of atom hopping and lattice distance, ΔE_k is the kinetic barrier, K is the Boltzmann constant, T is the temperature and M is the mobility. The reduction of ΔE_k causes the increased mobility. The increase in interface kinetics enables the interface to relax toward its equilibrium shape. Here, the acceleration effect of pulsed electric current contributes to the migration of grain boundaries and impurities. This enables a faster evolution of the interface morphology towards its equilibrium shape. Consequently, electric current induces grain coarsening (Figure 3.15). However, the electric current-enhanced, solute diffusion does not help us to understand the experimental observations on segregation retardation (Figure 3.12 and 3.13). According to the kinetics, an enhanced diffusion will promote the formation and coarsening of the χ phase precipitation, which seems to contradict the observation that there is a reduction in both the amount and size of the particles. This means that the experimental observations in the present

work cannot be understood by kinetics alone. The thermodynamics of alloys carrying electric current should also be considered.

A schematic diagram has been plotted in Figure 3.16, which provides an understanding of the effects of pulsed electric current on χ-phase precipitation in 316L stainless steel. From Figure 3.16, the relations existing between three different phases (A, B and C phases) with different electrical conductivities (σ_A, σ_B and σ_C) are shown: $\sigma_A = \sigma_B > \sigma_C$. As reported in previous studies [168, 172] the electrical conductivities of phases affect the distribution of electric current during pulsed, electric- current treatment. This influence on distribution of electric current contours consequently, leads to changes in free energy of the system. Thus the system free energy in Figure 3.16b can be significantly changed by the differences in the electrical conductivities between phase A and phase C in comparison with those between phase B and phase C in Figure 3.16a.

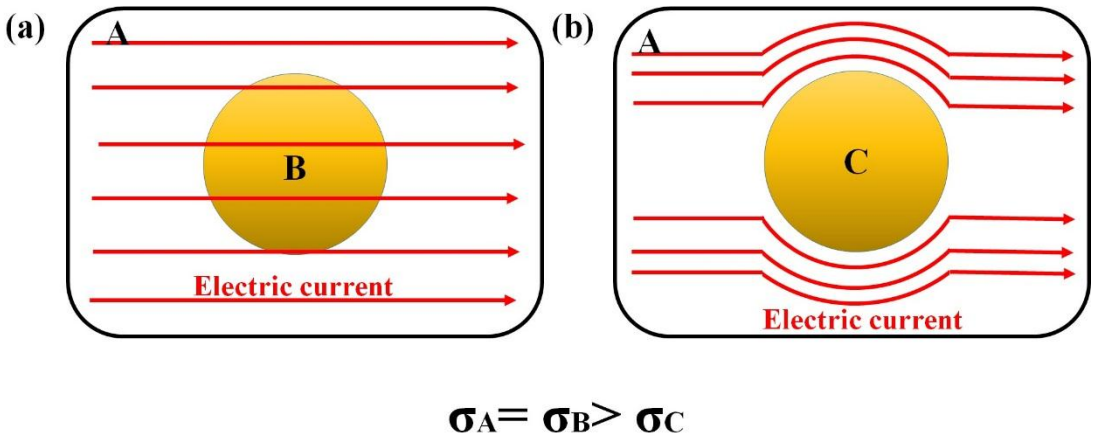


Figure 3.16: Schematic diagrams of spherical precipitate in steel matrix under EPT. (a) represents the distribution of current across the microstructure consisting of a precipitate (B) and steel matrix (A): the electrical conductivity of precipitate is the same as steel matrix). The current lines directly pass the precipitate and matrix without any changing. (b) shows the

distribution of current across the microstructure consisting of a precipitate (C) and steel matrix (A): the electrical conductivity of a precipitate is less than that of steel matrix. The current lines are altered due to the discrepancy of electrical conductivity between precipitate and matrix.

The total system free energy of a steel specimen without EPT ($\Delta G_{total}^{\gamma\to\chi}$) consists of two terms, the chemical free energy of the bulk phases (ΔG_{chem}) and the surface energy (ΔG_{surf}). The microstructure evolution (e.g. precipitation of χ phase) is spontaneously activated within steel matrix when $\Delta G_{total}^{\gamma\to\chi} = \Delta G_{chen} + \Delta G_{surf} < 0$ at 750 °C (based on the Gibbs free energy diagram for phase transformation from austenite to χ phase), as displayed in Figure 3.17.

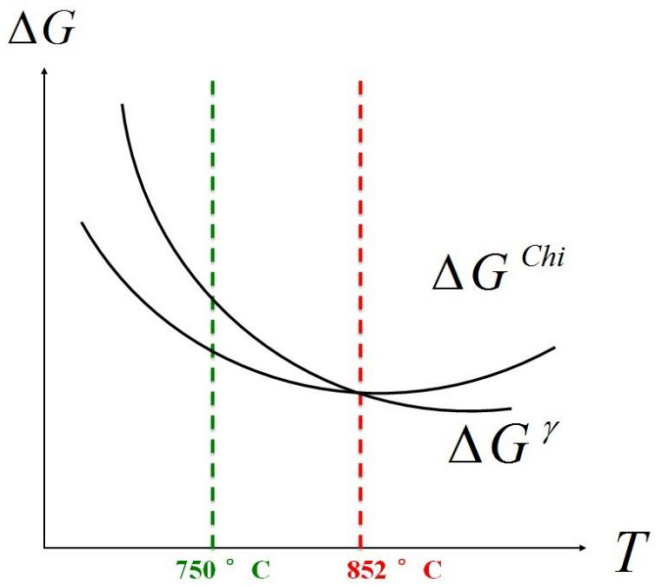


Figure 3.17: Gibbs free energy change as a function of temperature for χ-phase and austenite. The red line represent the phase transformation temperature (χ-phase ↔ austenite), whereas the green line correspond to the operation temperature of current experiment.

With EPT, another term called the free energy associated with the passing electric current (ΔG_{elec}) is added into the total system free energy, which is expressed as

$$\Delta G_{total}^{\gamma\rightarrow\chi} = \Delta G_{chem} + \Delta G_{surf} + \Delta G_{elec} \tag{3.3}$$

For the steel sample with EPT, the precipitation of χ phase is retarded or dissolved when $\Delta G_{elec} > 0$. The expression of ΔG_{elec} can be mathematically presented as

$$\Delta G_{elec} = \frac{\mu}{8\pi}\iint \frac{\vec{j}_b(r)\vec{j}_b(r') - \vec{j}_a(r)\vec{j}_a(r')}{|r-r'|} dr dr' \tag{3.4}$$

where $\vec{j}_b(r)$ is the current density distribution after precipitate evolution, $\vec{j}_a(r)$ is the current density distributions before precipitate evolution, μ is the magnetic permeability, *r* and *r′* are two different positions inside the steel sample. Values for the electrical conductivity of all the phases before and after structural evolution are required to calculate the distribution of current density. The segregation of alloying elements (such as Mo and Cr) affects not only the electrical conductivity in the precipitates but also that in the matrix. The Gibbs free energy change induced by the differences of electrical conductivity between inclusions (Pb) and Cu-Zn alloy matrix can be used to explain why Pb can be effectively moved to grain boundaries under EPT [142]. In current research, the electrical conductivity of a steel sample was increased from 1.82×10^6 s/m to 2.21×10^6 s/m (approximately 21.4%) with EPT. This increase in the electrical conductivity of a steel sample under EPT, is in agreement with the theoretical and experimental prediction that highly- conductive phase is frequently promoted by means of an electric current. In the case of precipitation in 316L stainless steels, the precipitation of χ phase is not only retarded but is also dissolved with EPT.

3.5 Conclusion

In summary, this work has verified that the precipitate/grain boundary in metals can be retarded by utilising differences in their electrical conductivities.

（1） Passing electric current affects the microstructural evolution by both retardation of χ-phase precipitation and the promotion of Σ3 grain boundaries in cold-rolled 316L stainless steel; this helps to reduce the detrimental effects induced by precipitation at elevated temperature.

（2） The mechanical properties of the steel are also optimized by reductions in both the size and the number of intermetallic χ-particles. The Σ3 grain boundaries increases the ductility of the metal due to its highly regular and coherent structure with lower energy state (compared with those of other high angle grain boundaries). Therefore, EPT can be a promising method to improve ductility and balance the corrosion-resistance for many engineering applications such as nuclear reactors.

Chapter 4 Stability of delta-ferrite in 2205 duplex stainless steel with electropulsing

4.1 Introduction

Duplex stainless steels (DSS) such as 2205, consists of austenite (γ) and delta-ferrite (δ-ferrite) phases (Figure 4.1). These steels have been intensively investigated in recent years due to their remarkable mechanical properties, good corrosion and oxidization resistance [176–180]. The mechanical properties of the steels are strongly dependent on the stability of phases. This is because the softening effect usually does not occur in DSS until high temperature, which is partly attributed to the dissolution of hard precipitates and phases. For instance, the mechanical properties (especially strength in DSS) is linked significantly to the stability of delta-ferrite. [179, 180]. The investigation of stability of delta-ferrite is important for the fabrication of DSS with high strength properties. The stability of delta-ferrite is mainly controlled by the eutectoid decomposition [177]:

$$\delta \rightarrow \sigma + \gamma' \tag{4.1}$$

where δ is delta-ferrite, σ is sigma-phase enriched in Cr and Mo and γ' is secondary austenite phase. In the temperature range between 350 to 835 ºC, a higher annealing temperature leads to a higher diffusion rate of alloying elements (e.g. Cr, Mo and Ni atoms); this results in the acceleration of the eutectoid decomposition of delta-ferrite [177]. When the temperature exceeds 835 ºC, precipitates formed by the eutectoid decomposition will dissolve and cause softening of the DSS matrix [178].

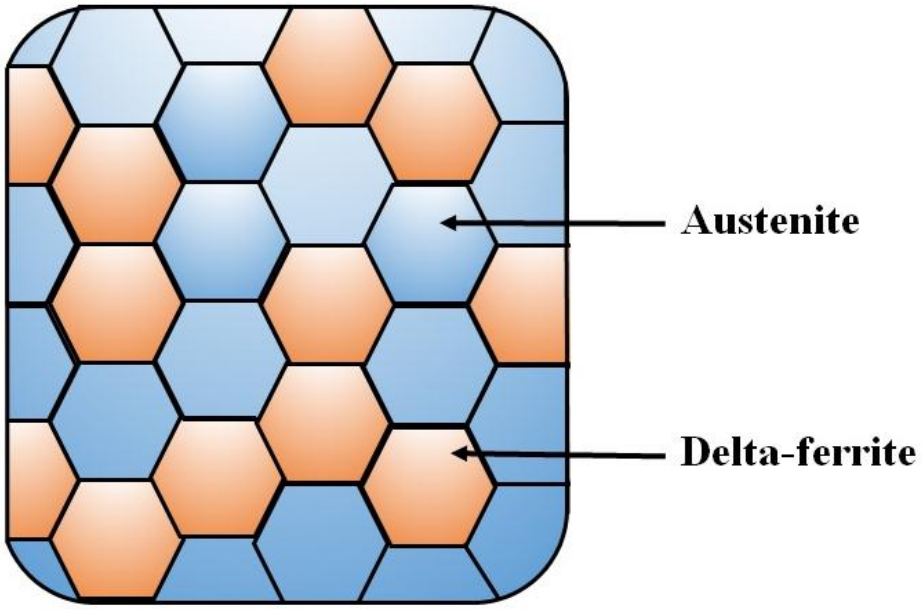


Figure 4.1: A schematic diagram illustrates the microstructure of 2205 duplex stainless steel consisting of austenite (blue) and delta-ferrite phases (orange).

There are two ways of reducing the softening effect induced by high temperature heat treatments (above 835 ºC) in DSS. In the first strategy the hard precipitates, or phases, are stabilised directly via chemical reactions. The second strategy is to alter the associate phase transformation so as to promote the generation of hard precipitates and phases via external fields.

EPT, is one example of a typical external field and is widely designed to affect the solid phase transformation in many alloys due to its coupling of thermal and electric effects [49–67]. The high density of electric current was initially proven to influence diffusion-controlled , solid phase transformation through electromigration [173, 175]. The extent of phase transformation occurring is dependent on the parameters of electric current and the prior treatment of the materials. Shortly after this observation, a martensitic phase transformation

from α-Ti to β-Ti was induced by high-current-density EPT in a Ti alloy, which was attributed to Joule heating [174]. This Joule heating generated by the electric current can be the order of 10^6 Ks^{-1}. Recently, it was found that the dissolution rate of β-phase in aged AZ91 alloys was accelerated and the Vickers hardness value of AZ91 alloys was reduced by EPT due to its electric effects [35, 36, 46, 47]. Furthermore, the extent and direction of the phase transformations in both ZA22 and ZA27 [52, 55, 63–66] can be altered by varying the current density and frequency of EPT. This has been mainly attributed to the electric wind force induced by EPT, which increases the atomic diffusion flux. Consequently, the EPT can be considered as an external stress to change the Gibbs free energy for either forward or reverse phase transformations [49–67]. In addition to phase transformation, the grain size is also affected by EPT [68–133]. For instance, the size of graphite can be significantly reduced and the decomposition of cementite accelerated by EPT in graphite iron due to the coupling of thermal and electric effects of EPT [181–183]. Based on these effects of EPT, most experiments with EPT have been processed using a high- current -density and a short duration of time. However, the use of high- current- density and a short time duration, frequently, lead to a combination of thermal and electric effects which are not easy to distinguish from one another. In order to avoid the thermal effect and precisely understand the electric effects of EPT on microstructure evolution of alloys, a novel experimental process needs to be designed. A combination of low-current-density, EPT and annealing treatments may be the appropriate way to investigate the electric effects of EPT on solid phase transformation.

However, the mechanism responsible for the effect of EPT on the stability of delta-ferrite below solid solution temperature is still unclear. This lack of knowledge has impeded the understanding of EPT and made it difficult to be widely developed in industry. Due to the

existence of a strong relationship between electrical resistivity of phases and electric current, it is important to investigate the stability of delta-ferrite in cold-rolled DSS under EPT. It is also important to understand the electric effects of EPT on the kinetics and thermodynamics of the delta-ferrite decomposition.

4.2 Materials and methods

4.2.1 Materials selection and prior treatments

In this research, a duplex stainless steel plate with a chemical composition (wt. %) 0.03 C, 2.00 Mn, 1.00 Si, 0.015 S, 0.035 P, 22.00 Cr, 5.00 Ni, 3.00 Mo, 0.15 N (so-called 2205 DSS) was hot rolled to 3mm thickness and annealed at high temperature to obtain dual phases (ie. δ-ferrite and γ-phase). The steel plate was further cold-rolled with a 50% reduction from 3.00 mm to 1.50 mm in thickness and subsequently, cut into many regular samples (1.5×2.0×15 mm) with their longest edge direction (e.g. longitudinal plane) parallel to the rolling direction, as shown in Figure 4.2.

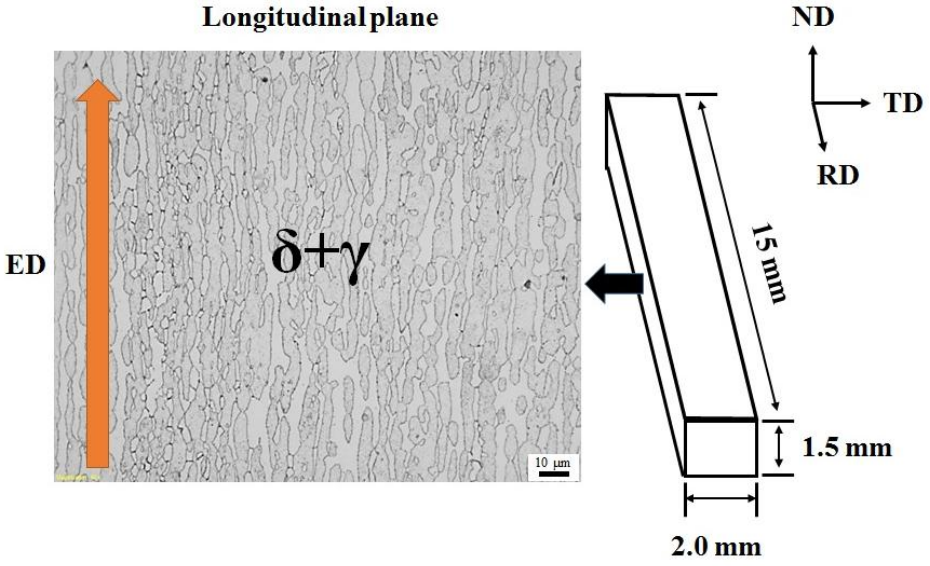


Figure 4.2: A steel specimen (2×1.5×15 mm) and its microstructure on longitudinal plane (contains both delta-ferrite and austenite). Note: ED is electric current direction (marked by orange arrow), ND is normal direction, TD is transverse direction and RD is rolling direction.

4.2.2 Experimental set-up of EPT

The experimental set up for EPT, shown schematically in Figure 4.3, was used in this study.

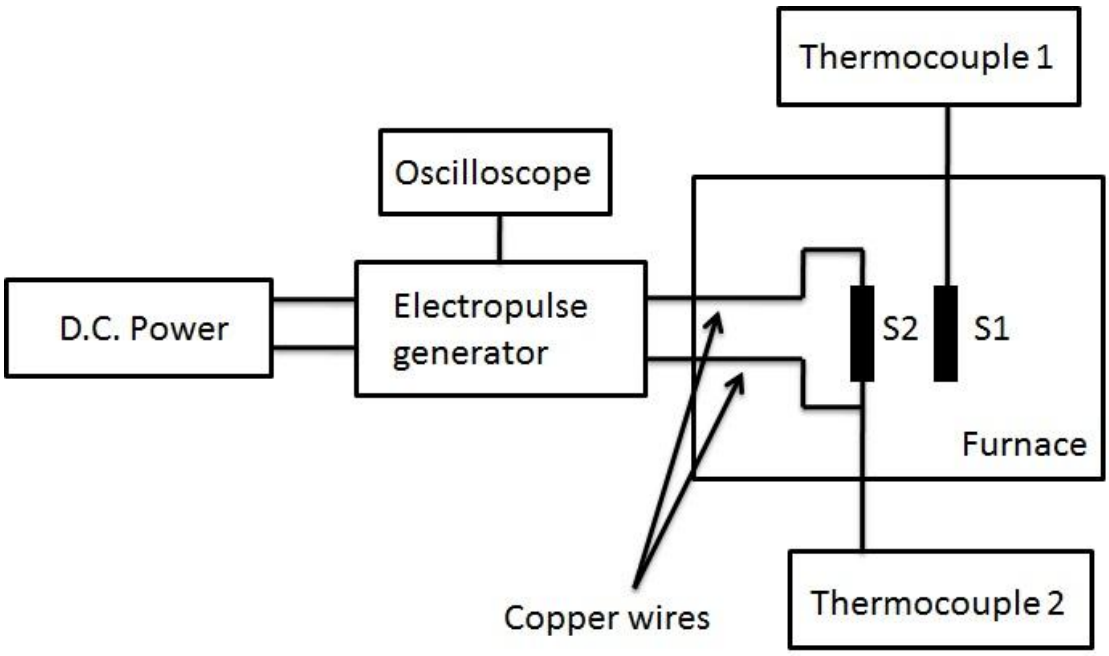


Figure 4.3: Schematic diagram of the experimental set up for EPT.

Figure 4.3 shows that the pulsed electric current is provided by an electropulse-generator linked to a direct current power unit. The embedded electrical feed-back system in the pulse generator makes it possible to retain a constant current during experiments. The pulses applied in the present work has a 60 μs duration, 1 Hz frequency and a 5×10^{7} Am^{-2} current

density. A pair of steel samples were placed on S1 position (connected with thermocouple 1) and S2 position (connected with thermocouple 2) in a furnace. Copper wires connected S2 and the electropulse-generator to let a pulsed electric current go through S2. The direction of pulsed electric current was parallel to the rolling direction and the temperatures were measured and calibrated by thermocouples. The samples with- and without- EPT were carried out for 40 minutes and subsequently, quenched into cold water at ambient temperature. In order to make a comparison between steel samples with- and without- EPT, pairs of steel samples were randomly selected and then treated at the same annealing temperature (approximately 835 ^{o}C).

4.2.3 Metallographic observations and properties test

The metallographic microstructures of the samples were observed using the following procedures. The samples were mechanically mounted, then ground and polished, and chemically etched with Marble reagent (a mixed solution: 4g $CuSO_4$, 20ml HCl and 20ml H_2O). The microstructure characterizations were then carried out by using an optical microscope and a Scanning Electron Microscope (SEM LEO). The chemical composition of each phases were detected using Dispersive X-ray Spectroscopy (EDS INCA). The phases present in the samples were identified by X-ray Diffraction (XRD PANalytical MRDs) using Cu K_α radiation. The percentage of each phase, the grain size and Σ3 grain boundary distribution were measured by Electron Backscattered Diffraction (JEOL 6400 EBSD). Vickers hardness was measured using a Zwick digital 3103 IRHD Micro Compact Hardness Tester with 2 kg load for all samples. The electrical resistance of the samples before and after EPT were measured with a Microhmmeter (DO5000 series). The same procedures were repeated for 3 pairs of different samples. Similar results were obtained in these tests.

4.3 Experimental results

4.3.1 Thermodynamic calculation of equilibrium phase diagram

MTDATA software with TCFE4 database were used to carry out thermodynamic calculations for the DSS. The phase diagram is shown in Figure 4.4. Austenite and delta-ferrite phases coexist for temperatures up to 900 ^{o}C. The decomposition of delta-ferrite to secondary austenite and sigma-phase started at approximately 835 ^{o}C and finished at about 770 ^{o}C. The sigma-phase became completely dissolved when the temperature exceeded 835 ^{o}C.

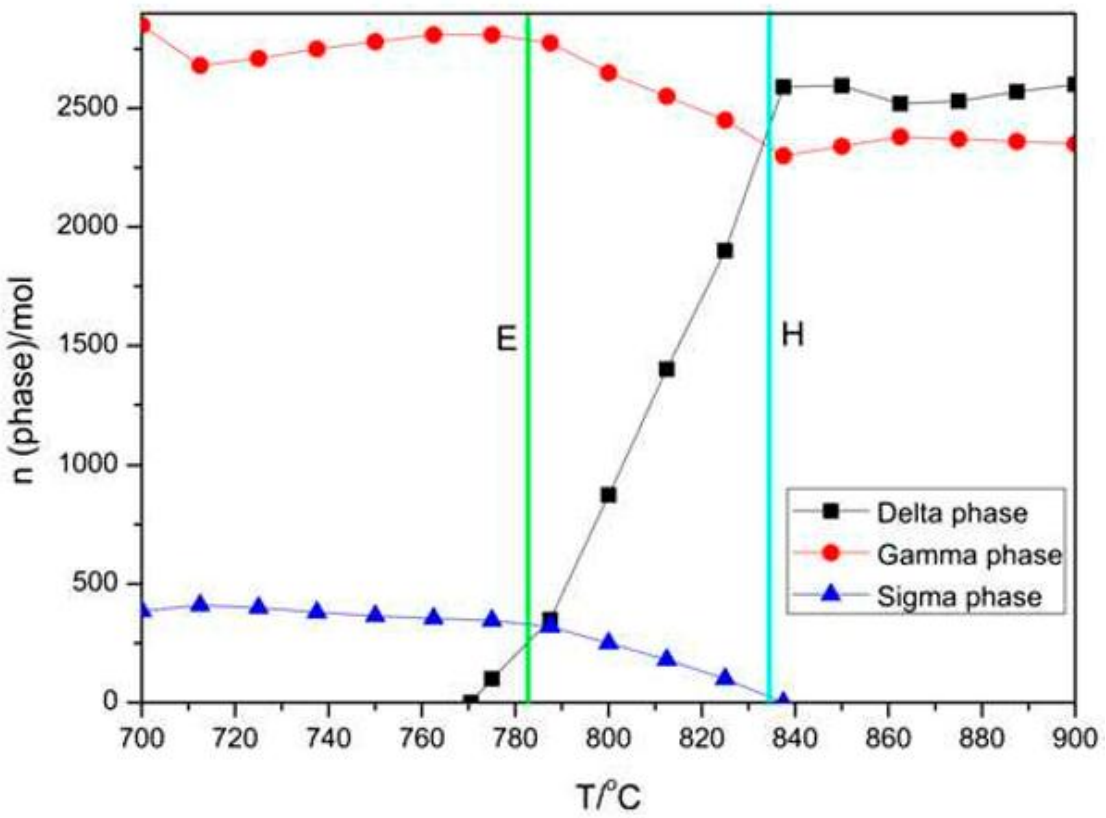


Figure 4.4: Equilibrium phase diagram of a 2205 duplex stainless steel calculated by MTDATA with TCFE4 database. The blue, red and black lines represent the sigma, austenite and delta-ferrite phases, respectively.

4.3.2 Microstructure observations

Figure 4.2 is an optical image of longitudinal microstructure of cold-rolled DSS. It displays mixed phases: one is delta-ferrite (grey regions) and another is austenite (bright regions). High-resolution SEM was utilized to observe the microstructure of DSS in more detail. Figure 4.5 shows the SEM images for the samples with and without EPT at different magnifications.

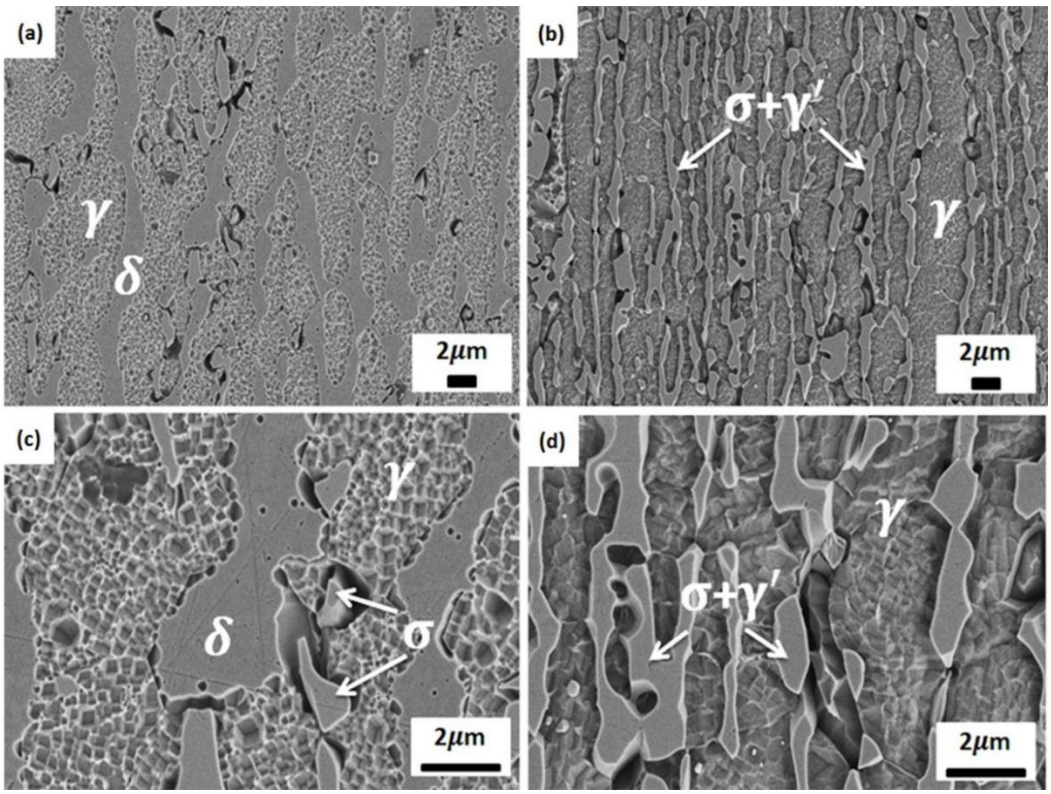


Figure 4.5: SEM images for steel samples without EPT ((a) and (c)) and with EPT ((b) and (d)) in the longitudinal plane.

It can be seen from Figure 4.5 that there are three distinct phases: delta-ferrite, austenite and sigma-phase, which are clearly indicated and labelled in DSS without EPT. Delta-ferrite and austenite are two dominant phases, whereas a little amount of sigma phase was found around phase boundaries. EPT causes significant change of the microstructure. Figure 4.5 illustrate that the secondary austenite and sigma phases tend to coarsen whereas the delta-ferrite seems to be shrink under EPT. XRD was utilized to quantitatively measure the amount of phases in the DSS with and without EPT. The spectra were plotted in Figure 4.6.

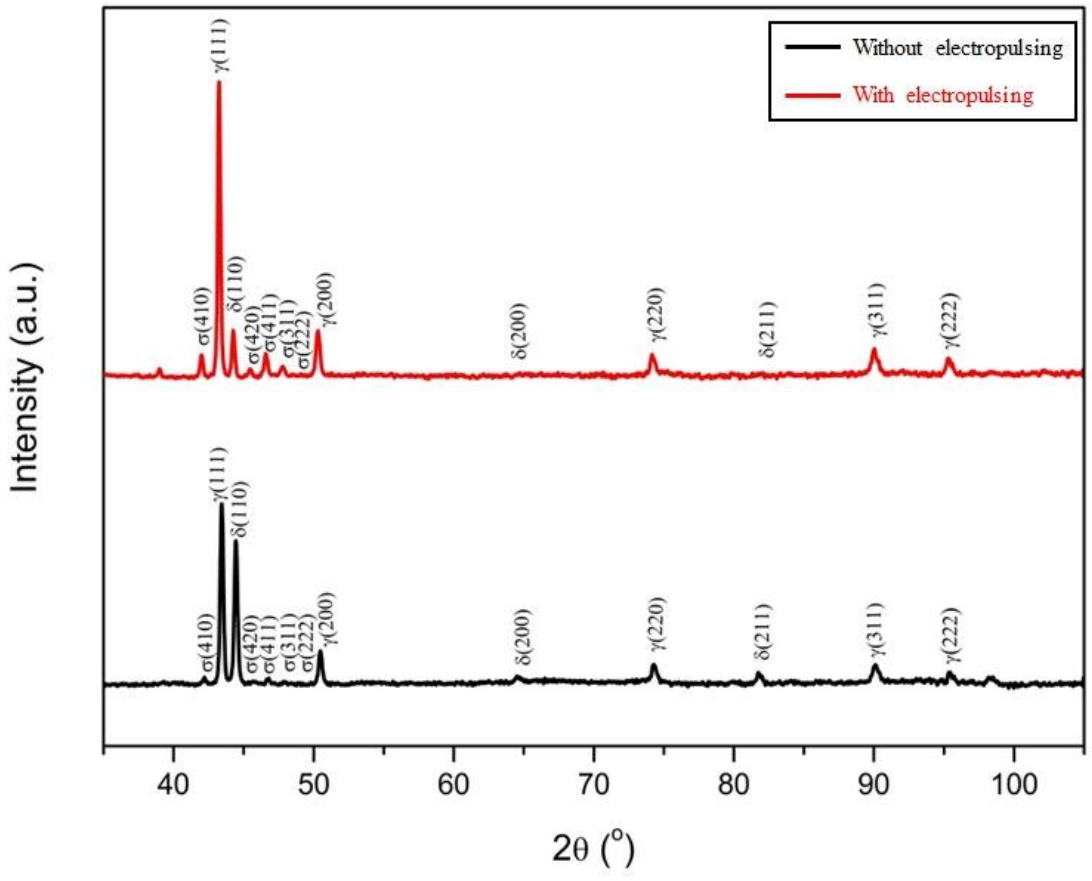


Figure 4.6: XRD spectra of steel samples without EPT and with EPT at 835°C.

In comparison with the DSS without EPT, three delta-ferrite peaks: (110), (200) and (211) were dramatically reduced after EPT. Quantitative calculation illustrated that the amount of secondary austenite, as well as that of sigma-precipitate, were increased while the amount of delta-ferrite was decreased under EPT. The volume fraction of each phase in DSS with and without EPT are displayed in Table 4.1.

Table 4.1: The volume fraction delta-ferrite, austenite and sigma phases in steels without and with EPT.

	Volume fraction (%) without EPT	Volume fraction (%) with EPT
δ-ferrite	54.0	5.2
γ-phase	44.8	87.68
Sigma-phase	1.2	7.12

Table 4.1 shows that the calculated volume fractions of each phase in DSS without EPT are in good agreement with those calculated MTDATA software, as indicted in Figure 4.4. For the DSS without EPT, the line H represents the volume fraction of each phase at 835°C. After EPT, the volume fraction of each phase in DSS was changed, which is labelled as line E in Figure 4.4. However, the corresponding temperature for the line E is about 780 °C. Given the fact that the temperatures in steel samples were actually 835°C, it can be subsequently concluded that the EPT promoted the decomposition of delta-ferrite: ($\delta \rightarrow \sigma + \gamma'$). The

transition should be harder to occur at high temperature. Therefore, secondary austenite (the majority phase) is stabilized by EPT. This allows sigma-phase (the minority phase) particles to survive to higher temperature. Those two types of particles provide strengthening of the steel at high temperatures.

EBSD is used for further detection of the volume fraction changes for each phase in DSS with and without EPT. Figure 4.7 are EBSD phase maps for the steel sample without and with EPT, where red region is the phase γ, green region the phase δ, and white region the phase σ.

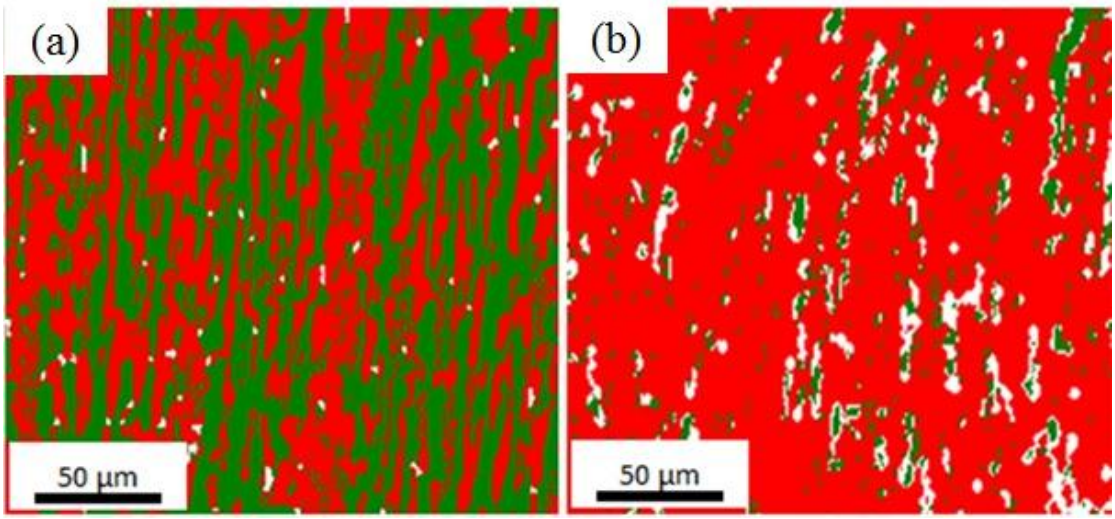


Figure 4.7: EBSD map for phase fraction measurement: (a) steel sample without EPT and (b) steel sample with EPT. Red region represents austenite, green region corresponds to delta-ferrite and white region is sigma phase.

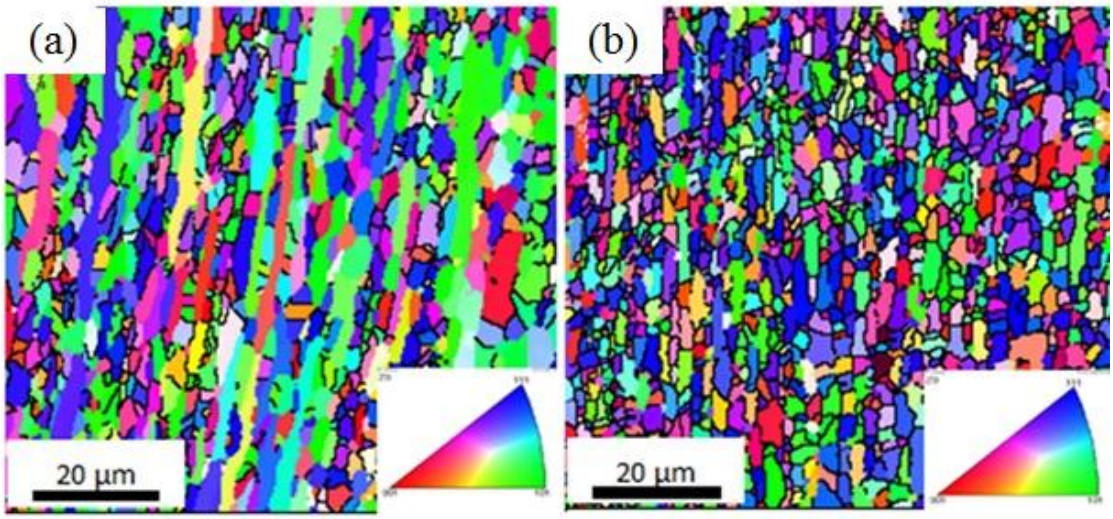


Figure 4.8: EBSD mapping for grain size measurement: (a) steel sample without EPT and (b) steel sample with EPT.

According to the image analysis, EBSD gives a similar volume fraction of phases to that measured by XRD. This proves that EPT stabilizes secondary austenite and sigma-phase so that both phases can be retained at high temperature. EBSD orientation maps for steel samples without and with EPT are illustrated in Figure 4.8.

A significant change of grain size for both phases was observed in DSS under EPT: one is the γ-phase from 0.894 µm to 0.651 µm and another is the δ-phase from 0.649 µm to 0.483 µm. This is attributed to the electric-current enhancing the dislocation mobility in cold-rolled samples under EPT. The fractions of Σ3 grain boundary within the DSS steel matrix with and without EPT have been also measured by EBSD. The results are shown in Figure 4.9.

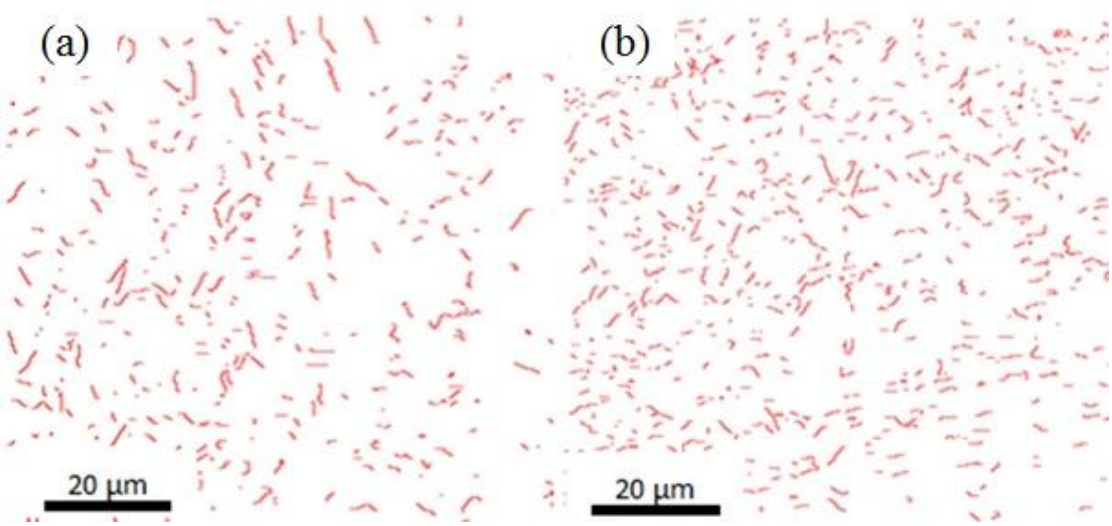


Figure 4.9: EBSD maps for Σ3 grain boundary distribution measurement: (a) steel sample without EPT and (b) steel sample with EPT.

The overall Σ3 grain boundary fraction was increased in both γ-phase and δ ferrite from 22.6% to 27.5%. This increase in Σ3 grain boundary fraction aids corrosion resistance and is highly recommended in terms of grain boundary engineering. The chemical composition in each phase with and without EPT were characterized by EDS. The results are displayed in Figure 4.10 and Table 4.2.

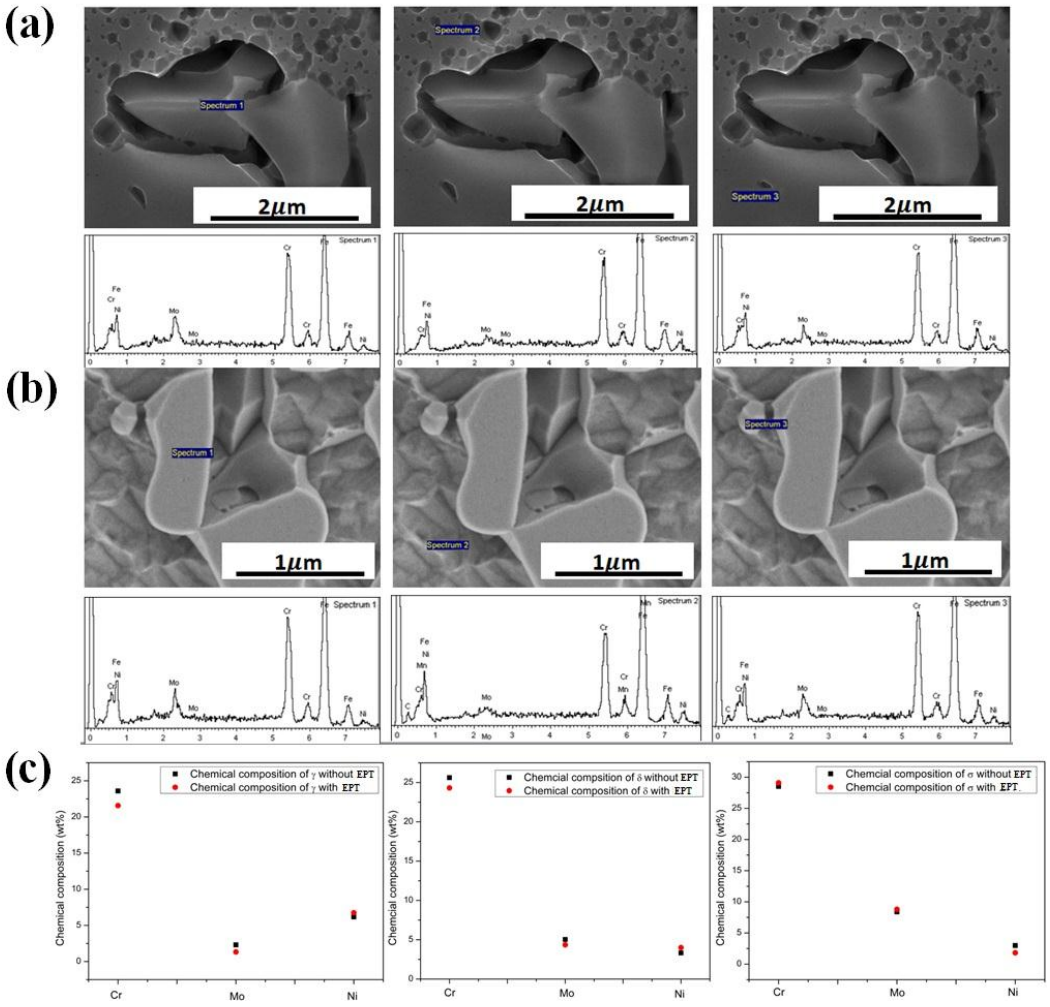


Figure 4.10: EDS spectra for austenite, delta-ferrite and sigma phases in the duplex stainless steel treated at 835 ºC (a) without EPT and (b) with EPT. The positions 1, 2 and 3 correspond to the sigma, austenite and delta-ferrite phases, respectively.

Table 4.2: Chemical compositions measured by EDS

	In sample without EPT (wt.%)				In sample with EPT (wt.%)			
Phase	Cr	Mo	Ni	Fe	Cr	Mo	Ni	Fe
γ	23.59	2.31	6.17	Balance	21.57	1.33	6.75	Balance
δ	25.62	5.03	3.32	Balance	24.31	4.35	4.00	Balance
σ	28.53	8.40	2.98	Balance	29.10	8.80	1.82	Balance

From Figure 4.10 and Table 4.2, it can be clearly seen that the chemical composition of the phases in DSS changed after EPT. EPT effectively promotes more Ni diffusion in and more Cr and Mo diffusion out from the austenite. In contrast the sigma-phase with EPT has higher Cr and Mo and lower Ni contents than that without EPT.

4.3.3 Property measurements

The Vickers hardness of quenched steel samples with and without EPT is shown in Figure 4.11d. It was found that the Vickers hardness of sample increased from 316HV to 472.4HV, an increase of 49.4%. The change of hardness is attributed to the change of phase fractions. The increased amount of secondary austenite and sigma phases provide strengthening to the DSS. EPT accelerates the eutectoid decomposition. One can predict that EPT increases the tensile strength of DSS because of the proportional relationship between Vickers hardness and strength. When the annealing temperature reaches 950 ^{o}C, the hardness of the samples without and with EPT were decreased to a similar level due to the dissolution of the secondary austenite and sigma-phases.

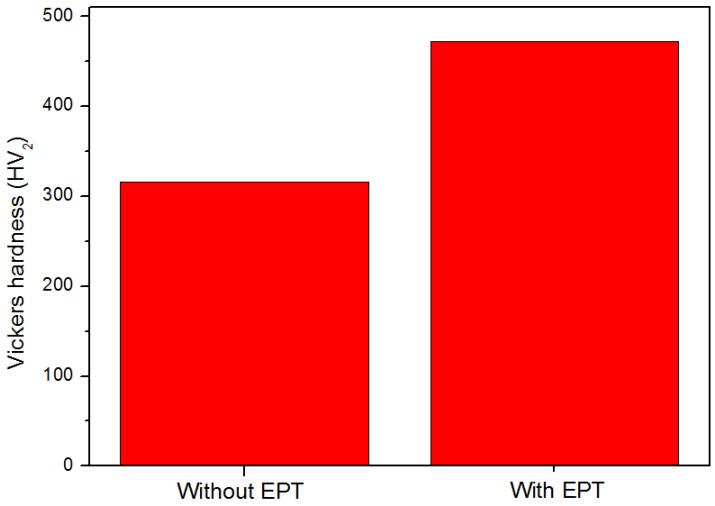


Figure 4.11: Vickers hardness of the samples without and with EPT.

4.4 Discussion

4.4.1 Thermal effect of EPT

It is known that electric current causes temperature elevation [168]. In the current research the electropulse generator provides a relatively low current density ~50A/mm^2. The total energy for each pulse is

$$Q_e = I^2 Rt \tag{4.2}$$

where R is the electrical resistance of the sample and Δt is the pulse duration. When Q_e is fully consumed to heat up the sample, it has

$$Q_e = mc\Delta T \tag{4.3}$$

where m and c are the mass and specific heat of the steel sample, respectively. ΔT is the temperature increased by the electrical current.

Substituting Equation 4.3 into Equation 4.2 to gives

$$\Delta T = I^2 R \Delta t / (mc) \tag{4.4}$$

It is known that $R = \rho_e L / S$ and $m = \rho_d LS$, where ρ_e, L, S and ρ_d are the electrical resistivity, length, cross-section area and density of the sample. Substituting *R* and *m* into the Equation 4.4, one obtains

$$\Delta T = \frac{j^2 \rho_e \Delta t}{c \rho_d} \tag{4.5}$$

where Δt is the pulse duration and *j* is the average electric current density. The following values are adopted for duplex stainless steel has $C = 450 J/(kg \cdot K)$, $\rho_{\mathrm{d}} = 7.8 \times 10^3 kg/m^3$ and $\rho_e = 9.58 \times 10^{-8} \Omega \cdot m$. The current density used in the present work, $j = 50 A/mm^2$, would give rise to a temperature elevation of 4.09×10^{-3} K with an electropulse of 60 μs duration. The electropulse was applied with 1 Hz frequency. Thus the rate of peak temperature rise due to the electric current is 4.09×10^{-3} K/s. The magnitude of any Joule heating in the present work, is hence negligible. The observed effects of EPT on the DSS. in particluar, the delta-ferrite decomposition must be due to other athermal effects.

4.4.2 Electric effect of EPT

4.4.2.1 Kinetic of EPT

In DSS, the eutectoid decomposition of delta-ferrite can be activated by heat treatments as the precipitation of secondary austenite and sigma-phase simultaneously [176–180]. This is due to the increases in diffusion rate of alloying elements in delta-ferrite matrix resulting from the increased energy provided by the heat treatments. The diffusion rate of alloying elements in delta-ferrite is about 100-fold faster than that of austenite (which is a consequence of the different crystallographic structure) [178]. Consequently, the sigma-phase appears more quickly in delta-ferrite than it does in austenite. The formation of sigma-phase (enriched in Cr

and Mo) causes the delta-ferrite to be depleted in these elements. This may, consequently, cause it to transform into secondary austenite. A schematic diagram depicting the mechanism of sigma-phase nucleation around the phase boundary (i.e. delta-ferrite and austenite interface) is plotted in Figure 4.12 [177, 178]. The formation of the sigma-phase is brought about by the absorption of Cr and Mo, and rejection of the Ni to adjacent ferrite region, which in turn transforms into secondary austenite.

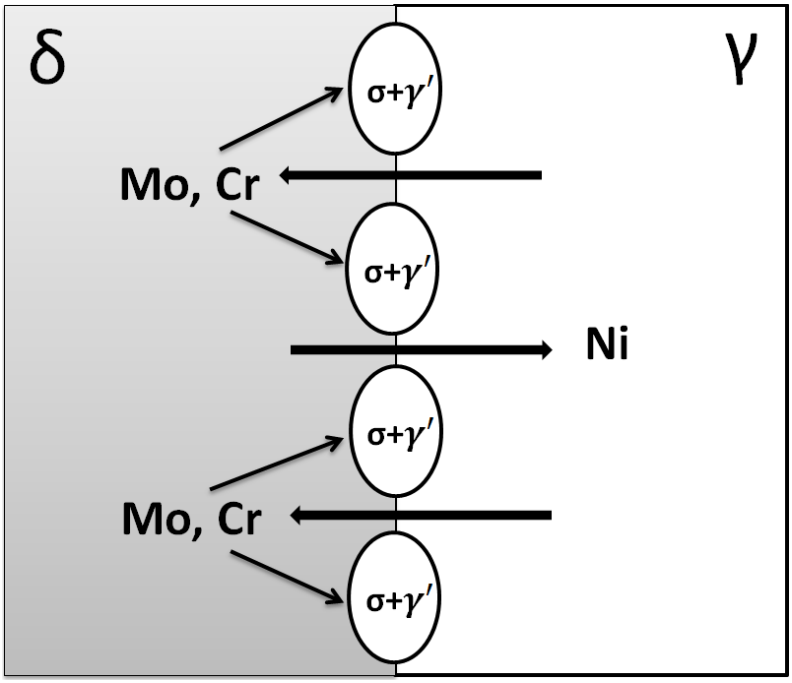


Figure 4.12: A schematic diagram showing the diffusion mechanisms of alloying elements between delta-ferrite and austenite at high temperature treatment. The sigma phase and secondary austenite precipitate along the phase boundary between austenite and delta-ferrite.

It is well-known that EPT promotes the atomic drift flux of atoms, which can be described in the Nernst-Einstein equation [46, 47, 56, 92],

$$J_i = \frac{N_i D_i}{KT}\left(KT\frac{\partial \ln X_i}{\partial X} - \Omega\frac{\partial \sigma}{\partial X} + Z^* e\rho j\right) \quad (4.6)$$

where D_i is the pertinent diffusion coefficient, N_i is the density of the i[th] atom species, Z^* is an effective valance, e is the charge on an atom, ρ is the resistivity, j is the current density, X_i is the concentration of the ith solute, Ω is the atom volume, $-\frac{\partial \sigma}{\partial X}$ is the stress gradient, K is the Boltzmann constant and T is the absolute temperature. In the present work, the thermal effect of EPT will be neglected due to the extremely small Joule heating temperature. As a result, the total atomic flux induced by EPT (J) arises mainly from the electric effect, which can be expressed as [36, 146]

$$J = 2ND_i Z^* e\rho f j_m \tau_p \quad (4.7)$$

Equation 4.7 shows that the atomic flux depends on current density j_m, duration τ_p and frequency f of the EPT. In this experiment, the diffusion fluxes for the alloying elements' (Cr, Mo and Ni) in a DSS sample at 835 ^{o}C were accelerated by applying a low current density. EPT to accelerate the diffusion rate of the alloying elements is strongly supported by the EDS results shown in Figure 4.10.

4.4.2.2 Thermodynamics of EPT

The electrical resistivity (ρ) of pure iron is strongly dependent to the temperature, as can be seen from Figure 4.13 [184].

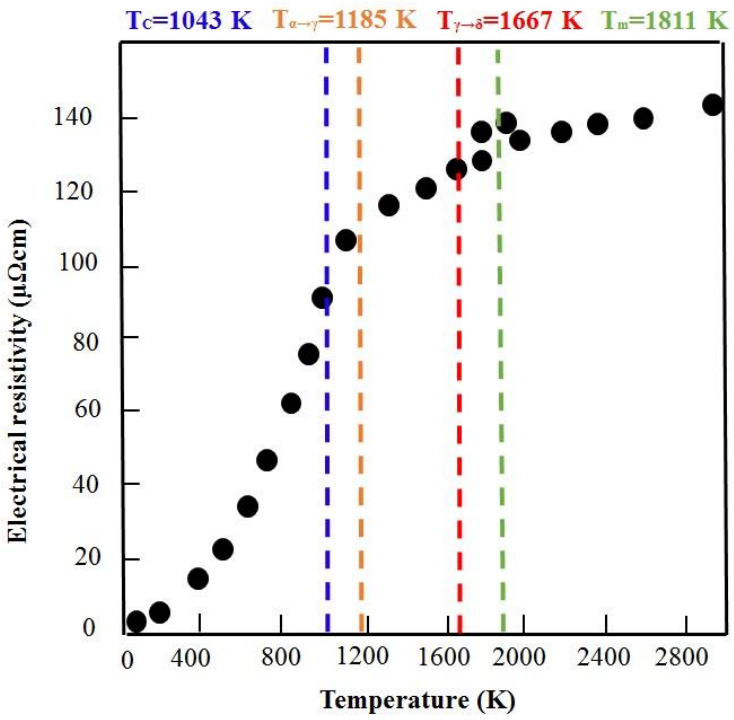


Figure 4.13: Electrical resistivity of iron as a function of temperature. Note: $T_{\alpha \rightarrow \gamma}$ is transformation temperature from α-ferrite to γ-phase, $T_{\gamma \rightarrow \delta}$ is transformation temperature from γ-phase to δ-ferrite and T_m is melting point.

It can be seen from Figure 4.13, that the transition from body-centred-cubic (delta-ferrite) to the face-centred-cubic (austenite) in pure iron at $T_{\gamma \rightarrow \delta}$ (1394 ^{o}C). is accompanied by a decrease in the electrical resistivity. The electrical resistivity values obtained by experimental measurements indicate values of around $1.28\times10^{-6}\Omega\cdot m$ for delta-ferrite and $1.26\times10^{-6}\Omega\cdot m$ for austenite [184]. The resistivity-temperature coefficient for delta-ferrite is smaller than that for austenite. One can therefore reasonably suggest that the electrical resistivity of the delta-ferrite is expected to be $1.30\times10^{-6}\,\Omega\cdot m$, which is higher than that of austenite ($1.05\times10^{-6}\,\Omega\cdot m$) at approximately 1108K (835 ^{o}C). Although the electrical resistivity-temperature relations for steels may differ from that for pure iron, the temperature- and structure- dependencies of the

electrical resistivity for steels should not differ from those of iron since Fe is the major component in steels. Literature studies indicate that electric current promotes the formation of phases with low electrical resistivity [99, 168, 172]. On this basis it would be expected that once the electrical resistivity of austenite is lower than that of delta-ferrite, EPT will tend to stabilize the austenite and destabilize the delta-ferrite in DSS. This behaviour arises from the of difference in Gibbs free energy of the system in DSS at elevated temperature.

When the electric current passes through the steel sample, there will be a consequent change in the system free energy. In steels, the system free energy of a steel contains three terms, namely, (i) the chemical free energy (ΔG_{chem}), (ii) the interface free energy (ΔG_{surf}) and (iii) the free energy associated with the electric current (ΔG_{elec}). The system free energy change in phase transformation (ΔG) under EPT is expressed as [99, 168]

$$\Delta G = \Delta G_{chem} + \Delta G_{surf} + \Delta G_{elec} \tag{4.8}$$

For the sample without EPT (i.e. $\Delta G_{elec} = 0$), the phase transformation occurs spontaneously when $\Delta G_{chem} + \Delta G_{surf} \leq 0$. For the sample with EPT, the phase transformation will be altered when ΔG_{elec} is added. The latter is derived from [49–67]

$$\Delta G_{elec} = \mu g(a,b)\xi(\sigma_A,\sigma_B)J^2\Delta\upsilon \tag{4.9}$$

where μ is the magnetic permeability in vacuum, g is a positive geometric factor for coarse grained materials, a is the radius of phase A, b is the radius of phase B, J is current density, $\Delta\upsilon$ is the volume of a nucleus and $\xi(\sigma_A,\sigma_B) = \dfrac{\sigma_B - \sigma_A}{\sigma_A + 2\sigma_B}$ is a factor which depends on the electrical conductivity (ie. the reciprocal electrical resistivity) of the two phases. When b≫a,

$g(a,b)=\left[\frac{3}{2}\ln(\frac{b}{a})-\frac{65}{48}-\frac{5}{48}\xi\right]b^2>0$. The calculation of ΔG_{elec} requires knowledge of the electrical conductivity of each phase. These electrical conductivity values can be calculated using the Quantum theory [99, 168]. Three possible scenarios are shown in Figure 4.14, (involving the relative magnitude of the electrical conductivities of phases A and B) and how these affect the phase transformation (phase B → phase A)

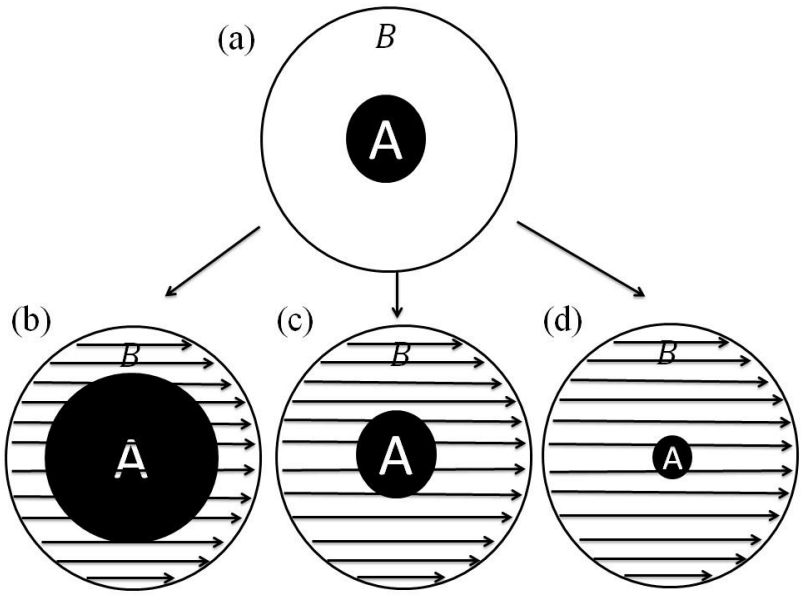


Figure 4.14: Schematic diagrams showing the effect of applying EPT on the phase transformation. (a) the original microstructure of alloy contains phase (B) and phase (A); (b) the phase transformation (i.e. the phase fraction change) is moved forward when the electrical conductivity of B is less than A; (c) the phase transformation is unaltered when the electrical conductivity of B is equal to A; (d) the phase transformation is retarded when the electrical conductivity of B is greater than A.

When $\sigma_A > \sigma_B$, the value of ΔG_{elec} < 0, and thus the total free energy of the phase transformation is reduced by using EPT. As a result, more phase A will be promoted in the sample compared with B, as shown in Figure 4.14b. When $\sigma_A = \sigma_B$, the phase transformation will not be affected by EPT due to $\Delta G_{elec} = 0$, as shown in Figure 4.14c. Furthermore, it can be seen from, Figure 4.14d shows that a reverse phase transformation (ie. B→A) can be activated by EPT when $\sigma_A < \sigma_B$ due to the effect on the free energy, $\Delta G_{elec} > 0$.

In the case of DSS, the steel matrix starts to soften as a result of the dissolution ($\sigma + \gamma' \rightarrow \delta$) but according to the equilibrium phase diagram of DSS (Figure 4.4) softening does not occur until the temperature exceeds 835 ºC. Most of precipitates (secondary austenite and sigma-phase) dissolve at this temperature and above. Using EPT, the pulsed electric current can promote the reverse phase transformation ($\delta \rightarrow \sigma + \gamma'$) which results in strengthening of DSS in comparison with untreated DSS. This is mainly attributed to the fact that the resistivity of austenite ($1.05\times10^{-6}\,\Omega$·m) is lower than that of delta-ferrite ($1.30\times10^{-6}\,\Omega$·m). On the other hand, EPT increases the Σ3 grain boundary fraction (shown in Figure 4.9) which is consistent with the thermodynamic prediction because Σ3 grain boundary has lower electrical resistivity (and more negative Gibbs energy) than that of a normal grain boundary [28]. The electrical resistivity of sample without and with EPT were measured to be $7.19\times10^{-7}\Omega$·m and $4.10\times10^{-7}\Omega$·m, respectively. This is in good agreement with previous work for the effect of EPT on reducing the electrical resistivity of steel [168, 172].

In general, the yield stress of alloys decreases with increasing temperature, as mentioned in *Introduction* section. The decrease of yield stress observed after annealing at temperatures between 800 and 1200°C in DSS can be attributed to decreasing δ-phase fraction [179, 180].

However, EPT retards the dissolution of secondary austenite and sigma-phases and thereby, strengthens DSS at high temperatures. In this case, the alloy is said to exhibit yield stress anomaly, which is typical of superalloys and leads to their use in applications requiring high strength at high temperatures. Furthermore, the precipitation strengthening of alloys (resulting from precipitates and carbides) is attained at the cost of a reduction in the corrosion resistance at high temperatures in stainless steels and superalloys [185, 186]. Consequently, a thermal barrier coating is usually added to superalloys [187] in order to enhance their oxidationon resistance at high temperature,. In the present work, EPT was found to promote the formation of Σ3 grain boundaries which compensated for the losses in corrosion resistance (due to the formation of σ particles). Therefore, EPT offers a potential way to improve the strength with a balanced corrosion-resistance in the treated steels.

4.5 Conclusions

To sum up, the phase transformation (e.g. delta-ferrite decomposition ($\delta \rightarrow \sigma + \gamma'$)) of DSS can be significantly modified by EPT. This change is the result of differences in the electrical properties of different phases. This subsequently allows one to alter the microstructure of DSS and optimize its mechanical properties.

(1) The temperature increase caused by the thermal effect of EPT (induced by electric current) was approximately 4.09×10^{-3} K, in the present DSS sample; this is considered to be negligible.

(2) The diffusion rates of alloying elements (e.g. Cr, Mo and Ni) were increased by applying electric current in delta-ferrite due to the kinetics of EPT; the enhanced diffusion rates promote the precipitation of (secondary austenite and sigma-phase) around phase boundaries.

(3) From a thermodynamic view, EPT stabilizes the high- electrical conductivity, phases/grain boundaries (e.g. austenite and Σ3 grain boundary) in DSS and hence promotes the reverse phase transformation $\delta \rightarrow \sigma + \gamma'$ at high temperature (835 ^{o}C). The surviving, hard sigma-phase particles and secondary austenite provide strengthening to the steel and make the steel strong at high temperature. In addition, the increased fraction of Σ3 grain boundaries under EPT should to compensate for the losses of corrosion resistance resulting from the formation of σ particles.

Chapter 5 Stability of κ-carbide in duplex lightweight steels under electropulsing

5.1 Structure and properties of κ-carbides in duplex lightweight steels

5.1.1 Introduction

With the consideration of reducing fuel consumption and CO_2 emission, the automotive and aerospace industries are becoming more focused on weight reduction. One suitable route to achieve the target is to use lighter and stronger Fe-Mn-Al-C based steels. Mn and Al are used to replace the expensive alloying elements such as Cr, Ni and Mo. TRIP and TWIP steels are automotive steels [188, 189]. Fe-Mn-Al-C steels can roughly be classified into three types: ferritic-based [190, 191], austenitic-based [190, 192, 193] and ferrite-austenite duplex-based steels [190, 194–196]. They are produced with different alloying compositions. The major benefit associated with Al addition is a weight reduction [190]. However, the addition of Al promotes the precipitation of κ-carbides in steels [188–222]. The κ-carbide has a perovskite structure and influences the mechanical properties of steels dependent upon its size, morphology, volume fraction and distribution [190, 194–196, 214, 215]. For instance, the nano-ordered, κ-carbides are frequently found in austenitic-based lightweight steel. They improve the mechanical properties significantly due to the existence of coherent γ/κ interface [190]. However, crack initiation takes place around the micro-sized, rod-like, κ-carbides during the rolling process for ferritic-based lightweight steels. Such behaviour is due to the appearance of a semi-coherent α/κ interface [189, 190, 194–196, 203, 213–215, 223]. The lattice mismatch between the steel matrix and κ-carbide for the above-mentioned two

interfaces is the key factor in balancing the mechanical properties because lower lattice mismatch is rewarded with better strengthening properties.

The control of the precipitation of κ-carbide and the control of its size, morphology, volume fraction and distribution in a steel matrix are the key issues for fabrication of lightweight steel. The κ-carbide precipitation was studied in conjunction with the Vickers hardness value by using SEM, TEM and XRD analysis.

5.1.2 Materials and methods

5.1.2.1 Materials selection and processing

A steel with a nominal chemical composition of Fe-34Mn-9Al-0.65C (wt.%) was cast using an induction melting furnace. An as-cast plate, 10 mm in thickness, was then solution treated for 4h at 1200 ^{o}C in order to homogenize all alloying elements throughout the entire steel plates. They were subsequently annealed at 600-800 ^{o}C for 6h before water quenching. The water quenched specimens were mounted, ground, polished and chemical etched with a mixed solution (2% Nital).

5.1.2.2 Microstructure observation and property measurement

Observations of the microstructure evolution and chemical composition for each phase in the specimens were carried out using a secondary electron microscopy (SEM) equipped with energy dispersive X-ray (EDX). The phases present were identified using X-ray diffraction (XRD: Cu K_{α} radiation; scan rate, 3^{o} min^{-1}; scan step size, 0.02^{o}). The volume fraction of austenite, ferrite and κ-carbide phase were measured and calculated using the integrated intensities of $(111)_{\gamma}$, $(200)_{\gamma}$, $(220)_{\gamma}$, $(311)_{\gamma}$, $(222)_{\gamma}$, $(110)_{\alpha}$, $(200)_{\alpha}$, $(211)_{\alpha}$, $(220)_{\alpha}$, $(111)_{\kappa}$,

$(200)_\kappa$, $(220)_\kappa$ and $(311)_\kappa$ peaks in the XRD spectra. Transmission electron microscopy (TEM) and selected area diffraction pattern (SADP) were carried out at an acceleration voltage of 200 kV in order to observe the microstructure in high resolution and to determine the phases present in the steel accurately, TEM Specimens (30 μm in thickness) for the steel were then punched into a disc with a diameter of 3 mm by a copper disk cutter. A twin-jet polisher with a chemical solution (10% perchloric acid and 90% acetic acid) at 15^{o}C was used to electro-polish the steel to thin films. The Vickers hardness of steel specimens under different annealing conditions was measured using a Vickers hardness tester with 1 kg load. The crystallographic structure of each phase present in these steels and the lattice misfit between phases were plotted and calculated using Crystal Maker software.

5.1.3 Experimental results and discussion

SEM micrographs of steel specimens after various annealing conditions and at different magnifications are shown in Figure 5.2a-f. Figure 5.2a and b shows an annealed steel specimen at 600 ^{o}C consisting of austenite, ferrite and some nano-particulate κ-carbides (0.17μm). The formation of nano-particulate κ-carbides in the ferrite is attributed to the high ratio of diffusivity between carbon in ferrite and in austenite, as shown in Figure 5.1.

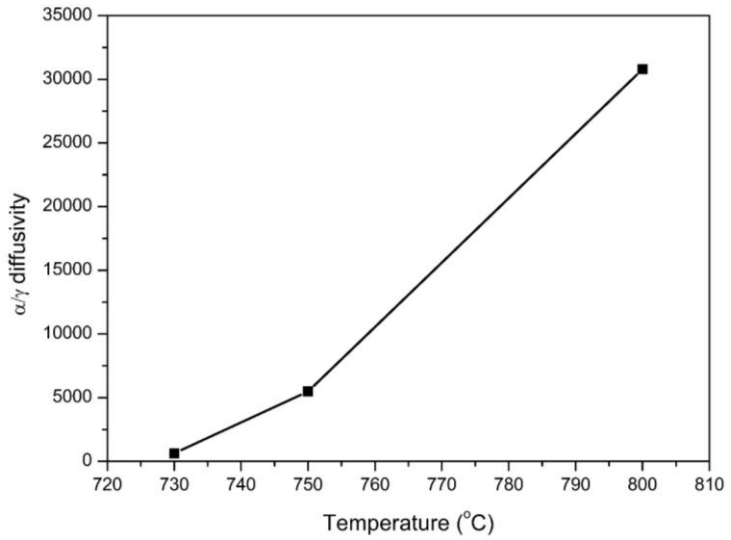


Figure 5.1: A schematic diagram showing the relationship between (D_α/D_γ) ratio and temperature.

The high diffusivity of carbon in ferrite leads to the formation of nano-particulate κ-carbides in ferrite at 600 °C. To further increase the annealing temperature up to 700 ^{o}C, these nano-particulate κ-carbides have grown into the micro-sized rod-like κ-carbides (about 0.26 μm in thickness) within the ferrite. In contrast, a large number of nano-ordered κ-carbides had started to precipitate within the austenite (Figure 5.2c and d). When the annealing temperature reaches up to 800 ^{o}C, most of the nano-ordered, κ-carbides dissolved in the austenite, whilst the rod-like κ-carbides continued to coarsen (to 1.63 μm in thickness) within the ferrite (Figure 5.2e and f). This indicates that the thermal stability of rod-like κ-carbides in ferrite is much better than that of nano-ordered κ-carbides in austenite.

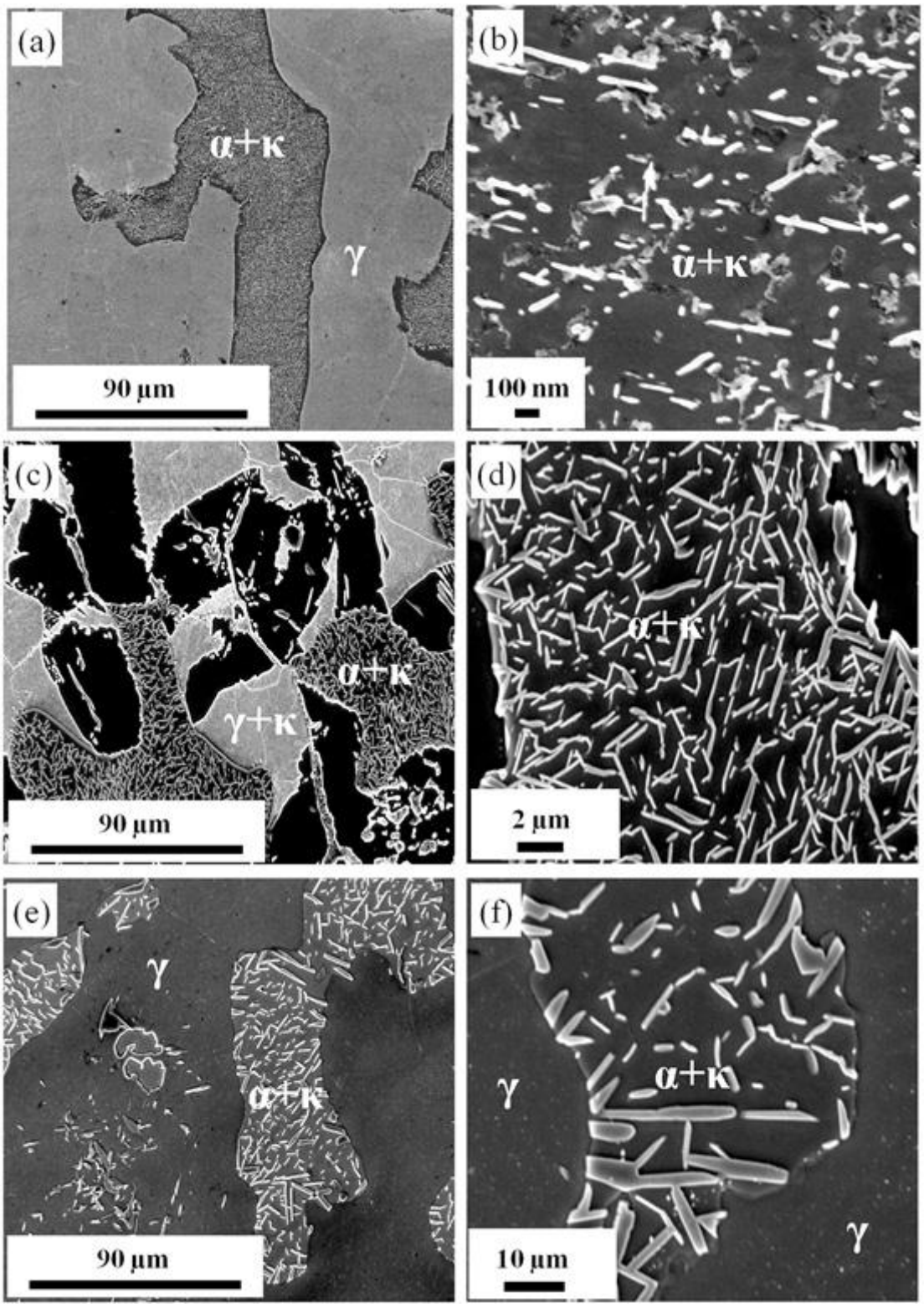


Figure 5.2: SEM micrographs of steel specimens annealed at (a-b) 600 ^{o}C for 6h, (c-d) 700 ^{o}C for 6h and (e-f) 800 ^{o}C for 6h.

High-resolution SEM, TEM and SADP were used to obtain high-resolution micrographs and to determine the orientation relationship between steel matrix and κ-carbide accurately for the steel specimen annealed at 700 °C (Figure 5.3a-f). High-resolution SEM and TEM bright field images for the nano-ordered κ-carbides in austenite are shown in Figure 5.3a and b, respectively. The nano-ordered κ-carbides are mainly formed by means of spinodal decomposition, which is typical for decompositions controlled by uphill diffusion without experiencing the nucleation stage. The SADP of κ-carbides and the corresponding schematic graph of the diffraction pattern are shown in Figure 5.3e. According to the calculations of lattice parameter and its crystallographic structure, the lattice parameter of nano-ordered blocks (κ-carbides) were 3.75 Å, whereas the lattice parameter of the bright phase (austenite) was 3.66 Å. The orientation relationship between κ-carbide and austenite were confirmed as: $(001)_{\kappa}$// $(001)_{\gamma}$ and $[001]_{\kappa}$ // $[001]_{\gamma}$, which are the same as the well-known orientation relationship between gamma and gamma prime in Ni-based super-alloys [211, 224]. The rod-like shape phase was confirmed to be κ-carbide with a lattice parameter 3.76 Å by using high-resolution SEM (Figure 5.3c), TEM (Figure 5.3d), SADP and its schematic graph (Figure 5.3f). The lattice parameter of the ferrite matrix was 2.87 Å. The orientation relationship between κ-carbide and ferrite was confirmed to be: $(1\text{-}11)_{\kappa}$ // $(110)_{\alpha}$ and $[011]_{\kappa}$ // $[001]_{\alpha}$. This orientation relationship corresponds to the well-known Nishiyama-Wasserman relationship. This is consistent with the previous results [204].

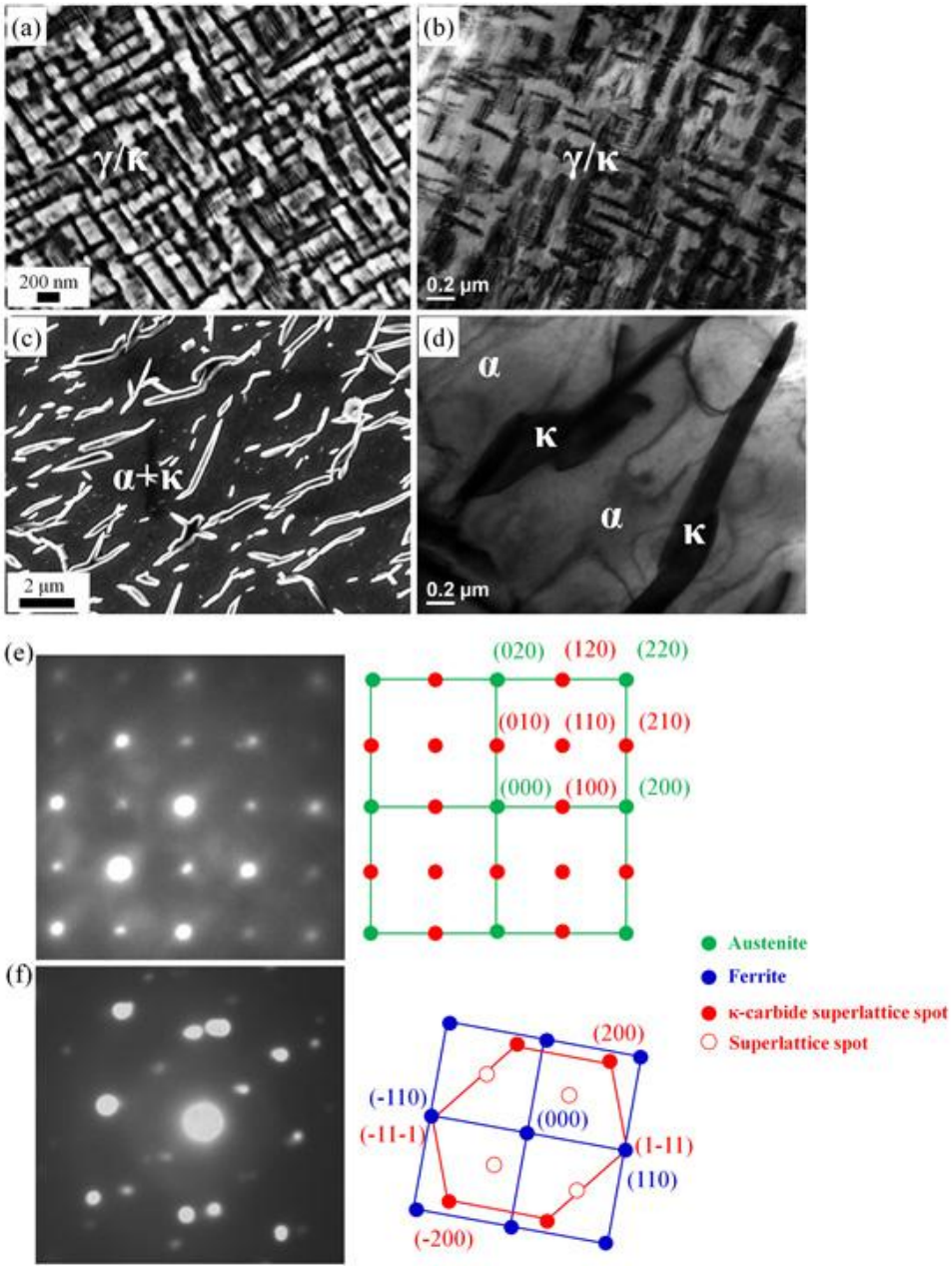


Figure 5.3: SEM micrographs of (a) the nano-ordered κ-carbide within austenite and (c) the rod-like κ-carbide within ferrite; TEM bright images of (b) the nano-ordered κ-carbide within austenite and (d) the rod-like κ-carbide within ferrite; (e) the SADP of the nano-ordered κ-carbide within austenite and their schematic diagram of SADP and (f) the SADP of rod-like κ-carbide within austenite and their schematic diagram of SADP.

The XRD spectra, its corresponding fraction of phases, and the Vickers hardness for Fe-34Mn-9Al-0.65C steel under different annealing conditions are shown in Figure 5.4a-c. It is seen that the austenite, ferrite and κ-carbide peaks appear simultaneously in Figure 5.4a. The fraction of each phase extracted and calculated from the XRD spectra are shown in Figure 5.4b. An increase in the annealing temperature (from 600 to 700 ^{o}C) results in a decrease in the fraction of ferrite (from 40.1 to 31.3 %) whereas the fraction of austenite decreased slightly (from 52.9 to 45.6 %). These reductions of fraction for both phases accompany a significant increase in the fraction of κ-carbide (from 7.0 to 23.1 %). It can be seen from Figure 5.4b that the precipitation of κ-carbide occurred in both the ferrite and the austenite at 700 ^{o}C. The maximum hardness value was obtained in the austenite with nano-ordered κ-carbides (702 HV). This value is much higher than that in ferrite with rod-like κ-carbide (523 HV) (Figure 5.4c). When the annealing temperature was increased to 800 ^{o}C, the fraction of κ-carbide decreased dramatically (from 23.1 to 5 %) due to complete dissolution of nano-ordered κ-carbides in the austenite and continuous coarsening of rod-like κ-carbide in the ferrite. The corresponding hardness values for austenite and ferrite decreased to 322 and 343 HV, respectively.

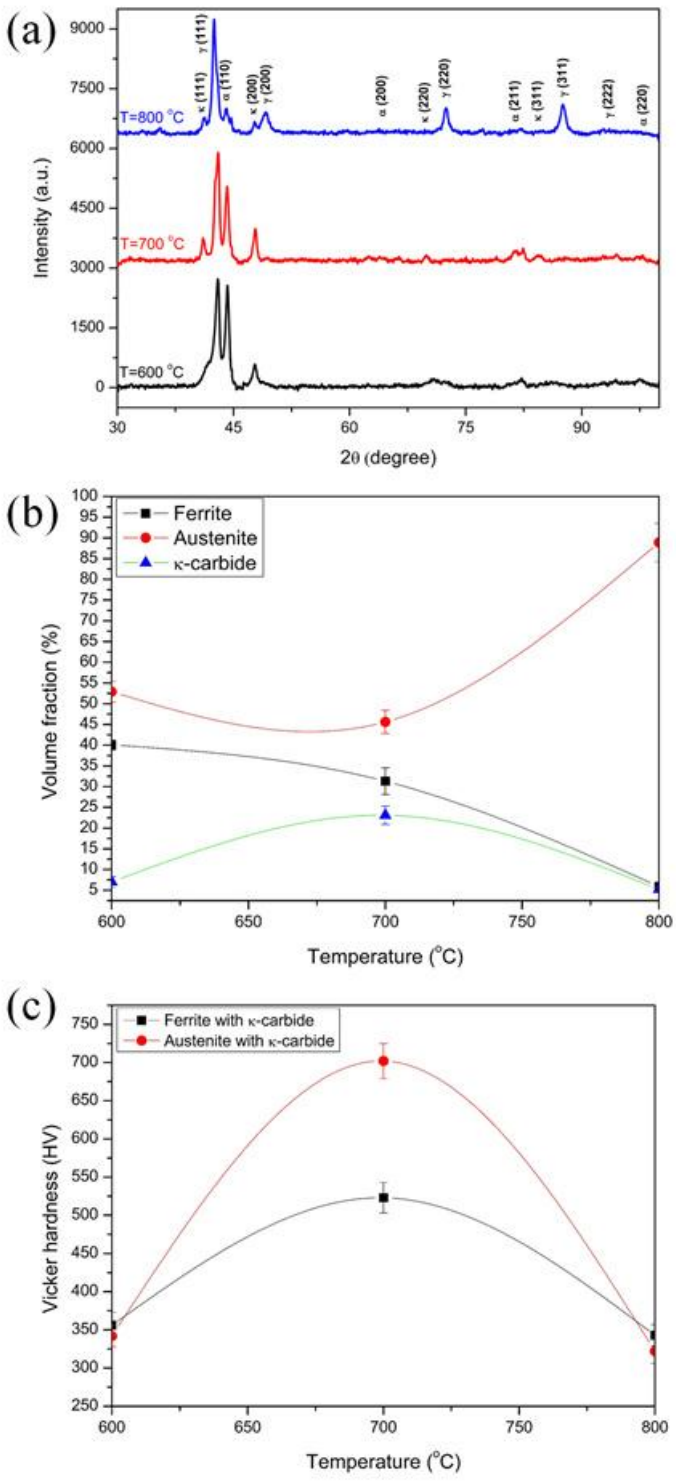


Figure 5.4: (a) XRD spectra for steel specimens annealed at 600-800 ^{o}C for 6h, (b) the calculated volume fraction of phases (austenite, ferrite and κ-carbide) via XRD results and (c) the Vickers hardness value of steel specimens annealed at 600-800 ^{o}C for ferrite and austenite regions.

The microstructure consisting of three regions (ferrite with rod-like κ-carbide, austenite with nano-ordered κ-carbide and carbide free austenite) was characterized. The concentration profiles of chemical elements across the phase interfaces are revealed using EDX measurements. The results are shown in Figure 5.5a-b.

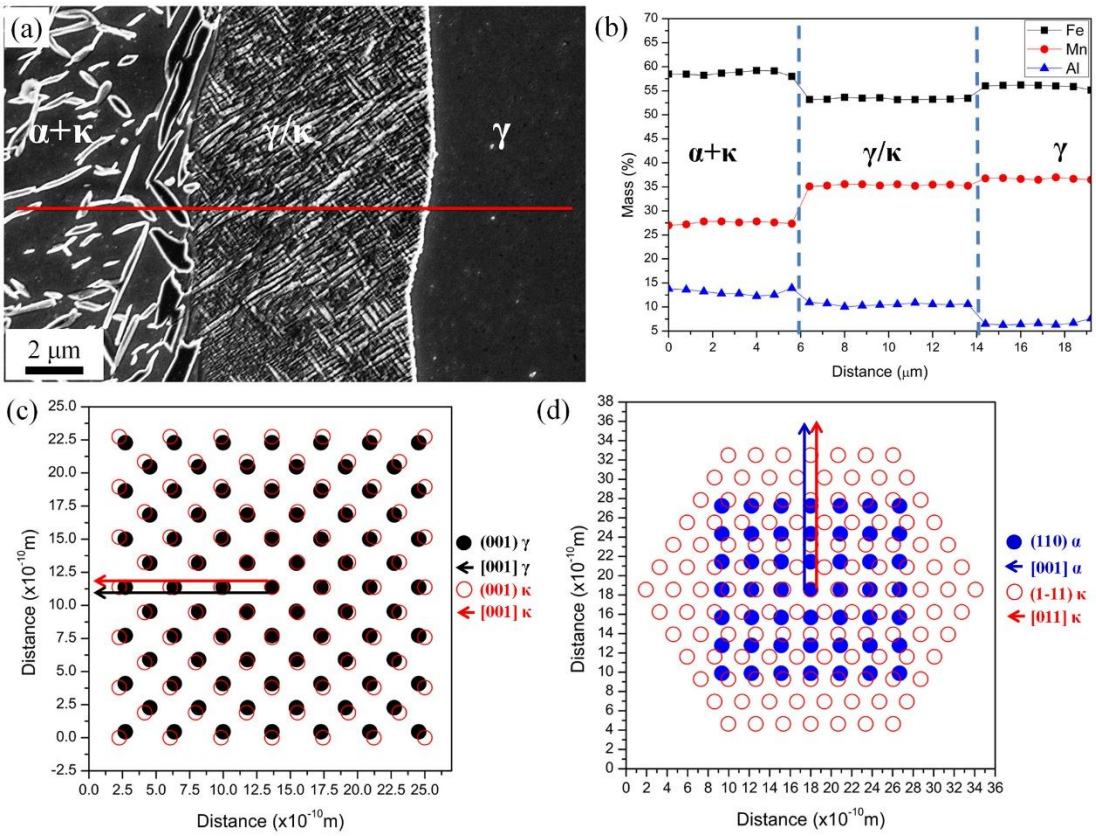


Figure 5.5: (a) SEM micrograph of the specific region contains three phases: austenite + ferrite, austenite + κ-carbide and carbide free austenite, (b) chemical compositions of alloying elements (Mn, Al and Fe) across the area marked by the red line, (c) a schematic diagram of lattice mismatch for 2 × 2 × 2 cells between κ-carbide and austenite, and (d) a schematic diagram of lattice mismatch for 2 × 2 × 2 cells between κ-carbide and ferrite.

It was found that austenite with nano-ordered κ-carbide has lower Al and higher Mn contents than those in ferrite with rod-like κ-carbide. The carbide-free austenite contains less Al and higher Mn than that in austenite with nano-ordered κ-carbide. This indicates that high Al promotes and stabilizes the formation of κ-carbide. κ-carbide in ferrite exhibits higher thermal stability rather than in austenite when the annealing temperature is increased. This is in good agreement with the experimental results mentioned previously. In addition, the diffusion of C in steel matrix plays an important role in influencing the thermal stability of κ-carbide. It is well-known that the diffusivity of C in ferrite is about 100 times faster than that in austenite at ca. 700 ^{o}C [178]. Higher C diffusivity promotes the nucleation of κ-carbide in ferrite. Simultaneously, the lower solubility of C in ferrite helps to stabilize the κ-carbide at high temperature.

Crystal Maker software was used to plot the unit cells of austenite, ferrite and κ-carbide. Bramifitt's planar lattice-matching model was used to predict the lattice misfit between phases [225]. A 2x2x2 expansion of the austenite unit cells in (001) plane along [001] direction was constructed to determine the orientation relationships between phases (Figure 5.3). This was overlapped with a 2x2x2 expansion of the κ-carbide unit cells in (001) plane along [001] direction (Figure 5.5c). It is noticed that the black solid symbols correspond to the austenite phase, whereas the red open symbols represent the κ-carbide. In Figure 5.5c, the lattice misfit along $[001]_{\kappa}$// $[001]_{\gamma}$ is calculated to be 2.7 %. Similarly, a 2x2x2 expansion of the ferrite unit cells in (110) plane along [001] direction and a 2x2x2 expansion of the κ-carbide unit cells in (1-11) plane along [011] direction had been constructed and overlapped together in Figure 5.5d, where blue solid symbols are the ferrite phase and the red open

symbols are the κ-carbide. It was easily found that the lattice misfit along $[011]_{\kappa}$ // $[001]_{\alpha}$ is much greater than that lattice misfit along $[001]_{\kappa}$ // $[001]_{\gamma}$ (2.7 %).

The small lattice misfit between austenite and κ-carbide indicates a much better strengthening effect than that derived for ferrite and κ-carbide. This is mainly attributed to the small elastic strain energy induced by the low lattice misfit. The small elastic strain energy leads to activation of the spinodal decomposition at low undercooling. This is due to the small kinetic barrier for a first order phase transition. The nano-ordered κ-carbide can be primarily precipitated in austenite via spinoidal decomposition due to the low lattice-misfit strain (Figure 5.3a and b) and thereby strengthen steel matrix. Alternatively, the high lattice misfit between ferrite and κ-carbide results in a significant increase in strain energy. The higher stain energy leads to a larger kinetic barrier for κ-carbide precipitation. As a result, the κ-carbides are precipitated in rod-like form in ferrite instead of nano-ordered, κ-carbides formed by spinodal decomposition.

5.1.4 Conclusion

(1) The precipitation characteristics of κ-carbide (size, morphology, volume fraction and distribution) in duplex Fe-34Mn-9Al-0.65C steel have been studied systematically for various annealing conditions (600-800 °C).

(2) The thermal stability of rod-like κ-carbides in ferrite was found to be much better than that exhibited by nano-ordered, κ-carbides in austenite. This was mainly attributed to the faster diffusion of C and higher solubility of Al in ferrite compared with the values in austenite.

(3) The lattice misfit between κ-carbides and ferrite was found to be higher than that between κ-carbides and austenite (2.7%). The low- lattice misfit resulted in a decrease in strain energy which in turn, initiated spinodal decomposition. Consequently, the nano-ordered κ-carbides in austenite (702HV) provide a better strengthening effect compared with that rod-like, κ-carbides formed in ferrite (523HV) at 700 ^{o}C.

(4) Reasonable thermo-mechanical processing is urgently required to design a suitable microstructure of duplex lightweight steels with various sizes, morphologies, volume factions and distribution of κ-carbides and to provide the necessary balance in their mechanical properties.

5.2 κ-carbide hardening in a low-density high-Al high-Mn multiphase steel

5.2.1 Introduction

Improving fuel efficiency and reducing vehicle emissions of CO_2 have become particularly important in the automotive steel industry [203, 217, 219, 226–228]. A good combination of specific strength and ductility of steel with low mass density is urgently required to comply with these requirements. Therefore, lightweight (Fe-Mn-Al-C quaternary system) steels have been actively investigated since the early 1990s, as novel automotive steels. They exhibit high strength and ductility [217, 190, 194–196, 204, 209, 211, 213, 217, 223], outstanding deformability [211], high impact toughness [212, 218], and excellent corrosion and oxidation resistance [188, 190, 229]. For these reasons, aluminium (Al) is widely used in as an alloying element in lightweight steels to lower the mass density and improve the corrosion and oxidization resistance (by forming a protective oxide layer). It is interesting to point out that the addition of Al can cause the formation of kappa (κ) carbide in lightweight steels. The κ-

carbide (a secondary phase with a perovskite (FCC based unit cell) ordered crystal structure) with a chemical composition $(Fe,Mn)_3AlC$, which contains one carbon atom (C) in the body position, one aluminium (Al) atom at the corner site and three iron (Fe)/manganese (Mn) atoms sited stochastically at the face centre positions, as shown in Figure 5.6 [188].

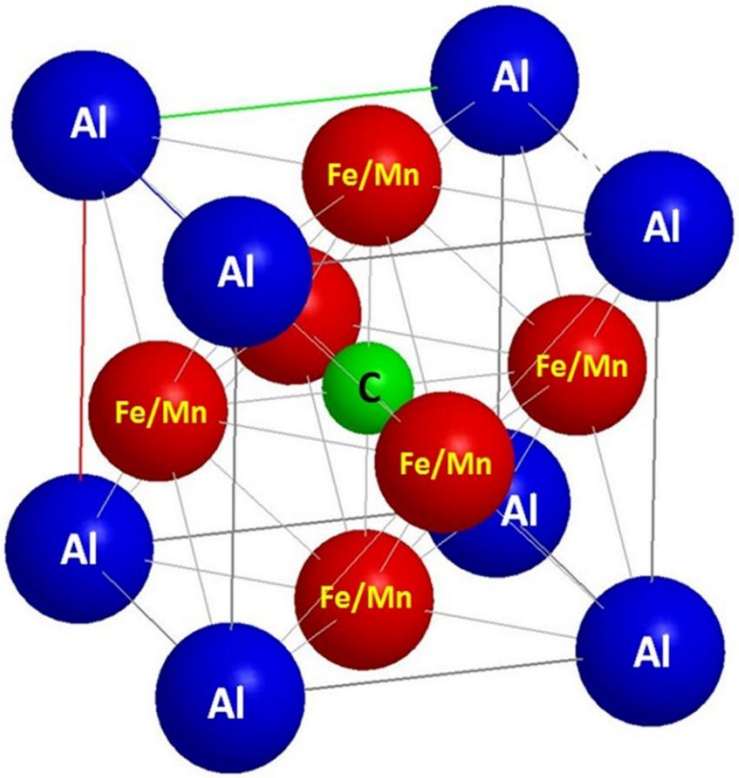


Figure 5.6: Schematic diagram showing a standard κ-carbide crystal structure.

It is common practice to strengthen the Fe-Mn-Al-C steels using various heat treatments [192, 204–206, 214, 222] to form the specific crystal structure of κ-carbide. κ-carbide has been regarded primarily as a harmful phase due to its hardness. Its formation has been inhibited in these steels by the addition of precipitation-hardening elements such as B, Ti and Nb [203, 205]. Recently, the formation of κ-carbide has become gradually accepted in lightweight

steels due to its remarkable ability to improve the strength and ductility of lightweight steels by controlling their size, morphology, volume fraction and distribution [190].

The formation of κ-carbides are concerned in the development of two types of lightweight steel, namely austenitic based steels (with relatively- high Mn and low- Al contents) and ferritic steels (with relatively low- Mn and high- Al) [190]. For the austenitic lightweight steels (15-30 wt.% Mn, 8-12 wt.% Al and 0.3-1.2 wt.% C), a spinoidal decomposition of austenite to κ-carbide can be observed in carbon-enriched zones by low temperature treatments in the temperature range of 427-677 ^{o}C [189, 207, 214, 197, 216]. These finely dispersed coherent κ-carbide (with a diameter of about 20-40 nm) in austenite can dramatically affect the mechanical properties of the steels [190]. The formation of this κ-carbide is predominantly controlled by the diffusion of both C and Al in austenite [214]. Therefore, the strengthening effect induced by κ-carbides occurs frequently in austenitic lightweight steels with high contents of C and Al. This results in the extraordinary properties of these steels (such as strengths >780 MPa and elongation of >30 %) which can be attributed to the formation of κ-carbide [203, 217].

Moreover, the κ-carbides are also found in the ferritic based lightweight steels with a chemical composition (0-8 wt.% Mn, 5-11 wt.% Al and 0-1 wt.% C) during cooling [190, 195, 196, 205]. By controlling a large amount of spherical κ-carbides bands can form and to distribute within the ferrite matrix. This leads to a simultaneous improvement in both strength and ductility [205]. However, unlike nano-sized ordered κ-carbides in austenite, the uncontrollable formation of lamellar, spherical κ-carbide bands in a ferrite matrix during continuous cooling frequently induces crack initiation and propagation in these steels [195, 196]. Considerable effort has been made to suppress the lamellar κ-carbides in ferrite during cooling.

Nowadays, over 12 wt.% Al is added to these lightweight steels [230]. The high Al concentration helps in the density reduction. However, high concentration of Al may lead to the formation of uncontrollable κ-carbides, which is a contradiction for improving mechanical properties of the steels. Rapid quenching from high temperature (>1000 ^{o}C) is frequently used in the lightweight steels processing [190] in order to reduce κ-carbide formation. The key factor affecting the mechanical properties of lightweight steel is to control the size, volume fraction and morphology of the κ-carbides.

There have been very few systematic studies providing an explanation of how the κ-carbides form in both austenite and ferrite phases under various annealing conditions. We have designed a high-Al duplex lightweight steel consisting of ferrite and austenite to monitor the whole precipitation behaviour of κ-carbides in both austenite and ferrite phases at various annealing treatments (500-1000 ^{o}C, 6-100 h). The nucleation, spheroidization, growth and dissolution of κ-carbides with their size, volume fraction and morphologies are observed using thermodynamic calculations, optical, SEM, TEM microscopes and XRD. Vickers hardness measurements were used to determine the correlation between microstructure modifications and mechanical properties of this duplex steel. In addition to the thermodynamic calculations, the effects of diffusion of alloying elements on phase transformation were analysed. XRD data provided direct evidence for detection of the κ-carbides formation and dissolution temperatures. The aim of the study was to obtain a systemic understanding of κ-carbides precipitation behaviour. This could lead to both the successful fabrication of austenitic, ferritic or duplex-based lightweight steels to make them suitable for automotive applications.

5.2.2 Materials and methods

5.2.2.1 Materials selection and thermomechanical processing

The steel with a chemical composition Fe-26Mn-9Al-0.75C (wt.%) used in this study was produced by an induction-melting furnace, as shown in Figure 5.7.

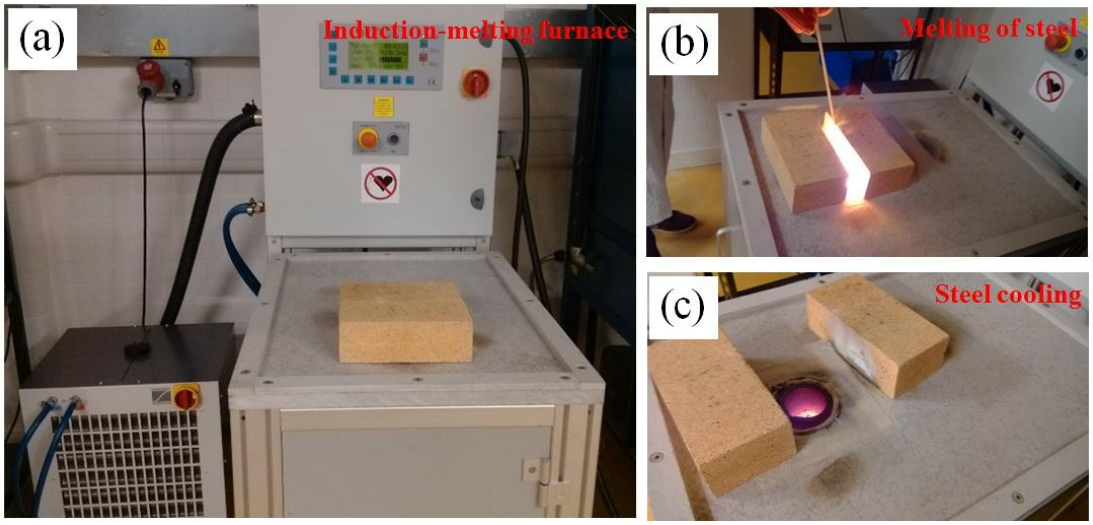


Figure 5.7: Photographs showing a process for steelmaking using induction furnace: (a) an induction furnace, (b) melting the steel and (c) waiting for the steel to cool.

After solidification, the steel ingot was taken out from a crucible and cut into a square shape. The sample was homogenised in a resistance furnace at 1200 ^{o}C for 4h and then hot rolled from 30 mm to 3 mm in thickness at 1000-1180 ^{o}C. The hot-rolled steel plate was again rolled at room temperature to produce a 1 mm thick steel sheet. The rolled sheet was annealed at 500-1000 ^{o}C for 6h to form a microstructure containing a mixture of ferrite, austenite and κ-carbides in order to observe the effect of temperature on the phase transformation of this steel. The annealing treatment was in 6-100 h at 600-800 ^{o}C to investigate the effect of annealing time on phase transformation of this steel. The sheet was subsequently cooled by water quenching to room temperature. For convenience the

specimens annealed at 500 (6h), 600 (6h), 600 (48h), 600 (100h), 700 (6h), 700 (48h),700 (100h), 800 (6h), 800 (48h), 800 (100h), 900 (6h), and 1000 (6h) ^{o}C are referred to as A1, A2, A3, A4, A5, A6, A7, A8, A9, A10, A11, and A12, respectively. The preheat treatments, rolling and annealing parameters for the square-shaped steel ingot are illustrated in Figure 5.8 and Table 5.1.

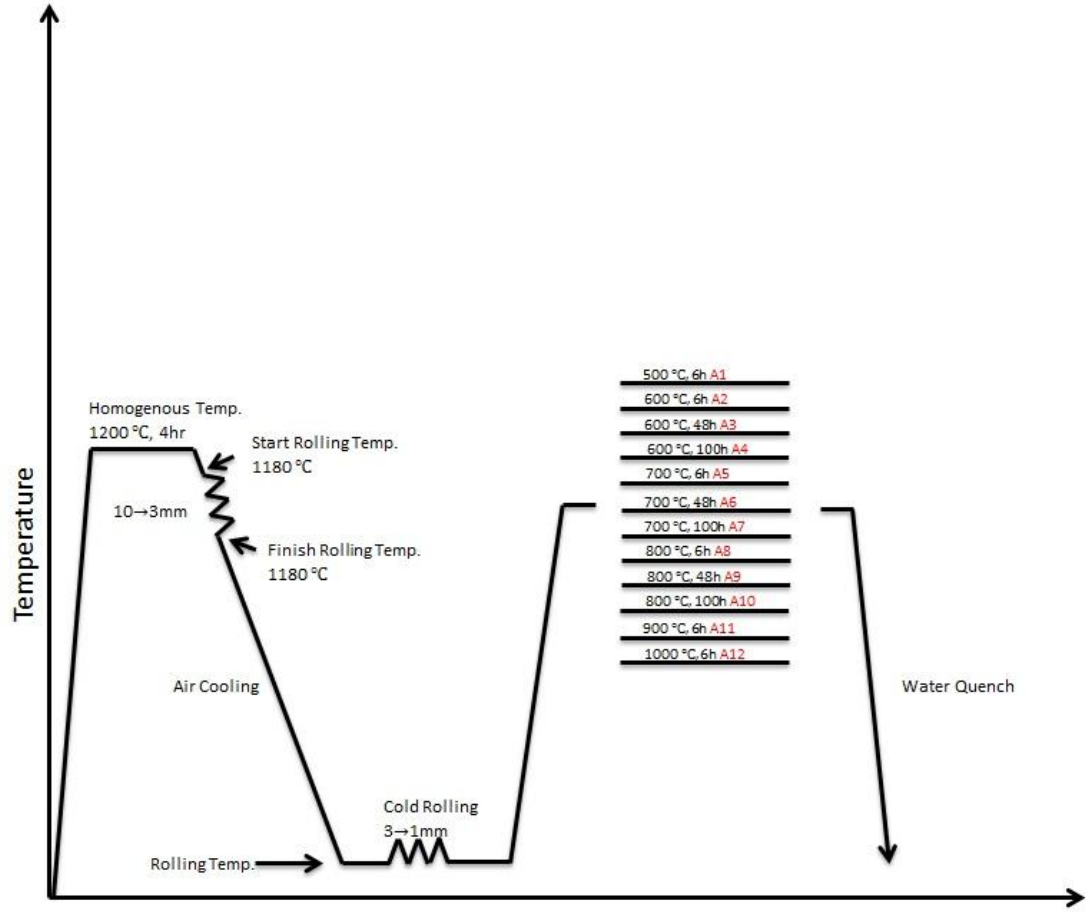


Figure 5.8: Schematic diagram showing the preheat treatment, rolling and annealing parameters for Fe-26Mn-9Al-0.75C (wt.%) steel specimens.

Table 5.1: Thermomechanical processing parameters for Fe-26Mn-9Al-0.75C steel.

Materials	Temperature (ºC)	Time (h)
A1	500	6
A2	600	6
A3	600	48
A4	600	100
A5	700	6
A6	700	48
A7	700	100
A8	800	6
A9	800	48
A10	800	100
A11	900	6
A12	1000	6

Aluminium reduces the weight of steel [230]. The density of the present steel (with approximately 9 wt.% aluminium in the steel) was measured by densitometry to be 6.47 gcm^{-3}. This brings an apparent reduction of 17.05% in comparison with pure iron (7.80gcm^{-3}). The hardness of steel specimens was measured using a Vickers hardness tester under a 2 Kg load.

5.2.2.2 Microstructure observation

The statistical measurements of the size, distribution and morphology of each phase in the as-treated and annealed specimens were obtained using optical, scanning electron microscopy (SEM), LEO 1525 microscope operated at 200 kV. For all optical and SEM observations, the steel specimens were polished and etched in a 2% nital solution. X-ray diffraction (XRD)

(CuK_α radiation, scan rate 1^o min^{-1}, scan step size 0.03^o) was used to determine the phases. The volume fractions of phases were measured using XRD analysis. Integrated intensities of the $(111)_\gamma$, $(200)_\gamma$, $(220)_\gamma$, $(311)_\gamma$; $(110)_\alpha$, $(200)_\alpha$, $(211)_\alpha$, $(220)_\alpha$ and $(111)_\kappa$, $(200)_\kappa$, $(220)_\kappa$, $(311)_\kappa$ peaks were used for XRD analysis. For transmission electron microscopy (TEM) analysis, the specimens were mechanically polished to a thickness of 30 μm and punched to prepare disc specimens with diameter of 3mm by a copper disk cutter. They were then jet polished to prepare thin foil specimens by a mixture solution of perchloric acid (10 %) and acetic acid (90 %) with 20V at 15 ^oC. The thin foils were observed in a TEM (JEOL 2000FX, Japan) operated at acceleration voltage of 200 kV. The duplex microstructures (optical, SEM and TEM), and diffraction pattern of each phase of cold-rolled steel specimen are displayed in Figure 5.9.

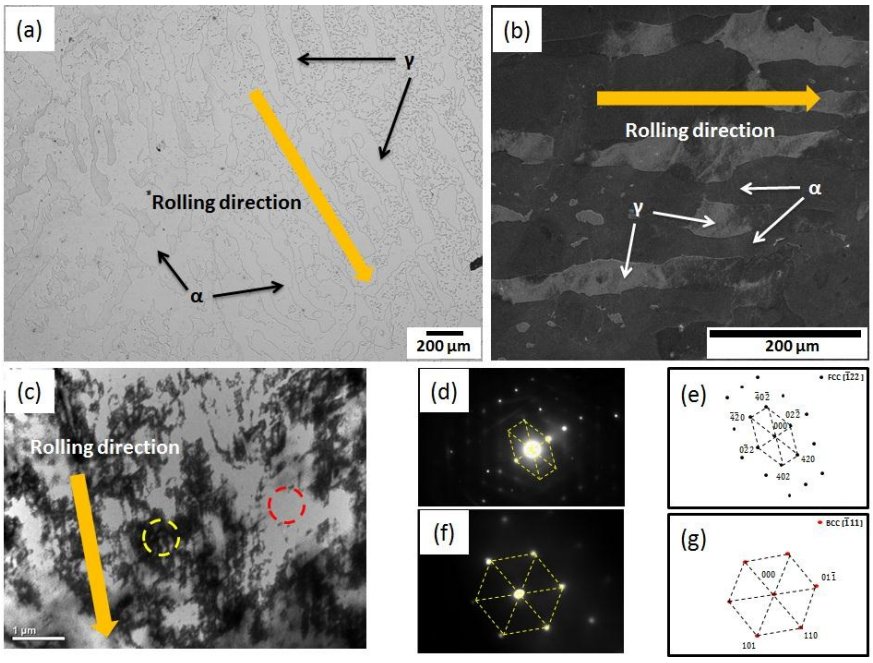


Figure 5.9: (a) Optical, (b) SEM, (c) TEM pictures, (d)-(e) diffraction patterns analysis of austenite and (f)-(g) diffraction patterns analysis of ferrite in the cold rolled specimen. All yellow arrows represent the cold rolling directions.

5.2.3 Experimental results

5.2.3.1 Thermodynamic calculation of high temperature equilibrium phase diagram

Thermo-Calc 3.1 with the TCFE 7.0 database was used to calculate the phase diagram for Fe-26Mn-9Al-0.75C (wt.%) steel at high temperature (Figure 5.10). Austenite (FCC) and ferrite (BCC) phases region co-existed up to a temperature around 1500 K. The decomposition of austenite to ferrite and κ-carbides started at about 906 K (633 ^{o}C) and finished at about 710 K (437^{o}C). κ-carbide started to dissolve when the temperature exceeded 906 K (633 ^{o}C).

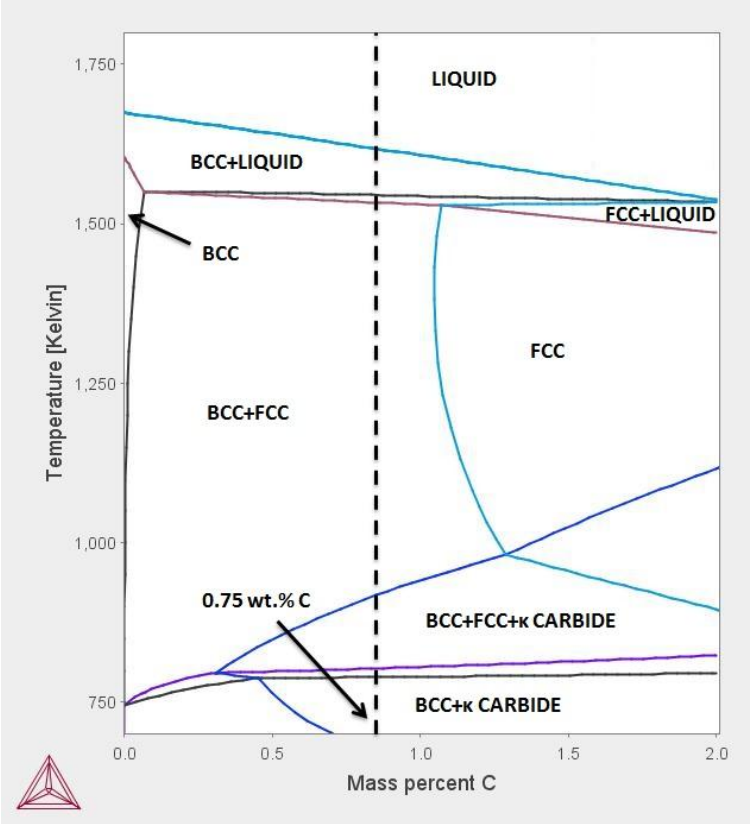


Figure 5.10: Phase diagram of Fe-26Mn-9Al-0.75C (wt.%) steel.

5.2.3.2 Non-equilibrium phase diagram of annealed steel

The XRD data of steel specimens (A1, A2, A5, A8, A11, A12) under annealing treatments for a temperature range from 500^{o}C to 1000^{o}C for 6 h are shown in Figure 5.11.

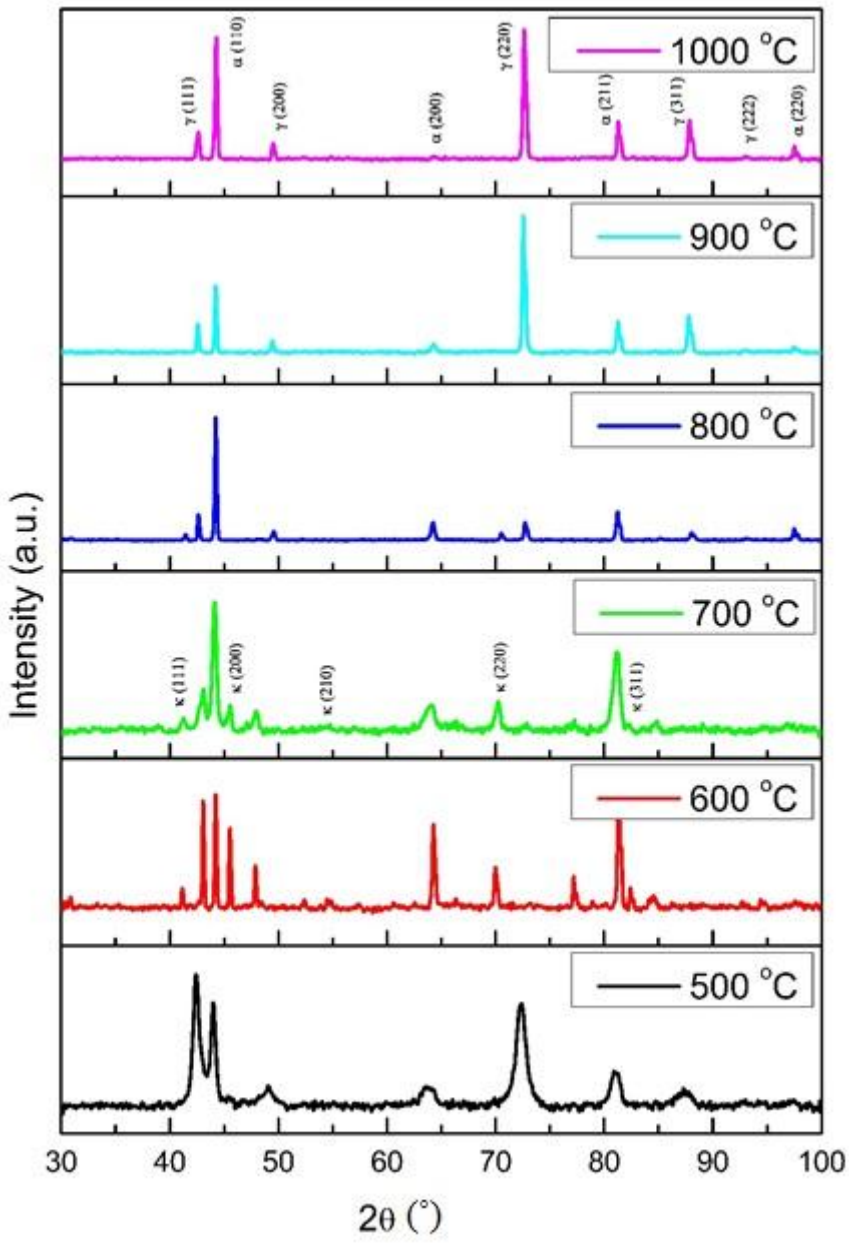


Figure 5.11: X-ray diffraction spectra (Cu K_α incident radiation) of steel specimens annealed at 500-1000 ^oC.

When the annealing temperature was increased from room temperature to 500 ^oC, there were only ferrite and austenite in the specimen (A1). κ-carbide starts to appear in the specimen (A2) when the annealing temperature reached 600 ^oC. This indicated that austenite had

dramatically decomposed to κ-carbide and ferrite. When the temperature reached 700 ^{o}C, three kinds of peak were identified. These indicated the co-existence of austenite, ferrite and κ-carbides in the steel specimen (A5) due to the eutectoid decomposition. At 800^{o}C, both κ-carbide and ferrite peaks decrease whilst the austenite peaks increase due to the dissolution of the κ-carbide. When the temperature increases to 900 ^{o}C, all κ-carbides peaks disappear in the steel specimen (A11) and the ferrite peaks continually decreases but austenite peaks increases. Finally, only ferrite and austenite peaks existed in the steel specimen (A12) at 1000 ^{o}C. From these observations, we may conclude that the triplex phases only exist in the temperature range from 600 to 800 ^{o}C (ie. for samples A2, A5, and A8).

From the XRD results, the changes in volume fraction for each phase as a function of temperature have been calculated and are plotted in Figure 5.12. The Vickers hardness of steels under different annealing conditions were also measured and are shown in Figure 5.12.

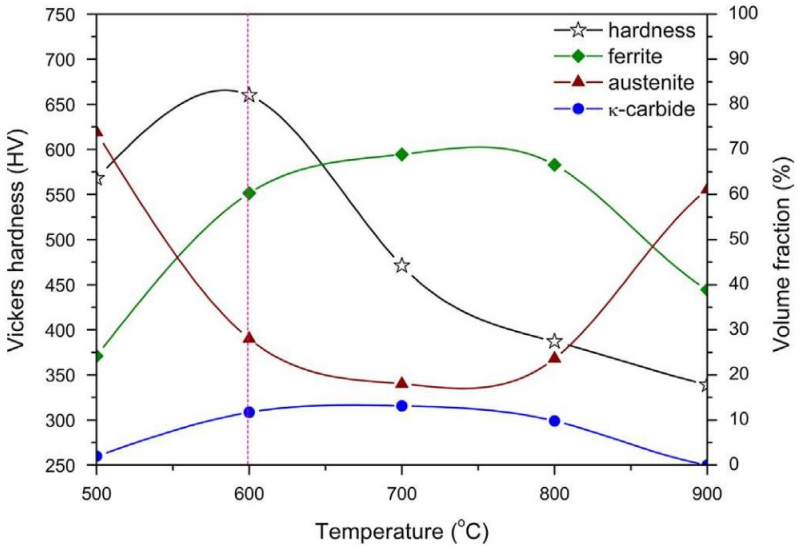


Figure 5.12: The volume fraction of each phase and the Vickers hardness of sample as a function of temperature.

When the temperature was increased from 500 to 600 ^{o}C, the fraction of austenite decreased from 74.8 to 28.0 %. Both ferrite and κ-carbide fractions increased up to 60.3 and 11.7 %, respectively. This reduction of austenite fraction indicates the onset of the austenite decomposition ($\gamma \rightarrow \alpha + \kappa$). Under this annealing temperature range, the hardness rapidly increased to a maximum value (672 HV), which corresponds to a yield stress of above 1.1 GPa (at 600 ^{o}C) in the stress-strain curve shown in Figure 5.13. This strengthening mechanism is attributed mainly to the combined effects of the fine lamellar κ-carbides in austenite and the dispersed, nano-sized, particulate κ-carbides in ferrite.

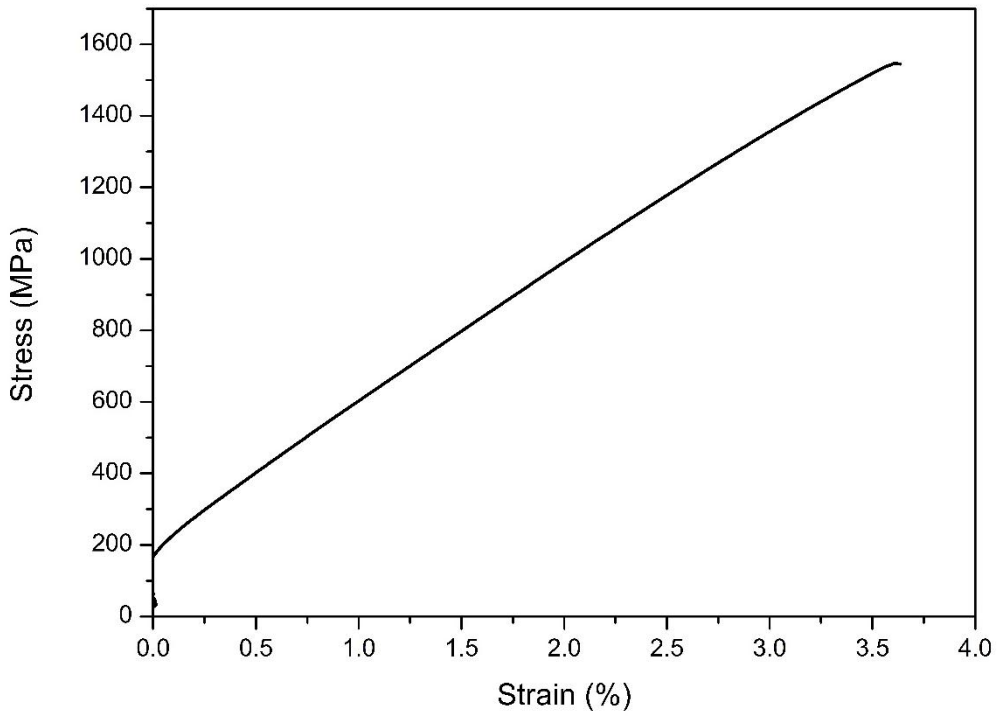


Figure 5.13: A schematic drawing of a stress-strain curve for the steel sample annealed at 600 ^{o}C for 6h.

When the temperature was in a range 600-700 ^{o}C, the volume fraction of austenite decreased to 18 %, whilst the κ-carbides increased slightly from 11.7 to 13.1 % and ferrite increased from 60.3 to 68.9 %. The hardness was significantly reduced to 474 HV due to the partial-dissolution and spheriodization of the κ-carbides. From 700-800 ^{o}C, the volume fraction of austenite increased to 23.6 %, whilst both ferrite and κ-carbides were decreased slightly to 66.6 and 9.8 %, respectively. The hardness decreased continuously. For the temperature range 800-900 ^{o}C, the volume fraction of austenite increased to 61.1%., whilst the κ-carbides decreased to minimum value and ferrite decreased to 38.9 %. The hardness decreased, simultaneously, to a minimum value (331 HV). Above 900 ^{o}C, all the κ-carbides had dissolved in the steel matrix. The volume fraction of austenite increased to 65.1 %, while the ferrite decreased to 34.9 %.

The dissolution temperature of the κ-carbides in this steel was calculated and measured by the Thermo-Calc (633 ^{o}C) and XRD (600-700 ^{o}C), respectively. A discrepancy exists between Thermo-Calc and XRD results, which might be attributed to the different states of the steel specimen. For the thermodynamically calculated phase fraction, all phases are in the equilibrium state, whereas the phase fraction measured by XRD is for a non-equilibrium state.

5.2.3.3 Effects of annealing temperatures on κ-carbide

The microstructure evolution of sample A1 at 500 ^{o}C is shown in Figure 5.14.

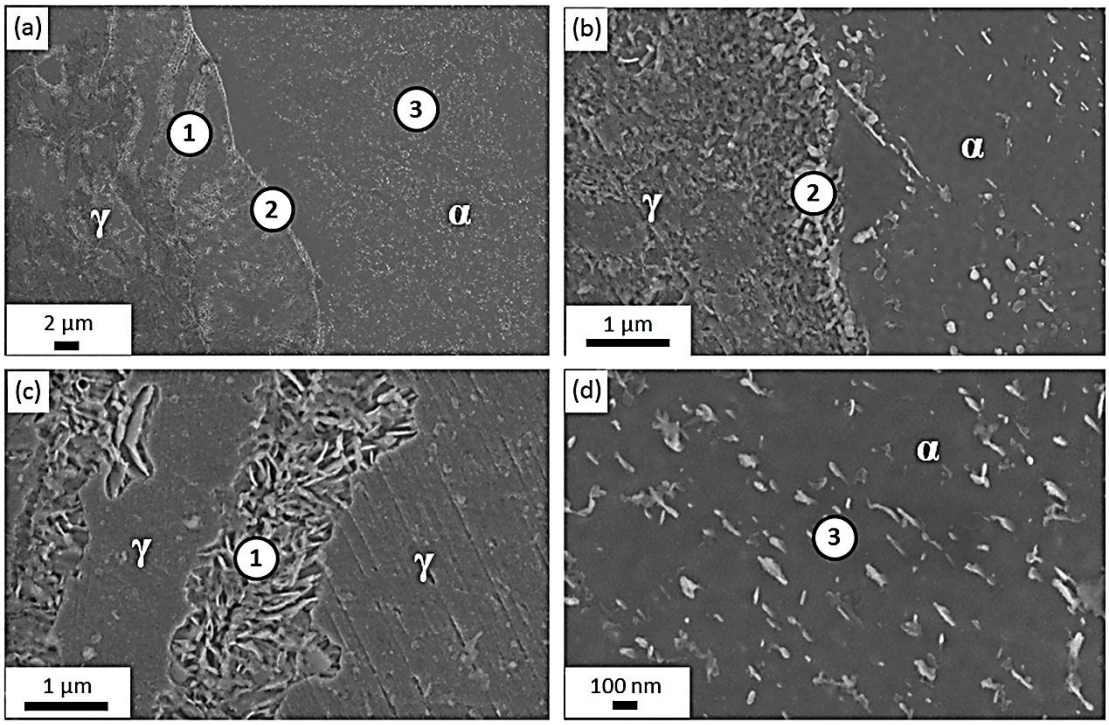


Figure 5.14: SEM micrographs showing (a) the microstructure evolutions of A1 annealed at 500 ^{o}C for 6 h, (b) κ-carbides precipitated at the phase boundary between α and γ, (c) lamellar κ-carbides starting to form at the grain boundary of γ and (d) particulate κ-carbides precipitated within α. Note: the position 1, 2 and 3 represent the austenite, phase boundary and ferrite, respectively.

At 500 ^{o}C, two major phases, austenite and ferrite, existed in A1 (Figure 5.14a) along with a small amount of κ-carbide. This differs from the XRD results since XRD is insensitive to small amounts of phases. Three positions (denoted 1, 3 and 2) show how the κ-carbides nucleate in austenite, ferrite and their phase boundary, respectively. It can be seen that lamellar κ-carbides start to nucleate at the grain boundary of austenite (Figure 5.14c). A small amount of particulate κ-carbide is observed in the ferrite matrix, as shown in Figure 5.14d.

When the temperature reached 600 ^{o}C in A2, the volume fraction of κ-carbides in positions 1 and 3 have increased dramatically (Figure 5.15a-d). This is consistent with the XRD results.

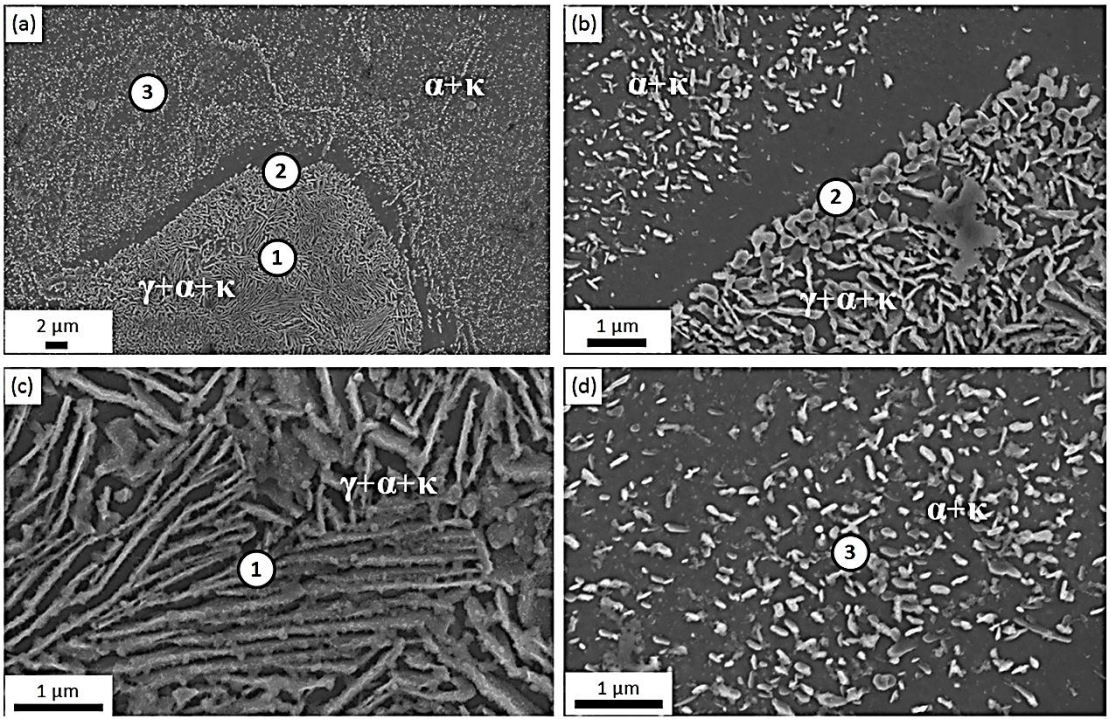


Figure 5.15: SEM micrographs showing (a) the microstructure evolutions of A2 annealed at 600 ^{o}C for 6 h, (b) κ-carbides coarsen at the phase boundary between α and γ, (c) lamellar κ-carbides fully precipitated by eutectoid decomposition within and γ and (d) particular κ-carbides coarsen within α.

It is worth pointing out that a large amount of lamellar κ-carbides are formed in the austenite regions due to the eutectoid decomposition, as shown in Figure 5.15c. The particulate κ-carbides also coarsened in the ferrite matrix as shown in Figure 5.15d. The morphology of κ-carbides was significantly changed from lamellar to spherical shape within the austenite phase in position 1 in A5 (Figure 5.16a-d) at 700 ^{o}C due to the spheroidization of lamellar κ-carbides.

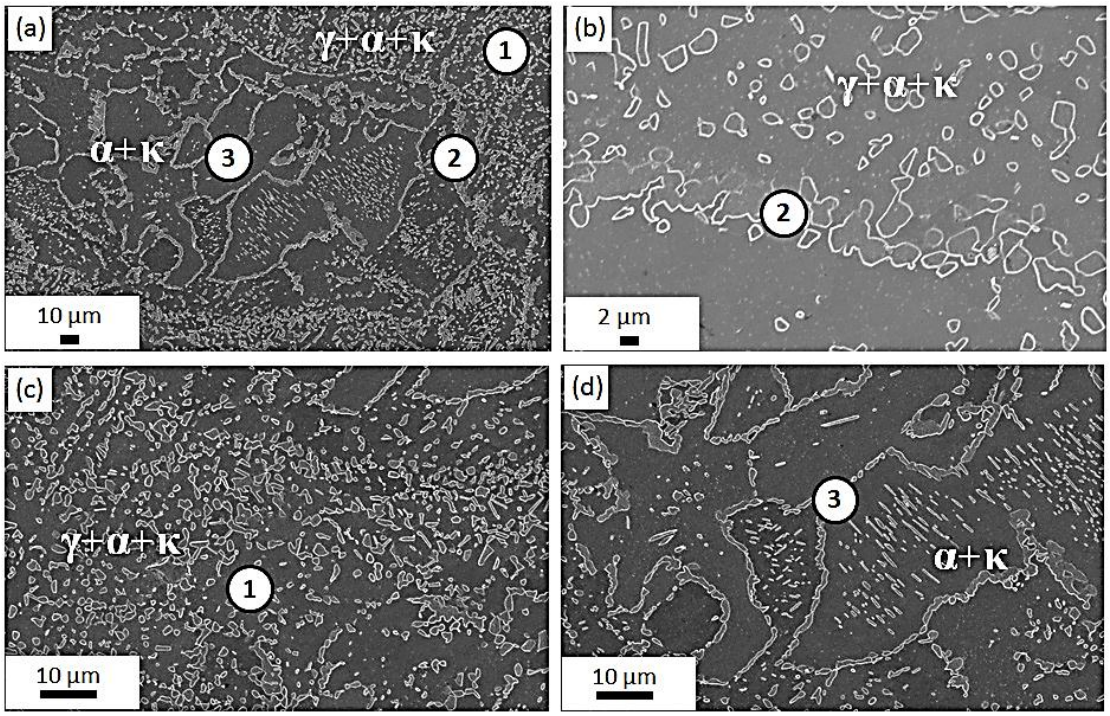


Figure 5.16: SEM micrographs illustrating (a) the microstructure evolution of sample A5 annealed at 700 ^{o}C for 6 h, (b) κ-carbides continually coarsen at the phase boundary between α and γ, (c) lamellar κ-carbides starting to spherodize and (d) particulate κ-carbides continually coarsening at grain boundary of α as band shape and in the grain interior as needle shape.

Simultaneously, κ-carbides start to form in both the grain interior of ferrite (as a needle shape) and at the ferrite grain boundary (as a band shape in position 3) as shown in Figure 5.16d. When the annealing temperature increased up to 800 ^{o}C (Figure 5.17a-d), most of κ-carbides in position of 2 and 3 in A8 had dissolved.

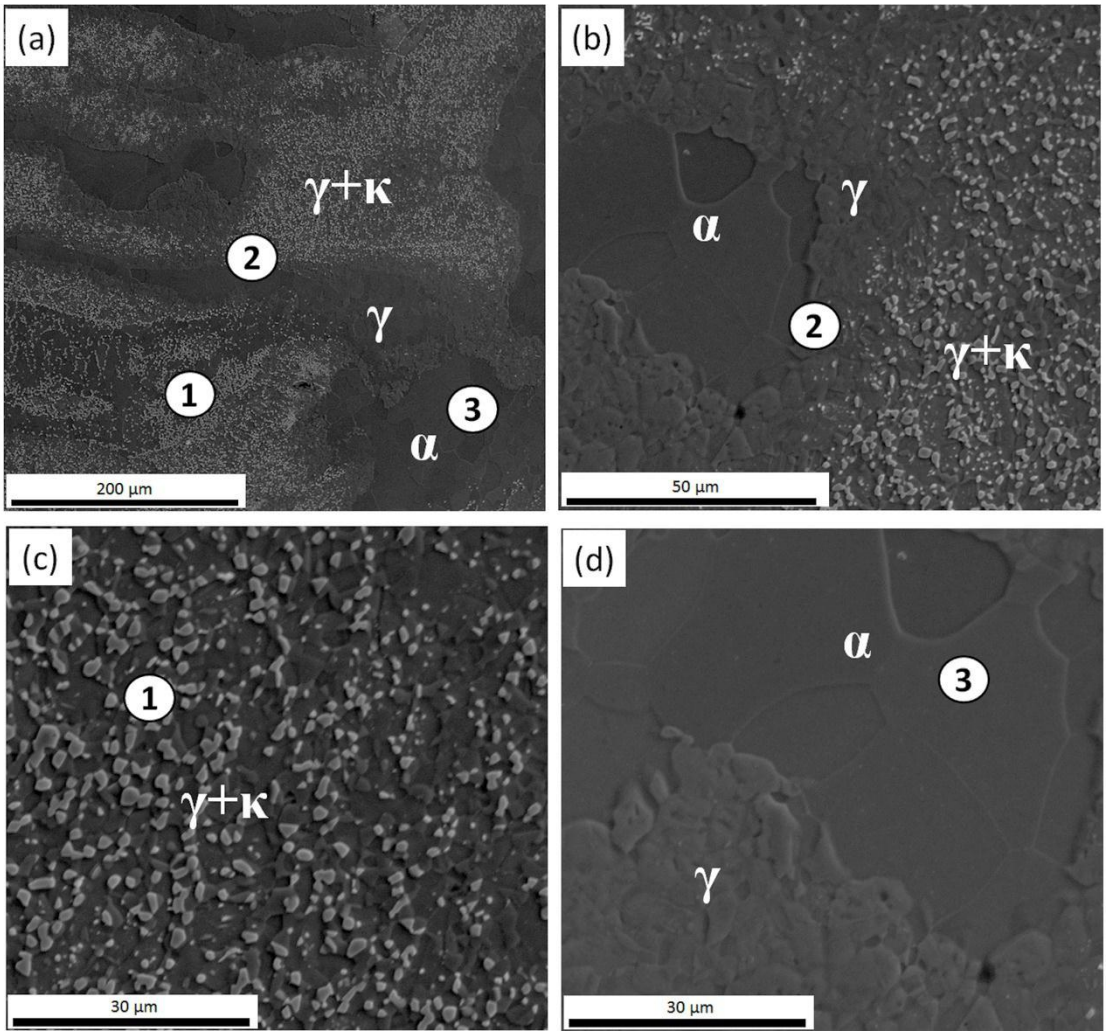


Figure 5.17: SEM micrographs illustrating (a) the microstructure evolutions of A8 annealed at 800 ^{o}C for 6 h, (b) κ-carbides dissolving completely at the phase boundary between α and γ, (c) spherical κ-carbides partially dissolving within the austenite matrix and (d) all κ-carbides dissolving within the ferrite matrix.

Figure 5.17c shows spherical κ-carbides within the austenite matrix are partially dissolved. All κ-carbides within the ferrite matrix are dissolved as shown in Figure 5.17d. When the annealing temperature was extended to the 900-1000 ^{o}C range (A11 and A12 in Figure 5.18a-

b), all the spherical κ-carbides within the austenite matrix were dissolved and only duplex phases (ferrite and austenite) remained in the steel matrix.

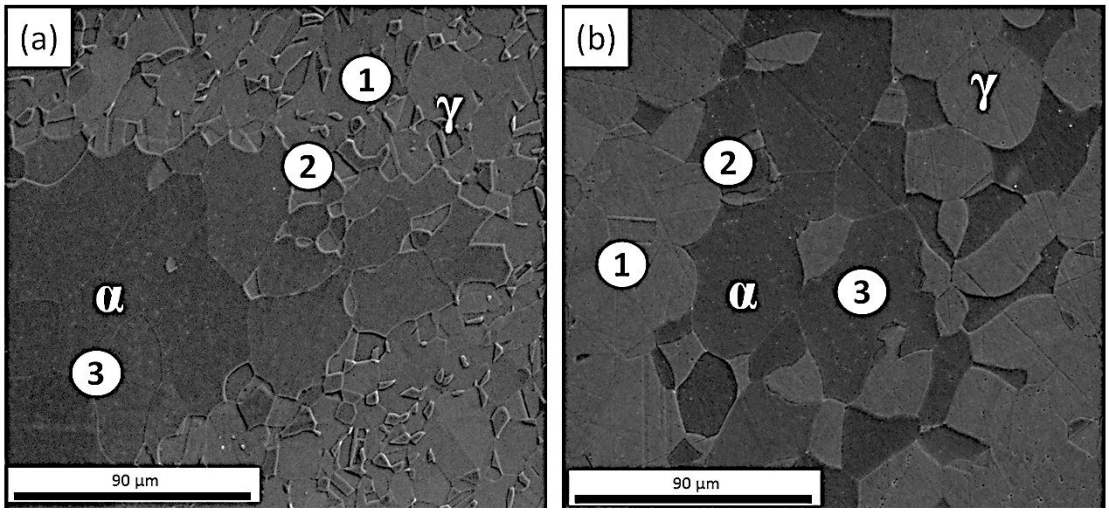


Figure 5.18: SEM micrographs illustrating (a) the microstructure evolution of sample A11, annealed at 900 ^{o}C for 6 h and (b) the microstructure evolution of sample A12 annealed at 1000 ^{o}C for 6 h. All κ-carbides in either position 1, 2 or 3 are dissolved completely.

On the basis of the above-mentioned SEM and XRD results, the phase transformation of lightweight steels can be classified into 5 stages, as shown schematically in Figure 5.19. All phase transformation stages are shown in detail in Table 5.2.

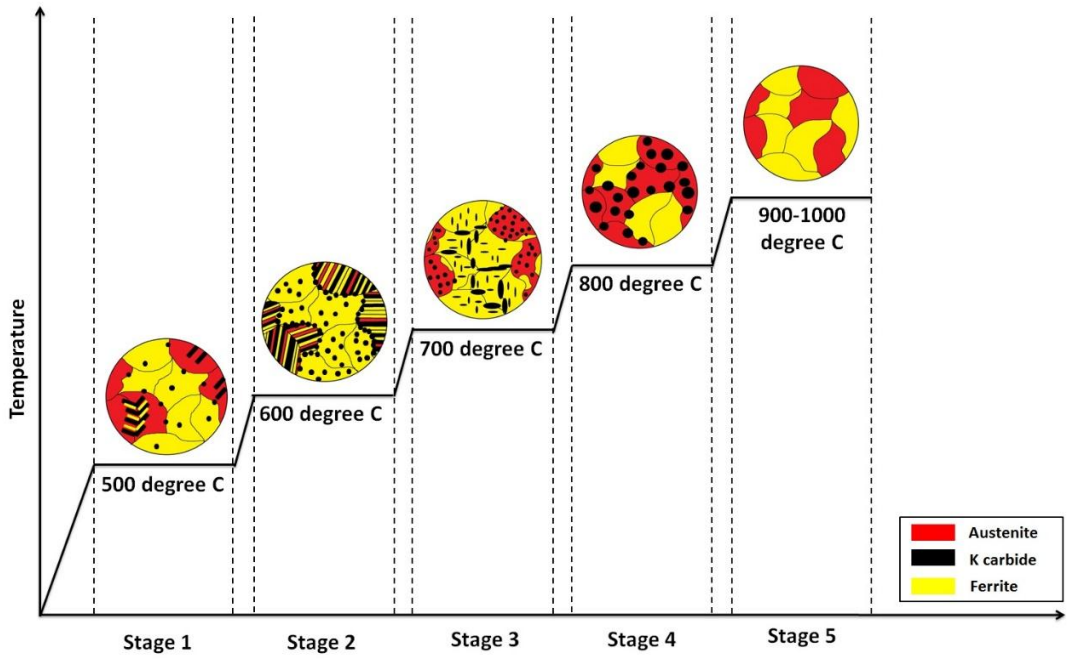


Figure 5.19: A schematic graph showing the 5 stages of microstructure evolution of steel specimens as a function of temperature.

Table 5.2: 5 phase transformation stages in Fe-26Mn-9Al-0.75C steel.

Stage	Temperature (^{o}C)	Microstructure evolutions	Phase transformation	Phases
1	500	A mixture phases consisting of ferrite , austenite and a little portion of κ-carbide	$\gamma \rightarrow \alpha + \kappa$	TRIPLEX (κ-carbide, ferrite and austenite)
2	600	Development of a large amount of lamellar κ-carbides in austenite and spherical κ-carbides in ferrite	$\gamma \rightarrow \alpha + \kappa$	TRIPLEX (κ-carbide, ferrite and austenite)
3	700	Fragmentation and spheroidization of lamellar κ-carbides in austenite, formation of	$\alpha + \kappa \rightarrow \gamma$	TRIPLEX (κ-carbide, ferrite and austenite)

		band shape of κ-carbides at grain boundary of ferrite and appearance of needle shape of κ-carbides in grain interior of ferrite		
4	800	Growth of spherical κ-carbides in austenite; significant dissolution of κ-carbides within ferrite	$\alpha + \kappa \rightarrow \gamma$	TRIPLEX (κ-carbide, ferrite and austenite)
5	900-1000	Complete dissolution of κ-carbides in steel matrix	$\alpha \rightarrow \gamma$	Duplex (ferrite and austenite)

TEM was used to determine the existence of the three different phases (austenite, ferrite and κ-carbides). The orientation relationships between κ-carbides and steel matrix were detected by selected area diffraction patterns (SADP) for A2 steel specimens. Figure 5.20 shows a TEM bright field image, SADP and its corresponding schematic diagram of SADP for A2.

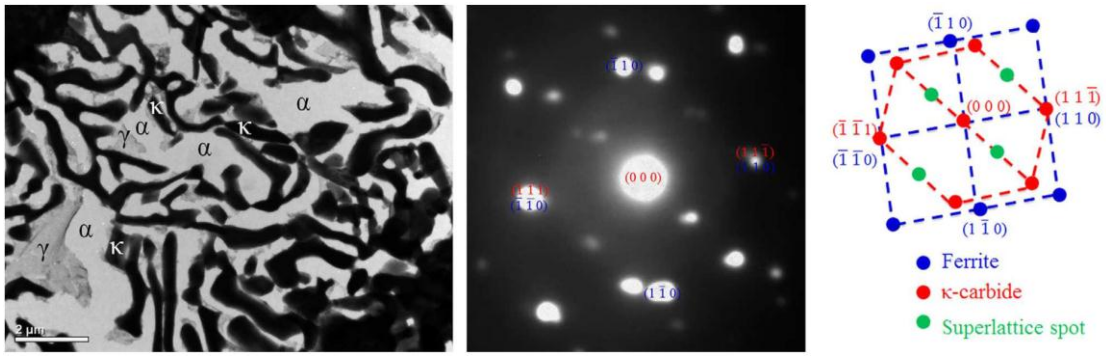


Figure 5.20: (a) TEM bright field image of A2 steel specimen, (b) SADP and (c) its corresponding schematic diagram of the N-W orientation relationship between κ-carbide and ferrite.

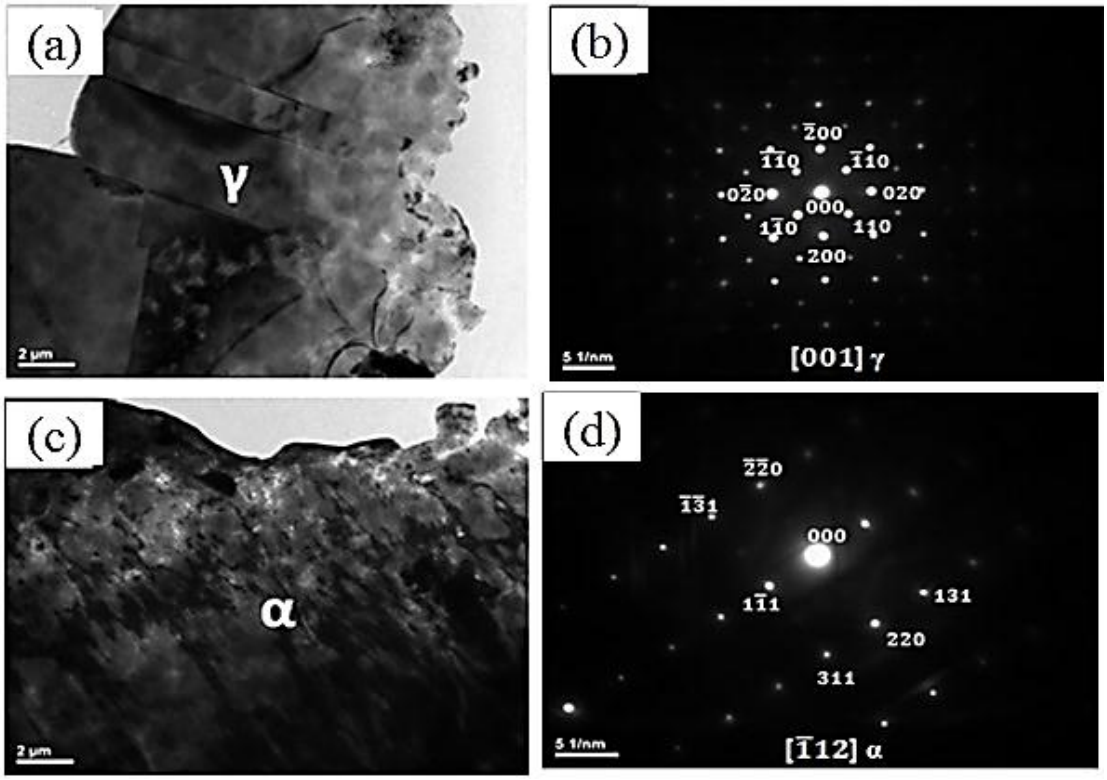


Figure 5.21: TEM micrographs in A11 steel show (a) bright field image of austenite and (b) its associated SADP; (c) bright field image of ferrite and (d) its corresponding SADP.

From the calculations of lattice parameters and crystal structure, the black lamellar shape phase is κ-carbides (with peroviskite structure) with lattice parameters 3.75 Å, whereas the light- grey phase is ferrite (BCC) with lattice parameters 2.92 Å. The orientation relationship between ferrite and κ-carbides is $(11\text{-}1)_{\kappa}$ // $(110)_{\alpha}$ and $[011]_{\kappa}$ // $[001]_{\alpha}$. This orientation is Nishiyama-Wasserman (N-W) relationship, which is consistent with the previous results [195, 196, 230]. For A11, only austenite (FCC with lattice parameters 3.62 Å) and ferrite (BCC with lattice parameters 2.90 Å) are confirmed from the calculations in Figure 5.21. This is consistent with the SEM and XRD observations.

5.2.3.4 Effects of annealing time on κ-carbide

The microstructural observations described above confirm that κ-carbides exist in a temperature range from 600-800 ^{o}C. The effect of annealing time (6-100h) on κ-carbide at this temperature range is shown in SEM micrographs (Figure 5.22 for A2, A3 and A4; Figure 5.23 for A5, A6 and A7; and Figure 5.24 for A8, A9 and A10).

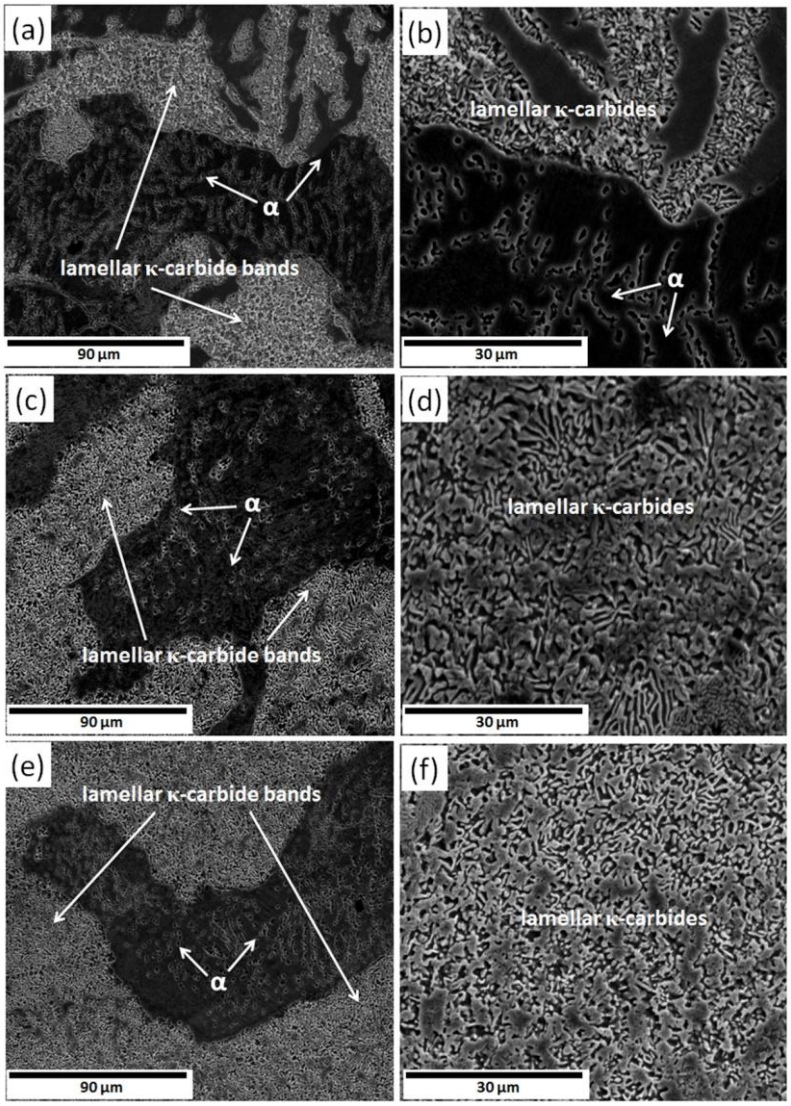


Figure 5.22: SEM micrographs of the (a-c) A2 with different magnifications, (d-f) A3 with different magnifications and (g-i) A4 with different magnifications, and they show that lamellar κ-carbides are continually coarsening in the steel matrix at 600 ^{o}C for 6 to 100h.

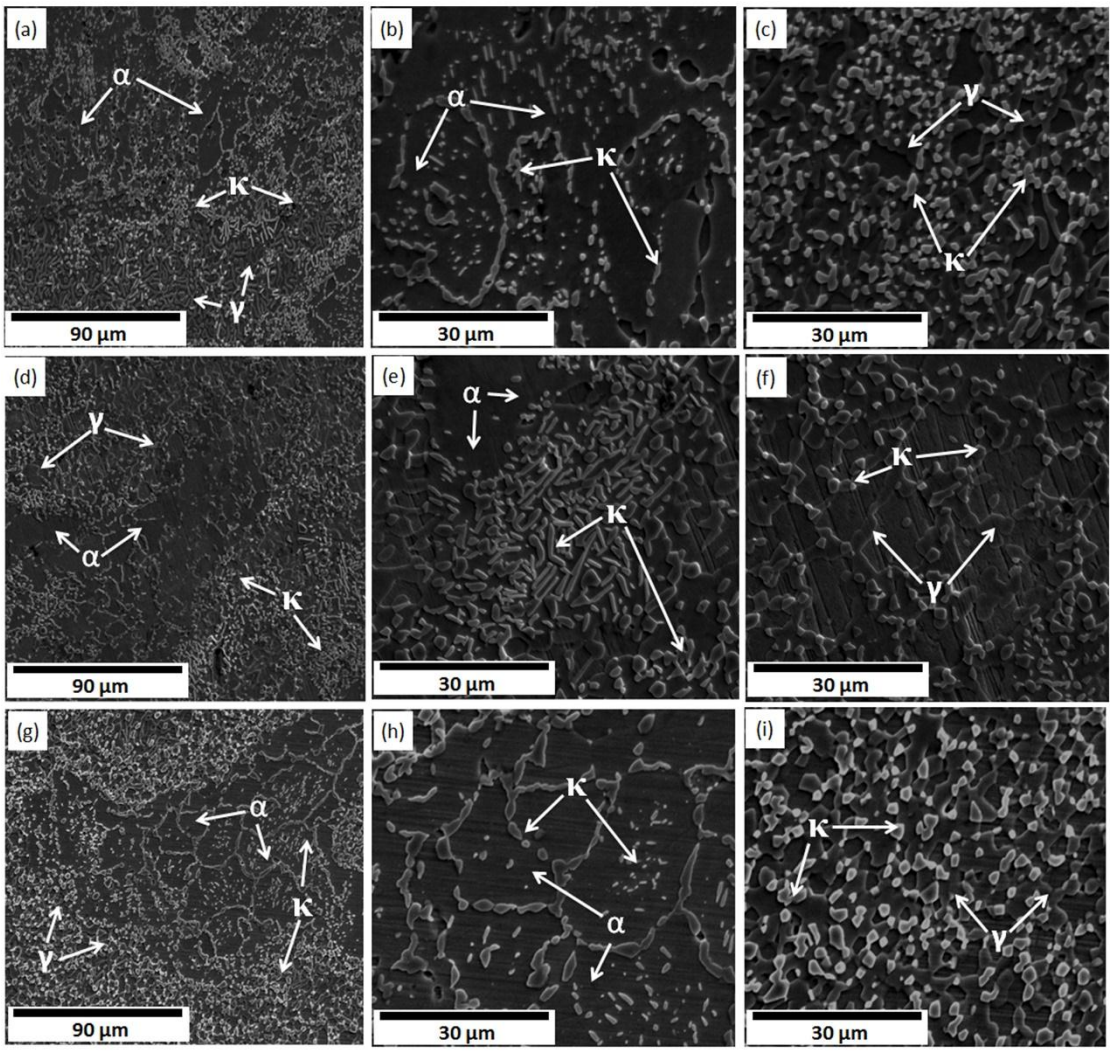


Figure 5.23: SEM micrographs of the (a-c) A5 with different magnifications, (d-f) A6 with different magnifications and (g-i) A7 with different magnifications, and they show that lamellar κ-carbides are transformed into spherical particles within austenite region and some boundary κ-carbide and needle -shaped κ-carbide start to precipitate in ferrite region at 700 ^{o}C for 6 to 100h.

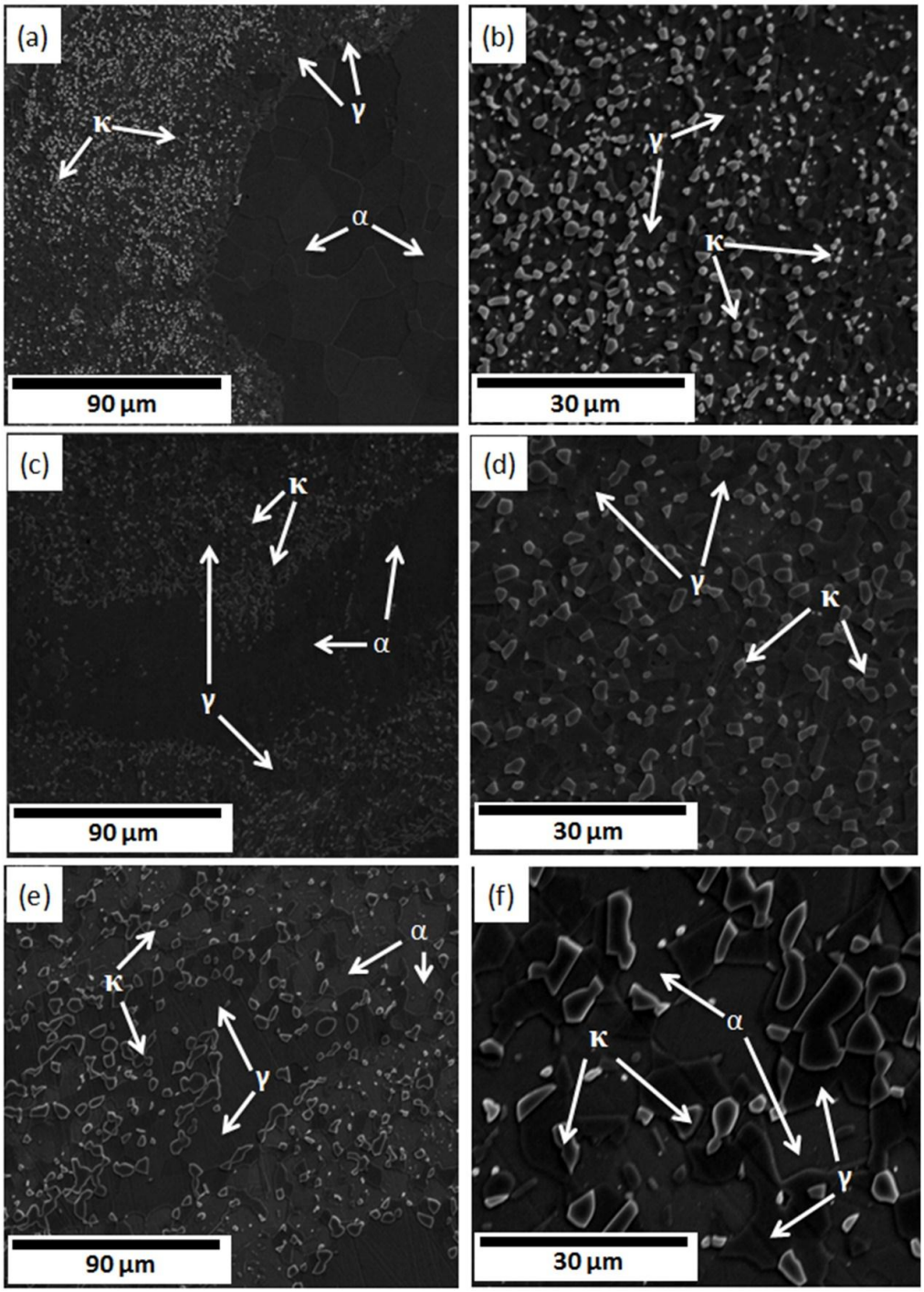


Figure 5.24: SEM micrographs of the (a-b) A8 with different magnification, (c-d) A9 with different magnification, (e-f) A10 with different magnification. They show that the spherical κ-carbide within the austenite region is growing continually and all κ-carbide in the ferrite region dissolves at 800 ^{o}C for 6 to 100h.

Both the size (based on the SEM micrographs of steel specimens above) and Vickers hardness of κ-carbide are plotted as a function of annealing time in 5.25.

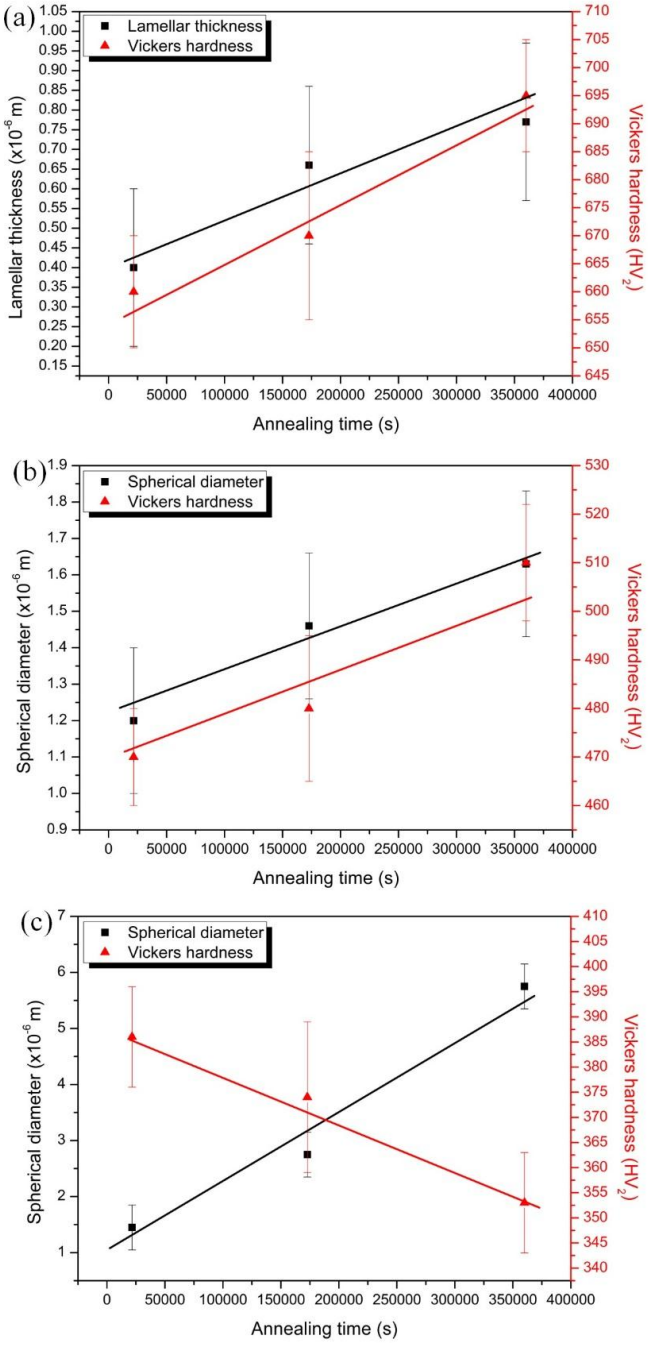


Figure 5.25: Vickers hardness of κ-carbide with (a) lamellar- shaped carbide in austenite at 600 ^{o}C for 6-100 h, (b) spherical- shaped carbide in austenite at 700 ^{o}C for 6-100 h and (c) spherical- shaped carbide in austenite at 800 ^{o}C for 6-100 h.

The lamellar thickness and hardness of κ-carbide increase by 52% and 5.8%, respectively. The specimens annealed at 600 ^{o}C and the annealing time increased from 6 to 100 h is shown in Figure 5.25a. Figure 5.25b presents the diameter of spherical κ-carbide. The thickness and hardness increased by 33% and 17%, respectively at 700 ^{o}C for treatments of 6 to100 h. However, most of κ-carbides in ferrite had disappeared in all the samples studied. The spherical κ-carbides in austenite coarsened significantly (1300%) with increasing annealing time (6-100 h) at 800 ^{o}C. This results in a reduction of the hardness by 9.3% (Figure 5.25c). This inversely proportional relationship between spherical κ-carbides size and Vickers hardness (Figure 5.25c) shows that the dissolution of spherical κ-carbides into the steel matrix occurs at 800 ^{o}C.

The effects of annealing temperature on the growth rate and hardness increase rate are shown in Figure 5.26. The growth rate of lamellar κ-carbide was determined to be about 1×10^{-12}m/s at 600 ^{o}C (A2. A3 and A4). The hardness increase rate was about 1×10^{-4} HV/s. Spherodization occurs at 700 ^{o}C (A5, A6 and A7) and all lamellar κ-carbide transformed into spherical κ-carbide. The growth rate of spherical κ-carbide diameter was determined to be about 1×10^{-12}m/s. The hardness value rate was 1×10^{-4} HV/s. At 800 ^{o}C (A8, A9 and A10), the growth rate of spherical κ-carbide was measured to be 10×10^{-11}m/s and the corresponding change rate of hardness values was -1×10^{-4} HV/s. It can be concluded that the growth rate of both lamellar κ-carbides and spherical κ-carbide at 600-700 ^{o}C is effectively prohibited in comparison with that of κ-carbide at 800 ^{o}C.

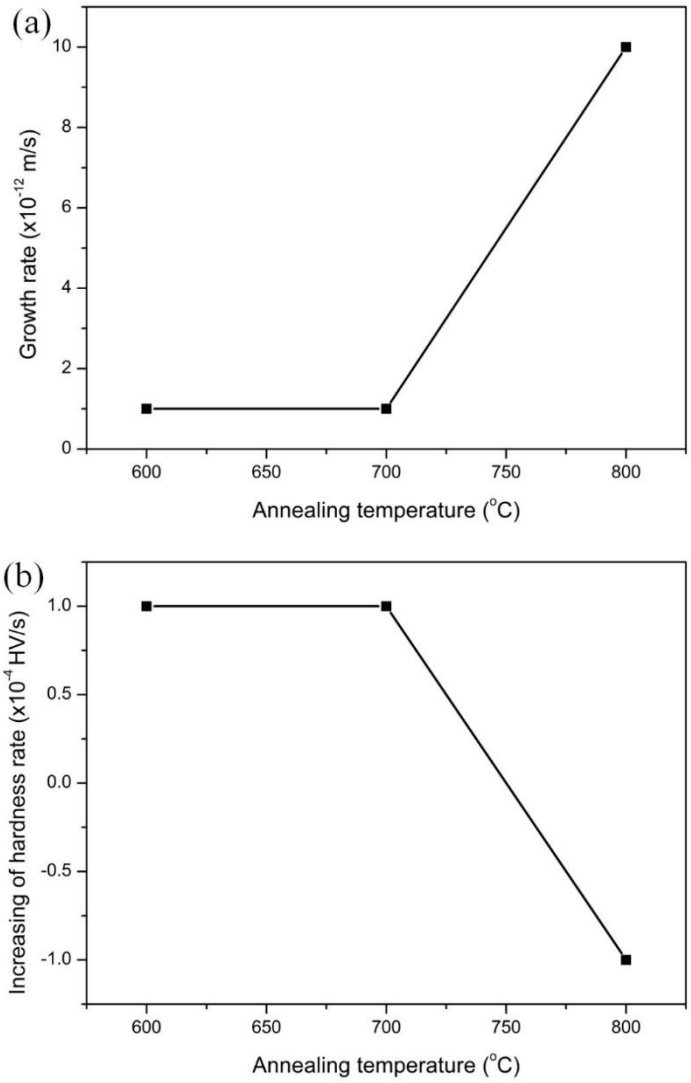


Figure 5.26: Diagrams showing (a) the growth rate of κ-carbide and (b) the increase in hardness rate as functions of temperature.

5.2.4 Discussion

The lightweight steel (Fe-26Mn-9Al-0.75C wt.%) basically contains three phases (austenite, ferrite and κ-carbides) with various sizes, volume fractions and morphologies, which affect the mechanical properties under different annealing temperature and time conditions. The

investigation of the precipitation behaviour of κ-carbides is particularly important for the fabrication of lightweight steel. This is due to the strong correlation between κ-carbides and mechanical properties. The κ-carbides are one of strengthening phases in lightweight steel and have a chemical composition of $(Fe,Mn)_3AlC$, which can be controlled by the segregation of alloying elements (C, Al and Mn) [190]. In stage 1 (A1 at 500 ^oC for 6h), two kinds of κ-carbides (lamellar κ-carbides and particulate κ-carbides) nucleate simultaneously in the austenite matrix and the ferrite matrix, respectively. The lamellar κ-carbides are frequently found at the grain boundaries of the austenite matrix (position 1 in Figure 5.14b) as a result of the decomposition of austenite ($\gamma \rightarrow \alpha + \kappa$). Alloying element behaviour (especially the C) has a dramatic effect. Thermo-Calc software was used to calculate the equilibrium concentrations of C, Al and Mn as a function of temperature from 500 to 1000 ^oC, as shown in Figure 5.27a-c. The ratio of phases (γ/α) of alloying elements as a function of temperature were obtained from Figure 5.27 and depicted in Figure 5.28.

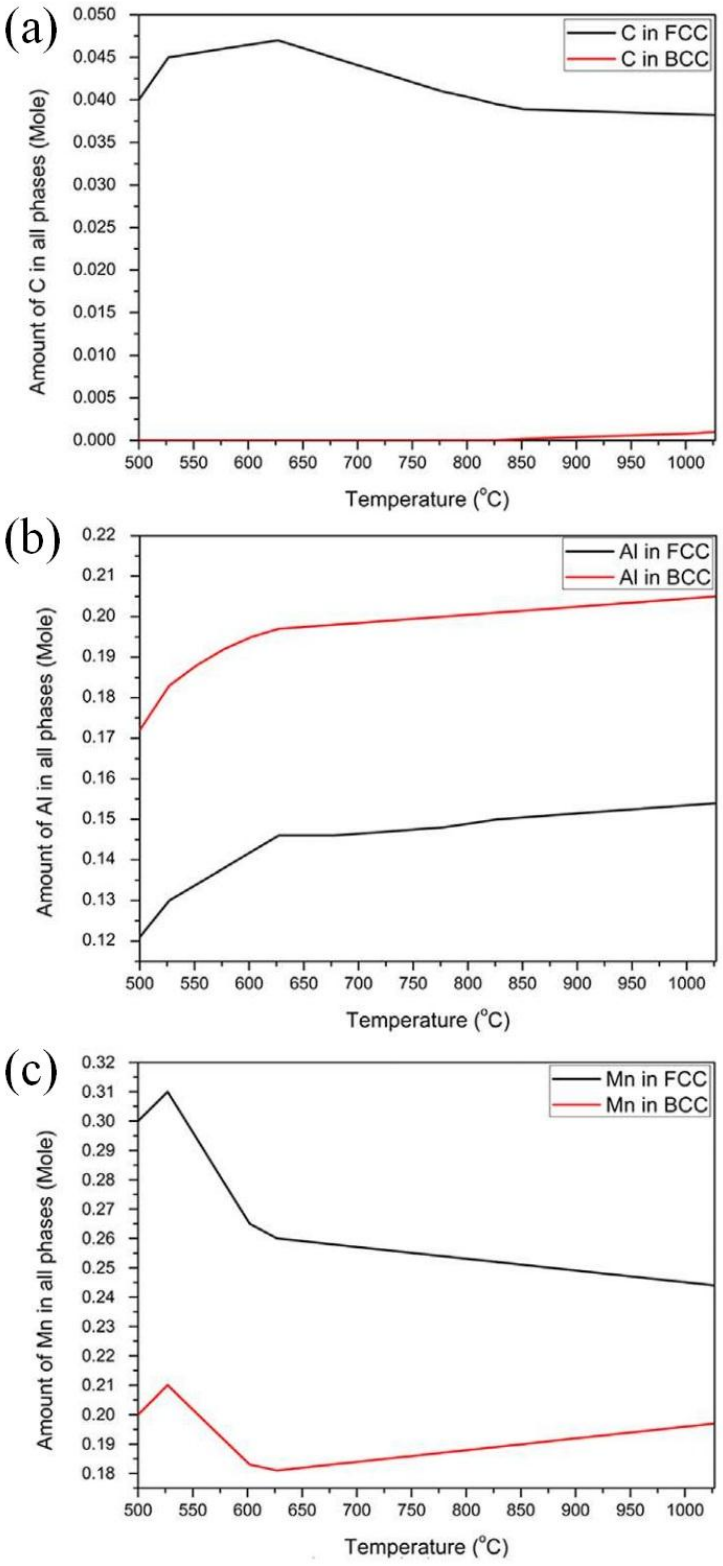


Figure 5.27: Diagrams showing calculated equilibrium concentration of (a) C, (b) Al and (c) Mn in ferrite and austenite using Thermo-Calc software.

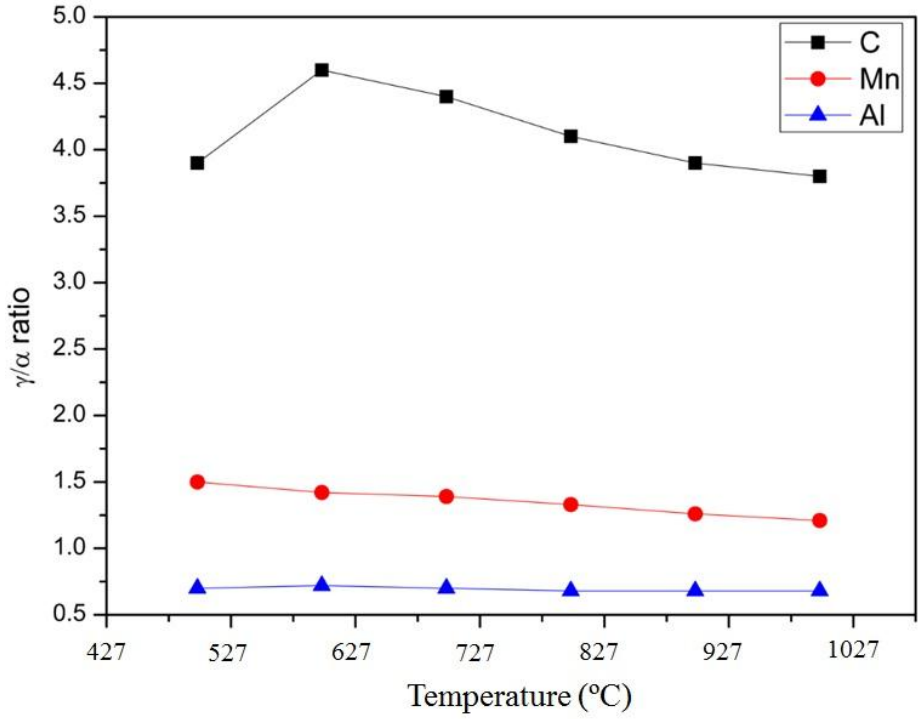


Figure 5.28: Diagram showing the relationship between the phase ratio, γ/α and temperature for C, Al and Mn in Fe-26Mn-9Al-0.75C steel.

It is noticed that the (γ/α) ratio of C is much higher than that of both Mn (γ/α=1.4-1.5) and Al (γ/α=0.5-0.6) from 500 to 1000 °C. This high (γ/α) ratio of C leads to a significant dissolution of C in austenite rather than in ferrite. Additionally, the diffusion behaviour of alloying elements play an important role in influencing the eutectoid decomposition, which can be generally expressed in the form of an Arrhenius relationships [198]:

$$D = A\exp(-\frac{Q}{RT}) \tag{5.1}$$

$$\ln(D) = \ln(A) + (-\frac{Q}{RT}) \tag{5.2}$$

where D refers to diffusion coefficient, A to frequency, Q to activation energy, T to absolute temperature and R=8.314 $J/(molK)$. For the temperature at 500-1000 °C, all three alloying

elements (C, Mn and Al) associated with the diffusion factors of Equation 5.2., as given in Table 5.3

Table 5.3: Factors related to diffusion coefficient of C, Mn and Al in steels.

Elements	Phase	Frequency, A (cm^2s^{-1})	Activation energy, Q (kJ mol^{-1})	Temperature range, T (K)	Reference
C	Austenite	0.23	148	700-1373	[33]
C	Ferrite	$6.2x10^{-3}$	80	700-1373	[33]
Mn	Austenite	0.16	261.7	1193-1553	[33]
Mn	Ferrite	0.35	219.8	1073-1173	[33]
Al	Ferrite	1.6	304.32	1048-1173	[36]

The diffusion coefficient as a function of temperature (based on the data in Table 5.3) is plotted in Figure 5.29.

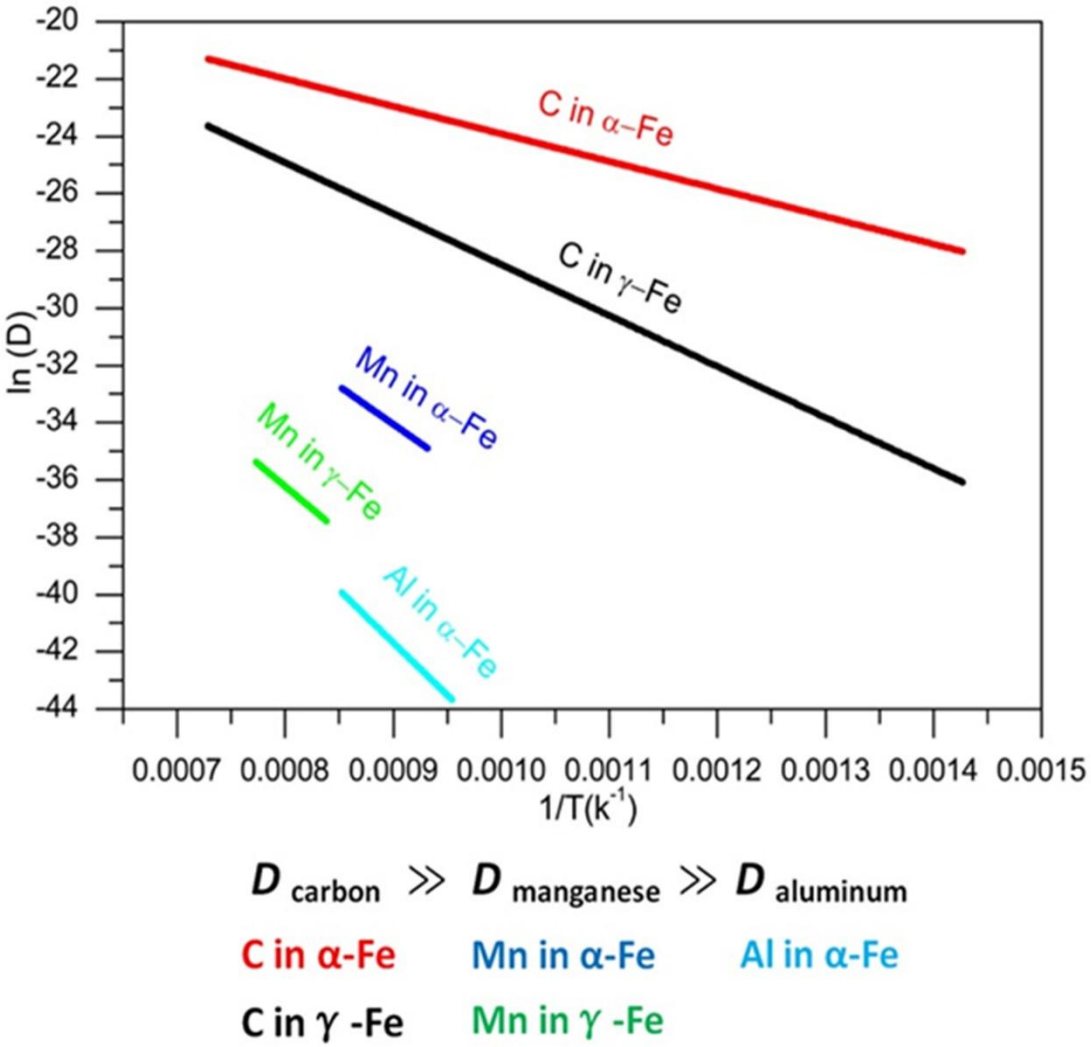


Figure 5.29: A schematic graph of diffusion coefficient as a function of temperature for C, Al and Mn in steels.

The diffusion coefficients of C in both ferrite and austenite are much higher than those of Al and Mn at 500-1000 ^{o}C. This is probably due to the atomic radius of the elements. C has an atomic radius 0.77 Å. Al and Mn have atomic radius 1.25 Å and 1.40 Å, respectively [1]. The combined effects of the higher (γ/α) ratio and a higher diffusion coefficient for C lead to an initiation of eutectoid decomposition in austenite. It can be seen that for position 3 in Figure

5.14d, a few κ-carbides (with sizes about 100 nm) are nucleated within the ferrite, which is attributed to the C diffusion from the neighbouring austenite.

In stage 2 (A2 at 600 ^{o}C for 6 h), more κ-carbides (up to 11.7%) are formed; this indicated that the eutectoid decomposition of austenite (which decreased from 74.8 to 28%) was significantly accelerated at 600 ^{o}C. A higher annealing temperature leads to both a higher (γ/α) ratio of C and a higher diffusion coefficient of C in austenite since this decomposition is related to the behaviour of alloying elements. As a result, the lamellar κ-carbides (with size about 0.4 μm) fully occupy the austenite matrix, as is shown in position 1 in Figure 5.15a. In addition, the percentage of lamellar κ-carbides in austenite can be roughly calculated to be 84% from image J in Figure 5.15c; this is significantly higher than that of particulate κ-carbides in ferrite (32%) in Figure 5.25d. This indicates that κ-carbides are easily and quickly formed in austenite, due to its specific, crystallographic structure. The κ-carbides are known to exhibit a perovskite structure, with a lattice constant in the range, 3.7-3.8 Å, which are similar to those for the austenite FCC structure. According to the TEM results in Figure 5.20, the lattice constant of ferrite, austenite and κ-carbides are determined to be 2.92, 3.62 and 3.75 Å, respectively. The lattice misfit (δ) between austenite and κ-carbides is calculated to be 3.47%; this shows the formation of the coherent, interface energy term (ΔG) between austenite and κ-carbides is relatively low. Consequently, more κ-carbides are formed in austenite rather than in ferrite. Annealing temperature and time would also be expected to have a great impact on the lamellar κ-carbides. It can be seen from Figure 5.25a, that slight increases in size are accompanied by increases in the hardness of lamellar κ-carbides. This can be explained by the decreasing of volume fraction of austenite at this temperature, which leads to an increase in the Mn contents which to stabilize it [214]. As a result, more Mn replaces the Fe to bond

with C which then form lamellar κ-carbides in austenite. These lamellar κ-carbides have a higher hardness because Mn-C bonds are stronger than those of Fe-C bonds.

The κ-carbides in position 1 and 2 are dramatically changed when the annealing temperature is increased up to 700 ^{o}C for 6 h for A5 in stage 3 (Figure 5.16a-d). For position 1 in Figure 5.16a, most of lamellar κ-carbides have transformed into spherical κ-carbides (with a diameter about 1.2 μm). This transformation is very similar to the spheridization of lamellar cementite in high-carbon, ferrite-pearlite steel. Thus the spheridization of lamellar κ-carbides in lightweight steels can be attributed to the reduction of surface free energy., The partial dissolution of lamellar κ-carbides also occurs in the austenite matrix, which can be directly proved by the variation of *d*-spacing of phases [231], as shown in Figure 5.30.

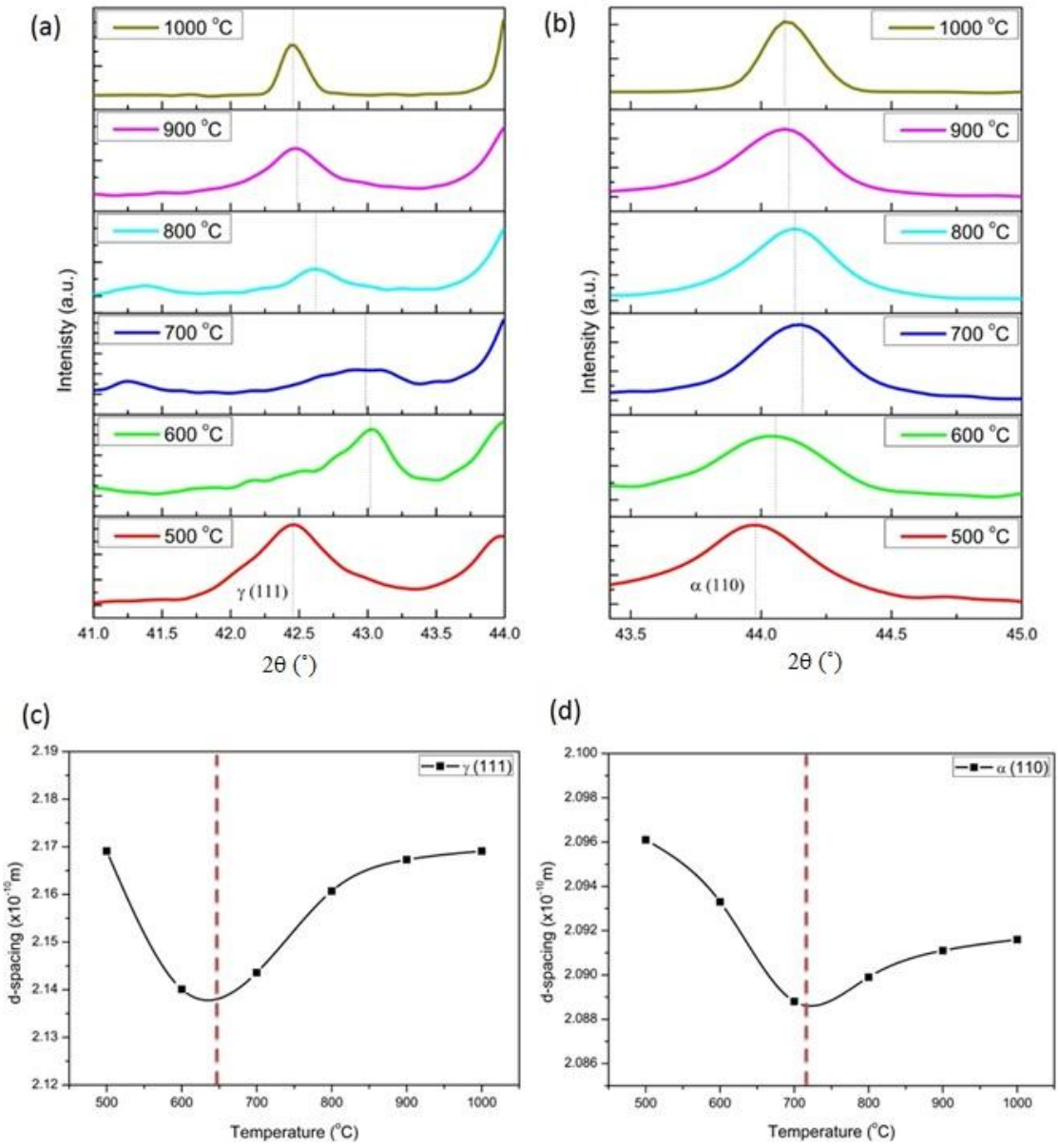


Figure 5.30: (a) XRD spectra of $(111)_\gamma$ peaks and (c) the *d*-spacing of $(111)_\gamma$ peaks as a function of temperature; (b) XRD spectra of $(110)_\alpha$ peaks and (d) the *d*-spacing of $(110)_\alpha$ peaks as a function of temperature. The red lines indicate the dissolution temperature of κ-carbides.

Figure 5.30a and c show that the *d*-spacing of $(111)_\gamma$ plane decreased from with increasing temperature between 500 and 645 ^oC. This reduction of *d*-spacing is associated with the

formation of lamellar κ-carbides in austenite because a lower value of the *d*-spacing for the $(111)_\gamma$ planes leads to increases in diffusion rate for the alloying elements (C, Mn, Al) in austenite. However, when the *d*-spacing starts to increase above 700 ^{o}C, the lamellar κ-carbides are partially dissolved. For the position 2 in Figure 5.16d, the κ-carbides were continually precipitated and then coarsened; the carbides were band- shaped for grain boundaries of ferrite and were needle- shaped in the grain interior of ferrite. This continually-increasing volume of κ-carbides within ferrite could be attributed to the partial dissolution of lamellar κ-carbides in austenite. As the lamellar κ-carbides dissolve into the austenite, more alloying elements will diffuse into neighbouring ferrite to form κ-carbides at 700 ^{o}C. Therefore, κ-carbides can nucleate and grow at the high -energy sites (such as the grain boundary and grain interior with defects). The *d*-spacing of the $(110)_\alpha$ plane (Figure 5.30b and d) provides direct evidence of κ-carbides precipitation behaviour in ferrite. The dissolution temperature for κ-carbides in ferrite is appromately 710 ^{o}C, which is much higher than that for κ-carbides in austenite (645 ^{o}C).

In the stage 4 (Figure 5.17), the annealing temperature is increased to 800 ^{o}C and last for 6h. A8 resulted in both a decrease in the volume fraction of κ-carbides and increased spheroidization of κ-carbide. This is attributed to the strong relationship which exists between diffusion and temperature. Higher temperatures lead to larger increases in the diffusion of alloying elements and thus promote the dissolution of κ-carbides [190]. Enhanced *d*-spacing of the phase also plays an important role in affecting the dissolution of κ-carbides. A larger *d*-spacing of phase indicates a higher capability to dissolve alloying elements in the phase and thus the phase has a greater ability to dissolve other phases. The dissolution rate of κ-carbides in ferrite was much faster at 800 ^{o}C. In comparison with dissolution rate of κ-carbides in

austenite. This was mainly attributed to the higher diffusion coefficient of C in ferrite (Figure 5.29).

Stage 5 shows the microstructure evolution of steel specimens (A11 and A12) annealing at 900-1000 ^{o}C for 6 h. It can be seen that all κ-carbides had completely dissolved and only a duplex mixture of austenite and ferrite remained in the steel matrix (Figure 5.18). These results are consistent with XRD and TEM results (Figure 5.12 and Figure 5.19).

The mechanical properties of steel specimens under annealing treatment were also analysed. The relationship between yield strength and hardness value has been established by Ashby, Jones and Tabor [220] and it can be expressed as the empirical equation below:

$$\tau_s = \frac{HV}{3} \tag{5.3}$$

The yield strength is equal twice the value of the stress according to the Tresca Criterion [220], as shown below:

$$2\tau_0 = \tau_s \tag{5.4}$$

Consequently, the hardness value is equal to 6-times the value of the stress:

$$6\tau_0 = HV \tag{5.5}$$

Since there is an inverse relationship between the strengthening effect and the spacing between secondary particles, a smaller spacing will lead to a higher stress (hardness) of the material [1]:

$$\tau_0 = \frac{HV}{6} = \frac{Gb}{\lambda} \tag{5.6}$$

where G is shear modulus, b is the magnitude of burger vector, λ is the spacing between secondary particles. Based on the precipitation hardening theory, the strengthening mechanisms induced by secondary particles can be divided into two types: one results from a dislocation cutting through particles and the other involves dislocations bowing around particles. The former type, indicates that the mechanical properties (hardness and stress) are proportional to the size of secondary particles (r), as expressed [1]:

$$\tau_0 = \frac{HV}{6} = \frac{\pi r}{bL}\gamma \tag{5.7}$$

where γ is the surface energy and L is the spacing between pinning points. The latter type will play an important role in influencing the strengthening mechanism when r exceeds a critical value ($r_{critical}$); the stress (hardness) is inversely proportional to r [1] in this case:

$$\tau_0 = \frac{HV}{6} = \frac{Gb}{L-2r} \tag{5.8}$$

On the basis of the above equations and Figure 5.26, it was predicted that the critical size of secondary particles is about 1.6 μm. This means that dislocation cutting becomes the dominant mechanism in strengthening steels when the size of precipitate is less than 1.6 μm. Conversely, the strengthening mechanism by the dislocation- bowing will become dominant when the size of precipitate is larger than 1.6 μm, which will weaken the steels.

5.2.5 Conclusion

The precipitation behaviour of κ-carbides has been systematically investigated in a Fe-26Mn-9Al-0.75C (wt.%) duplex, lightweight steel during annealing treatments of (500-1000 ^{o}C and

6-100 h). The following conclusions have been drawn from the thermodynamic calculations and experimental observations:

1. Isopleth phase diagram and non-equilibrium phase diagram of the steel at 500-1000 ^{o}C have been calculated by Thermo-Calc software and measured by XRD. These thermodynamically calculated results shows a difference from the XRD results.

2. The higher solubilities (γ/α ratio) and diffusion coefficients of alloying elements lead to the precipitation of κ-carbides in austenite rather than in ferrite.

3. The lower lattice misfit (δ) between austenite and κ-carbides results in a lower coherent interface energy and, in turn, easier and more rapid formation of κ-carbides in austenite.

4. The spheriodization of κ-carbides accompanied by partial dissolution in austenite was detected directly by XRD data (*d*-spacing). The variations in *d*-spacing also prove that the dissolution of temperature of κ-carbides in austenite is much lower than that in ferrite.

5. The mechanical properties of steel specimens can be effectively optimized by various annealing treatments when the size of κ-carbides is under 1.6 μm.

6. Experimental results show that the precipitation behaviour of κ-carbides is strongly dependent on the solubility and diffusion of alloying elements, the crystallographic structure and the *d*-spacing.

5.3 Electropulse-induced nanocrystallization of κ-carbide in duplex lightweight steels

5.3.1 Introduction

Lightweight Fe-Mn-Al-C quaternary steels have been developed and widely investigated in many research fields [190, 195, 196, 204–206, 212, 214–217, 230]. These steels have

outstanding properties, such as low density, an excellent combination of strength and plasticity, strong corrosion and oxidization resistance, compared with TWIP or TRIP steels [188, 190, 192, 196, 202, 204–206, 210, 214, 215, 232]. For instance, a tensile strength greater than 780 MPa and elongation of above 30 % can be achieved in these low- density, Fe-Mn-Al-C steels which make use of precipitation strengthening from the nano-sized κ-carbides ($(Fe,Mn)_3AlC$) [188]. These excellent mechanical properties are mainly achieved by manipulating the fraction, morphology, volume fraction and size distribution of κ-carbides within the steel matrix [188, 190, 204–206]. However, unlike other precipitates, the uncontrollable formation of lamellar κ-carbide bands in the ferrite matrix (from continuous cooling) frequently, induces crack- initiation and - propagation in these high-Al lightweight steels during rolling [194–196, 204–206, 214]. Thus, a method to suppress and retard the crack- formation during rolling is urgently required for the fabrication of high-performance, high-Al, lightweight steels.

The reduction of crack- formation in lightweight steels during the forming process has been tackled in previous studies through the precise control of heat treatments and through appropriate alloying element (e.g. Mn or C) additions. These methods effectively reduce the volume fraction of κ-carbide and alter the morphology of κ-carbide and thereby suppress cracking [195, 196].

It is proposed here that EPT could provide a more environmentally friendly, cheaper and efficient approach to reach the target (suppression of cracking). EPT is an instantaneous high-energy input technique which is widely used to modify the microstructures of many engineering metals and alloys by utilising their electrical properties [33–162]. EPT can effectively change the volume fraction of phases at the same time as promoting high electrical conductivity of the various phases during phase transformations or recrystallization

[68–133]. Therefore, the present study aims to investigate the possibility of utilizing EPT to produce ultrafine-grained microstructures and to promote high electrical conductivity of phases in Fe-Mn-Al-C steels.

For this purpose, two lightweight steels were selected as reference materials (Fe-26Mn-9Al-0.75C with lamellar κ-carbide and Fe-34Mn-9Al-0.65C with nano-ordered κ-carbide to investigate the effect Mn additions on both the morphology of κ-carbide and crack- formation during rolling. One of these specific lightweight steels (the one with the lower Mn content (26 wt.%)) containing lamellar κ-carbides was subsequently subjected to a pulsed electric current. With respect to the previously mentioned problem, this sub-chapter mainly aims to suppress crack- formation by manipulating the morphology and volume fraction of κ-carbide using EPT. The thermal and electric effects of EPT on lightweight steels are discussed from the viewpoint of the kinetic and thermodynamic aspects. The relevant experimental results (SEM, TEM, SADP and EBSD) are presented. The mechanisms are discussed for, when using a pulsed electric current to produce a desired microstructure, in order to suppress crack-formation in lightweight steels.

5.3.2 Materials and methods

The chemical compositions of the two steels used in present study are given in Table 5.4.

Table 5.4: Chemical compositions of two steels used in current experiment.

No.	Mn (wt.%)	Al (wt.%)	C (wt.%)	Fe (wt.%)
1	26	9	0.75	Balance
2	34	9	0.65	Balance

The thermo-mechanical processing for the steels have been described in Sections 5.1 and 5.2, as illustrated in Table 5.5.

Table 5.5: The thermomechanical processing parameters on the two steels.

Materials	Annealing temperature (°C)	Annealing time (h)
Fe-26Mn-9Al-0.75C	600	6
Fe-34Mn-9Al-0.65C	700	6

Two lightweight steel plates were first cold-rolled to 70% reduction via an auto-rolling machine in order to verify the possibility of using Mn additions o to increase the formability (suppression of cracking) for lightweight steels.

To verify the possibility of utilizing EPT to improve the formability (suppression of cracking) of lightweight steels, a specific lightweight- steel plate (Fe-26Mn-9Al-0.75C) was selected. In order to carry out comparisons of microstructure between with and without EPT for the Fe-26Mn-9Al-0.75C steel, a pulsed electric current generator was connected to the sample specimen edges (parallel to the rolling direction) and a pulsed electric current with frequency 1 Hz, duration 110 μs, voltage 2.5 kV and current density 1.92×10^{9} Am^{-2} are applied at room temperature. The overall experimental process of EPT on Fe-26Mn-9Al-0.75C steel were illustrated in Figure 5.31.

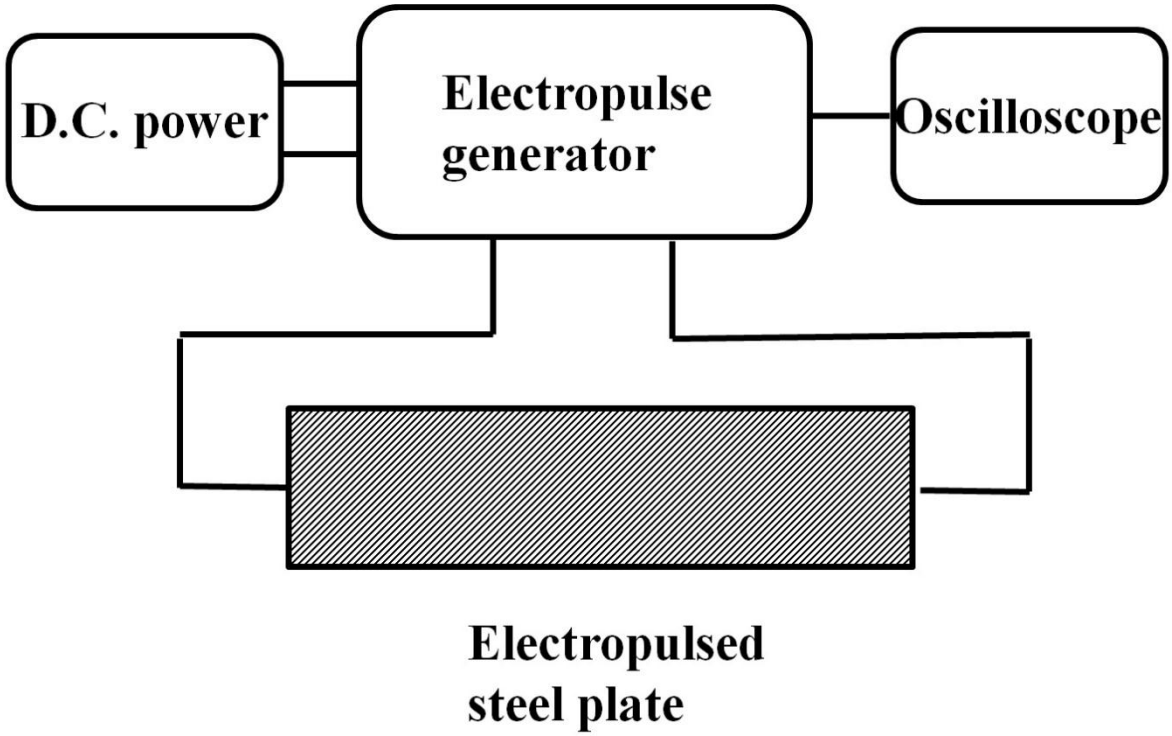


Figure 5.31: Schematic diagrams showing the EPT experiment.

Optical microscopy, high-resolution SEM (Leo) and TEM (2000FX) were used to observe the microstructure evolution of steel specimens (with and without EPT). For optical and SEM analysis, the sample specimens were ground, polished and etched in 2 wt. % Nital for 10s. For transmission electron microscopy (TEM) analysis, the specimens were mechanically polished to a thickness of 30 μm, punched to prepare disc- specimens (diameter 3 mm) using a copper disc cutter; these specimens were then jet polished to prepare thin foil specimens using a mixture solution of perchloric acid (10 %) and acetic acid (90 %) with 20 V at 15 ^{o}C. The thin foils were observed in a TEM (JEOL 2000FX, Japan) operated at an acceleration voltage of 200 kV. The grain size, after EPT, was then measured using Electron back-scattered diffraction (EBSD). The electrical conductivities of the steel specimens (with and without pulsed electric current) were measured using a Microhmmeter (DO5000 series).

5.3.3 Experimental results

The effects of Mn additions on crack formation in lightweight steels (Fe-26Mn-9Al-0.75C and Fe-34Mn-9Al-0.65C) after cold rolling were studied by optical micrographs shown in Figure 5.32. It was apparent that significant cracking was initiated and propagated within the Fe-26Mn-Al-0.75 steel plate. In contrast, there were no obvious signs of cracking occurring in the Fe-34Mn-9Al-0.65C steel plate. The formability of lightweight steels was improved by the Mn additions. High-resolution SEM, TEM and SADP were used to observe the microstructure evolution of steels with different Mn contents. Figure 5.32c and d show the SEM micrographs of Fe-26Mn-9Al-0.75C and Fe-34Mn-9Al-0.65C steels, respectively. It is obvious shows from Figure 5.32c that a huge amount of lamellar phases existing in the Fe-26Mn-9Al-0.75C steel matrix. These could be the sites where cracking is initiated. According to the TEM (Figure 5.32e) and SADP (Figure 5.32g) analysis, these lamellar phases are lamellar κ-carbide (with lattice parameter of 3.75 Å) which exhibit a typical N-W relationship ($(11\text{-}1)_\kappa$ // $(110)_\alpha$ and $[011]_\kappa$ // $[001]_\alpha$) with a ferrite matrix. SEM (Figure 5.32d), TEM (Figure 5.32f) and SADP (Figure 5.32h) confirm that a large number of nano-ordered, κ-carbide (with lattice parameters 3.75 Å) particles exist in the austenite matrix of another steel plate (Fe-34Mn-9Al-0.65C). The orientation relationship between κ-carbide and austenite is determined to be $(001)_\kappa$ // $(001)_\gamma$ and $[001]_\kappa$ // $[001]_\gamma$. The lattice mismatch between κ-carbide and steel matrix is probably the main reason why Mn additions are so effective in altering the formability of lightweight steels. For the Fe-26Mn-9Al-0.75C steel, the lattice mismatch between lamellar κ-carbide and ferrite is much greater than that between nano-ordered, κ-carbide and austenite (2.7%) in Fe-34Mn-9Al-0.65C steel. The larger mismatch results in a greater probability of generating cracks. These experimental results are

consistent with literature findings [195, 196]. Adding alloying elements such as Mn can change the morphology of κ-carbide in such a way that crack- formation is suppressed in lightweight steels during rolling.

In order to observe the κ-carbide stability under EPT for Fe-26Mn-Al-0.75C steel, numerous SEM micrographs and EBSD maps have been conducted, as shown in Figure 5.33. It was clearly shown that the lamellar κ-carbides are completely fragmented and refined into nano-sized spherical κ-carbides (250 nm) (Figure 5.33a and b). Figure 5.33c and d present EBSD maps for steel specimen with EPT and the average grain size of steel specimen was calculated to be 1.46 μm. EPT is an efficient method to affect the stability of κ-carbide as fabricating nanoscale κ-carbide (250 nm) and ultrafine grained microstructure (average 1.46 μm) for Fe-26Mn-9Al-0.75C steel.

Bright field TEM micrographs were used to further confirm the above-mentioned SEM results, as shown in Figure 5.34. EPT can significantly refine micro-scale lamellar κ-carbide (Figure Figure 5.34a and c) into nano-scale κ-carbide (Figure 5.34b and d). The orientation relationship between ferrite and κ-carbide remained the same as that in the N-W relationship for the steel specimen after EPT on the basis of SADP analysis (Figure 5.34e-h).

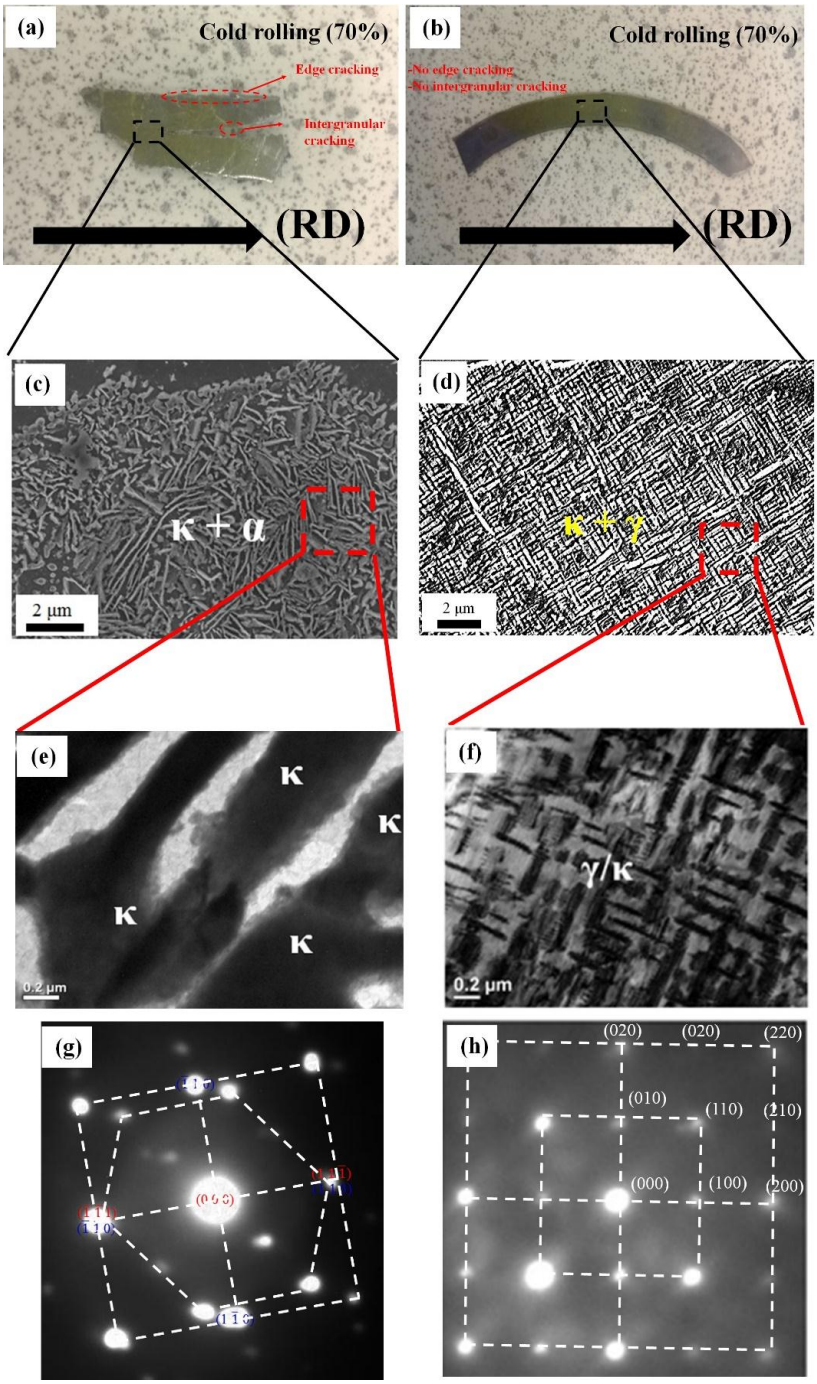


Figure 5.32: Optical micrographs of steel specimens (a) with 26Mn (b) with 34Mn, and their corresponding SEM images for microstructure (c) with 26Mn (d) with 34Mn. The TEM micrographs of (e) lamellar κ-carbide and (f) nano-ordered κ-carbide and their corresponding (g) SADP between lamellar κ-carbide and ferrite matrix, and (h) SADP between nano-ordered κ-carbide and austenite matrix.

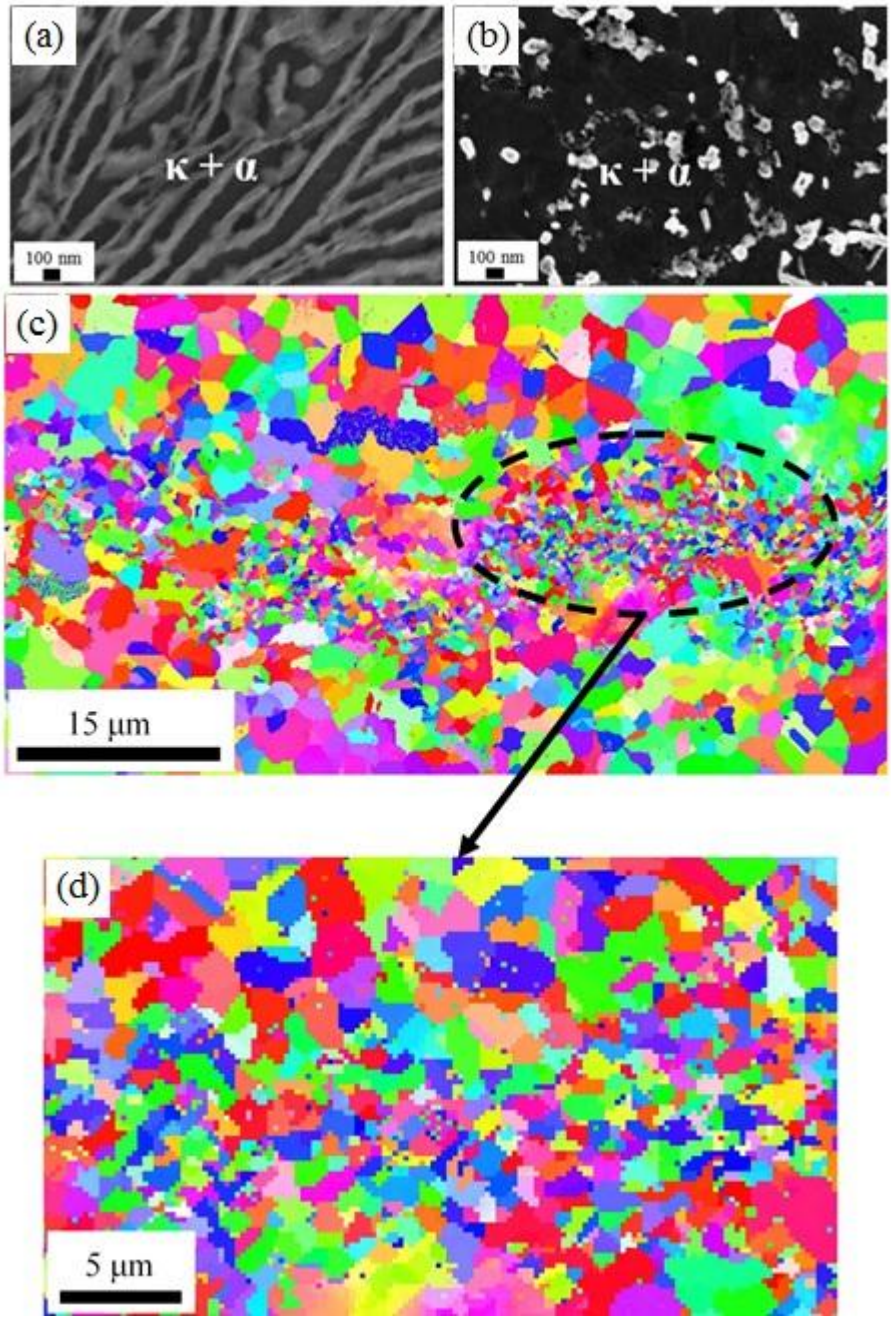


Figure 5.33: SEM micrographs of steel specimens (a) without and (b) with EPT. Most of lamellar κ-carbides are fragmented into nano-sized spherical κ-carbide particles. The EBSD maps of steel specimen with EPT (c-d) at different magnifications. The average grain size of steel specimen after EPT is appromately 1.46 μm.

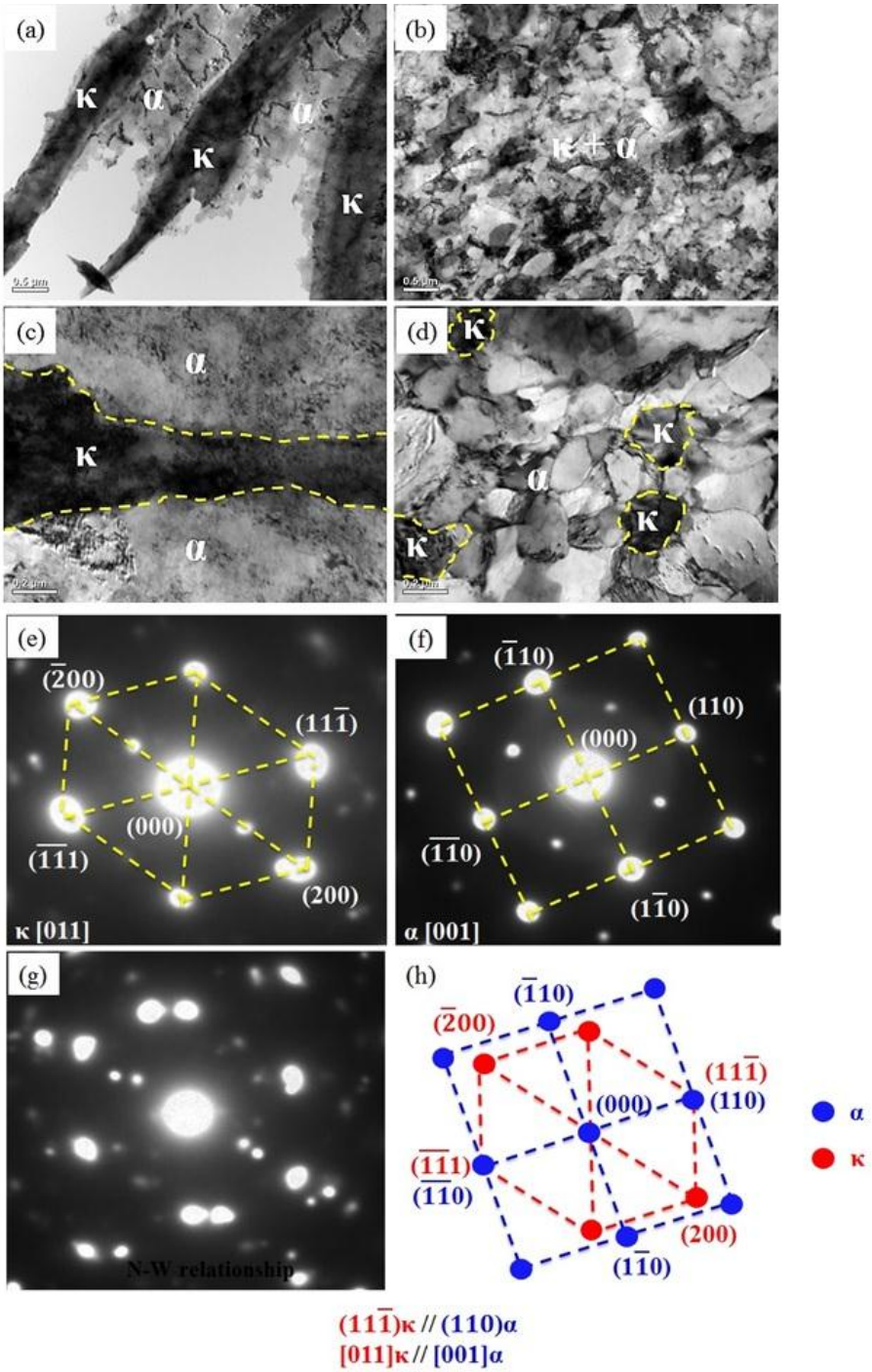


Figure 5.34: TEM bright images of steel samples (a and c) without EPT and (b and d) with EPT. Selected area diffraction patterns of (e) κ-carbide, (f) ferrite and (g and h) the N-W orientation relationship between κ-carbide and ferrite and its corresponding schematic diagram, respectively.

5.3.4 Discussion

It is well known that temperature plays an important role in affecting grain refinement during recrystallization. Usually, it is the pulsed electric current results in Ohmic heating (thermal effect) which impacts on the microstructural evolution in various alloys [68–133]. The temperature induced by a pulse of 110 μs in the electric current for this steel specimen is less than 200 ^{o}C. This is much lower than the recrystallization temperature 450-750 ^{o}C, Thus the observed grain refinement in this steel must be due to the non-thermal effect.

From the thermodynamic point of view, the Gibbs free energy associated with recrystallization process, (especially the nucleation rate of phases) is influenced by EPT [68–133]. For a steel containing dual phases (κ-carbide and ferrite), the geometric morphology of each phase has a great impact on the electrical property as shown in Figure 5.35 [99, 168]. The brown elongated κ-carbide has an electrical conductivity (σ_{κ}), which is lower than that of the green ferrite matrix (σ_{f}) due to the low carbon (less than 0.02 wt.%) and high iron fraction in ferrite phase at approximately 200 ^{o}C [99]. According to classical nucleation theory, the nucleation process takes place with EPT and can be expressed as [80, 92, 118, 128]:

$$I_e = I_r + \exp(\frac{-\Delta G_{elec}}{RT}) \tag{5.9}$$

where I_r is the nucleation rate of the cold-rolled steel sample without EPT, R is the Boltzmann constant, T is the absolute temperature, ΔG_{elec} is the additional Gibbs free energy induced by EPT. Among them, the ΔG_{elec} can be generally defined as [233]:

$$\Delta G_{elec} \propto j^2 \Delta v k \frac{(\alpha_B - \alpha_A)}{(\alpha_B + 2\alpha_A)} \tag{5.10}$$

where j is the current density, ΔV is the volume of particle, K is a material constant (K), α_B and α_A are the electrical conductivity of κ-carbide and ferrite, respectively. Since the electrical conductivity of κ-carbide is lower than that of ferrite ($\sigma_\kappa < \sigma_\alpha$), it can be predicted that $\Delta G_{elec} \leq 0$. Thus, the more negative the value of ΔG_{elec}, the more positive the value of the nucleation rate (I_e). Finally, grain refinement of the steel sample can be achieved by EPT through a reduction in the Gibbs free energy associated, with electric current.

Furthermore, the phase size and morphology can also affect the electrical conductivity of steel sample. In Figure 5.35a, the micro-sized, elongated κ-carbide and ferrite matrix reduces the electrical conductivity of the Fe-26Mn-9Al-0.75C steel. After passing a pulsed electric current, both the elongated κ-carbide and the ferrite matrix fragment from micro-scale particles to nano-scale, disconnected, circular grains occur. Hence to it is important create more flow routines forming along the pulsed sample, as displayed in Figure 5.35b [99, 168]. More flow routines make it easier the electric current to pass through the steel sample, which is strongly dependent on the specific property of EPT (i.e. electric-current treatment can significantly increase the electrical conductivity of sample by promoting more high-electrical-conductivity phases) [49–67]. Based on the analysis of SEM images (Figure 5.33a and b), pulsed electric current is unfavourable to promote the κ-carbide in this steel and hence to initiate the nano-crystallization of κ-carbide. The thermodynamics of steel associated with the pulsed electric current should be considered for the phase promotion phenomenon. The main hypothesis for the observed event may be developed from the fact that pulsed electric current can change the difference in Gibbs free energy of the steel system, via the difference

in electrical conductivity of each phase. The total Gibbs free energy (ΔG) of steel with pulsed electric current treatment can be generally expressed as [99, 168, 172]

$$\Delta G = \Delta G_{chem} + \Delta G_{surf} + \Delta G_{elec} \tag{5.11}$$

$$\Delta G_{elec} = \frac{\mu}{8\pi} \iint \frac{\vec{j}_b(r)\,\vec{j}_b(r') - \vec{j}_a(r)\,\vec{j}_a(r')}{\left|r - r'\right|} dr dr' \tag{5.12}$$

where ΔG_{chem} is the bulk phases chemical energy, ΔG_{surf} the interface free energy and ΔG_{elec} the pulsed electric current free energy, μ the magnetic permeability, r and r' are two different positions inside the sample specimen, $\vec{j}_b(r)$ and $\vec{j}_a(r)$ are current density without and with pulsed electric current, respectively. It can be predicted that $\Delta G_{elec} \le 0$ when $\vec{j}_b(r) \le \vec{j}_a(r)$. The sum of extra bulk chemical energy and interface free energy at equilibrium state will be increased as more ferrite phase promoted by pulsed electric current ($\Delta G_{chem} + \Delta G_{surf} = -\Delta G_{elec}$). Our measurements of the electrical conductivity for steel specimens without and with pulsed electric current are 6.37 × 10^6 S/m and 7.94 × 10^6 S/m, respectively. Thus the electrical conductivity of the specimen increased by 24.6 % when a pulsed electric current is applied. This is in good agreement with previous work for the non-thermal effect of a pulsed electric current on increasing the electrical conductivity of steel, obtained with theoretical predictions and experimental data. Thus, EPT enhances both the nucleation rate of a microstructure consisting of κ-carbide and ferrite, and promotes the formation of a high-electrical-conductivity phase (i.e. ferrite) in Fe-26Mn-9Al-0.75C steel.

The fragmentation of lamellar κ-carbide via EPT also benefits the formability of lightweight steel during rolling, as shown in Figure 5.35c and d. According to the literature, the long lamellar κ-carbides break to form micro-cracks; these cracks grow and coalesce with neighbouring micro-cracks to form large cracks, perpendicular to the force direction, which,

subsequently, lead to permanent fracture, as shown in Figure 5.35c. Conventionally, the crack formation during rolling can be prevented by temperature-control and by modifying the alloying element additions. EPT was used here to refine the long, lamellar κ-carbide to nano-scale particles and was found to be effective in suppressing and retarding crack formation, as shown in Figure 5.35d. Eventually, smaller amounts of smaller-sized κ-carbide can be fabricated by EPT in Fe-26Mn-9Al-0.75C steel and thereby, significantly improve the formability (suppressing crack- formation during rolling).

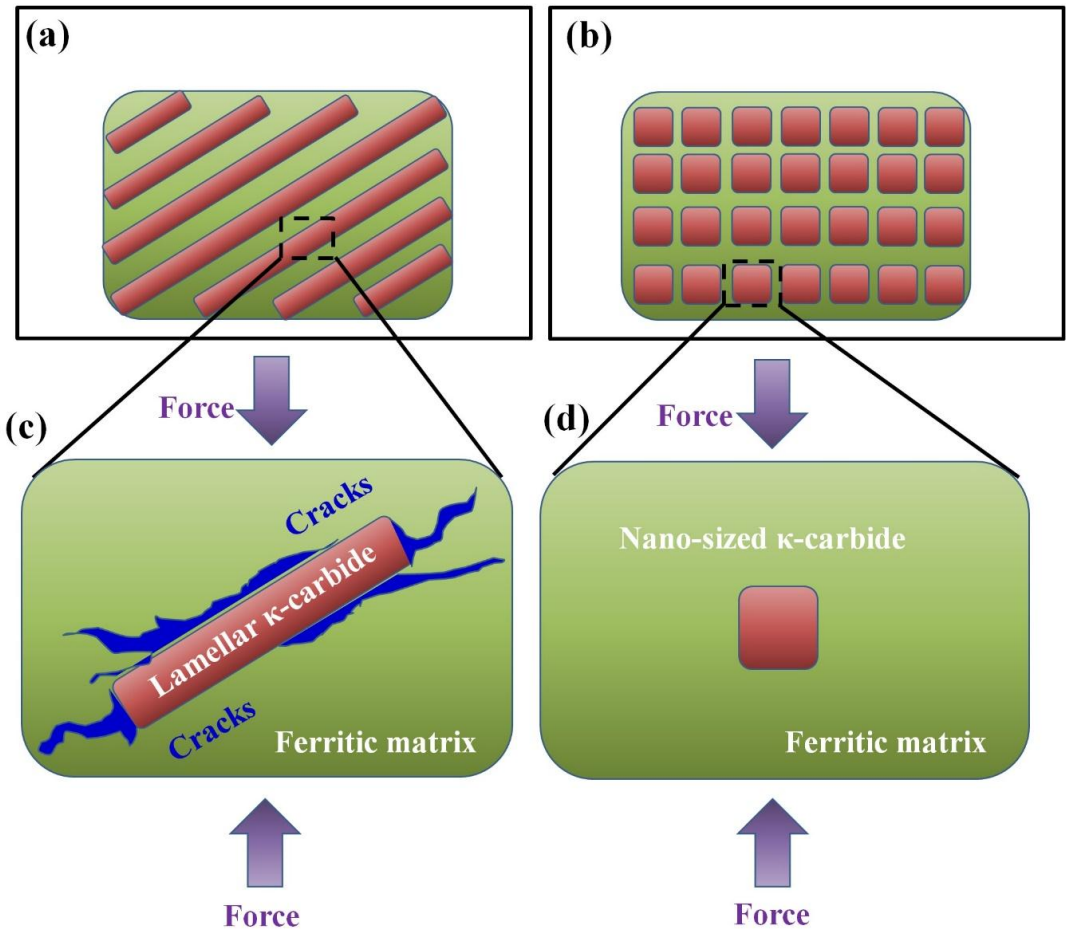


Figure 5.35: Schematic diagrams showing the effect of EPT on crack- formation: (a) and (c) microstructure evolution without EPT; and (b) and (d) microstructure evolution with EPT.

EPT can be a potential method to suppress and retard crack- formation effectively in Fe-26Mn-9Al-0.75C steel during rolling.

5.3.5 Conclusion

In summary, an ultrafine- grained microstructure, consisting of κ-carbide particles (with average grain size of 250 nm) and the ferrite matrix (with average grain size of 1.46 μm) was produced using EPT in a Fe-26Mn-9Al-0.75C lightweight steel.

(1) EPT is strongly dependent on the combination of thermal (Ohmic heating) and non-thermal effects (thermodynamic) of pulsed electric current.

(2) This ultrafine- grained, microstructure in lightweight steels is very beneficial to the formability (ie. in suppressing and retardating crack- formation) during rolling. This is mainly attributed to the increases in the nucleation rate and the promotion of the formation of phases with higher electrical conductivity.

(3) Microhmmeter measurements showed the electrical conductivity of sample increased from 6.37×10^6 S/m and 7.94×10^6 S/m after EPT, which is in good agreement with above-observed experimental results.

Chapter 6 Stability of martensite with pulsed electric current in dual-phase steels

6.1 Introduction

Dual-phase, ferritic-martensitic steels with favourable combinations of high strength and good ductility have attracted significant attention recently in the automotive industries [234–239]. Although, dual-phase steels have outstanding mechanical properties compared with conventional steels, it has been reported that isothermal tempering of martensite (involving slow heating rate, long holding time at tempering temperatures and slow cooling rate) such as welding frequently leads to softening of the heated-affected zone (HAZ) ie. a reduction in hardness for dual-phase steels [240–243].

In classical theory, the tempering of martensite occurs in four (temperature-related) stages during the softening process, as shown in Figure 6.1 [1].

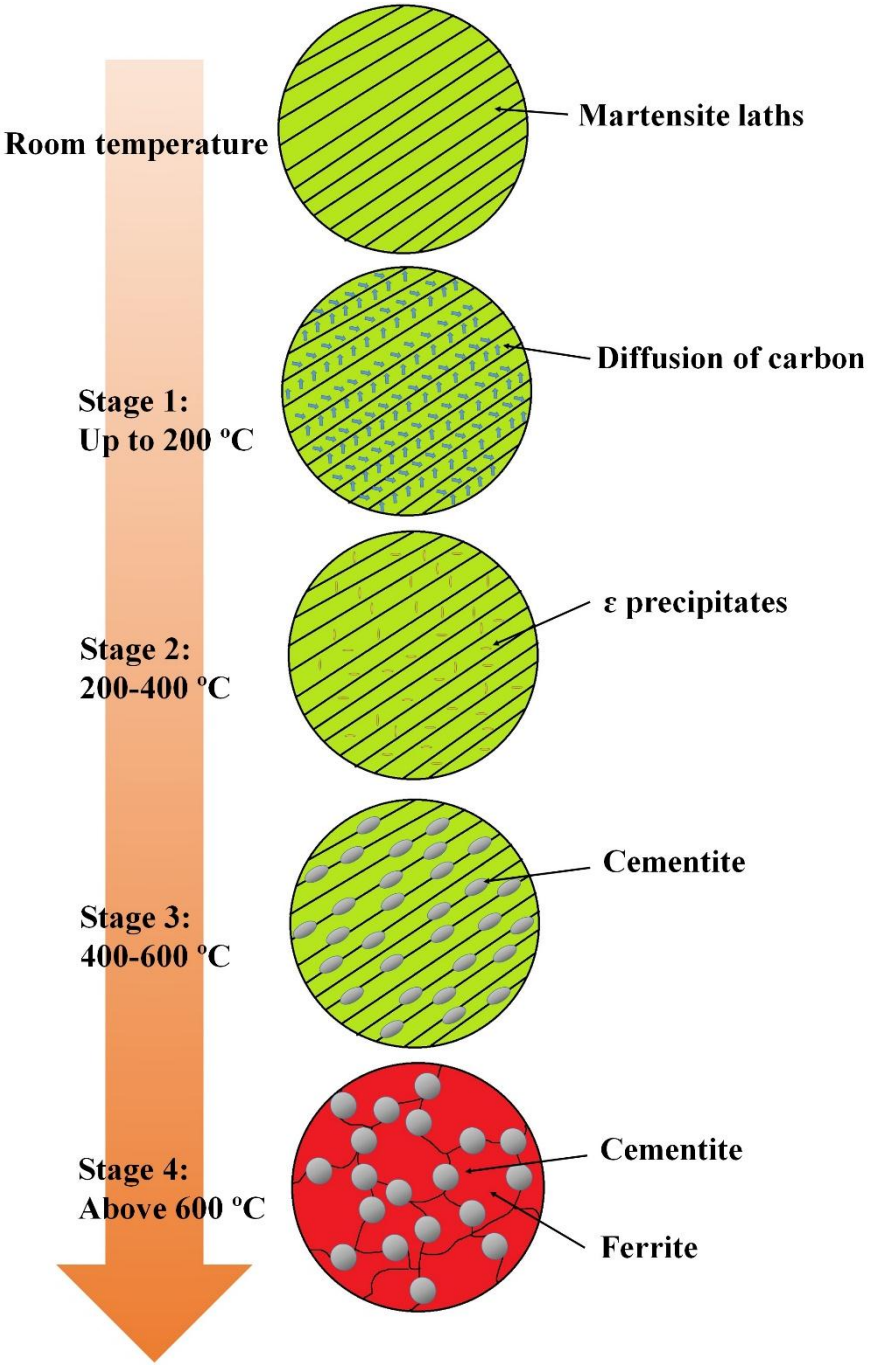


Figure 6.1: Four stages in the softening process for the tempering of martenite in dual-phase steels.

It can be clearly seen that the hardness of martensitic steels, just as dual-phase steels, are significantly affected by temperature. When the temperature is heated up to 200 ^{o}C at stage 1,

carbon atoms diffuse and segregate in some specific areas with a high-energy state, such as the grain boundaries [1]. During stage 2, various carbides, such as ε-carbide, start to precipitate in the range, 200-400 ^{o}C [1]. On further heating, cementite particles start to precipitate and spheroidize at grain boundaries at temperatures of 400-600 ^{o}C during stage 3 [1]. When the temperature exceeds 600 ^{o}C, most of the martensite laths havee recrystallized and the cementite particles have coarsened during stage 4 [1]. The total hardness of a dual-phase steel decreases continuously with increasing temperature during the four stages of softening process. However, this softening (induced by the tempering of martensite) frequently causes premature failure in the HAZ of dual-phase steels during welding due to concentration of high strain in the softened regions [244, 245]. Thus, many investigators have studied using non-isothermal tempering to replace isothermal tempering [242, 244, 246]. Non-isothermal tempering, as carried out in e.g. Nd:YAG laser welding involves a high heating rate, a short holding time at the tempering temperature and a high cooling rate. It was found that the non-isothermal tempering effectively decreases the softening by delaying stage 4 of the softening process [242]. Although, non-isothermal tempering is expected to decrease the hardness reduction, there is still a possibility of failure in the HAZ of dual-phase steel induced by softening still exist. Thus, a way of overcoming the softening during the tempering of martensite in welding, is still urgently required to aid the application of dual-phase steels in many industrial installations.

One possible way of solving the above-mentioned difficulties is to use electropulsing treatment (EPT), which is an instantaneous, high- energy- input method. Previous studies using EPT on polycrystalline metals and alloys have shown that grain refinement can be achieved through the combination of thermal and electric effects generated in EPT [68–133].

Thus, the mechanical properties (associated with the changing of grain size) can be subsequently modified by EPT.

Most publications on dual-phase steels have concentrated on the methods to decrease the reduction of hardness (softening) during tempering of martensite [241, 242, 247]. Consequently, the present work has been focused, principally, on designing a novel method to retard (or overcome) the softening during the tempering of martensite in dual-phase steels. The strengthening mechanism is responsible for the microstructural evolution under EPT observed in rapidly tempered specimens due to the thermal and electric effects. Consequently, in this study, the cold-rolled, dual-phase steels have been treated with EPT. The tensile mechanical behaviour and the Vickers hardness were measured along with the microstructural evolution, which was monitored using SEM and TEM. These methods provide direct evidence of grain refinement and data for the kinetics and thermodynamics model. This indicates improvements in all mechanical properties of the dual-phase steel, which has not been reported previously for steels of this grade.

6.2 Materials and methods

6.2.1 Material selections

The samples consisted of 1mm thick, dual-phase (DP600) steel plate containing ferrite and martensite phases (chemical composition (wt.%): 0.10C, 0.25Si, 1.70Mn, 0.02P, 0.005S, 0.040Al and balance Fe). The steel plate was cold rolled to the thickness of 0.5 mm through five passes and the total thickness reduction was 50 %.

6.2.2 Experimental setting

The steel samples were cut into dog-bone shape specimens (gauge length and width were 24.0 and 5.0 mm, respectively) with their longest edge perpendicular to the rolling direction, as shown in Figure 6.2.

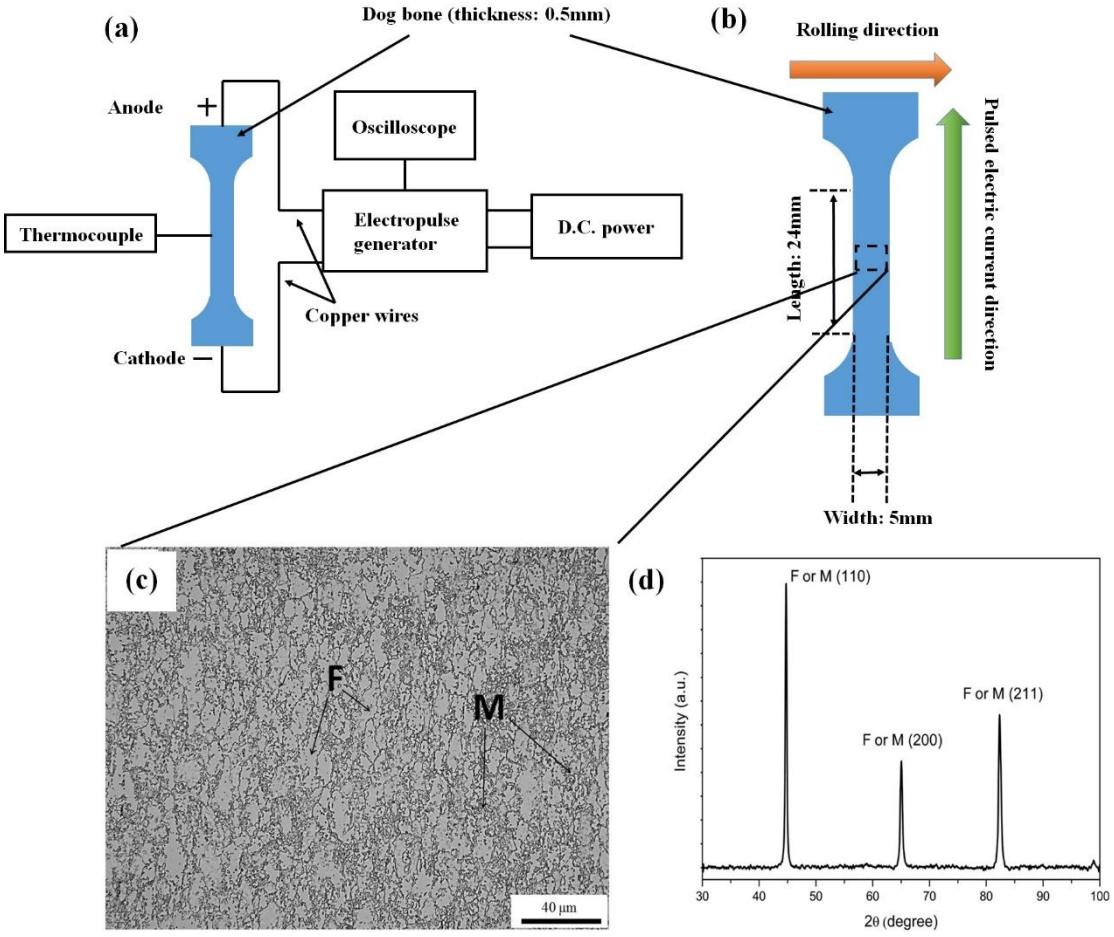


Figure 6.2: Schematic diagrams showing (a) experimental set-up of EPT; (b) a dog-bone shape sample (length: 24 mm; width: 5 mm and thickness: 0.5 mm); (c) an optical microstructure of dual-phase steel consisting of ferrite and martensite and (d) a XRD spectrum showing only body centred cubic phases (ferrite or martensite) exist in the steel sample. Note: F is ferrite and M is martensite.

In order to determine the effect of EPT, two sample groups were randomly selected and then one was subjected to EPT and the other used as a control (ie, without EPT). EPT was performed by converting the direct current into a pulsed electric current and the waveform of pulsed current was monitored, in-situ, by a digital storage oscilloscope, as shown in Figure 6.2. The pulsed electric current was applied by using, cathode and anode clips to clamp to the steel sample. The pulsed electric current was applied for a total duration of 110 μs and had a peak current density 5.67×10^{9} Am^{-2} at ambient temperature.

6.2.3 Microstructure observation

High-resolution scanning electron microscopy (SEM) and transmission electron microscopy (TEM) were to characterize the microstructure of treated samples and identify the phases present. The sample specimens were ground, polished and etched in 2 wt. % Nital for 5s for SEM analysis. The grain size and volume fraction of each phase were determined using, optical microscopy with ×100 magnification. This was used to randomly record the microstructure of samples at least 10 times and were then calculated by Image J. For TEM analysis, the specimens were mechanically polished to a thickness of 30 μm, punched to prepare disk specimens with a diameter of 3 mm by a copper disk cutter, and then jet polished to prepare thin foil specimens using a mixture solution of perchloric acid (10 %) and acetic acid (90 %) with 20 V at 15 ^{o}C.

6.2.4 Property measurement

The mechanical properties of the samples, before and after EPT, were measured at room temperature using a Zwick/Roell tensile test machine, with a strain rate 10^{-3} s^{-1}. The Software test Xpert II was used to fit and derive the yield stress (0.2% proof stress) and the elongation. A micro compact, hardness test machine (Zwick 3103 IRHD) with 10 kg load was used to measure the hardness value of samples. The electrical resistance of the samples (with and without EPT) was measured using a micro-ohmmeter (DO5000 series) at room temperature.

6.3 Results

6.3.1 Effects of EPT on microstructure evolutions

The optical microstructure of the cold-rolled steel specimen and its XRD spectrum are shown in Figure 6.2c and d, respectively. It clearly shows the presence of only two phases. The martensite phase (black regions) is randomly distributed along the grain boundary of the ferrite matrix (grey regions). The volume fraction of ferrite and martensite were calculated to be 63.4 % and 36.6 %, respectively from Image J. It was found that, after applying EPT, the martensite laths were significantly altered without changing the portion of the two regions, as shown in SEM micrographs (Figure 6.3).

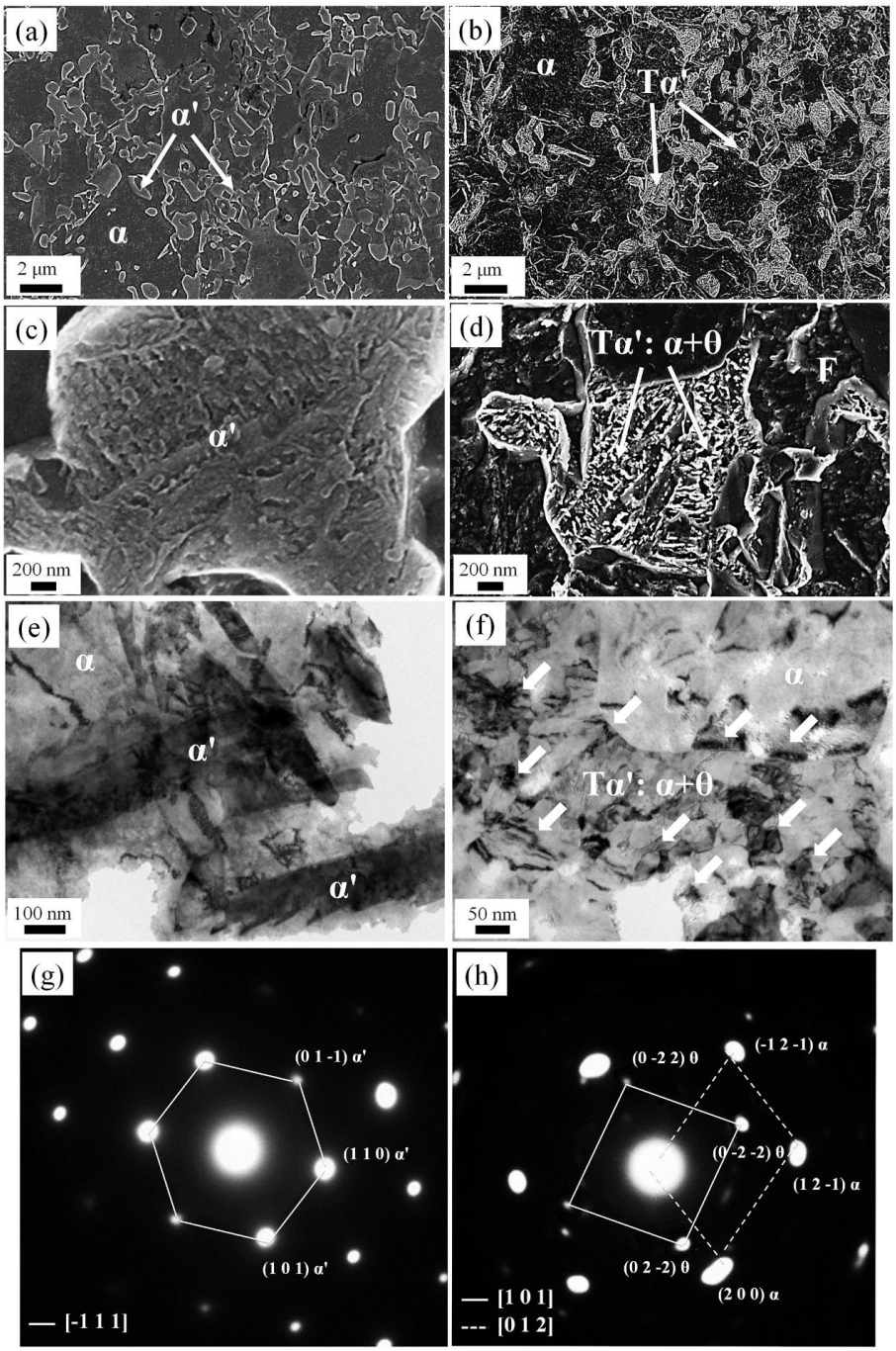


Figure 6.3: SEM images of steel samples (a and c) without EPT at different magnifications, (b and d) with EPT at different magnifications; TEM bright images of steel samples (e) without EPT and (f) with EPT; selected area diffraction pattern (SADP) for (g) martensite laths and (h) ferrite grains with cementite particle. Note: α' is martensite, Tα'(α+θ) is tempering martensite and α is ferrite.

Direct evidence of refinement can be clearly observed in martensitic regions (from micro-scale laths to nano-scale particles) in Figure 6.3. TEM observations and selected area diffraction patterns (SADP) have been conducted in order to observe the microstructure of the samples (with and without EPT) and to detail and identify the nature of the nano-particles. The bright field images of the morphologies of the martensite laths and the corresponding SADP, for the sample without EPT (Figure 6.3e and g, respectively). After EPT, a large number of nano-particles with average size 48±8 nm were found around the grain boundary of the ferrite (indicated by arrows in Figure 6.3f) and SADP confirmed that these nano-particles were cementite (Figure 6.3h). These nano-sized cementite particles have an orientation relationship ($[012]_{\alpha}$ // $[101]_{\theta}$) with the ferrite matrix [242]. In addition, the original martensite laths (Figure 6.3e) were partially decomposed into ultra-fine-grained ferrite with a size about 78±13 nm (Figure 6.3f) after applying EPT.

6.3.2 Effects of EPT on mechanical properties

Standard stress-strain curves of samples (without and with EPT) were measured and are plotted in Figure 6.4. It was found that EPT increased significantly both the yield stress and ultimate tensile strength of the steel sample whereas the elongation was only slightly affected by EPT (see Table 6.1). The Vickers hardness of samples was increased from 301±8 HV to 364±12 HV after EPT. The above-mentioned results indicate that EPT has a positive effect in the quest to optimize the mechanical properties.

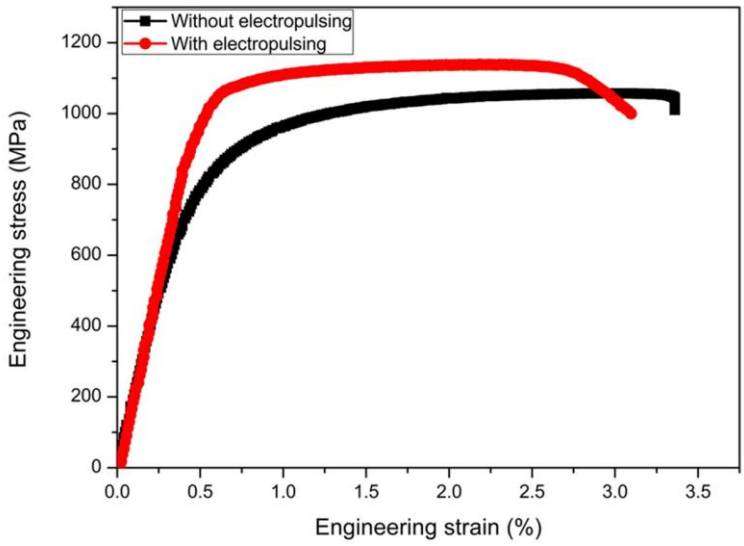


Figure 6.4: Diagram showing typical tensile engineering stress-strain curves of dual-phase steel samples (with and without EPT).

Table 6.1: Mechanical properties (ie. yield stress, UTS and elongation) of the steel samples (without and with EPT).

	Without EPT	With EPT	Increase by %
Yield stress (MPa)	773.26	1074.66	+38.98
UTS (MPa)	1034.25	1126.33	+8.90
Elongation (%)	3.31	3.12	-5.74

6.4 Discussion

6.4.1 Thermal effect of EPT

In general, the effects of EPT on microstructure evolution of polycrystalline metals and alloys can be divided into two types, namely the thermal and electric effects [99, 168, 172]. For the thermal effect of EPT, the temperature increase induced by joule heating can be expressed as $\Delta T = j^2 \Delta t \rho / C_p d$ [99, 168], where j the current density (5.67×10^9 A/m^2), ρ is the electrical resistivity of the steel sample (9.64×10^{-7} Ωm), Δt is the pulse duration (110 μs), C_p is the specific heat of steel sample (450 J/kg K) and d is the density of steel sample (7.9×10^3 kg/m^3). The temperature increase resulting from EPT is calculated to be about 685 ^{o}C, which corresponds to stage 4 in the softening process, as can be seen in Figure 6.5a.

A dramatic softening effect (reduction in hardness) occurs in dual-phase steel at stage 4 during the isothermal tempering of martensite, due to the coarsening of cementite and the decomposition of martensite (replaced by ferrite) [1, 242]. For example, The hardness of as-received, dual-phase steels decreased from (301±8 HV) to (190±3 HV) and (179±1 HV) with isothermal tempering at around 690 ^{o}C, for periods of (300s) and (5400s) , respectively [242], as shown in Figure 5.5b. Even if the non-isothermal tempering of martensite can only be delayed to stage 4 of the softening process the process will be successful. It retards the reduction of hardness from 301±8 HV to 269±7 HV [7]. However, our experiment shows the softening process was inhibited by the tempering of martensite in dual-phase steels under EPT. The Vickers hardness of steel sample with EPT was 364±12 HV, (cf 301 HV) an increase of 20.9 % over that of the steel sample without EPT. Furthermore, standard stress-strain curves for samples, with and without EPT, are shown in Figure 6.4. The yield stress for without EPT and with EPT, samples were recorded as from 773.26 MPa to 1074.66 MPa. This indicates that EPT strengthens the tempering of martensite during stage 4 of the

softening process in dual-phase steels, which cannot be interpreted on the basis of the thermal effect of EPT alone.

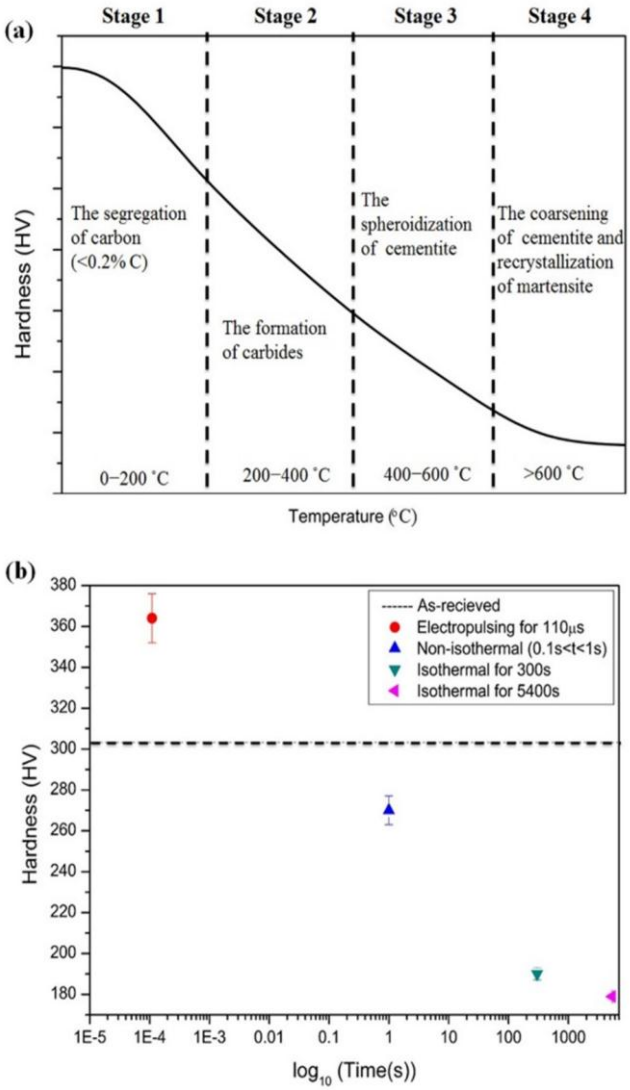


Figure 6.5: Diagrams showing a typical softening process contains four stages for the hardness of Fe-C martensitic steel tempered 1h at 100-700 ^{o}C and (b) the hardness of dual-phase steels tempered at about 700 ^{o}C for 110 μs (EPT), 0.1s<t<1 s (non-isothermal tempering), 300s (isothermal tempering) and 5400s (isothermal tempering), respectively [242].

6.4.2 Electric effect of EPT

Grain refinement is an effective method of improving the mechanical properties (such as Vickers hardness and yield stress, based on the Hall-Petch relationship) of polycrystalline metals and alloys. The relationship between stress and hardness is [26-28] is well known:

$$3\sigma_y = H_v \tag{6.1}$$

where σ_y is yield stress and H_v is the Vickers hardness. The yield stress and hardness can be expressed empirically as:

$$\sigma_y = \sigma_0 + k_y d^{-1/2} \tag{6.2}$$

$$H_y = H_0 + k_H d^{-1/2} \tag{6.3}$$

where σ_0 and H_0 are friction stress constants for tensile and hardness measurement, respectively, k_y and k_H are the unpinning parameters (breaking away of dislocation from interstitial sites) during tensile and hardness measurements, respectively; d is the grain size.

According to above-mentioned equations, the mechanical properties (i.e. yield stress and hardness) of dual-phase steels are strongly dependent to the grain size. This may be used to interpret the abnormal effect of EPT on the tempering of martensite in dual-phase steels. The microstructural characterization and its associated mechanical property data are in agreement with the yield stress and Vickers hardness data for the steel sample; these properties show significant improvement during the tempering of martensite under EPT which is associated with the formation of ultrafine-grained ferrite with nano-cementite particles. This strengthening mechanism induced by EPT is completely different from the softening mechanisms of isothermal or non-isothermal tempering [241, 242, 244]. This improvement of

mechanical properties associated with grain refinement can be analysed by two aspects of the electric effects of EPT: namely, kinetic and thermodynamic effects.

6.4.2.1 Kinetic effects of electric current

Cold working can effectively increase the dislocation density around the boundaries of martensite laths [248] in strain- free dual-phase steel samples, as shown in Figure 6.6a. From the kinetic viewpoint, it is well known that EPT has a significant effect on the dislocation migration behaviour (i.e. intersection and annihilation of dislocations) in cold-formed materials [173]. This is due to the electron wind force generated by EPT, which can scatter unevenly around dislocations and which, subsequently, reduces the kinetics barrier between two neighbour dislocations [99, 168]. Therefore, the mobility of dislocations can be enhanced, which can be expressed as [33]:

$$J = \frac{2NeZ^{*}D\rho j_{m} f \tau_{p}}{kT} \tag{5.4}$$

where ρ is the electrical resistivity of steel sample, f is the frequency of EPT, j_m is the current density of EPT, τ_p is the duration of EPT, J is the additional atomic diffusion flux, N is the density of atoms, Z^* is effective valence of the Fe ion (+3), e is the charge on an electron, K is the Boltzmann constant and T is the absolute temperature. From Equation 5.4, it can be clearly seen that the current density of EPT is proportional to the atomic diffusion flux. This proportional relationship indicate that EPT greatly increases the probability of intersection and annihilation of the dislocation, as shown in Figure 6.6b. Secondary particles, such as cementite, generally, nucleate at the intersection site of two partial dislocations at high

temperature. Thus EPT can promote a large number of nano-cementite particles within tempered martensite regions, as can be seen in Figure 6.6c.

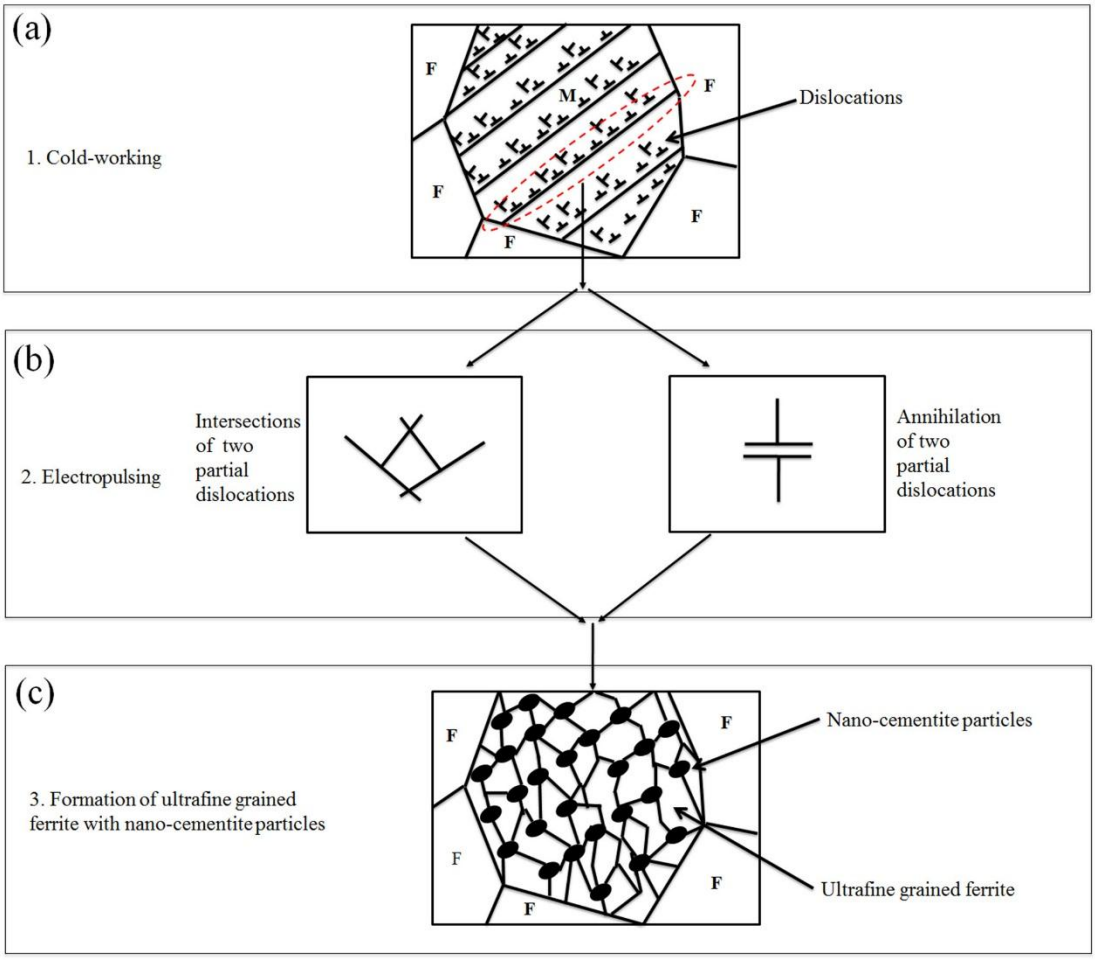


Figure 6.6: Diagrams showing (a) the microstructural evolution of dislocations in cold-formed steel sample, (b) the effect of EPT on intersection and annihilation of two partial dislocations and (c) the formation of ultrafine-grained ferrite with nano-cementite particles after EPT.

6.4.2.2 Thermodynamic of electric current

Since the temperature induced by EPT is about 685 ^{o}C, most martensite laths decomposed instantaneously to cementite and ferrite at this temperature range [241, 242, 244]. From the thermodynamic point of view, the Gibbs free energy associated with the recrystallization process, especially the nucleation rate of ferrite can be influenced by EPT [68–133]. According to classical nucleation theory, when EPT is applied, the nucleation rate for ferrite, can be expressed as [80, 92, 118, 128]:

$$I_e = I_r \exp(\frac{-\Delta G_{elec}}{RT}) \tag{6.4}$$

where I_r is the nucleation rate of the cold-rolled steel sample without EPT, R is the Boltzmann constant, T is the absolute temperature, ΔG_{elec} is the additional Gibbs free energy induced by EPT. The ΔG_{elec} can be, generally, defined as [233]:

$$\Delta G_{elec} \propto j^2 \Delta v K \frac{(\alpha_B - \alpha_A)}{(\alpha_B + 2\alpha_A)} \tag{6.5}$$

where j is the current density, ΔV is the volume of austenite particle, K is a material constant (K), α_B and α_A are the electrical conductivity of cementite and ferrite, respectively. It is well known that the electrical conductivity of the ferrite phase is higher than that of cementite in steels ($\sigma_\theta < \sigma_\alpha$). It can be predicted that $\Delta G_{elec} \leq 0$. Thus the more negative the value of ΔG_{elec} the greater (ie more positive) the value of nucleation rate (I_e). Simultaneously, dislocations ,as one of the common defects, have a negative effect on the electrical conductivity of a steel sample [99, 168]. Since the EPT enhances the probability of annihilation of dislocations; this will result in higher electrical conductivity of the steel sample due to the fewer dislocations after EPT. Our measurements indicate that the electrical conductivity for the steel samples, without and with, EPT are 1.04×10^6 Ω·m and 1.47×10^6 Ω·m, respectively. The electrical conductivity of the specimen is increased by 41.4 % with

EPT. Thus, EPT can enhance the nucleation rate of ferrite and effectively retard the growth rate of ferrite during recrystallization. Eventually, ultrafine-grained ferrite matrix within tempered martensite regions are produced by using EPT.

6.4.2.3 EPT on mechanical properties

All mechanical properties of dual-phase steels (namely yield stress, ultimate tensile stress and hardness) were all significantly increased EPT without losing elongation; this was mainly attributed to the formation of ultrafine-grained ferrite with nano-cementite particles. From the kinetic and thermodynamic aspects of EPT, the microstructure evolution can be due to various mechanisms (such as dislocation- migration and electrical conductivity changes, associated with nucleation rate during recrystallization). These experimental results and theoretical analysis, indicate that EPT is a potential candidate to retard (or even to recover) the softening problems encountered in the tempering of martensite in comparison during isothermal and non-isothermal tempering.

6.5 Conclusions

Electropulse-tempering can effectively strengthen the tempering of martensite by forming ultrafine-grained ferrite with nano-cementite particles. This is mainly attributed to the accelerated dislocation migration (kinetic) and to the enhanced nucleation rate of ferrite during recrystallization (thermodynamic) by EPT. Therefore, it is possible to use such phenomena to recover the softening which occurs in tempering of martensite in dual-phase steels; thus, the thermal and electric effects of EPT are more effective than isothermal or non-isothermal tempering in dealing with softening.

Chapter 7 Conclusion

The work carried out in this investigation covers a number of different problems which can be traced to the stability of various phases. In this study EPT has been used to tackle these various problems. The details of the various studies are shown in Table 7.1. It can be seen that EPT can be successfully applied to solving a variety of phase-stability problems occurring in a wide range of steels.

Table 7.1 Thesis review consists of four main sections.

Aspect	Stability of chi- phase precipitates	Stability of delta-ferrite phase transformation	Stability of lamellar κ-carbides	Stability of martensite
Steel	Austenitic stainless (wt.%) 2-3 Mo; 16-18.5 Cr; 10-14 Ni; 0.03C; balance Fe	2205 duplex stainless (wt.%) 2 Mn; 0.03 C; 1 Si; 0.035P; 22 Cr; 5 Ni; 3 Mo; 0.15N; balance Fe	Lightweight (wt.%) 26 Mn; 9 Al; 0.75C; balance Fe	Dual-phase (wt.%) 0.1C; 0.25Si; 1.7Mn; 0.02P; 0.005S; 0.04Al; balance Fe
Problem	Segregation of alloying elements; leads to stress & pitting corrosion	Dissolution of hard phases (ie. σ-phase +secondary austenite	Uncontrolled formation of lamellar carbide structure	Decomposition of martensite to cementite (Fe_3C) and ferrite
Cause	Depletion of alloying elements	Loss of strength	Cracks-initiation and propagation	Softening the steel matrix
Alternative treatment	High temperature treatment (above 1000 ^oC)	Adding alloying elements	Control of the temperatue range & modify alloy additions	Non-isothermal heating (ie. laser- heating)
Aim/Strategy for EPT	Homogenize alloying elements	Retain high strength at high temperature	Reduce crack- formation (improve formability)	Delay or recovery the softening process during tempering
EPT success	Reduce size and fraction of chi- phase precipitates	Promote the formation of hard phases at high temperature	Fragment lamellar κ-carbides into nano-crystalline size	Produce nano- crystalline Fe_3C & ultra-fine- grained ferrite
Advantages of EPT	Fast, cheap and no pollutions	Fast, cheap and no pollutions	Fast, cheap and no pollutions	Fast, cheap and no pollutions

From Table 7.1, it was obviously seen that this thesis mainly describes the mechanism underlying phase stability control for steels using electropulsing treatment (EPT). It was hypothesised that some detrimental phenomena occur in steels under variety of conditions. For example:

(i) Stress & pitting corrosion caused by precipitation due to alloying elements segregation.

(ii) Loss of strength caused by phase transformation.

(iii) Cracking formation initiated by lamellar carbide structure.

(iv) Softening problem promoted by tempering of martensite.

All phenomena mentioned above are strongly dependent on phase stability. Although several combinations of thermo-mechanical processing have been reported to effectively eliminate those detrimental phenomena, these involve high energy consumption and have low efficiencies, so are not suitable for the solution of the above. Therefore, in this thesis, the investigation of possibility of utilizing EPT to solve these engineering problems by affecting the phase stability. There are carried out in four sections: (i) the stability of χ-phase in 316L stainless steel; (ii) the stability of delta-ferrite in 2205 duplex stainless steel; (iii) the stability of lamellar κ-carbide in Fe-Mn-Al-C lightweight steel and (iv) the stability of martensite in dual-phase steel.

- For the stability of χ-phase, an experiment under EPT at high temperature was used to affect the precipitation behaviour of χ-phase in the 316L stainless steel. It was found that EPT can effectively retard and suppress the precipitation of χ-phase and hence to reduce their fraction and size within the steel matrix. Finally, the alloying elements (e.g. Mo) can be homogenised across the whole microstructure.

- For the stability of delta-ferrite, a phase transformation ($\delta \rightarrow \sigma + \gamma'$) can be efficiently modified by applying electric current in 2205 duplex stainless steel at high temperature.

The hard phases (ie. sigma phase and secondary austenite) were retained under EPT to improve the strength property at high temperature.

- For the stability of κ-carbide, a duplex lightweight steel was used to verify the feasibility of using EPT to refine the size of carbide. It was observed that the lamellar κ-carbide can be effectively fragmented from microscale to nanoscale range via nano-crystallization. This significant refinement can efficiently suppress and retard the crack-formation during rolling process.

- For the stability of martensite in dual-phase steel, EPT was used to refine the steel matrix (e.g. nano-crystallization) and hence to improve the strength property in order to recover the softening effect.

Chapter 8 Suggestions of future work

Future work should be directed toward implementing and operating EPT technique for apply in the modern industry (e.g. nuclear power plant, aerospace and automotive applications). In order to improve the reliability of EPT on the optimizing of microstructural evolutions and associated properties for engineering alloys, it is necessary to modify the EPT parameters (e.g. frequency, duration, time, current density, voltage and etc.) so that appropriate parameters are selected which is more stable than those used in current thesis. It also would be possible to extend this study of EPT in four directions. They are expected to be: (i) fragmentation of carbide, (ii) recrystallization of matrix, (iii) acceleration of atom diffusion and (iv) the change of electrical conductivity. Additionally, the safety problems and commercial applications of utilizing EPT are also required to consider in future works. All above-mentioned key points are summarized in the Table 8.1.

Table 8.1 Tasks achieved by EPT in thesis and future applications.

Direction of EPT	Observations	Commercial applications	Safety problems
Fragmentation of carbide	1.Refine lamellar κ-carbides into nano-scale particles in duplex lightweight steel (Chap 5)	It can be used in automotive industry to imrpove the mechncial properties espcaiily for lightweight steels	High current density of EPT may cause some detrimental effects such as high temperature and high volatge
Recrystallization of matrix	1.Refine steel matrix (both delta-ferrite and austenite in duplex stainless steel) (Chap 4) 2.Refine steel matrix (ferrite in duplex lightweight steel) (Chap 5) 3.Refine steel matrix (ferrite in dual-phase steel) (Chap 6)	It can be used in automotive industry to optimze the strength properties espcaiily for polycrystallied steels	High current density of EPT may cause some detrimental effects such as high temperature and high volatge
Diffusion of atoms	1.Accelerate alloying elements (Cr, Mo and Ni) in duplex stainless steel (Chap 4) 2.Promote the motion of dislocations in (dual-phase steel) (Chap 6)	It can be used in automotive industry to accelerate the diffusion process and reduce the dislocation density espcaiily for cold-formed steels	High current density of EPT cause some detrimental effects such as high temperature and high volatge
Increase electrical conductivity of steel	1.Reduce the χ-phase formation in 316L stainless steel due to $\sigma_\chi < \sigma_\gamma$ (Chap 3) 2.Increase the secondary austenite formation in duplex stainless steel since $\sigma_\delta < \sigma_\gamma$ (Chap 4) 3.Reduce the κ-carbides formation in duplex lightweight steel due to $\sigma_\kappa < \sigma_\alpha$ (Chap 5) 4.Promote the nucleation rate in dual-phase steel due to $\sigma_\theta < \sigma_\alpha$ (Chap 6)	1. It can be used in nuclear power plant to dissolve the precipitates within fuel cladding applications and hence to improve their corrosion, oxidization and cracking resistance 2. It can be used in aerospace industry to retain high strength phase during high temperature treatments 3. It can be used in lightweight industry to improve the mechanical properties by optimizing the size and distribution of carbides	Applying electric current during operating temperature for steel component in nuclear power plant may influence electronic devices

To sum up, the tasks completed by EPT can be divided into three groups: (i) grain refinement (nano-crystallization and ultrafine grained microstructure); (ii) diffusion and (iii) phase modification, which can be used in nuclear power plant, aerospace and automotive industries.

- For the grain refinement, the nucleation and recrystallization rate can be significantly enhanced using EPT due to the reduction in activation barrier (the combination of thermal and electric effects). This can be used to enhance the mechanical properties for automotive steels.

- For the diffusion, the atom movements (alloying elements and dislocations) can be dramatically accelerated due to the electromigration effect (kinetic) under EPT. This can be used to promote the phase formation with high hardness for aerospace applications.
- For the phase modification, the phase stability of steel is mainly controlled by the electrical conductivity of each phase. This is attributed to the Gibbs free energy (thermodynamic) change with the differences in electrical properties (e.g. electrical conductivity) under EPT. This can be used to increase the formation of phases with higher electrical conductivity and hence to dissolve some detrimental precipitates within steel matrix for nuclear power plant.

Reference

[1] H. K. D. H. Bhadeshia and R. W. K. Honeycombe, *Steels: Microstructure and properties*, 3rd editio. Elsevier Ltd., Butterworth-Heinemann, Oxford, UK, 2006.

[2] D. J. Branagan, "Enabling Factors Toward Production of Nanostructured Steel on an Industrial Scale," *J. Mater. Eng. Perform.*, vol. 14, no. 1, pp. 5–9, 2005.

[3] A. Y. Jang and H. W. Lee, "Influence of sigma phase on pitting resistance depending on solidification mode in AISI316l weld metal," *Metall. Mater. Trans. A Phys. Metall. Mater. Sci.*, vol. 43, no. 6, pp. 1736–1741, 2012.

[4] T. Takahashi and M. Nagumo, "Flow stress and work-hardening of pearlitic steel," *Trans. Japan Inst. Met.*, vol. 11, pp. 113–119, 1970.

[5] T. Goldman, B. Holmes, and I. D. Mclvor, *Effect of Second Phase Particles on the Mechanical Properties of Steel*. IOM Communications Ltd, 1971.

[6] C. S. Ary, J. a. Scott, and J. E. Spruiell, "Tensile properties of thermal-mechanically pretreated type 316 austenitic stainless steel," *Metall. Trans.*, vol. 5, no. 7, pp. 1695–1697, 1974.

[7] H. K. D. H. Bhadeshia, "Advances in Physical Metallurgy and Processing of Steels. Design of Ferritic Creep-resistant Steels.," *ISIJ Int.*, vol. 41, no. 6, pp. 626–640, 2001.

[8] M. J. Cieslak, A. M. Ritter, and W. F. Savage, "Chi-Phase Formation During Solidification and Cooling of CF-8 M Weld Metal," *Weld. Res. Suppl.*, vol. 63, pp. S133–S140, 1984.

[9] C. Donadille, R. Valle, P. Dervin, and R. Penelle, "Development of texture and microstructure during cold-rolling and annealing of F.C.C. alloys: Example of an austenitic stainless steel," *Acta Metall.*, vol. 37, no. 6, pp. 1547–1571, 1989.

[10] C. Punckt, M. Bölscher, H. H. Rotermund, a S. Mikhailov, L. Organ, N. Budiansky, J. R. Scully, and J. L. Hudson, "Sudden onset of pitting corrosion on stainless steel as a critical phenomenon.," *Science*, vol. 305, no. 5687, pp. 1133–1136, 2004.

[11] Y. Song, T. N. Baker, and N. A. Mcpherson, "A study of precipitation in as-welded 3 16LN plate using 3 16L/3 17L weld metal," *Mater. Sci. Eng. A*, vol. 212, no. 3, pp. 228–234, 1996.

[12] J. E. Spruiell, J. a. Scott, C. S. Ary, and R. L. Hardin, "Tensile properties of thermal-mechanically pretreated type 316 austenitic stainless steel," *Metall. Trans.*, vol. 5, no. 7, pp. 1695–1697, 1974.

[13] R. C. Thomson and H. K. D. H. Bhadeshia, “Changes in chemical-composition of carbides in 2.25Cr-1Mo power-plant steel. 1. Bainitis microstructure,” *Mater. Sci. Technol.*, vol. 10, pp. 193–204, 1994.

[14] G. S. Was, P. Ampornrat, G. Gupta, S. Teysseyre, E. a. West, T. R. Allen, K. Sridharan, L. Tan, Y. Chen, X. Ren, and C. Pister, “Corrosion and stress corrosion cracking in supercritical water,” *J. Nucl. Mater.*, vol. 371, no. 1–3, pp. 176–201, 2007.

[15] D. N. Wasnik, G. K. Dey, V. Kain, and I. Samajdar, “Precipitation stages in a 316L austenitic stainless steel,” *Scr. Mater.*, vol. 49, no. 2, pp. 135–141, 2003.

[16] K. M. Zhang, J. X. Zou, T. Grosdidier, C. Dong, and D. Z. Yang, “Improved pitting corrosion resistance of AISI 316L stainless steel treated by high current pulsed electron beam,” *Surf. Coatings Technol.*, vol. 201, no. 3–4, pp. 1393–1400, 2006.

[17] K. Zhang, J. Zou, T. Grosdidier, C. Dong, and D. Yang, “Improved pitting corrosion resistance of AISI 316L stainless steel treated by high current pulsed electron beam,” *Surf. Coatings Technol.*, vol. 201, no. 3–4, pp. 1393–1400, 2006.

[18] W. D. Callister, *Materials Science and Engineering: An Introduction*, 7th editio. John Wiley & Sons, Inc.USA, 2007.

[19] K. W. Burns and F. B. Pickering, “Deformation and fracture of ferrite-pearlite structures,” *J. Iron Steel Inst.*, vol. 202, pp. 899–906, 1964.

[20] W. Hume-Rothery, *The Structures of Alloys of Iron : an Elementary Introduction*, 1st editio. Pergamon Press, 1966.

[21] P. G. Winchell and M. Cohen, “The strength of martensite,” *Transctions ASM*, vol. 55, pp. 347–361, 1962.

[22] R. A. Grange, “Strengthening Steel by Austenite Grain Refinement,” *Trans. Am. Soc. Mater.*, vol. 59, pp. 26–48, 1966.

[23] J. M. Chilton and P. M. Kelly, “The strength of ferrous martensite,” *Acta Metall.*, vol. 16, pp. 637–656, 1968.

[24] E. O. Hall, “The Deformation and Ageing of Mild Steel: III Discussion of Results,” *Proc. Phys. Soc. Sect. B*, vol. 64, pp. 747–753, 1951.

[25] H. J. Petch, “The cleavage strength of polycrystals,” *J. Iron Steel Inst.*, vol. 174, pp. 25–28, 1953.

[26] A. H. Cottrell and N. J. Petch, “Fracture,” in *Swampscott Conference*, 1959.

[27] N. Tsuji, Y. Ito, Y. Saito, and Y. Minamino, “Strength and ductility of ultrafine grained aluminum and iron produced by ARB and annealing,” *Scr. Mater.*, vol. 47, no. 12, pp. 893–899, Dec. 2002.

[28] K. Lu, L. Lu, and S. Suresh, “Strengthening materials by engineering coherent internal boundaries at the nanoscale,” *Science (80-.).*, vol. 324, pp. 349–352, 2009.

[29] K. Edalati, S. Toh, T. Furuta, S. Kuramoto, M. Watanabe, and Z. Horita, “Development of ultrahigh strength and high ductility in nanostructured iron alloys with lattice softening and nanotwins,” *Scr. Mater.*, vol. 67, no. 5, pp. 511–514, 2012.

[30] H. T. Wang, N. R. Tao, and K. Lu, “Architectured surface layer with a gradient nanotwinned structure in a Fe-Mn austenitic steel,” *Scr. Mater.*, vol. 68, no. 1, pp. 22–27, 2013.

[31] F. K. Yan, G. Z. Liu, N. R. Tao, and K. Lu, “Strength and ductility of 316L austenitic stainless steel strengthened by nano-scale twin bundles,” *Acta Mater.*, vol. 60, no. 3, pp. 1059–1071, 2012.

[32] K. Lu, F. K. Yan, H. T. Wang, and N. R. Tao, “Strengthening austenitic steels by using nanotwinned austenitic grains,” *Scr. Mater.*, vol. 66, no. 11, pp. 878–883, 2012.

[33] Y. B. Jiang, G. Y. Tang, L. Guan, S. N. Wang, Z. H. Xu, C. H. Shek, and Y. H. Zhu, “Effect of electropulsing treatment on solid solution behavior of an aged Mg alloy AZ61 strip,” *J. Mater. Res.*, vol. 23, no. 10, pp. 2685–2691, 2008.

[34] Y. B. Jiang, G. Y. Tang, C. H. Shek, and Y. H. Zhu, “Effect of electropulsing treatment on microstructure and tensile fracture behavior of aged Mg–9Al–1Zn alloy strip,” *Appl. Phys. A*, vol. 97, no. 3, pp. 607–615, 2009.

[35] Y. B. Jiang, G. Y. Tang, C. H. Shek, Y. H. Zhu, L. Guan, S. N. Wang, and Z. H. Xu, “Improved ductility of aged Mg-9Al-1Zn alloy strip by electropulsing treatment,” *J. Mater. Res.*, vol. 24, no. 05, pp. 1810–1814, 2009.

[36] Y. B. Jiang, G. Y. Tang, C. H. Shek, Y. H. Zhu, and Z. H. Xu, “On the thermodynamics and kinetics of electropulsing induced dissolution of beta-Mg17Al12 phase in an aged Mg-9Al-1Zn alloy,” *Acta Mater.*, vol. 57, no. 16, pp. 4797–4808, 2009.

[37] T. J. Koppenaal and C. R. Simcoe, “The effect of electric current on the ageing of an Al−4 Pct Cu alloy,” *Trans. Metall. Soc. AIME*, vol. 227, pp. 615–618, 1963.

[38] H. M. Liao, G. Y. Tang, Y. B. Jiang, Q. Xu, S. D. Sun, and J. N. Liu, “Effect of thermo-electropulsing rolling on mechanical properties and microstructure of AZ31 magnesium alloy,” *Mater. Sci. Eng. A*, vol. 529, no. 1, pp. 138–142, 2011.

[39] W. B. Liu, Y. H. Wen, N. Li, and S. Z. Yang, “Effects of electropulsing treatment on stress-induced ε martensite transformation of a pre-deformed Fe17Mn5Si8Cr5Ni0.5NbC alloy,” *Mater. Sci. Eng. A*, vol. 507, no. 1–2, pp. 114–116, 2009.

[40] W. B. Liu, Y. H. Wen, N. Li, and S. Z. Yang, “Further improvement of shape memory effect in a pre-deformed Fe-Mn-Si-Cr-Ni-Nb-C alloy by smaller NbC precipitated

through electropulsing treatment," *J. Alloys Compd.*, vol. 472, no. 1–2, pp. 591–594, 2009.

[41] W. B. Liu, N. Li, Y. H. Wen, S. C. Zhang, and S. Z. Yang, "Effects of amount of pre-deformation on precipitation of NbC particles and shape memory effect of Fe17Mn5Si8Cr5Ni0.5NbC alloy during electropulsing treatment," *Trans. Nonferrous Met. Soc. China (English Ed.*, vol. 22, no. SUPPL. 1, pp. s193–s197, 2012.

[42] Y. Onodera and K. I. Hirano, "The effect of a.c. frequency on precipitation in AI-5.6 at % Zn," *J. Mater. Sci.*, vol. 19, pp. 3935–3939, 1984.

[43] Y. Onodera and K. I. Hirano, "Effect of Direct Electric precipitation in a bulk AI-4 wt % Cu alloy," *J. Mater. Sci.*, vol. 11, pp. 809–816, 1979.

[44] Y. Onodera, A. Sakuma, and K. I. Hirano, "Current dependence of the retardation of precipitation by direct-current stress in Al-3.3 at% Mg," *J. Mater. Sci.*, vol. 28, no. 14, pp. 3835–3838, 1993.

[45] X. F. Xu, Y. G. Zhao, B. D. Ma, and M. Zhang, "Rapid precipitation of T-phase in the 2024 aluminum alloy via cyclic electropulsing treatment," *J. Alloys Compd.*, vol. 610, pp. 506–510, 2014.

[46] D. Zhang, S. To, Y. H. Zhu, H. Wang, and G. Y. Tang, "Static electropulsing-induced microstructural changes and their effect on the ultra-precision machining of cold-rolled AZ91 alloy," *Metall. Mater. Trans. A Phys. Metall. Mater. Sci.*, vol. 43, no. 4, pp. 1341–1346, 2012.

[47] D. Zhang, S. To, Y. H. Zhu, H. Wang, and G. Y. Tang, "Dynamic Electropulsing Induced Phase Transformations and Their Effects on Single Point Diamond Turning of AZ91 Alloy," *J. Surf. Eng. Mater. Adv. Technol.*, vol. 02, no. 01, pp. 16–21, 2012.

[48] Z. Zhu, J. Wang, and L. Zhou, "Experimental Study on Influence of Electropulsing to Microstructural Evolution of Billet," *Proc. 2nd Int. Conf. Electron. Mech. Eng. Inf. Technol.*, pp. 1409–1414, 2012.

[49] H. Mizubayashi, T. Takahashi, K. Nakamoto, and H. Tanimoto, "Nanocrystalline Transformation and Inverse Transformation in Metallic Glasses Induced by Electropulsing," *Mater. Trans.*, vol. 48, no. 7, pp. 1665–1670, 2007.

[50] H. Song and Z. J. Wang, "Grain refinement by means of phase transformation and recrystallization induced by electropulsing," *Trans. Nonferrous Met. Soc. China (English Ed.*, vol. 21, no. SUPPL. 2, pp. s353–s357, 2011.

[51] X. Su, S. J. Wang, X. OuYang, P. Song, G. M. Xu, and D. H. Jiang, "Physical and mechanical properties of 7075 sheets produced by EP electro- and electromagnetic cast rolling," *Mater. Sci. Eng. A*, vol. 607, pp. 10–16, 2014.

[52] S. To, Y. H. Zhu, W. B. Lee, and X. M. Liu, “Dynamic Electropulsing Induced Phase Transformations in a Furnace Cooled Zn-Al Based Alloy (ZA22),” *Mater. Trans.*, vol. 51, no. 11, pp. 1997–2004, 2010.

[53] S. To, Y. H. Zhu, W. B. Lee, X. M. Liu, and Y. B. Jiang, “Effects of Current Density on Elongation of an Electropulsing Treated Zn-Al Based Alloy,” *Mater. Trans.*, vol. 50, no. 12, pp. 2772–2777, 2009.

[54] S. To, Y. H. Zhu, W. B. Lee, X. M. Liu, Y. B. Jiang, and G. Y. Tang, “Effects of current density on electropulsing-induced phase transformations in a Zn-Al based alloy,” *Appl. Phys. A Mater. Sci. Process.*, vol. 96, no. 4, pp. 939–944, 2009.

[55] S. To, Y. H. Zhu, W. B. Lee, G. Y. Tang, X. M. Liu, and Y. B. Jiang, “Effects of Dynamic Electropulsing on Phase Transformation of a Zn-Al Based Alloy,” *Mater. Trans.*, vol. 50, no. 5, pp. 1105–1112, 2009.

[56] X. X. Ye, Z. T. H. Tse, and G. Y. Tang, “Mechanical properties and tensile fracture of Ti–Al–V alloy strip under electropulsing-induced phase change,” *J. Mater. Res.*, vol. 30, no. 02, pp. 206–223, 2014.

[57] X. X. Ye, Z. T. H. Tse, G. Y. Tang, Y. B. Geng, and G. L. Song, “Influence of electropulsing globularization on the microstructure and mechanical properties of Ti–6Al–4V alloy strip with lamellar microstructure,” *Mater. Sci. Eng. A*, vol. 622, pp. 1–6, 2015.

[58] F. C. Zhang, M. Zhang, B. Lv, and J. H. Li, “Effect of high-energy-density pulse current on solidification microstructure of FeCrNi alloy,” *Mater. Sci.*, vol. 13, no. 2, pp. 120–122, 2007.

[59] J. Zhang, L. H. Zhan, and S. F. Jia, “Effects of Electric Pulse Current on the Aging Kinetics of 2219 Aluminum Alloy,” *Adv. Mater. Sci. Eng.*, vol. 2014, pp. 1–8, 2014.

[60] W. Zhang, M. L. Sui, and Y. Z. Zhou, “Orientated Nanometer-Sized Fragmentation of TiC Particles by Electropulsing **,” *Adv. Eng. Mater.*, no. 9, pp. 697–700, 2002.

[61] Y. Z. Zhou, J. D. Guo, W. Zhang, and G. H. He, “Influence of electropulsing on nucleation during phase transformation,” *J. Mater. Res.*, vol. 17, no. 12, pp. 3012–3014, 2002.

[62] Y. Z. Zhou, W. Zhang, J. D. Guo, and G. H. He, “Diffusive phase transformation in a Cu–Zn alloy under rapid heating by electropulsing,” *Philos. Mag. Lett.*, vol. 84, no. 5, pp. 341–348, 2004.

[63] Y. H. Zhu, S. To, W. B. . Lee, X. X. Liu, Y. B. Jiang, and G. Y. Tang, “Electropulsing-induced phase transformations in a Zn–Al-based alloy,” *J. Mater. Res.*, vol. 24, no. 08, pp. 2661–2669, 2009.

[64] Y. H. Zhu, S. To, and X. M. Liu, “Influence of Spinodal Decomposition on the Plastic Behavior of Dynamic Electropulsing Treated ZA22 Alloy,” *Mater. Trans.*, vol. 53, no. 8, pp. 1363–1370, 2012.

[65] Y. H. Zhu, S. To, and X. M. Liu, “Use of EBSD to study electropulsing induced reverse phase transformations in a Zn-Al alloy (ZA22),” *J. Microsc.*, vol. 242, no. 1, pp. 62–69, 2011.

[66] Y. H. Zhu, S. To, X. M. Liu, and G. L. Hu, “Effect of static electropulsing on microstructure and elongation of a Zn-Al alloy (ZA22),” *Metall. Mater. Trans. A Phys. Metall. Mater. Sci.*, vol. 42, no. 7, pp. 1933–1940, 2011.

[67] Y. H. Zhu, S. To, X. M. Liu, G. L. Hu, and Q. Xu, “Static electropulsing-induced phase transformations of a cold-deformed ZA27 alloy,” *J. Mater. Res.*, vol. 26, no. 14, pp. 1696–1701, 2011.

[68] T. P. Barnak, A. F. Sprecher, and H. Conrad, “Colony (grain) size reduction in eutectic Pb-Sn casting by electropulsing,” *Scr. Metall.*, vol. 32, no. 6, pp. 879–884, 1995.

[69] V. F. Bashev, a. S. Baskevich, V. a. Ivanov, and a. a. Kostina, “Effect of alternating electric current on mechanical properties and structure of industrial accumulator alloys,” *Phys. Met. Metallogr.*, vol. 113, no. 11, pp. 1061–1067, 2012.

[70] S. P. Belyaev, N. N. Resnina, a. V. Irzhak, V. V. Istomin-Kastrovsky, V. V. Koledov, D. S. Kuchin, V. G. Shavrov, P. Ari-Gur, a. V. Shelyakov, and N. Y. Tabachkova, “Amorphous–crystalline Ti2NiCu alloy rapidly quenched ribbons annealed by DSC and electric pulses,” *J. Alloys Compd.*, vol. 586, pp. S222–S224, 2014.

[71] Y. S. Chao, Z. H. Lai, K. Y. He, and H. R. Er, “Microstructural relaxation of amorphous alloy Fe79Si7B14 during electropulsing,” *Mater. Sci. Eng. A*, vol. 181–182, pp. 982–985, 1994.

[72] W. B. Dai and X. L. Wang, “Effect of Electric Current on the Inclusions in a Cu-Zn Alloy,” *Mater. Trans.*, vol. 51, no. 5, pp. 892–895, 2010.

[73] W. B. Dai, X. L. Wang, L. Zhao, and J. K. Yu, “Formation of Nanotwins in Cold-Rolled Cu-Zn Alloy by Electric Current Pulses,” *Mater. Trans.*, vol. 52, no. 11, pp. 2022–2026, 2011.

[74] X. N. Du, B. Q. Wang, and J. D. Guo, “Formation of nanocrystalline surface of a Cu–Zn alloy under electropulsing surface treatment,” *J. Mater. Res.*, vol. 22, no. 07, pp. 1947–1953, 2007.

[75] M. Gao, G. H. He, F. Yang, J. D. Guo, Z. X. Yuan, and B. L. Zhou, “Effect of electric current pulse on tensile strength and elongation of casting ZA27 alloy,” *Mater. Sci. Eng. A*, vol. 337, no. 1–2, pp. 110–114, 2002.

[76] T. Hao, H. Tanimoto, and H. Mizubayashi, “Transformation to Nanocrystallites in Amorphous Alloys Induced by Resonant Electropulsing,” *Mater. Trans.*, vol. 46, no. 12, pp. 2898–2907, 2005.

[77] G. L. Hu, C. H. Shek, Y. H. Zhu, G. Y. Tang, and X. Qing, “Effect of Electropulsing on Recrystallization of Fe-3%Si Alloy Strip,” *Mater. Trans.*, vol. 51, no. 8, pp. 1390–1394, 2010.

[78] G. L. Hu, Y. H. Zhu, G. Y. Tang, C. H. Shek, and J. N. Liu, “Effect of Electropulsing on Recrystallization and Mechanical Properties of Silicon Steel Strips,” *J. Mater. Sci. Technol.*, vol. 27, no. 11, pp. 1034–1038, Nov. 2011.

[79] Y. B. Jiang, L. Guan, G. Y. Tang, C. H. Shek, and Z. H. Zhang, “Influence of electropulsing treatment on microstructure and mechanical properties of cold-rolled Mg-9Al-1Zn alloy strip,” *Mater. Sci. Eng. A*, vol. 528, no. 16–17, pp. 5627–5635, 2011.

[80] Y. B. Jiang, L. Guan, G. Y. Tang, and Z. H. Zhang, “Improved mechanical properties of Mg–9Al–1Zn alloy by the combination of aging, cold-rolling and electropulsing treatment,” *J. Alloys Compd.*, vol. 626, pp. 297–303, 2015.

[81] Y. B. Jiang, G. Y. Tang, C. H. Shek, J. X. Xie, Z. H. Xu, and Z. H. Zhang, “Mechanism of electropulsing induced recrystallization in a cold-rolled Mg-9Al-1Zn alloy,” *J. Alloys Compd.*, vol. 536, pp. 94–105, 2012.

[82] Z. H. Lai, H. Conrad, Y. S. Chao, S. Q. Wang, and J. Sun, “Effext of electropulsing on the microstructure and properties of iron-based amorphous alloys,” *Scr. Metall.*, vol. 23, no. c, pp. 305–310, 1989.

[83] Z. H. Lai, H. Conrad, G. Q. Teng, and Y. S. Chao, “Nanocrystallization of amorphous Fe–Si–B alloys using high current density electropulsing,” *Mater. Sci. Eng. A*, vol. 287, no. 2, pp. 238–247, 2000.

[84] B. H. Lee, S. S. Hong, K. H. Lee, and Y. D. Kim, “Pulse electric current sintering of nanostructured Fe-Co alloy,” *J. Alloys Compd.*, vol. 385, no. 1–2, pp. 264–268, 2004.

[85] J. Li, J. H. Ma, Y. L. Gao, and Q. J. Zhai, “Research on solidification structure refinement of pure aluminum by electric current pulse with parallel electrodes,” *Mater. Sci. Eng. A*, vol. 490, no. 1–2, pp. 452–456, 2008.

[86] Q. C. Li, R. X. Li, G. W. Chang, and Q. J. Zhai, “Research of microstructure of spherical graphite iron by electropulsing annealing,” *J. Mater. Process. Technol.*, vol. 209, no. 4, pp. 2015–2020, 2009.

[87] Q. C. Li, R. X. Li, D. S. Lin, G. W. Chang, and Q. J. Zhai, “Influence of Electropulsing Pretreatment on Solid-State Graphitization of Spherical Graphite Iron,” *J. Iron Steel Res. Int.*, vol. 19, no. 12, pp. 66–72, 2012.

[88] Q. C. Li, R. X. Li, X. D. Yue, G. W. Chang, and Q. J. Zhai, “Effect of electropulsing on the formation of graphite during solid-state graphitization of spherical graphite iron,” *Mater. Chem. Phys.*, vol. 112, pp. 402–406, 2008.

[89] X. H. Li, Z. S. Gao, W. Li, K. W. Zhang, J. W. Zhang, and X. Y. Zhang, “Study of the microstructure of alpha-Fe/Nd2Fe14B nanocomposites prepared by electropulsing heating amorphous NdFeCoB,” *Mater. Lett.*, vol. 59, no. 22, pp. 2782–2785, 2005.

[90] X. L. Liao, Q. J. Zhai, J. Luo, W. J. Chen, and Y. Y. Gong, “Refining mechanism of the electric current pulse on the solidification structure of pure aluminum,” *Acta Mater.*, vol. 55, no. 9, pp. 3103–3109, 2007.

[91] X. L. Liao, Q. J. Zhai, C. J. Song, W. J. Chen, and Y. Y. Gong, “Effects of electric current pulse on stability of solid/liquid interface of Al–4.5wt.% Cu alloy during directional solidification,” *Mater. Sci. Eng. A*, vol. 466, no. 1–2, pp. 56–60, 2007.

[92] Y. Liu, J. F. Fan, H. Zhang, W. Jin, H. B. Dong, and B. S. Xu, “Recrystallization and microstructure evolution of the rolled Mg – 3Al – 1Zn alloy strips under electropulsing treatment,” *J. Alloys Compd.*, vol. 622, pp. 229–235, 2015.

[93] Y. Liu, L. Wang, H. H. Liu, X. D. Lu, and B. J. Zhang, “Effects of Pulse Current on Dynamic Recrystallization Behavior of GH4169 Superalloy,” *Mater. Trans.*, vol. 53, no. 8, pp. 1400–1404, 2012.

[94] B. D. Ma, Y. G. Zhao, H. Bai, J. Ma, J. T. Zhang, and X. F. Xu, “Materia ls and Design Gradient distribution of mechanical properties in the high carbon steel induced by the detour effect of the pulse current,” *Mater. Des.*, vol. 49, pp. 168–172, 2013.

[95] B. D. Ma, Y. G. Zhao, J. Ma, H. C. Guo, and Q. Yang, “Formation of local nanocrystalline structure in a boron steel induced by electropulsing,” *J. Alloys Compd.*, vol. 549, pp. 77–81, 2013.

[96] J. H. Ma, J. Li, Y. L. Gao, L. X. Jia, Z. Li, and Q. J. Zhai, “Improving the carbon macrosegregation in high-carbon steel by an electric current pulse,” *Met. Mater. Int.*, vol. 15, no. 4, pp. 603–608, 2009.

[97] H. Mizubayashi, N. Kameyama, T. Hao, and H. Tanimoto, “Crystallization under electropulsing suggesting a resonant collective motion of many atoms and modification of thermodynamic parameters in amorphous alloys,” *Phys. Rev. B*, vol. 64, no. 5, pp. 1–10, 2001.

[98] A. A. Potapova, N. N. Resnina, and V. V. Stolyarov, “Shape Memory Effects in TiNi-Bbased Alloys Subjected to Electroplastic Rolling,” *J. Mater. Eng. Perform.*, vol. 23, no. July, pp. 2391–2395, 2014.

[99] R. S. Qin, E. I. Samuel, and a. Bhowmik, “Electropulse-induced cementite nanoparticle formation in deformed pearlitic steels,” *J. Mater. Sci.*, vol. 46, no. 9, pp. 2838–2842, 2011.

[100] D. Räbiger, Y. H. Zhang, V. Galindo, S. Franke, B. Willers, and S. Eckert, "The relevance of melt convection to grain refinement in Al-Si alloys solidified under the impact of electric currents," *Acta Mater.*, vol. 79, pp. 327–338, 2014.

[101] A. Rahnama and R. S. Qin, "Electropulse-induced microstructural evolution in a ferritic–pearlitic 0.14% C steel," *Scr. Mater.*, vol. 96, pp. 17–20, 2015.

[102] A. Rahnama and R. S. Qin, "The effect of electropulsing on the interlamellar spacing and mechanical properties of a hot-rolled 0.14% carbon steel," *Mater. Sci. Eng. A*, vol. 627, pp. 145–152, 2015.

[103] E. I. Samuel, A. Bhowmik, and R. S. Qin, "Accelerated spheroidization induced by high intensity electric pulse in a severely deformed eutectoid steel," *J. Mater. Res.*, vol. 25, no. 06, pp. 1020–1024, 2010.

[104] H. Song and Z. J. Wang, "Improvement of mechanical properties of cold-rolled commercially pure Ti sheet by high density electropulsing," *Trans. Nonferrous Met. Soc. China (English Ed.*, vol. 22, no. 6, pp. 1350–1355, 2012.

[105] H. Song and Z. J. Wang, "Effect of electropulsing on dislocation mobility of titanium sheet," *Trans. Nonferrous Met. Soc. China (English Ed.*, vol. 22, no. 7, pp. 1599–1605, 2012.

[106] H. Song, Z. J. Wang, and X. D. He, "Improving in plasticity of orthorhombic Ti2AlNb-based alloys sheet by high density electropulsing," *Trans. Nonferrous Met. Soc. China (English Ed.*, vol. 23, no. 1, pp. 32–37, 2013.

[107] H. Y. Sun, J. S. Wang, L. J. Cao, and Q. G. Xue, "Effect of electropulsing treatment on the crystallization kinetics of Zr55Ni5Al10Cu30 bulk metallic glass," *Thermochim. Acta*, vol. 537, pp. 80–85, 2012.

[108] G. Q. Teng, Y. S. Chao, L. Dong, Y. Geng, and Z. H. Lai, "Features of Nanocrystallization of Metallic Glass Density Electropulsing Fe 78B 13Si 9 Induced by High-Current-," *J. Appl. Physcis*, vol. 35, pp. 5320–5325, 1996.

[109] G. Q. Teng, Y. S. Chao, and Z. H. Lai, "Rapid nanocrystallization from amorphous Fe78B13Si9 by high current density electropulsing," *J. Mater. Sci. Lett.*, vol. 14, pp. 144–145, 1995.

[110] T. M. Wang, J. J. Xu, T. Q. Xiao, H. L. Xie, J. Li, T. J. Li, and Z. Q. Cao, "Evolution of dendrite morphology of a binary alloy under an applied electric current: An in situ observation," *Phys. Rev. E - Stat. Nonlinear, Soft Matter Phys.*, vol. 81, no. 4, pp. 1–4, 2010.

[111] T. M. Wang, J. Zhu, H. J. Kang, Z. N. Chen, Y. N. Fu, W. X. Huang, and T. Q. Xiao, "In situ synchrotron X-ray imaging on morphological evolution of dendrites in Sn–Bi hypoeutectic alloy under electric currents," *Appl. Phys. A*, vol. 117, no. 3, pp. 1059–1066, 2014.

[112] X. L. Wang, Y. B. Wang, Y. M. Wang, B. Q. Wang, and J. D. Guo, "Oriented nanotwins induced by electric current pulses in Cu-Zn alloy," *Appl. Phys. Lett.*, vol. 91, no. 16, pp. 2005–2008, 2007.

[113] S. H. Xiao, J. D. Guo, and S. X. Li, "The effect of electropulsing on dislocation structures in [233] coplanar double-slip-oriented fatigued copper single crystals," *Philos. Mag. Lett.*, vol. 82, no. 11, pp. 617–622, 2002.

[114] S. H. Xiao, J. D. Guo, S. D. Wu, G. H. He, and S. X. Li, "Recrystallization in fatigued copper single crystals under electropulsing," *Scr. Mater.*, vol. 46, no. 1, pp. 1–6, 2002.

[115] Q. Xu, L. Guan, Y. B. Jiang, G. Y. Tang, and S. N. Wang, "Improved plasticity of Mg-Al-Zn alloy by electropulsing tension," *Mater. Lett.*, vol. 64, no. 9, pp. 1085–1087, 2010.

[116] Q. Xu, G. Y. Tang, and Y. B. Jiang, "Thermal and electromigration effects of electropulsing on dynamic recrystallization in Mg-3Al-1Zn alloy," *Mater. Sci. Eng. A*, vol. 528, no. 13–14, pp. 4431–4436, 2011.

[117] Q. Xu, G. Y. Tang, Y. B. Jiang, G. L. Hu, and Y. H. Zhu, "Accumulation and annihilation effects of electropulsing on dynamic recrystallization in magnesium alloy," *Mater. Sci. Eng. A*, vol. 528, no. 7–8, pp. 3249–3252, 2011.

[118] X. F. Xu, Y. G. Zhao, B. D. Ma, J. T. Zhang, and M. Zhang, "Rapid grain refinement of 2024 Al alloy through recrystallization induced by electropulsing," *Mater. Sci. Eng. A*, vol. 612, pp. 223–226, 2014.

[119] Z. Xu, G. Tang, F. Ding, S. Tian, and H. Tian, "The effect of multiple pulse treatment on the recrystallization behavior of Mg-3Al-1Zn alloy strip," *Appl. Phys. A Mater. Sci. Process.*, vol. 88, no. 2, pp. 429–433, 2007.

[120] Z. H. Xu, G. Y. Tang, S. Q. Tian, and J. C. He, "Research on the engineering application of multiple pulses treatment for recrystallization of fine copper wire," *Mater. Sci. Eng. A*, vol. 424, no. 1–2, pp. 300–306, 2006.

[121] X. X. Ye, T. Liu, Y. D. Ye, H. B. Wang, G. Y. Tang, and G. L. Song, "Enhanced grain refinement and microhardness of Ti – Al – V alloy by electropulsing ultrasonic shock," *J. Alloys Compd.*, vol. 621, pp. 66–70, 2015.

[122] X. X. Ye and G. Y. Tang, "Effect of coupling asynchronous acoustoelectric effects on the corrosion behavior, microhardness and biocompatibility of biomedical titanium alloy strips," *J. Mater. Sci. Mater. Med.*, vol. 26, no. 1, 2015.

[123] Y. Yuan, W. Liu, B. Q. Fu, H. Y. Xu, G. N. Luo, G. Y. Tang, and Y. B. Jiang, "The effects of electropulsing on the recrystallization behavior of rolled pure tungsten," *J. Mater. Res.*, vol. 27, no. 20, pp. 2630–2638, 2012.

[124] W. Zhang, M. L. Sui, K. Y. Hu, D. X. Li, X. N. Guo, G. H. He, and B. L. Zhou, "Formation of nanophases in a Cu–Zn alloy under high current density electropulsing," *J. Mater. Res.*, vol. 15, no. 10, pp. 2065–2068, 2000.

[125] W. Zhang, M. L. Sui, Y. Z. Zhou, J. D. Guo, G. H. He, and D. X. Li, "Evolution of microstructure in TiC/NiCr cermet induced by electropulsing," *J. Mater. Res.*, vol. 18, no. 07, pp. 1543–1550, 2003.

[126] Y. H. Zhang, C. J. Song, L. Zhu, H. X. Zheng, H. G. Zhong, Q. Y. Han, and Q. J. Zhai, "Influence of electric-current pulse treatment on the formation of regular eutectic morphology in an Al-Si eutectic alloy," *Metall. Mater. Trans. B Process Metall. Mater. Process. Sci.*, vol. 42, no. 3, pp. 604–611, 2011.

[127] Y. G. Zhao, B. D. Ma, H. C. Guo, J. Ma, Q. Yang, and J. S. Song, "Electropulsing strengthened 2GPa boron steel with good ductility," *Mater. Des.*, vol. 43, pp. 195–199, 2013.

[128] Y. S. Zheng, G. Y. Tang, J. Kuang, and X. P. Zheng, "Effect of electropulse on solid solution treatment of 6061 aluminum alloy," *J. Alloys Compd.*, vol. 615, pp. 849–853, 2014.

[129] Y. Z. Zhou, S. H. Xiao, and J. D. Guo, "Recrystallized microstructure in cold worked brass produced by electropulsing treatment," *Mater. Lett.*, vol. 58, no. 12–13, pp. 1948–1951, 2004.

[130] Y. Z. Zhou, W. Zhang, M. L. Sui, D. X. Li, G. H. He, and J. D. Guo, "Formation of a Nanostructure in a Low-carbon Steel Under High Current Density Electropulsing," *J. Mater. Res.*, vol. 17, no. 05, pp. 921–924, 2002.

[131] Y. Z. Zhou, W. Zhang, B. Q. Wang, and J. D. Guo, "Ultrafine-grained microstructure in a Cu–Zn alloy produced by electropulsing treatment," *J. Mater. Res.*, vol. 18, no. 08, pp. 1991–1997, 2003.

[132] Y. Z. Zhou, W. Zhang, B. Q. Wang, G. H. He, and J. D. Guo, "Grain refinement and formation of ultrafine-grained microstructure in a low-carbon steel under electropulsing," *J. Mater. Res.*, vol. 17, no. 8, pp. 2105–2111, 2002.

[133] R. F. Zhu, G. Y. Tang, S. Q. Shi, and M. W. Fu, "Microstructure evolution of copper strips with gradient temperature in electropulsing treatment," *J. Alloys Compd.*, vol. 581, pp. 160–165, 2013.

[134] X. N. Du, S. M. Yin, S. C. Liu, B. Q. Wang, and J. D. Guo, "Effect of the electropulsing on mechanical properties and microstructure of an ECAPed AZ31 Mg alloy," *J. Mater. Res.*, vol. 23, no. 06, pp. 1570–1577, 2008.

[135] L. Guan, G. Y. Tang, P. K. Chu, and Y. B. Jiang, "Enhancement of ductility in Mg–3Al–1Zn alloy with tilted basal texture by electropulsing," *J. Mater. Res.*, vol. 24, no. 12, pp. 3674–3679, 2009.

[136] L. Guan, G. Y. Tang, Y. B. Jiang, and P. K. Chu, "Texture evolution in cold-rolled AZ31 magnesium alloy during electropulsing treatment," *J. Alloys Compd.*, vol. 487, no. 1–2, pp. 309–313, 2009.

[137] G. L. Hu, G. Y. Tang, Y. H. Zhu, and C. H. Shek, "Electropulsing induced texture evolution in the recrystallization of Fe-3 pct Si alloy strip," *Metall. Mater. Trans. A Phys. Metall. Mater. Sci.*, vol. 42, no. 11, pp. 3484–3490, 2011.

[138] G. L. Hu, Z. H. Wang, Y. H. Zhu, J. N. Liu, and G. Y. Tang, "Dynamic Electropulsing Induced Evolution of Basal Texture and Its Effect on Properties of Magnesium Alloy AZ61," *Mater. Trans.*, vol. 52, no. 8, pp. 1565–1568, 2011.

[139] G. L. Hu, Y. H. Zhu, C. H. Shek, and G. Y. Tang, "Electropulsing-induced G-texture evolution in a deformed Fe–3%Si alloy strip," *J. Mater. Res.*, vol. 26, no. 07, pp. 917–922, 2011.

[140] Y. B. Jiang, G. Y. Tang, C. H. Shek, and W. Liu, "Microstructure and texture evolution of the cold-rolled AZ91 magnesium alloy strip under electropulsing treatment," *J. Alloys Compd.*, vol. 509, no. 11, pp. 4308–4313, 2011.

[141] C. Y. Liu, Y. J. Hu, Y. S. Liu, H. W. Tseng, T. S. Huang, C. T. Lu, Y. C. Chuang, and S. L. Cheng, "Epitaxial Cu-Sn bulk crystals grown by electric current," *Acta Mater.*, vol. 61, no. 15, pp. 5713–5719, 2013.

[142] X. L. Wang, J. D. Guo, Y. M. Wang, X. Y. Wu, and B. Q. Wang, "Segregation of lead in Cu-Zn alloy under electric current pulses," *Appl. Phys. Lett.*, vol. 89, no. 6, pp. 10–13, 2006.

[143] X. X. Ye, G. Y. Tang, G. L. Song, and J. Kuang, "Effect of electropulsing treatment on the microstructure, texture, and mechanical properties of cold-rolled Ti–6Al–4V alloy," *J. Mater. Res.*, vol. 29, no. 14, pp. 1500–1512, 2014.

[144] X. F. Zhang, W. J. Lu, and R. S. Qin, "Removal of MnS inclusions in molten steel using electropulsing," *Scr. Mater.*, vol. 69, no. 6, pp. 453–456, 2013.

[145] X. F. Zhang, W. J. Lu, and R. S. Qin, "Morphology and distribution control of MnS inclusions in molten steel by electropulsing," *Mater. Res. Innov.*, vol. 18, pp. 244–248, 2014.

[146] R. F. Zhu, J. N. Liu, G. Y. Tang, S. Q. Shi, and M. W. Fu, "Properties, microstructure and texture evolution of cold rolled Cu strips under electropulsing treatment," *J. Alloys Compd.*, vol. 544, pp. 203–208, 2012.

[147] Y. H. Zhu, J. Jiang, Y. K. Xiao, C. M. Luk, and W. E. Lai, "Electropulsing-induced microstructure evolution and its effect on electrical conductivity of (Bi0.25Sb0.75)2Te3 thin films," *Scr. Mater.*, vol. 69, no. 3, pp. 219–222, 2013.

[148] Y. H. Zhu, S. Q. Jiang, D. D. Zhao, G. J. Cheng, H. W. Zhang, and W. E. Lai, "Electropulsing induced crystal orientation change and its effects on electric

conductivity of nanofilms of Zn-Al alloys," *Appl. Phys. A Mater. Sci. Process.*, vol. 111, no. 4, pp. 1241–1245, 2013.

[149] X. F. Zhang and R. S. Qin, "Controlled motion of electrically neutral microparticles by pulsed direct current," *Sci. Rep.*, vol. 5, p. 10162, 2015.

[150] X. F. Zhang and R. S. Qin, "Preparation of surface coatings on a conductive substrate by controlled motion of graphene nanoflakes in a liquid medium," *Appl. Surf. Sci.*, vol. 329, pp. 276–280, 2015.

[151] A. Hosoi, T. Kishi, and Y. Ju, "Healing of Fatigue Crack by High-Density Electropulsing in Austenitic Stainless Steel Treated with the Surface-Activated Pre-Coating," *Materials (Basel).*, vol. 6, no. 9, pp. 4213–4225, 2013.

[152] S. V. Konovalov, a. a. Atroshkina, Y. F. Ivanov, and V. E. Gromov, "Evolution of dislocation substructures in fatigue loaded and failed stainless steel with the intermediate electropulsing treatment," *Mater. Sci. Eng. A*, vol. 527, no. 12, pp. 3040–3043, 2010.

[153] H. Q. Lin, Y. G. Zhao, Z. M. Gao, and L. G. Han, "Effects of pulse current stimulation on the thermal fatigue crack propagation behavior of CHWD steel," *Mater. Sci. Eng. A*, vol. 478, no. 1–2, pp. 93–100, 2008.

[154] H. Q. Lin, Y. G. Zhao, Y. Zhao, L. G. Han, J. Ma, and Q. C. Jiang, "Effect of Pulse Electric Current Stimulation on the Microstructure, Mechanical Properties and Thermal Fatigue Behavior of Cast-hot-working Die Steel," *ISIJ Int.*, vol. 48, no. 2, pp. 212–217, 2008.

[155] H. Song and Z. J. Wang, "Microcrack healing and local recrystallization in pre-deformed sheet by high density electropulsing," *Mater. Sci. Eng. A*, vol. 490, no. 1–2, pp. 1–6, 2008.

[156] X. Ye, X. Li, G. Song, and G. Tang, "Effect of recovering damage and improving microstructure in the titanium alloy strip under high-energy electropulses," *J. Alloys Compd.*, vol. 616, pp. 173–183, 2014.

[157] A. Pozdnyakova, A. Giuliani, J. Dutkiewicz, A. Babutsky, A. Chyzhyk, J. a. Roether, F. Rustichelli, and M. G. Ortore, "Analysis of porosity in NiTi SMA's changed by secondary pulse electric current treatment by means of ultra small angle scattering and micro-computed tomography," *Intermetallics*, vol. 18, no. 5, pp. 907–912, 2010.

[158] R. S. Qin and S. X. Su, "Thermodynamics of crack healing under electropulsing," *J. Mater. Res.*, vol. 17, no. 8, pp. 2048–2052, 2002.

[159] Y. Z. Zhou, J. D. Guo, M. Gao, and G. H. He, "Crack healing in a steel by using electropulsing technique," *Mater. Lett.*, vol. 58, no. 11, pp. 1732–1736, 2004.

[160] Y. Z. Zhou, D. C. Qiao, G. H. He, and J. D. Guo, “Improvement of mechanical properties in a saw blade by electropulsing treatment,” *Mater. Lett.*, vol. 57, no. 9–10, pp. 1566–1570, 2003.

[161] Y. Z. Zhou, Y. Zeng, G. H. He, and B. L. Zhou, “The healing of quenched crack in 1045 steel under electropulsing,” *J. Mater. Res.*, vol. 16, no. 01, pp. 17–19, 2001.

[162] R. S. Qin, S. X. Su, J. D. Guo, G. H. He, and B. L. Zhou, “Suspension effect of nanocrystalline grain growth under electropulsing,” *Nanostructured Mater.*, vol. 10, no. 1, pp. 71–76, 1998.

[163] K. Lu, F. K. Yan, H. T. Wang, and N. R. Tao, “Strengthening austenitic steels by using nanotwinned austenitic grains,” *Scripta Materialia*, vol. 66, no. 11. pp. 878–883, 2012.

[164] W. A. Salandro, J. J. Jones, C. Bunget, L. Mears, and J. T. Roth, *Electrically Assisted Forming: Modelling and control*, 1st editio. Springer International Publishing Switerland, 2015.

[165] L. Guan, G. Tang, and P. K. Chu, “Recent advances and challenges in electroplastic manufacturing processing of metals,” *J. Mater. Res.*, vol. 25, no. 07, pp. 1215–1224, 2010.

[166] D. H. Bratland, O. Grong, H. Shercliff, O. R. Myhr, and S. Tjotta, “Overview No. 124: modelling of precipitation reactions in industrial processing,” *Acta Mater.*, vol. 45, no. 1, pp. 1–22, 1997.

[167] M. P. Ryan, D. E. Williams, R. J. Chater, B. M. Hutton, and D. S. McPhail, “Why stainless steel corrodes.,” *Nature*, vol. 415, no. 6873, pp. 770–774, 2002.

[168] R. S. Qin, A. Rahnama, W. J. Lu, X. F. Zhang, and B. Elliott-Bowman, “Electropulsed steels,” *Mater. Sci. Technol.*, vol. 30, no. 9, pp. 1040–1044, 2014.

[169] M. Michiuchi, H. Kokawa, Z. J. Wang, Y. S. Sato, and K. Sakai, “Twin-induced grain boundary engineering for 316 austenitic stainless steel,” *Acta Mater.*, vol. 54, no. 19, pp. 5179–5184, 2006.

[170] G. S. Rohrer, “Grain boundary energy anisotropy: A review,” *J. Mater. Sci.*, vol. 46, no. 18, pp. 5881–5895, 2011.

[171] V. Randle, “Grain boundary engineering: an overview after 25 years,” *Mater. Sci. Technol.*, vol. 26, no. 3, pp. 253–261, 2010.

[172] X. F. Zhang and R. S. Qin, “Electric current-driven migration of electrically neutral particles in liquids,” *Appl. Phys. Lett.*, vol. 114106, pp. 9–14, 2014.

[173] H. Conrad, “Effects of electric current on solid state phase transformations in metals,” *Mater. Sci. Eng. A*, vol. 287, no. 2, pp. 227–237, 2000.

[174] Z. S. Xu, Z. H. Lai, and Y. X. Chen, “Effect of electric-current on the recrystallization behavior of cold-worked alpha-Ti,” *Scr. Mater.*, vol. 22, pp. 187–190, 1988.

[175] S. T. Pai and J. P. Marton, “Electromigration in metals,” *Can. J. Phys.*, vol. 55, no. 2, pp. 103–115, 1977.

[176] S. K. Ghosh and S. Mondal, “High temperature ageing behaviour of a duplex stainless steel,” *Mater. Charact.*, vol. 59, no. 12, pp. 1776–1783, 2008.

[177] A. Kashiwar, N. P. Vennela, S. L. Kamath, and R. K. Khatirkar, “Effect of solution annealing temperature on precipitation in 2205 duplex stainless steel,” *Mater. Charact.*, vol. 74, pp. 55–63, 2012.

[178] R. Badji, M. Bouabdallah, B. Bacroix, C. Kahloun, B. Belkessa, and H. Maza, “Phase transformation and mechanical behavior in annealed 2205 duplex stainless steel welds,” *Mater. Charact.*, vol. 59, no. 4, pp. 447–453, 2008.

[179] H. S. Cho and K. M. Lee, “Effect of cold working and isothermal aging on the precipitation of sigma phase in 2205 duplex stainless steel,” *Mater. Charact.*, vol. 75, pp. 29–34, 2013.

[180] G. Fargas, M. Anglada, and a. Mateo, “Effect of the annealing temperature on the mechanical properties, formability and corrosion resistance of hot-rolled duplex stainless steel,” *J. Mater. Process. Technol.*, vol. 209, no. 4, pp. 1770–1782, 2009.

[181] Q. Li, R. Li, G. Chang, and Q. Zhai, “Research of microstructure of spherical graphite iron by electropulsing annealing,” *J. Mater. Process. Technol.*, vol. 209, no. 4, pp. 2015–2020, 2009.

[182] Q. C. Li, R. X. Li, D. S. Lin, G. W. Chang, and Q. J. Zhai, “Influence of Electropulsing Pretreatment on Solid-State Graphitization of Spherical Graphite Iron,” *J. Iron Steel Res. Int.*, vol. 19, no. 12, pp. 66–72, 2012.

[183] Q. Li, R. Li, X. Yue, G. Chang, and Q. Zhai, “Effect of electropulsing on the formation of graphite during solid-state graphitization of spherical graphite iron,” vol. 112, pp. 402–406, 2008.

[184] Y. Mohammad, S. P.Ch., and G. R. K., “High-pressure and high-temperature electrical resistivity of ferromagnetic transition metals: Nickel and iron,” *Phys. Rev. B*, vol. 34, pp. 8086–8100, 1986.

[185] K. Ravindranath and S. N. Malhotra, “The influence of aging on the intergranular corrosion of 22 chromium-5 nickel duplex stainless steel,” *Corros. Sci.*, vol. 37, no. 1, pp. 121–132, 1995.

[186] I. A. Ibrahim, F. A. Mohamed, and E. J. Lavernia, “Particulate reinforced metal matrix composites - a review,” *J. Mater. Sci.*, vol. 26, no. 5, pp. 1137–1156, 1991.

[187] K. Shirvani, S. Mastali, a. Rashidghamat, and H. Abdollahpour, “The effect of silicon on thermal shock performance of aluminide-thermal barrier coatings,” *Corros. Sci.*, vol. 75, pp. 142–147, 2013.

[188] W. K. Choo, J. H. Kim, and J. C. Yoon, “Microstructural change in austenitic Fe-30.0wt%Mn-7.8wt%Al-1.3wt%C initiated by spinodal decomposition and its influence on mechanical properties,” *Acta Metall.*, vol. 45, no. 12, pp. 4877–4885, 1997.

[189] A. Etienne, V. Massardier-Jourdan, S. Cazottes, X. Garat, M. Soler, I. Zuazo, and X. Kleber, “Ferrite Effects in Fe-Mn-Al-C Triplex Steels,” *Metall. Mater. Trans. A*, vol. 45, no. 1, pp. 324–334, Sep. 2013.

[190] H. Kim, D.-W. Suh, and N. J. Kim, “Fe–Al–Mn–C lightweight structural alloys: a review on the microstructures and mechanical properties,” *Sci. Technol. Adv. Mater.*, vol. 14, no. 1, p. 014205, Feb. 2013.

[191] J. Herrmann, G. Inden, and G. Sauthoff, “Deformation behaviour of iron-rich iron-aluminum alloys at low temperatures,” *Acta Mater.*, vol. 51, no. 10, pp. 2847–2857, 2003.

[192] K. Choi, C.-H. Seo, H. Lee, S. K. Kim, J. H. Kwak, K. G. Chin, K.-T. Park, and N. J. . Kim, “Effect of aging on the microstructure and deformation behavior of austenite base lightweight Fe–28Mn–9Al–0.8C steel,” *Scr. Mater.*, vol. 63, no. 10, pp. 1028–1031, Nov. 2010.

[193] I. Gutierrez-Urrutia and D. Raabe, “Multistage strain hardening through dislocation substructure and twinning in a high strength and ductile weight-reduced Fe-Mn-Al-C steel,” *Acta Mater.*, vol. 60, no. 16, pp. 5791–5802, 2012.

[194] C.-H. Seo, K. H. Kwon, K. Choi, K.-H. Kim, J. H. Kwak, S. Lee, and N. J. Kim, “Deformation behavior of ferrite–austenite duplex lightweight Fe–Mn–Al–C steel,” *Scr. Mater.*, vol. 66, no. 8, pp. 519–522, Apr. 2012.

[195] S. S. Sohn, B.-J. Lee, S. Lee, and J.-H. Kwak, “Effects of aluminum content on cracking phenomenon occurring during cold rolling of three ferrite-based lightweight steel,” *Acta Mater.*, vol. 61, no. 15, pp. 5626–5635, Sep. 2013.

[196] S. S. Sohn, B.-J. Lee, S. Lee, N. J. Kim, and J.-H. Kwak, “Effect of annealing temperature on microstructural modification and tensile properties in 0.35 C–3.5 Mn–5.8 Al lightweight steel,” *Acta Mater.*, vol. 61, no. 13, pp. 5050–5066, Aug. 2013.

[197] L. Bartlett and D. Van Aken, “High Manganese and Aluminum Steels for the Military and Transportation Industry,” *Jom*, vol. 66, no. 9, pp. 1770–1784, 2014.

[198] E. A. Brandes and G. B. Brook, *Smithcells metals reference book*, 7th editio. Great Brittain, Bath press, 1992.

[199] Z. H. Cai, H. Ding, R. D. K. Misra, and H. Kong, "Unique serrated flow dependence of critical stress in a hot-rolled Fe–Mn–Al–C steel," *Scr. Mater.*, vol. 71, pp. 5–8, Jan. 2014.

[200] Z. H. Cai, H. Ding, R. D. K. Misra, H. Kong, and H. Y. Wu, "Unique impact of ferrite in influencing austenite stability and deformation behavior in a hot-rolled Fe–Mn–Al–C steel," *Mater. Sci. Eng. A*, vol. 595, pp. 86–91, Feb. 2014.

[201] K. M. Chang, C. G. Chao, and T. F. Liu, "Excellent combination of strength and ductility in an Fe–9Al–28Mn–1.8C alloy," *Scr. Mater.*, vol. 63, no. 2, pp. 162–165, Jul. 2010.

[202] M.-S. Chen, H.-C. Cheng, C.-F. Huang, C.-Y. Chao, K.-L. Ou, and C.-H. Yu, "Effects of C and Cr content on high-temperature microstructures of Fe–9Al–30Mn–xC–yCr alloys," *Mater. Charact.*, vol. 61, no. 2, pp. 206–211, Feb. 2010.

[203] G. Frommeyer and J. A. Jimenez, "Structural Superplasticity at Higher Strain Rates of Hypereutectoid Fe-5.5Al-1Sn-1Cr-1.3C Steel," *Metall. Mater. Trans. A*, vol. 36, no. February, pp. 295–300, 2005.

[204] S. Y. Han, S. Y. Shin, B.-J. Lee, S. Lee, N. J. Kim, and J.-H. Kwak, "Effect of Tempering Time on Microstructure, Tensile Properties, and Deformation Behavior of a Ferritic Light-Weight Steel," *Metall. Mater. Trans. A*, vol. 44, no. 1, pp. 235–247, Aug. 2012.

[205] S. Y. Han, S. Y. Shin, H.-J. Lee, B.-J. Lee, S. Lee, N. J. Kim, and J.-H. Kwak, "Effects of Annealing Temperature on Microstructure and Tensile Properties in Ferritic Lightweight Steels," *Metall. Mater. Trans. A*, vol. 43, no. 3, pp. 843–853, Nov. 2011.

[206] S. Y. Han, S. Y. Shin, S. Lee, N. J. Kim, J.-H. Kwak, and K.-G. Chin, "Effect of Carbon Content on Cracking Phenomenon Occurring during Cold Rolling of Three Light-Weight Steel Plates," *Metall. Mater. Trans. A*, vol. 42, no. 1, pp. 138–146, Oct. 2010.

[207] J. Jeong, C.-Y. Lee, I.-J. Park, and Y.-K. Lee, "Isothermal precipitation behavior of κ-carbide in the Fe–9Mn–6Al–0.15C lightweight steel with a multiphase microstructure," *J. Alloys Compd.*, vol. 574, pp. 299–304, Oct. 2013.

[208] P. J. Jacques, "Transformation-induced plasticity for high strength formable steels," *Curr. Opin. Solid State Mater. Sci.*, vol. 8, no. 3–4, pp. 259–265, Jun. 2004.

[209] S. W. Hwang, J. H. Ji, E. G. Lee, and K.-T. Park, "Tensile deformation of a duplex Fe–20Mn–9Al–0.6C steel having the reduced specific weight," *Mater. Sci. Eng. A*, vol. 528, no. 15, pp. 5196–5203, Jun. 2011.

[210] Y. U. Heo, Y. Y. Song, S. J. Park, H. K. D. H. Bhadeshia, and D. W. Suh, "Influence of silicon in low density Fe-C-Mn-Al steel," *Metall. Mater. Trans. A Phys. Metall. Mater. Sci.*, vol. 43, no. 6, pp. 1731–1735, 2012.

[211] Y. Kimura, K. Handa, K. Hayashi, and Y. Mishima, “Microstructure control and ductility improvement of the two-phase γ-Fe/κ-(Fe, Mn)3AlC alloys in the Fe–Mn–Al–C quaternary system,” *Intermetallics*, vol. 12, no. 6, pp. 607–617, Jun. 2004.

[212] J.-W. Lee, J.-G. Duh, and J.-H. Wang, “Mechanical property evaluation of cathodic arc plasma-deposited CrN thin films on Fe–Mn–Al–C alloys,” *Surf. Coatings Technol.*, vol. 168, no. 2–3, pp. 223–230, May 2003.

[213] K.-T. Park, “Tensile deformation of low-density Fe–Mn–Al–C austenitic steels at ambient temperature,” *Scr. Mater.*, vol. 68, no. 6, pp. 375–379, Mar. 2013.

[214] J.-B. Seol, D. Raabe, P. Choi, H.-S. Park, J.-H. Kwak, and C.-G. Park, “Direct evidence for the formation of ordered carbides in a ferrite-based low-density Fe–Mn–Al–C alloy studied by transmission electron microscopy and atom probe tomography,” *Scr. Mater.*, vol. 68, no. 6, pp. 348–353, Mar. 2013.

[215] S. Y. Shin, H. Lee, S. Y. Han, C.-H. Seo, K. Choi, S. Lee, N. J. Kim, J.-H. Kwak, and K. G. Chin, “Correlation of Microstructure and Cracking Phenomenon Occurring during Hot Rolling of Lightweight Steel Plates,” *Metall. Mater. Trans. A*, vol. 41, no. 1, pp. 138–148, Oct. 2009.

[216] H. Springer and D. Raabe, “Rapid alloy prototyping: Compositional and thermo-mechanical high throughput bulk combinatorial design of structural materials based on the example of 30Mn-1.2C-xAl triplex steels,” *Acta Mater.*, vol. 60, no. 12, pp. 4950–4959, 2012.

[217] Y. Sutou, N. Kamiya, R. Umino, I. Ohnuma, and K. Ishida, “High-strength Fe–20Mn–Al–C-based Alloys with Low Density,” *ISIJ Int.*, vol. 50, no. 6, pp. 893–899, 2010.

[218] C. J. Wang and J. H. Jaw, “Study of wear behavior of nitride layers in Fe-Mn-Al-C alloys,” *Surf. Coatings Technol.*, vol. 177–178, no. 03, pp. 477–482, 2004.

[219] S. Vercammen, B. Blanpain, B. C. De Cooman, and P. Wollants, “Cold rolling behaviour of an austenitic Fe–30Mn–3Al–3Si TWIP-steel: the importance of deformation twinning,” *Acta Mater.*, vol. 52, no. 7, pp. 2005–2012, Apr. 2004.

[220] P. Zhang, S. X. Li, and Z. F. Zhang, “General relationship between strength and hardness,” *Mater. Sci. Eng. A*, vol. 529, no. 1, pp. 62–73, 2011.

[221] S. Zaefferer, J. Ohlert, and W. Bleck, “A study of microstructure, transformation mechanisms and correlation between microstructure and mechanical properties of a low alloyed TRIP steel,” *Acta Mater.*, vol. 52, no. 9, pp. 2765–2778, May 2004.

[222] C. S. Wang, C. N. Hwang, C. G. Chao, and T. F. Liu, “Phase transitions in an Fe–9Al–30Mn–2.0C alloy,” *Scr. Mater.*, vol. 57, no. 9, pp. 809–812, Nov. 2007.

[223] S.-J. Park, B. Hwang, K. H. Lee, T.-H. Lee, D.-W. Suh, and H. N. Han, “Microstructure and tensile behavior of duplex low-density steel containing 5mass% aluminum,” *Scr. Mater.*, vol. 68, no. 6, pp. 365–369, Mar. 2013.

[224] K. Ishida, H. Ohtani, N. Satoh, R. Kainuma, and T. Nishizawa, “Phase equilibria in Fe-Mn-Al-C alloys.,” *ISIJ Int.*, vol. 30, no. 8, pp. 680–686, 1990.

[225] B. L. Bramfitt, “The effect of carbide and nitride additions on the heterogeneous nucleation behavior of liquid iron,” *Metall. Trans.*, vol. 1, no. 7, pp. 1987–1995, 1970.

[226] K. Kaygusuz, “Energy and environmental issues relating to greenhouse gas emissions for sustainable development in Turkey,” *Renew. Sustain. Energy Rev.*, vol. 13, no. 1, pp. 253–270, Jan. 2009.

[227] K. Hashimoto, M. Yamasaki, K. Fujimura, T. Matsui, K. Izumiya, M. Komori, A. A. El-Moneim, E. Akiyama, H. Habazaki, N. Kumagai, A. Kawashima, and K. Asami, “Global CO2 recycling—novel materials and prospect for prevention of global warming and abundant energy supply,” *Mater. Sci. Eng. A*, vol. 267, no. 2, pp. 200–206, Jul. 1999.

[228] M. Ritzkowski and R. Stegmann, “Controlling greenhouse gas emissions through landfill in situ aeration,” *Int. J. Greenh. Gas Control*, vol. 1, no. 3, pp. 281–288, Jul. 2007.

[229] D. G. Morris, M. a. Muñoz-Morris, and L. M. Requejo, “New iron–aluminium alloy with thermally stable coherent intermetallic nanoprecipitates for enhanced high-temperature creep strength,” *Acta Mater.*, vol. 54, no. 9, pp. 2335–2341, May 2006.

[230] K. H. Kim, J. S. Lee, and D. L. Lee, “Influence of silicon on the spheroidization of cementite in nypereutectiod bearing steels,” *Mater. Sci. Forum*, vol. 654, pp. 154–157, 2010.

[231] X. F. Zhang, H. Terasaki, and Y. Komizo, “In situ investigation of structure and stability of niobium carbonitrides in an austenitic heat-resistant steel,” *Scr. Mater.*, vol. 67, no. 2, pp. 201–204, 2012.

[232] M. C. Ha, J.-K. Koo, J.-K. Lee, S. W. Hwang, and K.-T. Park, “Tensile deformation of a low density Fe–27Mn–12Al–0.8C duplex steel in association with ordered phases at ambient temperature,” *Mater. Sci. Eng. A*, vol. 586, pp. 276–283, Dec. 2013.

[233] Y. Dolinsky and T. Elperin, “Thermodynamics of nucleation in current-carrying conductors,” *Phys. Rev. B*, vol. 50, pp. 52–58, 1994.

[234] M. Calcagnotto, D. Ponge, and D. Raabe, “Effect of grain refinement to 1??m on strength and toughness of dual-phase steels,” *Mater. Sci. Eng. A*, vol. 527, no. 29–30, pp. 7832–7840, 2010.

[235] G. Avramovic-Cingara, Y. Ososkov, M. K. Jain, and D. S. Wilkinson, “Effect of martensite distribution on damage behaviour in DP600 dual phase steels,” *Mater. Sci. Eng. A*, vol. 516, no. 1–2, pp. 7–16, 2009.

[236] K. Mukherjee, S. S. Hazra, and M. Militzer, “Grain refinement in dual-phase steels,” *Metall. Mater. Trans. A Phys. Metall. Mater. Sci.*, vol. 40, no. 9, pp. 2145–2159, 2009.

[237] W. Gan, S. S. Babu, N. Kapustka, and R. H. Wagoner, "Microstructural effects on the springback of advanced high-strength steel," *Metall. Mater. Trans. A Phys. Metall. Mater. Sci.*, vol. 37, no. 11, pp. 3221–3231, 2006.

[238] C. W. Zheng, D. Raabe, and D. Z. Li, "Prediction of post-dynamic austenite-to-ferrite transformation and reverse transformation in a low-carbon steel by cellular automaton modeling," *Acta Mater.*, vol. 60, no. 12, pp. 4768–4779, 2012.

[239] M. Delincé, Y. Bréchet, J. D. Embury, M. . D. Geers, P. J. Jacques, and T. Pardoen, "Structure-property optimization of ultrafine-grained dual-phase steels using a microstructure-based strain hardening model," *Acta Mater.*, vol. 55, no. 7, pp. 2337–2350, 2007.

[240] E. Biro, J. R. McDermid, S. Vignier, and Y. Norman Zhou, "Decoupling of the softening processes during rapid tempering of a martensitic steel," *Mater. Sci. Eng. A*, vol. 615, pp. 395–404, 2014.

[241] D. C. Saha, D. Westerbaan, S. S. Nayak, E. Biro, A. P. Gerlich, and Y. Zhou, "Microstructure-properties correlation in fiber laser welding of dual-phase and HSLA steels," *Mater. Sci. Eng. A*, vol. 607, pp. 445–453, 2014.

[242] V. H. Baltazar Hernandez, S. S. Nayak, and Y. Zhou, "Tempering of martensite in dual-phase steels and its effects on softening behavior," *Metall. Mater. Trans. A Phys. Metall. Mater. Sci.*, vol. 42, no. 10, pp. 3115–3129, 2011.

[243] N. Sreenivasan, M. Xia, S. Lawson, and Y. Zhou, "Effect of Laser Welding on Formability of DP980 steel," *J. Eng. Mater. Technol.*, vol. 130, no. 4, p. 041004, 2008.

[244] M. M. Xia, E. Biro, Z. L. Tian, and Y. N. Zhou, "Effects of Heat Input and Martensite on HAZ Softening in Laser Welding of Dual Phase Steels," *ISIJ Int.*, vol. 48, no. 6, pp. 809–814, 2008.

[245] S. K. Panda, N. Sreenivasan, M. L. Kuntz, and Y. Zhou, "Numerical Simulations and Experimental Results of Tensile Test Behavior of Laser Butt Welded DP980 Steels," *Jounral Eng. Mater. Technol.*, vol. 130, pp. 769–776, 2008.

[246] T. Furuhara, K. Kobayashi, and T. Maki, "Control of Cementite Precipitation in Lath Martensite by Rapid Heating and Tempering," *ISIJ Int.*, vol. 44, no. 11, pp. 1937–1944, 2004.

[247] N. Farabi, D. L. Chen, J. Li, Y. Zhou, and S. J. Dong, "Microstructure and mechanical properties of laser welded DP600 steel joints," *Mater. Sci. Eng. A*, vol. 527, no. 4–5, pp. 1215–1222, 2010.

[248] A. Inoue and K. Hashimoto, *Amorphous and Nano-crystalline Materials: Preparation, Properties, and Application*, 1st editio. Springer International Publishing Switerland, 2001.

Chapter 9 Appendix

Publication list

1. W. J. Lu, X.F. Zhang, R. S. Qin
   The stability of precipitates under electropulsing in 316L stainless steel

   Materials Science and Technology, DOI: 10.1179/1743284714Y.0000000743, (2015)

2. W.J. Lu and R.S. Qin
   Effects of electropulsing on the microstructure evolution of 316L stainless steel

   Advanced Materials Research, Vol. 922, pp. 441-445 (2014)

3. W. J. Lu, X.F. Zhang, R. S. Qin
   Electropulsing-induced steels strengthening at high temperature

   Philosophical Magazine Letters, Vol.94, pp.688-695 (2014)

4. W. J. Lu, X.F. Zhang, R. S. Qin
   κ-carbide hardening in a low-density high-Al high-Mn multiphase steel

   Materials Letters, Vol. 138, pp. 96-99 (2015)

5. W. J. Lu, X.F. Zhang, R. S. Qin
   The structure and properties of κ-carbides in duplex lightweight steels

   Ironmaking & Steelmakingy, DOI: 10.1179/1743281215Y.0000000007, (2015)

6. X.F. Zhang, W.J. Lu, and R.S. Qin
   Removal of MnS inclusions in molten steel using electropulsing

   Scripta Materialia, Vol. 69, pp 453-456, (2013).

7. X.F. Zhang, W. J. Lu, R. S. Qin
   Morphology and distribution control of MnS inclusions in molten steel by electropulsing *Materials Research Innovations*, Vol. 18, pp. 244-248, (2014).

8. X.F. Zhang, W. J. Lu, R. S. Qin
   Oriented sulphides induced by electric current in medium carbon steel

   Philosophical Magazine Letters, Vol. 95, pp. 101–109, (2015).

9. R.S. Qin, A. Rahnama, W.J. Lu, X.F. Zhang, B. Elliott-Bowman
   Electropulsed steels

   Materials Science and Technology, Vol. 30, pp.1040-1044 (2014)